

Aus dem Bereich der Biophysik
Theoretische Medizin und Biowissenschaften
der Medizinischen Fakultät
der Universität des Saarlandes, Homburg/Saar

**Voltammetric and Electron Spin Resonance Studies
of Cyclic Hydroxylamine CMH and Its Application
to Monitor Transient Radicals in
Dioxygenase Enzymes**

*Dissertation zur Erlangung des Grades eines
Doktors der Naturwissenschaften*
der Medizinischen Fakultät
der UNIVERSITÄT DES SAARLANDES

2016

vorgelegt von: Nhat Nguyen Bui
geb. am: 07.11.1984 in Thua Thien Hue, Vietnam

Nhat Nguyen Bui

Institut für Biophysik

Kirrbergerstr. Geb. 48

66424 Homburg/Saar, Deutschland

E-Mail: nguyen.bui@uks.eu

CONTENTS

ZUSAMMENFASSUNG	I
SUMMARY	IV
LIST OF TABLES	vi
LIST OF FIGURES	vii
LIST OF ABBREVIATIONS.....	xvii
1. Introduction	1
2. Methodology.....	5
2.1. Voltammetry	5
2.1.1. Cyclic voltammetry	8
2.1.2. Differential Pulse Voltammetry (DPV).....	11
2.1.3. Square-wave Voltammetry (SWV)	11
2.2. Electron Paramagnetic Resonance (EPR) Spectroscopy.....	13
Relaxation and saturation	15
Hyperfine splitting.....	16
Powder EPR	18
g-anisotropy	18
Zero-field splitting	19
EPR spectrum of TEMPOL.....	19
Co-spectrum	21
Evaluation of CMH and TAM measurements in enzyme reactions	22
2.3. Dioxygenases	25
2.3.1. Metal-cofactor of quercetinases	26
2.3.2. 1H-3-Hydroxy-4-oxoquinoline 2,4-dioxygenase (Hod)	32
3. Materials and Methods	34
3.1. Materials	34
3.2. Methods	35
3.2.1. Electron Paramagnetic Resonance (EPR)	35
3.2.2. Voltammetry	36
3.2.3. Nuclear Magnetic Resonance (NMR)	37
3.2.4. Fluorescence Spectroscopy	37
4. Results.....	38

4.1.	CMH	38
4.1.1.	Redox properties and reactions of CMH.....	39
	Redox behaviour of CMH.....	39
	Effect of pH on CMH redox behavior	42
	Reaction of CMH with oxygen (O ₂)	52
	Reaction of CMH with superoxide (KO ₂) and hydrogen peroxide (H ₂ O ₂).....	54
4.1.2.	CMH application for H ₂ O ₂ quantification in HRP assay.....	61
	Reaction stoichiometry of H ₂ O ₂ with CMH	63
4.2.	Cofactor-independent 1 <i>H</i> -3-Hydroxy-4-oxoquinaldine 2,4-dioxygenase (Hod)	66
	Transient radicals were detected with CMH for the enzymatic reaction pathway identification.	67
	The Stoichiometry of the Products of CMH Oxidation Reveals that Two Radical Species are Formed in the Hod Reaction.	69
	Redox behavior of MHOQ and BHOQ was studied with cyclic voltammetry.....	70
4.3.	Metal-cofactor Quercetin-2,4-dioxygenase (Quercetinase, QueD).....	75
4.3.1.	Redox properties of flavonol substrates (Quercetin, Myricetin, Rhamnetin, 3-Hydroxyflavone). 76	
4.3.2.	Roles of the metal-binding site and transient radical detection with CMH in the enzymatic reaction pathway of Quercetinase.....	83
5.	Discussion	102
	Redox properties and reactivity of cyclic hydroxylamines	102
	Towards the reaction mechanism of Hod and quercetinase enzymes	107
	Reaction intermediates in Hod enzyme and mechanistic details.....	108
	Detection of oxidative intermediates and mechanistic implication for Quercetinase.....	110
	APPENDIX	118
	REFERENCES	124
	PUBLICATIONS.....	137
	ACKNOWLEDGEMENTS	138
	CURRICULUM VITAE.....	139

ZUSAMMENFASSUNG

In dieser Arbeit werden die zyklischen Hydroxylamine 1-Hydroxy-3-Methoxycarbonyl-2,2,5,5-Tetramethyl-Pyrrolidin (CMH) und 1-Hydroxy-3-Carboxy-2,2,5,5-Tetramethyl-Pyrrolidin (CPH) hinsichtlich ihrer Anwendung als Spinsonden in biologischen und physiologischen Systemen untersucht. Insbesondere wird der katalytische Mechanismus von zwei Dioxygenasen bakteriellen Ursprungs, der kofaktor-freien 1*H*-3-Hydroxy-4-Oxoquinaldine 2,4-Dioxygenase (Hod) und der metallhaltigen Quercetin-2,4-Dioxygenase (Quercetinase, QueD), charakterisiert.

Induziert durch Redoxprozesse transformiert die CMH Spinsonde zu einem recht stabilen Nitroxid-Radikal, das mit Elektron Spin Resonanz (EPR) Techniken erfasst werden kann, und das damit hochsensitiv als Monitor für biologisch wichtige und transiente organische Radikale und physiologisch relevante reaktive Sauerstoffspezies (ROS) wie Superoxid und Wasserstoffperoxid dienen kann. Mit Hilfe der EPR Spektroskopie werden die Elektrontransfereigenschaften des CMH genutzt, um die Bildung der sehr kurzlebigen transienten Radikale (oder Radikalpaare) in der ringspaltenden Konversion der Substrate durch Hod und QueD Enzyme zu verfolgen.

Um die Randbedingungen der in solchen komplexen Enzymreaktionen möglichen Elektrontransferprozesse zu verstehen, wurden mit voltammetrischen Methoden Redoxuntersuchungen der relevanten redoxaktiven Spezies (CMH, CPH sowie Substrate) durchgeführt. Die so erhaltenen grundlegenden Informationen zum Elektrontransfer, zu den Mittelpunktspotenzialen und den pH-Abhängigkeiten erwiesen sich als essenziell, um die Redoxreaktionen in den Dioxygenasen zu klären.

Das Hod-Enzym ist eine Dioxygenase, die weder einen Kofaktor noch ein Metallion für die Katalyse enthält oder benötigt. In enger Kooperation mit der Mikrobiologie-Gruppe der Universität Münster konnte durch chemische Analyse und durch EPR-Daten aus Messungen mit der Spinprobe CMH gezeigt werden, dass als erster Schritt der Reaktion der Transfer eines einzelnen Elektrons vom gebundenen Substrat zu O₂ stattfindet, und ein Radikalpaar entsteht, welches dann zum Peroxyintermediat rekombiniert. Diese Arbeit verfolgte gezielt den voltammetrischen Ansatz, um die Randbedingungen für den Elektrontransfer zwischen Substrat und Sauerstoff zu erfassen. In dem abgeleiteten Modell einer „Substrat-assistierten Sauerstoffaktivierung“ ist es die wesentliche Funktion des Enzyms, das Umfeld für die

Bildung des Substratanions und die Anpassung der Redoxbedingungen für einen effektiven Elektrontransfer vom Substrat zum O₂ bereit zu stellen.

Als zweites Enzym wurde die Quercetinase untersucht, die zur Gruppe der metallhaltigen Dioxygenasen gehört. Abhängig von ihrem Ursprung können diese verschiedene divalente Metalle einbauen; so ist z.B. die QueD aus *Aspergillus* spp (Pilz) ein Kupferprotein, während die bakterielle QueD aus *B. subtilis* mit Mn²⁺ am aktivsten ist. Unsere Untersuchungen befassten sich mit dem katalytischen Reaktionsmechanismus der kambialistischen QueD aus *Streptomyces* sp strain FLA, die mit Ni die höchste Aktivität zeigt gefolgt von Co und Mn. Wichtige Erkenntnisse zum Reaktionsmechanismus konnten aus EPR-Messungen abgeleitet werden, mit denen wiederum unter Ausnutzung der Elektrontransfereigenschaften des CMH die Existenz intermediärer Radikalzustände in den CoQueD-Varianten E76H, Y117A und I66A nachgewiesen werden konnten. Diese transienten Zustände in den Proteinvarianten haben eine längere Lebenszeit und sind für einen Elektronenübertrag von CMH besser zugänglich, was in der Wild Typ Form offensichtlich nicht gegeben ist. Die Erhaltung des Valenzzustandes des Metallions wurde mit Hilfe der EPR gezeigt, was darauf hindeutet, dass das Metall nicht direkt an Redoxübergängen (Elektrontransfers) der Katalyse beteiligt ist. Die Modifikation der Ligandenumgebung des Co in der E76H-Variante führt zu einem oder zwei spingekoppelten Radikalen in der Nähe des Co-Ions, was für die Variante NiQueD-E76H nicht beobachtet wurde. In CoQueD-E76H, nicht jedoch in NiQueD-E76H, läuft die Aktivierung des Substrates ohne Beteiligung des Sauerstoffs ab, was den Einfluss der elektronischen Eigenschaften des Metallions auf den Aktivierungsmechanismus bestätigt.

Die vorliegende Arbeit beschreibt zudem die Entwicklung einer EPR-basierten Nachweismethode für das an sich nicht EPR-aktive H₂O₂ durch CMH als Elektronendonator. Dieser Teilaspekt wurde initiiert durch die Notwendigkeit, das in Hod durch Reduktion des transienten Superoxids mit CMH erzeugte Wasserstoffperoxid quantitativ zu bestimmen. Diese EPR-basierte Methode stellt damit ein weiteres Werkzeug dar, in physiologischen Systemen das durch katalysierte oder spontane Dismutierung von Superoxid gebildete Wasserstoffperoxid als eine wichtige Komponente der ROS nachzuweisen. Es wird gezeigt, dass CMH als Kosubstrat der Meerrettich-Peroxidase fungiert und mit H₂O₂ in einem strikten Verhältnis von 2:1 korreliert ist. Im Prinzip erlaubt es dieser Assay, die Produktion von Superoxid und die folgende Bildung von H₂O₂ im selben experimentellen Ansatz zu

bestimmen. Er wird beispielhaft auf ein Superoxid produzierendes System angewendet und mit fluoreszenz-basierten Methoden verglichen.

SUMMARY

The thesis presents the study of cyclic hydroxylamine 1-hydroxy-3-methoxycarbonyl-2,2,5,5-tetramethyl-pyrrolidine (CMH) and 1-hydroxy-3-carboxy-2,2,5,5-tetramethyl-pyrrolidine (CPH) for application as spin probes in biological and physiological systems, particularly for characterizing the catalytic reaction mechanism of two dioxygenase enzymes, the cofactor-independent 1*H*-3-Hydroxy-4-oxoquinaldine 2,4-dioxygenase (Hod) and the metal-cofactor containing quercetin-2,4-dioxygenase (Quercetinase, QueD), both of bacterial origin.

Induced by redox processes the CMH spin probe is transforming to a quite stable nitroxide radical, accessible by electron paramagnetic resonance (EPR) techniques, and is highly sensitive to monitor biologically important transient organic radicals and physiologically relevant reactive oxygen species (ROS), superoxide and hydrogen peroxide. Using EPR spectroscopy, the electron transfer properties of CMH were exploited to monitor the formation of very short-lived transient radicals (or radical pairs) in the 2,4-dioxygenolytic ring cleaving conversion of substrates by Hod and QueD enzymes.

To understand the prerequisites for possible electron transfer reactions occurring in such complex enzyme reactions, redox studies of all relevant redox active species (CMH, CPH and enzyme substrates) were performed by using voltammetric methods. Fundamental information on electron transfer, mid-peak potential and pH-dependency were obtained and proved to be essential to explain the redox reactions in the dioxygenases.

Hod enzyme is a dioxygenase that is known not to contain or require any cofactor or metal ions for catalysis. In close cooperation with a microbiological group (University Münster), its catalytic reaction was shown to start with a single electron transfer from the bound substrate anion to O₂ forming a radical pair, which then recombines to a peroxide intermediate, as proven by chemical analysis and EPR data obtained from interaction studies of the spin probe CMH. This work was focusing on the voltammetric approach to explore the conditions for electron transfer between substrate and dioxygen. In the derived model of “substrate assisted oxygen activation”, the major role of the enzyme is to provide an environment for substrate anion formation and for adjusting the reaction conditions for efficient electron transfer from the substrate anion to O₂.

The second studied enzyme, quercetinase, belongs to the group of metal-containing dioxygenases. Depending on their origin, they are known to be capable of incorporating

different divalent metal ions, for example fungal *Aspergillus* spp. QueD is a copper protein while bacterial *B. subtilis* QueD is most active with Mn^{2+} . Our study focused on researching the catalytic reaction mechanism of the cambialistic QueD from *Streptomyces* sp. strain FLA, that is most active with Ni followed by Co and Mn. Important insights into the reaction mechanism were derived from EPR studies proving the presence of intermediate radical states for CoQueD variants E76H, Y117A and I66A exploiting the electron transfer properties of CMH. In contrast to the wild type QueD, these transient states in the variant proteins are sufficiently long-lived and better accessible for electron transfer from CMH, which is obviously impeded in the wild type protein. The conservation of valence state of metal ions has been proven by EPR analysis that proposes a non-redox role of metal cofactor in catalysis. Modification of Co ligand sphere in the E76H variant leads to one or two radicals close to the Co-center showing spin coupling, which was not seen for NiQueD-E76H. In CoQueD-E76H but not in NiQueD-E76H, activation of substrate is shown to occur without participation of oxygen and thus confirms the importance of electronic properties of the metal ion for the activation mechanism.

The thesis also describes the development of an EPR-based method to determine the otherwise EPR-silent H_2O_2 by exploiting CMH as an electron donor. This piece of work was initially inspired by the necessity to quantitatively measure hydrogen peroxide produced by reduction of transient superoxide with CMH for the Hod enzyme. This EPR-based method is providing an additional tool applicable to physiological systems, where hydrogen peroxide is also formed in the catalyzed or spontaneous dismutation of superoxide as an essential ROS. We show that CMH serves as a co-substrate for horseradish peroxidase correlating to H_2O_2 in a strict 2:1 ratio. In principle, the assay allows to measure superoxide production and subsequent H_2O_2 formation in the same experimental setting. As an example, it is applied to superoxide producing systems and compared to standard fluorescence based methods.

LIST OF TABLES

Table 2-1. Standard reduction potentials of selected transition metal cations (adapted from Fetzner S.).....	31
Table 4-1. Experimental chemical shifts of CMH and CPH in neutral and alkaline solutions (pD 8, 13).....	50
Table 4-2. Apparent Steady-state Kinetic Parameters of HodC and HodC-W160A.....	68
Table 4-3. Midpotential E_{mid} (vs. SHE) of flavonols in PB (50 mM, pH 7.4).....	81

LIST OF FIGURES

- Figure 2-1. Simple electrode reaction (adapted from reference)..... 7
- Figure 2-2. Models of the electrical double layer at a positively charged surface: (a) the Helmholtz model, (b) the Gouy–Chapman model, and (c) the Stern model, showing the inner Helmholtz plane (IHP) and outer Helmholtz plane (OHP). The IHP refers to the distance of closest approach of specifically adsorbed ions (generally anions) and OHP refers to that of the non-specifically adsorbed ions. The OHP is also the plane where the diffuse layer begins. d is the double layer distance described by the Helmholtz model. The potential ψ_0 and ψ at the electrode surface and the electrode/electrolyte interface, respectively, are indicated as black graphs according to the model (adapted from reference)..... 8
- Figure 2-3. (Left panel) Cyclic voltammetry potential waveform. (Right panel) Typical cyclic voltammogram where i_{pc} , E_{pc} and i_{pa} , E_{pa} show the peak cathodic and anodic current and potential respectively for a reversible reaction (adapted from reference). 9
- Figure 2-4. (Left panel) Square-wave waveform showing the amplitude E_{sw} , step height ΔE , square-wave period T , delay time T_d , and current measurement times 1 and 2 (adapted from). (Right panel) Square-wave voltammogram of two electrode reactions of CMH (2mM) in PB (pH 7.4, 50 mM), in which the net current is indicated in black, forward current in light grey and backward in grey. Parameters were amplitude 50 mV, step height ΔE 5 mV and frequency 10 Hz..... 13
- Figure 2-5. EPR absorption spectrum (left) and first derivative spectrum (right part). The red dotted line indicates the correspondence of absorption maximum and zero crossing of derivative spectrum.. 15
- Figure 2-6. Nitroxide EPR single crystal spectra (left panel) along the principal axes show different field position due to anisotropic g -factor and variable hyperfine couplings of ^{14}N nucleus ($m_I = -1, 0, +1$) for the anisotropic A -tensor. For a solution spectrum (right panel) the isotropic hyperfine splitting of the triplet signal is observed according to the transitions between the energy states (upper graph). (Taken from Bordignon-tutorial)..... 20
- Figure 2-7. (Left panel) Temporal evolution of EPR spectra in the HodC reaction with BHOQ. The single spectrum (top) indicates the spectral segment used for presentation of intensity changes of CM and TAM radical signals. (Right panel, top) EPR spectra of CM and TAM radicals for different reaction times. While the intensity of CM is increasing, the TAM signal is attenuated for the decrease in concentration of dissolved oxygen. The blue and red rectangles indicate the lines of both radicals used for evaluation of concentration. The chemical structure of TAM (tetrathiatriarylmethyl radical) is shown in lower right panel..... 23
- Figure 2-8. Evolution of CM^\bullet signal (solid black line) and decay curve of TAM^\bullet (dotted black line) in the conversion of BHOQ by HodC. The CM^\bullet signal is referenced to the left y-axis, while TAM signal

- is related to the right y-axis (100% O₂ corresponds to about 220 μM dissolved oxygen). The maximal (saturated) CM[•] concentration of 38.4 ± 0.02 μM and characteristic time t of 540.5 ± 2.5 s are determined from the Weibull fit (green dashed trace). Initial rates of CM[•] formation (3.15 ± 0.06 μM/min) and O₂ consumption (11.3 ± 0.02 μM/min) are derived from linear fits (red and magenta solid lines). 25
- Figure 2-9. Crystal structure of *A. japonicas* QueD (cyan) and *B. subtilis* QueD (blue). In each structure, two beta-barrel folds can be seen, but in *A. japonicas* QueD only one domain contains a metal ion. Copper ions are shown in magenta; iron ions are shown in red. Some residues of the cupin domain are colored orange and yellow. These residues are metal-binding (HHEH) in both domains of *B. subtilis* QueD and the N-terminal domain of *A. japonicas* QueD, but they are non-metal-binding (FFNF) in *A. japonicas* QueD's C-terminal domain (adapted from). 28
- Figure 2-10. Hypothetical reaction mechanism of bacterial quercetinases (*Streptomyces* QueD) (adapted from Fetzner S.). 31
- Figure 2-11. Catalytic dyad residues in the active site of dioxygenase Hod, the substrate is shown in yellow (adapted from Fetzner S.). 33
- Figure 4-1. Cyclic voltammogram (CV) of CMH (2 mM) in PB (50 mM, pH 7) at 100 mV/s scan rate shows two well separated redox transitions, CM[•]/CMH (I) and CM⁺/CM[•] (II). E_{p,a} and E_{p,c} stand for oxidation and reduction peak potentials, respectively. The mid-peak potentials, E_{mid} = ½ (E_{p,a} + E_{p,c}), of transition I and II are +0.15 V and +0.91 V (vs. SHE), respectively. 39
- Figure 4-2. Oxidation and reduction currents of redox couple CM[•]/CMH (A) and CM⁺/CM[•] (B) vs. square root of scan rate (v^{1/2}) in PB (50 mM, pH 7). Oxidation and reduction potentials of redox couple CM[•]/CMH (C) and CM⁺/CM[•] (D) vs. logarithm of scan rate (log v) in PB (50 mM, pH 7). All values were derived from CVs of scan rate variation (10, 20, 50...500 mV/s) (Figure A 1 in Appendix). Red lines are linear fits and the corresponding functions are given. Both transitions are diffusion controlled as described by the linear correlation of i_p vs. v^{1/2}, transition I is quasi-reversible with one electron transfer derived from linear fit function of E_p vs. log v, whereas transition II is fully-reversible with independent potential vs. log v. 41
- Figure 4-3. (Left panel) Selected CVs of CMH (2 mM) in PB (50 mM) in the range of pH 1-14 at 100 mV/s scan rate show the shift in potential of transition I, whereas transition II remains unaffected. Color code in figure legend indicates pH of solution. Arrows indicate the oxidation/reduction waves of the variable transition I (dotted arrows) and stable transition II (solid arrows). (Right panel) pH dependence of mid-peak potentials (E_{mid}) of redox couples CM[•]/CMH (I) and CM⁺/CM[•] (II) in pH 1-14, E_{mid} was derived from the CVs in the left panel. In pH range 2-12 transition I is linearly dependent on pH with a shift of -68.8 mV of E_{mid} per pH unit while transition II is pH independent. At pH > 12 CMH is assumed to transform to CPH (see NMR data below in Figure 4-4, Figure 4-5). 42

- Figure 4-4. $^1\text{H-NMR}$ data of CMH (5 mM) in pD 1, pD 3, pD 8 and pD 13. The asterisks are indicative for the signals of CMH observed at pH 8, 12 protons of 4 methyl CH_3 groups (δ 1.1-1.4), 2 multiplet lines of methylene CH_2 group (δ 2.0-2.2), 1 doublet of doublet pattern of CH group (δ 3.0-3.1) and a singlet line of 3 protons of methyl CH_3 of methoxy group (δ 3.7), which remained identically at pD 13. At pD 13, CMH transforms to CPH in the hydroxyl-substitution reaction with an inequivalent ratio, the balls represent signals of CPH, the heart indicates the methoxy group which was released after the hydroxyl group attack. At pD 3 spectral pattern and proton number are maintained, but all signals shift to higher ppm and become broader, whereas at extreme pD 1 the spectrum shows a symmetrical splitting with respect to two different CMH configurations, most probably due to the steric effect caused by the attachment of deuterium ion (D^+) to the lone electron pair of the nitroxide group. 46
- Figure 4-5. $^1\text{H-NMR}$ data of CPH (5 mM) in pD 1, pD 3, pD 8 and pD 13. The red balls display the signals of CPH at pD 8, which is identical to signals found in CMH pD 13 (Figure 4-4), four methyl CH_3 groups (δ 1.3-1.5), two methylene CH_2 (δ 2.1-2.3) and one CH group (δ 2.7-3.1). As observed for CMH, the signals shift to higher ppm, get broader at pD 3 and show a splitting at pD 1, whereas the spectrum is conserved at pD 13 with only a slight shift and line broadening. 48
- Figure 4-6. Enlarged $^1\text{H-NMR}$ signals of (A) methyl-proton resonance and (B) methylene- and methine (methanetriyl)proton resonance patterns of CMH (pD 8 – black line, pD 13 – blue line), CPH (pD 13 – red line). In panel A, the methyl-proton pattern, the blue lines (CMH, pD13) are composed of black lines (CMH, pD8) and red lines (CPH, pD13). The three additional lines (marked with asterisk) of CMH pD13 spectrum are arising from CPH methyl protons, and one (marked with ball) is superimposing with a CMH resonance. In panel B the new line (2.82 ppm) (marked with asterisk) in CMH at pD13 is associated to the corresponding CPH CH-ring proton. The same holds for the methylene protons of CPH (apart from line width). 49
- Figure 4-7. CVs of 2 mM CMH (blue line) and CPH (magenta line), both recorded at 100 mV/s scan rate, and CPH at 900 mV/s (grey line) in PB (50 mM, pH 7.4). The arrow points at the oxidation wave of CPH (900 mV/s) (transition I) which is only pronounced at high scan rate (>250 mV/s). The mid-peak potentials E_{mid} of redox couples $\text{CP}^\bullet/\text{CPH}$ and $\text{CP}^+/\text{CP}^\bullet$ were -0.05 V and $+0.87$ V (vs. SHE), respectively. The absence of the first oxidation wave of CPH (pH 7.4, 100 mV/s) is consistent with the diminishing current of transition I in CMH at pH 13, associated with the transformation of CMH to CPH at high pH (>12.5) (refer to Figure 4-3). 51
- Figure 4-8. Modeling of CMH protonation states was obtained from webpage calculation <http://aceorganic.pearsoncmg.com/epoch-plugin/public/pKa.js> - doubly protonated CMH-H^+ at $\text{pH}<2$, mono-protonated CMH at $2<\text{pH}<12$ and deprotonated CM^- at $\text{pH}>12$ 52
- Figure 4-9. (Left panel) CM^\bullet background formation of CMH (2 mM) in solutions of pH 2 (olive), pH 7 (black) and pH 13 (magenta). Condition with O_2 presence is shown as solid curves and without O_2 as

dotted curves. The initial formation of CM^\bullet was observed by linearly fitting the initial phase of all curves (conditions, or measurements). pH 13 shows a massively high increase of CM^\bullet and saturates when O_2 is consumed. The same behavior with much smaller signal is observed for pH 7 while nearly no CM^\bullet formation is seen for pH 2. Right panel shows the evolution of CM^\bullet at pH 13. Parameters were set to 0.02 mT modulation amplitude, 0.63 mW microwave power, 20 ms time constant for all measurements. 53

Figure 4-10. (Left panel) CVs of CMH (2 mM) with increasing concentrations of KO_2 in PB (50 mM, pH 7) at 100 mV/s scan rate. By addition of KO_2 , the redox couple $\text{CM}^\bullet/\text{CMH}$ is not affected, whereas the current of redox couple $\text{CM}^+/\text{CM}^\bullet$ is increased with oxidation ($i_{p,a}$) and reduction current ($i_{p,c}$) depending on the KO_2 concentration added (shown in the right panel). Both currents increase linearly but unequally with increasing KO_2 concentration, the oxidation peak current shows a slope of 5.2 μA per 1 mM KO_2 , which is 13-fold higher than the reduction current (slope of -0.4). A new reduction peak at -0.55 V, observed on the reverse scan of CV, is associated to the reduction of O_2 55

Figure 4-11. (A) Reaction kinetics of CMH (1 mM) with added KO_2 in PB (50 mM, pH 7) forming CM^\bullet is shown in dots. Color code indicates addition of different concentrations KO_2 (0.2, 0.5, 1 to 11 mM). Integrated fits are shown in red curves. EPR parameters were set to 0.02 mT modulation amplitude, 0.63 mW microwave power, 20 ms time constant. In the first 10 – 20 minutes an initial steep increase of CM^\bullet signal is observed, the maximum concentrations of CM^\bullet (1 mM) increase up to roughly equimolar condition (1 mM KO_2 addition) and then decrease with higher KO_2 concentrations (with exception of 0.2 mM KO_2 addition). The rate constant k_2 of the later slow decay, as derived from the integrated fit functions of panel A, are plotted against KO_2 concentration and shown in panel B. (C) Individual spectra of CM^\bullet formed at different pH (1, 2, 7) in the reaction of 2 mM CMH and 4 mM KO_2 57

Figure 4-12. Reaction kinetics of 0.5 mM CMH with different concentrations of H_2O_2 (0, 0.05, up to 3 mM) in PB (50 mM, pH 7). EPR parameters were set to 0.02 mT modulation amplitude, 0.63 mW microwave power, 20 ms time constant. Only small signals around the CM^\bullet background are observed independent on H_2O_2 concentration. 58

Figure 4-13. (Left panel) CVs of CMH (1 mM) with increasing concentrations of H_2O_2 in PB, pH 7 at 100 mV/s scan rate. Similar behavior is observed as for the KO_2 addition, the redox couple $\text{CM}^\bullet/\text{CMH}$ is unaffected, but both oxidation ($i_{p,a}$) and reduction current ($i_{p,c}$) of redox couple $\text{CM}^+/\text{CM}^\bullet$ are increased by adding H_2O_2 as shown in the right panel. However, again the increment of current is unsymmetrical; the oxidation peak current shows a slope of 7.9 μA per 1 mM H_2O_2 , which is 3.4-fold higher than the reduction current (slope of -2.3). A new reduction peak at -0.55 V again associated to the reduction of O_2 is observed on the reverse scan. 59

Figure 4-14. Concentration dependence of redox potentials for some relevant redox couples. By definition, the possible electron transfer is driven from a reduced species (more negative potential on the right hand side) to an oxidized species (more positive potential on the left hand side) and can occur thermodynamically. In this diagram, CMH can be reduced to CM^{\bullet} by $O_2^{\bullet-}/O_2^{2-}$ (arrow 1), or also by H_2O_2/H_2O , OH^{\bullet} (arrow 3), but is not affected by ascorbate ($AscH^-$). On the other hand, CM^{\bullet} is possibly oxidized to CM^+ by high flux of $O_2^{\bullet-}$ albeit with a smaller driving force (arrow 2), as well as being reduced to CMH by ascorbyl radical (Asc^{\bullet}). However, the dismutation of CM^{\bullet} is not favored in this diagram (dashed arrow 1). 61

Figure 4-15. Reaction kinetics of CMH oxidation in the assay of HRP with H_2O_2 concentration of 0.1-10 μM (A) and 10-100 μM (B). The H_2O_2 concentrations are given for each trace and were added to the assay mixture of CMH (600 μM) and HRP (1 U/ml (catalyzed for 0.1- 2 $\mu M H_2O_2$), 5 U/ml (5-10 $\mu M H_2O_2$) and 50 U/ml (10-100 $\mu M H_2O_2$)) in PB (50 mM, pH 7.4) solution. The parameters of EPR measurements were set at 0.1 mT modulation amplitude, 0.2 mW microwave power. All reaction curves were background corrected and show a typical linear initial increase and later saturation of CM^{\bullet} signal. (C) Calibration curve of H_2O_2 and CMH in the HRP assay (black scatter) as shown by plotting the saturating CM^{\bullet} concentrations, derived from reaction curves in panel A-B, against H_2O_2 concentration. The slope of 2.1, derived from the linear equation, represents the reaction stoichiometry of CMH: H_2O_2 which is close to the expected 2:1 stoichiometry. 65

Figure 4-16. Kinetic analysis of fluorescent signal of resorufin caused by Amplex UltraRed oxidation in the assay of HRP with H_2O_2 concentrations of 0.1-10 μM (left panel). Color code identifies the H_2O_2 concentration that was added to the assay mixture of 15 μM Amplex UltraRed and 25 mU/ml HRP in PB (50 mM, pH 7.4) solution. All reaction curves were background subtracted and partly show a typical linear initial increase and later saturation of fluorescent resorufin signals. The right panel shows the calibration curve, plotting the fluorescence signals, derived from the saturating signals of resorufin on the left panel, against H_2O_2 concentration (black scatter). An excellent linearity, as judged from the coefficients of determination (R^2) of 0.9988, is observed for the linear fit of calibration curve (red line). Fluorescence was measured with a fluorescence-based 96-well plate reader using excitation at 535 ± 9 nm and emission at 590 ± 20 nm. Data are the mean of triplicate readings. Experiments were performed with E. Slowik..... 66

Figure 4-17. Kinetics of CM^{\bullet} formation and O_2 consumption during the enzyme-catalyzed conversion of MHOQ (A) and BHOQ (B). The contents of the assay mixtures are indicated in the insets. Solid lines: formation of CM^{\bullet} ; dashed lines: consumption of dioxygen, as deduced from the time course of the TAM signals. Constant intensities of the TAM signal from control experiments were defined to correspond to 100% of dissolved O_2 . The stable minimum of the TAM intensity after conversion of MHOQ and BHOQ by HodC or HodC-W160A, respectively, was assumed to represent 0% O_2 . Traces are the means of at least 3 replicates. 69

- Figure 4-18. Concentrations of CM^\bullet and H_2O_2 , formed during the HodC-W160A catalyzed oxidation of different concentrations of BHOQ. All reactions were incubated until full conversion of the organic substrate. Final CM^\bullet concentrations were corrected for background oxidation, and the corresponding H_2O_2 concentrations were corrected for the spontaneous decay of H_2O_2 as deduced from control experiments..... 70
- Figure 4-19. Cyclic voltammograms and pH-dependence. Graph A shows the CV of 0.4 mM MHOQ (black, line) and BHOQ (black, dashed) recorded with a scan rate of 100 mV/s at pH 7.8 and 7.4 (PB 50 mM), respectively. The arrows indicate the first oxidation peak and the less intense reduction peak which were used to estimate the mid-peak redox potential for MHOQ. The CV of CMH (olive) is shown for comparison. The response of the buffer is given as the dashed black line. The pH dependence of the first oxidation peak of MHOQ is shown in graph B (small wine dots with line). The derived midpoint potentials E_{mid} (vs. Ag/AgCl) of this substrate (Hod) are represented by the larger black dots which were fit with a linear function (black dashed line). The two black lines correspond to the potential change induced by a 10^5 -fold excess of the reduced or oxidized species as calculated from the Nernst equation. $[\text{Hod}^\bullet]_{\text{max}}$ indicates the one electron oxidized radical species, $[(\text{Hod})\text{Hod}^-]_{\text{max}}$ stands for the protonated or deprotonated reduced substrate MHOQ. The olive squares and dashed lines represent the behavior of transition $\text{CM}^\bullet/\text{CMH}$ of CMH with pH, which is quite similar to that of Hod. The olive lines are the 10^5 -fold excess potential limits. The midpotential E_{mid} of $\text{O}_2/\text{O}_2^{\bullet-}$ and the potential change for excess oxygen are given in blue. The black arrow visualizes the driving force for the electron transfer from Hod^- to O_2 , the olive arrow from CMH to substrate radical with a potential marked by the x..... 72
- Figure 4-20. Modeling of the MHOQ substrate protonation states. The color code of the inset structures relates them to the pH curves..... 74
- Figure 4-21. CVs of quercetin (0.4 mM) in 50% EtOH: PB (50 mM, pH 7.4) at 100 mV/s scan rate. Three oxidation peaks I, II and III are observed at +0.48 V, +0.81 V and +1.2 V (vs. SHE) respectively in the large potential window (black). Whereas in the narrow potential window (green) a reduction peak I', associated to oxidation peak I, is observed at +0.33 V (vs. SHE) exhibiting a reversible character of the first electron transfer $\text{Quer}^\bullet/\text{Quer}$ 78
- Figure 4-22. (Left panel) CVs of the first redox couple $\text{Quer}^\bullet/\text{Quer}$ of quercetin (0.4 mM) in 50% EtOH:PB (50 mM) in the pH range of 4-13 at 100 mV/s scan rate. Arrows indicate the oxidation ($E_{\text{p,a}}$) and reduction peak potential ($E_{\text{p,c}}$) at pH 4. The pH-dependence of midpotentials E_{mid} of $\text{Quer}^\bullet/\text{Quer}$, derived from the CVs on the left panel, is shown in the right panel. The derived midpotentials E_{mid} were fit with a linear function (red line). A linear relationship of E_{mid} (pH) is observed with a slope of -48 mV per pH unit, implying one proton number is involved in this reaction according to the Nernst equation $E_{\text{mid}} = E - 2.303RTpHmanF$ (m, proton number). 79

- Figure 4-23. pH-dependence of the mid-peak potentials E_{mid} (vs. Ag/AgCl) of quercetin substrate (red dots) and CMH (olive squares). The derived mid-peak potentials E_{mid} were fit with a linear function (olive and red dashed lines). The olive (CMH) and red solid lines (quercetin) correspond to the potential change induced by a 10^5 -fold excess of the reduced or oxidized species as calculated from the Nernst equation ($[\text{CM}^\bullet]_{\text{max}}$ and $[\text{Quer}^\bullet]_{\text{max}}$ indicate the one electron oxidized radical species, $[\text{CMH}]_{\text{max}}$ and $[(\text{Quer})\text{Quer}^-]_{\text{max}}$ stand for the protonated or deprotonated reduced CMH and quercetin. The mid-peak potential of $\text{O}_2/\text{O}_2^{\bullet-}$ and the potential change for excess oxygen are given in blue. The red arrow visualizes the driving force for the electron transfer from Quer or Quer⁻ to O_2 , the olive arrow from CMH to substrate radical. 80
- Figure 4-24. On the left side are the CVs of the first redox pair of 0.4 mM myricetin (A), rhamnetin (B) and 3-hydroxyflavone (C) in 50% EtOH:PB (50 mM) in the pH range 2.2-13 at 100 mV/s scan rate. On the right side is the respective pH dependence of the midpotentials E_{mid} of given flavonols, which were derived from CVs. The arrows indicate the first redox pair (oxidation and reduction peaks, except for 3-hydroxyflavone showing only oxidation peak) at pH 2.2, color code identifies other pH values. The derived midpotentials E_{mid} were fit with a linear function (red lines). 82
- Figure 4-25. (Left panel) EPR spectra of (a) anoxic Fe-QueD (1.57 mM), (b) addition of 2-fold molar excess of quercetin, (c) exposing for 30 min and (d) 90 min to air. Signal of high-spin ($S = 3/2$) Fe^{3+} species as a sharp line at around 150 mT ($g \approx 4.3$, dashed line) and broad additional features around 75 mT ($g \approx 9.8$) are observed for the Fe-enzyme (a), diminish with quercetin addition (b) and recover again when exposing to air (c,d). Spectra were recorded at 8 K, microwave power 2 mW and modulation amplitude 0.5 mT. Kinetics of CM^\bullet formation in the quercetin conversion catalyzed by Fe- and Mn-substituted enzymes (wild type and E76 variant) is shown in the right panel. Only small signal of CM^\bullet formation following a linear kinetic is observed for reactions and controls. The assay contained enzyme (0.1 U/ml), quercetin (400 μM in DMSO) and 600 μM CMH. The contents of the assay mixtures are given in the figure legend. 85
- Figure 4-26. No signals indicative for Ni species (Ni^+ , Ni^{3+}) is observed in the EPR spectra of anoxic NiQueD-WT (A-a) and -E76H variant (B-a) at the resting state, and after addition of 2-fold molar excess of quercetin (A-b, B-b). The dashed lines indicate the signals of trace metal Mn^{2+} , Cu^{2+} (around 330 mT, $g \approx 2.05$, red), Fe^{3+} (around 150 mT, $g \approx 4.3$, blue) and broad signal arises from background (at 200 mT, black). Spectra are not background corrected. EPR spectra were recorded at 8-15 K, modulation amplitude 0.7 mT and microwave power 2 mW. The kinetics of CM^\bullet formation in the conversion of quercetin catalyzed by Ni-QueD-WT and -I66A variant is shown in panel C and D, respectively. Controls in C, D are fit with straight lines. As compared to the controls, a slight curvature of the small CM^\bullet signal is indicative for a reaction of both Ni-WT and I66A variant (blue traces). The assay contained enzyme (0.1 U/ml), quercetin (200 μM in DMSO) and CMH (600 μM in H_2O). The contents of the assay are indicated in figure legends. 87

- Figure 4-27. (A) EPR spectra of anoxic Co-QueD wild type (1.13 mM) at 8 K in the resting state (a), after addition of a 2-fold molar excess of quercetin (3 mM) (b), and after exposure to air for 60 s (c) and 10 minutes (d). (B) EPR spectra of anoxic Co-QueD-E76H (2.8 mM) at 15 K in the resting state (a), after addition of a 2-fold excess of quercetin (5 mM) (b), and after being exposed in air for 30 s (c), 5 minutes (d), and 10 minutes (e). (D) EPR spectra of the organic radical signal recorded in narrow field window with the same condition in color code of panel A. (C) Temperature dependence of the Co^{2+} signals of oxic Co-QueD-E76H in the resting state. Parameters settings were microwave power 2 mW, modulation amplitude 0.7 mT (panel A, B, C) and 0.4 mT (panel D). The signals marked with asterisks arise from some amount of Mn^{2+} ($g \approx 2.005$), and (or) Cu^{2+} ($g \approx 2.05$). The dashed lines indicate the signal of Co^{2+} at $g \approx 6$ (blue in A, B and C), $g \approx 3.8$ and $g \approx 3.1$ (red in A, B and C) and the signal of the organic radical at $g \approx 2$ (black in B, D). 90
- Figure 4-28. Unusual behavior in signal intensity is observed for the organic radical formed in the anoxic mixture of Co-QueD-E76H and quercetin (2-fold molar excess) by applying different microwave powers (left panel) and temperatures (right panel). Modulation amplitude was set at 0.4 mT, temperature 15K (left panel) and microwave power 2 mW (right panel). 91
- Figure 4-29. Simulation trial with an $S=1$ spin system approximately reproducing the experimental pattern (see Figure 4-28). Isotropic g -tensor was assumed with a zero field splitting of $D=44\text{G}$ ($=4.4$ mT) and a rhombic parameter $E=6$ G ($=0.6$ mT). The pattern is shifted to higher field because a higher mw-frequency was used. Arrows are indication of line splittings. 92
- Figure 4-30. EPR spectra of anoxic Co-QueD-I66A (A-a) and -Y117A (B-a) at 8 K in the resting state, and no observation of organic radical after addition of a 2-fold excess of quercetin (A-b, B-b). The dashed lines indicate the signal of Co^{2+} at $g \approx 6$ (blue). The signal marked with asterisk arises from small amounts of Cu^{2+} and Mn^{2+} . Parameter settings: are of microwave power 2 mW, modulation amplitude 0.7 mT. Spectra in A are not baseline corrected. 92
- Figure 4-31. Oxidation of CMH by QueD enzymes produces very low yields for CoQueD-wt (A) and much higher signals for CoQueD-E76H (B) and CoQueD-I66A and -Y117A (C). Controls in A are fit with linear, reactions in B, C with exponential-linear functions. The dashed lines monitor oxygen consumption by TAM radical. Constant intensities of the TAM signal from control experiments were defined to correspond to 100% of dissolved O_2 . The stable minimum of the TAM intensity after conversion of quercetin was assumed to represent 0% O_2 . Concentrations: enzyme (0.6 U/ml in A, 0.1 U/ml in B, C), 400 μM quercetin, 600 μM CMH and 4 μM TAM. The contents of the assay mixtures are indicated in the insets. 93
- Figure 4-32. Dependence of the catalytic conversion of quercetin on the enzyme activity (A) and substrate concentration (B). The assays contain quercetin (500 μM , panel A), Co-QueD-E76H (0.1 U/ml, panel B) and CMH (600 μM) in PB pH 7.4 (20 mM). The contents of assay mixtures are given in figure legends. Note that the EPR signal intensity is used as y-axis scale. 95

- Figure 4-33. (A) Oxidation of CMH in anoxic reaction of CoQueD variants with quercetin. Only CoQueD-E76H variant shows a notable amount of CM^\bullet following a linear kinetic (blue solid trace), oxygen consumption was monitored by TAM signal (blue dashed trace). (B) CM^\bullet formation in anoxic reaction of different concentration of CoQueD-E76H (two different batches, numbered with (1) and (2) in figure legend). The assay contains of CoQueD-E76H (10, 50, 100 μM), CMH (600 μM) and quercetin (500 μM in DMSO) in PB (pH 7.4, 20 mM). The contents of the assay mixtures are indicated in the insets. 97
- Figure 4-34. Kinetics of CM^\bullet formation in anoxic ES complex of CoQueD-E76H under limited CMH (A), and protein concentration (B). Red lines are fit of curves; in B background of CM^\bullet formation in control was subtracted. Concentrations are (A) protein 100 μM , quercetin 500 μM , and (B) quercetin 500 μM , CMH 600 μM in PB pH 7.4 (20 mM). The contents of the assay mixtures are indicated in the insets. 98
- Figure 4-35. Formation of CM^\bullet during the conversion of other flavonol substrates, 3-hydroxyflavone, rhamnetin (A) and myricetin (B), catalyzed by Co-QueD-E76H enzyme. Only very small CM^\bullet formation following a linear kinetic is observed for 3OH-hydroxyflavone and rhamnetin around background CM^\bullet formation, whereas a burst of CM^\bullet arises nonlinearly for myricetin. The assay composition: enzyme (0.6 U/ml), substrate (400 μM) and CMH (600 μM) in PB pH 7.4 (20 mM). The contents of the assay mixtures are indicated in the figure legends. 100
- Figure 4-36. EPR spectra shows loss of organic radical in CoQueD-E76H ES-complex upon release of NO from NO-donor NOC-5 at different concentrations (c, 1 mM; d, 2 mM; e, 3 mM), trace a is the oxic state and b the anoxic state with quercetin, the inset shows close-up of organic radical 1mM of NOC5 (nitroxide source) in addition. Parameters settings: microwave power 2 mW and modulation amplitude 0.7 mT..... 101
- Figure 5-1. Concentration dependence of redox potentials for some relevant redox couples. By definition, the electron transfer is thermodynamically possible from a reduced species (more negative potential on the right hand side) to an oxidized species (more positive potential on the left hand side). Diagram A demonstrates the thermodynamically favored electron transfer with respect to concentration ratio and pH. At pH 7, both CMH and CPH are not able to reduce O_2 . However, at pH above 12, O_2 can possibly be reduced to $\text{O}_2^{\bullet-}$ by CPH according to the lower measured mid-peak potentials (arrow 1, dashed), superoxide in turn can efficiently oxidize CMH to CM^\bullet (arrow 3), and CPH can also reduce CM^\bullet (arrow 2) to regain the CMH and forming CP^\bullet . In diagram B, CMH can be reduced to CM^\bullet by $\text{O}_2^{\bullet-}/\text{O}_2^{2-}$ (solid arrow) or also by $\text{H}_2\text{O}_2/\text{H}_2\text{O}$, OH^\bullet (dotted-dashed arrow), but is not affected by ascorbate (AscH^-). On the other hand, CM^\bullet is possibly oxidized to CM^+ by high flux of $\text{O}_2^{\bullet-}$ albeit with a smaller driving force (dotted arrow), as well as being reduced back to CMH by ascorbyl radical (Asc^\bullet) forming DHAsc or by $\text{O}_2^{\bullet-}$ producing O_2 (dashed arrow). However, the dismutation of CM^\bullet is not favored in this diagram. 105

Figure 5-2. Proposed reaction mechanism of wild-type QueD protein and QueD-E76H. (3H1E) and (4H) denote the 3His/1Glu and 4His-ligand sphere, respectively; the organic substrate quercetin is abbreviated as SH, and Me^{2+} stands for Ni and Co ions. 114

Figure 5-3. pH-dependence of the mid-peak potentials E_{mid} (vs. Ag/AgCl) of Hod substrate (black squares) and quercetin substrate (red dots). The derived mid-peak potentials E_{mid} of these substrates were fit with a linear function (black and red dashed lines). The black (Hod) and red solid lines (quercetin) correspond to the potential change induced by a 10^5 -fold excess of the reduced or oxidized species as calculated from the Nernst equation ($[Hod^{\bullet}]_{max}$ and $[Quer^{\bullet}]_{max}$ indicate the one electron oxidized radical species, $[Hod(Hod^-)]_{max}$ and $[Quer(Quer^-)]_{max}$ stand for the deprotonated reduced substrates Hod and quercetin. The mid-peak potential of $O_2/O_2^{\bullet-}$ and the potential change for excess oxygen are given in blue. The black arrow visualizes the driving force for the electron transfer from Hod^- to O_2 , and the red arrow from $Quer^-$ to O_2 116

LIST OF ABBREVIATIONS

CMH	1-hydroxy-3-methoxycarbonyl-2,2,5,5-tetramethyl-pyrrolidine
TAM	tetrathiatriarylmethyl radical
TEMPO	(2,2,6,6-Tetramethyl-piperidin-1-yl)oxyl radical
HCl	hydrochloric acid
NaOH	sodium hydroxide
K ₂ HPO ₄	potassium phosphate dibasic
KH ₂ PO ₄	potassium phosphate monobasic
DMSO	dimethyl sulfoxide
C ₂ H ₆ O	ethanol, ethyl alcohol
MHOQ	3-Hydroxy-2-methyl-4(1 <i>H</i>)-quinolinone
BHOQ	2-Butyl-3-hydroxy-4(1 <i>H</i>)-quinolinone
DF	deferoxaminemethanesulfonate
DETC	diethyldithiocarbamate
HRP	horseradish peroxidase
EPR	electron paramagnetic resonance spectroscopy
NMR	nuclear magnetic resonance spectroscopy
CV	cyclic voltammetry
SWV	square wave voltammetry
DPV	differential pulse voltammetry
SHE	standard hydrogen electrode
Ag/ AgCl	saturated silver/ silver chloride electrode

$E_{p,a}$	anodic peak potential
$E_{p,c}$	cathodic peak potential
$i_{p,a}$	anodic peak current
$i_{p,c}$	cathodic peak current
E_{mid}	mid-peak potential

1. INTRODUCTION

Oxygen is one of the most abundant chemical elements on earth found mainly in oxides of the lithosphere and water. In the atmosphere (or dissolved in water) it normally exists as a gas in form of diatomic molecules. Dioxygen is constantly produced in the biosphere by photosynthetic processes and is continuously consumed by aerobic organisms in respiratory processes for energy formation as well as for synthesis of cellular components. In technical applications it is the major oxidant in combustion processes. Oxygen is having two unpaired electrons in its electronic ground state that contribute to a total spin of $S=1$, a triplet state, which is the cause for the observed paramagnetism of dioxygen. The direct reaction of the triplet state oxygen with a singlet chemical species (spin-paired, $S=0$) to form singlet products would violate a fundamental principle of physics, the conservation of angular momentum. Due to this spin forbidden reaction, oxygen is chemically relatively unreactive in its triplet ($S=1$) ground state which means that it represents a low-probability or high-energy process. To overcome this barrier ground-state dioxygen has to be activated which is achieved by heating, exposure to light or by catalysts. One possible pathway is activation of an organic substrate to a radical, which can react with O_2 in a spin-allowed process. Another pathway is to activate O_2 , either by orbital overlap with a suitable transition metal ion, or by electron transfer from a potent electron donor to form a reduced oxygen species.

For oxygen activation in living organisms, the latter path is central in the generation of so-called reactive oxygen species (ROS) including superoxide radical ($O_2^{\bullet-}$), hydrogen peroxide (H_2O_2) and extremely reactive hydroxyl radicals (OH^\bullet), all of which are known to have a crucial role in both physiology and pathophysiology.¹ ROS can be generated from a variety of sources both endogenous and exogenous via diverse enzymatic pathways such as NADPH oxidases – NOX1-5, L-amino acid oxidases, cytochrome P450 enzymes, cyclooxygenases, lipoxygenases, and xanthine oxidase (XO) in cell membranes, mitochondria, peroxisomes, and endoplasmic reticulum.^{2,3} Importantly, it is reported that the relative rates of ROS production and degradation are regulating the balance between appropriate redox states and oxidative stress in cells.⁴ ROS in moderate levels have crucial functions in health through mechanisms including signaling, biosynthetic processes, and host defense.^{1,5,6,7} In fact, too low levels of ROS may result in decreasing antimicrobial defense (e.g. chronic granulomatous disease), hypothyroidosis, low blood pressure or loss of otoconia.^{8,9} On the other hand, overproduction of ROS is thought to be involved in many age-associated diseases, including

Alzheimer's¹⁰ and Parkinson's disease¹¹, or cardiovascular diseases¹², neurological disorders^{13,14}, cancer^{15,16}, and chronic inflammation¹⁷.

In view of the important role of ROS production in physiological and biological systems, accurate measurements of ROS are essential to clarify how ROS are generated and how they act on cells, tissues and organs. To date, a variety of methods has been developed which is available for ROS detection and quantification in biological systems.¹⁸ Established methods such as spin trapping, chemiluminescent probes, fluorescent probes, or superoxide detection by cytochrome c are used but also many limitations are described.¹⁸ For example, the nitron spin traps (DMPO, DEPMPO, EMPO) have a very low efficacy for $O_2^{\bullet-}$ trapping, detecting mainly extracellular $O_2^{\bullet-}$, and their radical adducts can be reduced by reductants such as ascorbate via bioreduction or biodegradation processes limiting their life time;¹⁹ dihydroethidium (DHE) used as fluorescent probe not only forms the specific 2-hydroxyethidium (2-OH-E⁺) adduct of $O_2^{\bullet-}$ but additionally a secondary fluorescent ethidium product via nonspecific redox reactions which is overlapping the fluorescent spectra of 2-OH-E⁺ leading to an inaccurate measure of the desired product 2-OH-E⁺;²⁰ cytochrome c detects only extracellular $O_2^{\bullet-}$, has low sensitivity, is not specific and can be effectively reduced by ascorbate and flavin enzymes.^{21,22}

In the past decade, a number of new methods have been developed that showed substantial improvements and advantages for ROS detection.¹⁸ Among them, a new group of spin probes, the cyclic hydroxylamines, has been introduced by S. Dikalov and others to detect $O_2^{\bullet-}$ with high efficiency.^{23,24,25,26,27,28,29,30} In this group the cyclic hydroxylamine 1-hydroxy-3-methoxycarbonyl-2,2,5,5-tetramethyl-pyrrolidine (CMH) and 1-hydroxy-3-carboxy-2,2,5,5-tetramethylpyrrolidine (CPH) are most interesting due to their variant cell permeability for intra- and/or extracellular $O_2^{\bullet-}$ detection. Via one electron reduction (for example with $O_2^{\bullet-}$), the very stable CM or CP nitroxide radical (CM[•] or CP[•]) is formed which is measurable with electron paramagnetic resonance (EPR). However, it has been mentioned in several reports that these cyclic hydroxylamines can be involved in additional reactions of complex physiological systems containing potential redox reactants such as ascorbate, glutathione or redox active proteins.^{31,32,33} Due to such complex redox properties these cyclic hydroxylamines have received more and more concerns. However, despite of numerous reported studies, their redox behavior has not been clarified yet. Therefore, it was one essential aim of the presented study to fully understand the redox behavior of CMH and CPH for an interpretation of redox pro-

cesses as well as competitive reactions occurring in complex biological and physiological systems. This part of study was performed using voltammetry, a powerful electroanalytical technique for determining the redox potential and electron transfer. With this approach, we were focusing on a detailed understanding of the interaction with superoxide, hydrogen peroxide and some redox active additives, which is particularly important for the EPR-based application of cyclic hydroxylamines, recently established in our laboratory, to measure the primary superoxide radical produced by NADPH oxidase (NOX) enzyme system of human CD14⁺ monocytes under different stimulatory or inhibitory conditions.

In the course of the project we also followed the idea to develop an EPR-based assay to directly measure hydrogen peroxide, formed by dismutation of superoxide or its reduction by CMH, exploiting the redox properties of cyclic hydroxylamines. In analogy to the established fluorescence based AmplexRed assay, which uses N-acetyl-3,7-dihydroxyphenoxazine (AmplexRed) as a substrate for the horseradish peroxidase (HRP)-catalyzed reaction to detect H₂O₂,³⁴ CMH should be tested if it works as an electron donor to horseradish peroxidase as was suspected from the redox properties. Here, it was the aim to establish an EPR-protocol to measure superoxide production and subsequent H₂O₂ formation in the same experimental setting, and to compare it with standard fluorescence based methods.

In addition of being central to ROS formation, molecular oxygen is an important substrate in the aerobic microbial degradation of polycyclic aromatic hydrocarbons (PAH). These compounds are widespread environmental pollutants in soil and sediments^{35,36} or are products of plants and their degradation. Some of those have attracted increasing attention because they are suspected of having mutagenic, carcinogenic or teratogenic effects on animals.³⁷ In general, the breakdown of aromatic compounds by ring cleavage is an essential biochemical step in Nature's "carbon" cycle and is performed by several kinds of micro-organisms.³⁸ Many microbial enzymes such as oxygenases, dehalogenases, reductases, hydroxylases and dehydrogenases are involved in the degradation of these substances. Among them, oxygenases are key enzymes for aerobic biodegradation of aromatic compounds because they are involved in the initial reaction of degradation and also catalyse ring cleavage which is the essential step for the complete mineralization of these compounds.³⁹

In classification of oxygenases, monooxygenases (often called hydroxylases) transfer one oxygen atom to the substrate and reduce the other oxygen atom to water, while dioxygenases incorporate both atoms of dioxygen into the product(s) of the reaction. Because direct incor-

poration of molecular oxygen into substrates is a “spin-forbidden” process, the majority of oxygenases depend on an organic cofactor or transition metal ion for catalysis, such as reduced flavin or pterin cofactors and mainly iron, copper or manganese ions.⁴⁰ Recently, several oxygenases and oxidases have been identified that neither contain nor require any cofactor,⁴¹ which are also able to activate substrate and/or oxygen to perform the required function.

This part of the study focuses on several aspects of the catalytic reaction of two dioxygenases, the metal-cofactor containing quercetin 2,4-dioxygenase (quercetinase, QueD) and the cofactor-free 1*H*-3-hydroxy-4-oxoquinoline 2,4-dioxygenase (Hod). Both belong to the small group of carbon monoxide forming enzymes^{42,43,44,45,46,47,48,49,50,51} that catalyze the incorporation of two O-atoms into the substrate, and the cleavage of two C–C bonds associated with the release of CO. In literature, mechanistic models are discussed which postulate the activation of substrate and/or oxygen as transient radical species, substrate radical and superoxide, possibly forming a highly reactive caged radical pair during the catalytic process (for details see section methodology). Particularly, the existence of the radical pair in the catalytic reaction of Hod and QueD has not been proven.

It was therefore a major goal of this work (which was performed in close cooperation with the group of Prof. Susanne Fetzner, head of the Institute for Molecular Microbiology and Biotechnology, University of Münster) to find clear experimental evidence for the activation steps of both proteins. To approach this task, the redox and electron transfer properties of the Hod-substrate and quercetin essential for postulated radical formation were thoroughly explored by voltammetric methods in our laboratory. For monitoring the presence of oxidative or reductive radical species EPR is applied as method of choice with the aim to characterize the ongoing radical reactions or to identify the participating species relying on spin trapping with nitron spin traps or redox activation of cyclic hydroxylamines. The focus of our EPR approach was set on quercetinase substituted with different metal cations to infer on the possible roles of the metal in the activation of substrate and/or oxygen supporting it via redox or spin state transitions or by providing suitable structural environment. This aspect was considered important with respect to a comparison with the cofactor-free Hod-enzyme. Finally, additional information on mechanistic details was expected from experiments with modified QueD protein carrying amino acid substitutions in the binding pocket, or near and at the metal binding site.

2. METHODOLOGY

2.1. Voltammetry

Voltammetry is one of the electroanalytical techniques widely used in analytical chemistry and industrial processes. These methods are generally used for the fundamental studies of redox processes, determination of electron transfer and reaction mechanisms, kinetic rates and kinetic constants of reaction. They are commonly applied for the quantitative determination of pharmaceutical compounds, the metal ion concentrations in water, for measuring the redox potentials and number of electrons transferred. In voltammetry, in a 3-electrode configuration electrochemical cell, the potential is applied between working electrode (WE) and reference electrode (RE) that increases or decreases with time to give as output the current vs. potential between WE and counter electrode (CE). In this section I refer to literatures of Cynthia G. Zoski⁵² (2007) Handbook of Electrochemistry and J. J. Lingane⁵⁴ (1958) Electroanalytical Chemistry.

Terminology (Taken from reference⁵²)

The definitions follow the IUPAC instructions,⁵³ as some terms have specific meanings in electrochemistry.⁵⁴

Anode: electrode where the oxidation takes place.

Auxiliary (Counter) Electrode (CE): electrode that helps the current flowing through the cell; the current travels between WE and CE; typically no processes of interest (under study) occur at the surface of CE, example: Pt wire.

Cathode: electrode where the reduction takes place.

Electrode: it is the conductive phase where the electron transfer occurs; it can be an anode or a cathode.

Interface (Junction): in an electrochemical cell, it represents the location where two distinct phases come in contact with each other: solid–liquid (electrode–solution), two liquids of different concentrations and/or compositions (reference electrode–solution), etc.

Nernstian: a reversible redox process that follows equilibria equations.

Faradaic current: current generated by reduction or oxidation of some chemical substance at electrode.

Non-faradaic: processes that follow Ohm's law; they are comprised of all processes that occur at the electrode (excluding chemical reactions) and account for solution conductivity and capacitive charging.

Normal/Standard Hydrogen Electrode (NHE/SHE): it is the standard reference electrode; all standard potentials are referred to NHE; its potential is by definition 0.000 V.

Oxidation: refers to the process in which a chemical species loses one or more electrons; it is the reverse of the reduction.

Oxidizing Agent/ Oxidant (O): the chemical species that undergoes reduction, enabling the oxidation of a different species.

Redox Couple: the chemical species that has at least two oxidation states, and thus can act either as the reduced or the oxidized species (depending on the oxidation state); example: $\text{Fe}^{3+}/\text{Fe}^{2+}$.

Reducing Agent/ Reductant (R): the chemical species that undergoes oxidation enabling the reduction of different species.

Reduction: refers to the process in which a chemical species gains one or more electrons; it is the reverse of the oxidation.

Reference Electrode (RE): electrode that can maintain a constant potential under changing experimental conditions; the WE potential is referenced vs. the RE potential; REs are typically anodes in electrochemical cells; example: NHE.

Standard Reduction Potential (E_0 [V vs. NHE]): is defined as the potential of the reduction half-reaction at the electrode, with respect to the NHE; each redox couple has a fixed standard reduction potential.

Supporting Electrolyte: an ionic substance (typically a dissociated salt) that is present in a solution to ensure its conductivity; example: KCl. The supporting electrolyte reduces the migration effects in the solution; it does not undergo redox chemistry, and thus its ions are called spectator ions. Sometimes the supporting electrolyte is referred to simply as the electrolyte.

Working Electrode (WE): electrode where the redox processes under study occur; WEs are typically cathodes; example: ion-selective electrode or noble metal.

Electrode reactions

Electrode reactions refer to the oxidation or reduction processes that take place at the interface region between electrode and solution. They are heterogeneous reactions and involve many steps:

Reactant (O) moves to the interface, this is termed as mass transport. Electron transfer can occur via quantum-mechanical tunneling (typical tunneling distances between the electrode and reactant are less than 2 nm).

The product (R) moves away from the electrode and fresh reactant comes to the surface.

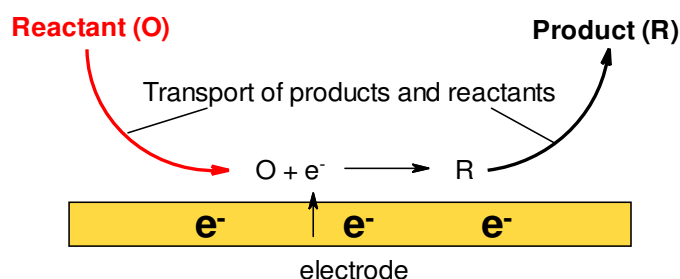


Figure 2-1. Simple electrode reaction (adapted from reference⁵⁵).

Electrical double layer

Electrical double layer is a region between two different phases where charge is separated across the interface. It can be a metal under potential or due to ionic groups on the surface of a dielectric. In the double layer, the water molecules of the solution align themselves with the electric field generated by applying a potential to the metal. In the Helmholtz model, there are two layers of opposite charge (molecules or ions) formed at the interface of electrode and electrolyte. The later models, proposed by Louis Georges Gouy, David Leonard Chapman and Otto Stern, defined two regions of ion distribution—the inner region called the compact layer or Stern layer and the diffuse layer.

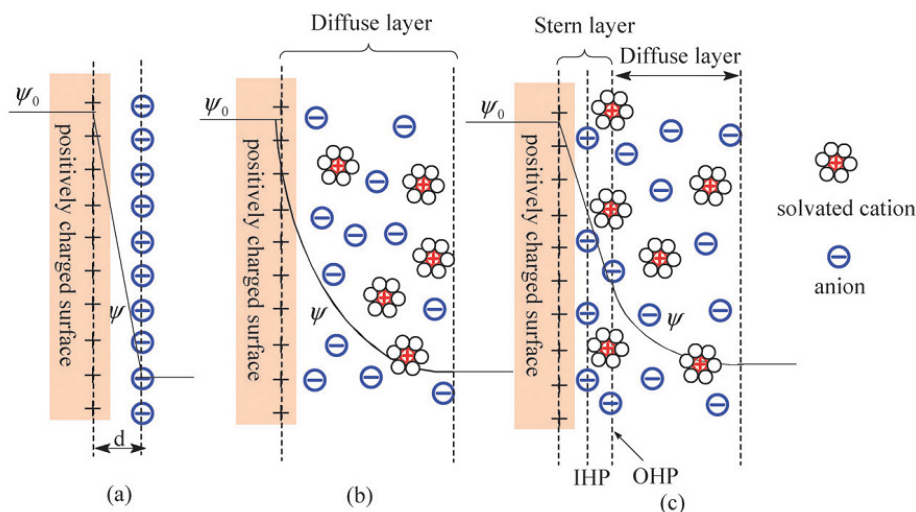


Figure 2-2. Models of the electrical double layer at a positively charged surface: (a) the Helmholtz model, (b) the Gouy–Chapman model, and (c) the Stern model, showing the inner Helmholtz plane (IHP) and outer Helmholtz plane (OHP). The IHP refers to the distance of closest approach of specifically adsorbed ions (generally anions) and OHP refers to that of the non-specifically adsorbed ions. The OHP is also the plane where the diffuse layer begins. d is the double layer distance described by the Helmholtz model. The potential ψ_0 and ψ at the electrode surface and the electrode/electrolyte interface, respectively, are indicated as black graphs according to the model (adapted from reference⁵⁶).

2.1.1. Cyclic voltammetry

In Cyclic Voltammetry (CV) the voltage is swept between two values E_1 and E_2 versus time at a fixed potential rate. When the voltage reaches E_2 the scan is reversed and the voltage is swept back to E_1 (Figure 2-3 left panel). The typical cyclic voltammogram of a solution which contains an electrochemically active species is the current-potential response shown in Figure 2-3 right panel. The resulting current vs. applied potential curve is described for an ideal, reversible system (i.e., the electron transfer rate is fast enough to maintain the surface concentration of oxidized and reduced species at the value required by Nernst equation).

The Nernst equation describes the relationship of the potential of an electrode and the concentrations of the two species (O as oxidized and R as reduced form), which are involved in the redox reaction at the electrode in equilibrium; it is only valid for a reversible system with fast kinetics: $O + ne^- \leftrightarrow R$

$$E = E^0 + \frac{RT}{nF} \ln \frac{C_O^*}{C_R^*}$$

where E^0 (V) is the standard reduction potential for the redox couple O/ R, C_O^* (M) is the bulk concentration of the oxidized species O and C_R^* (M) is the bulk concentration of the reduced

species R, n is the number of electrons transferred. R is the molar gas constant ($8.3144 \text{ J mol}^{-1} \text{ K}^{-1}$), T is absolute temperature in Kelvin and F is the Faraday constant ($9.6485 \cdot 10^4 \text{ C mol}^{-1}$).

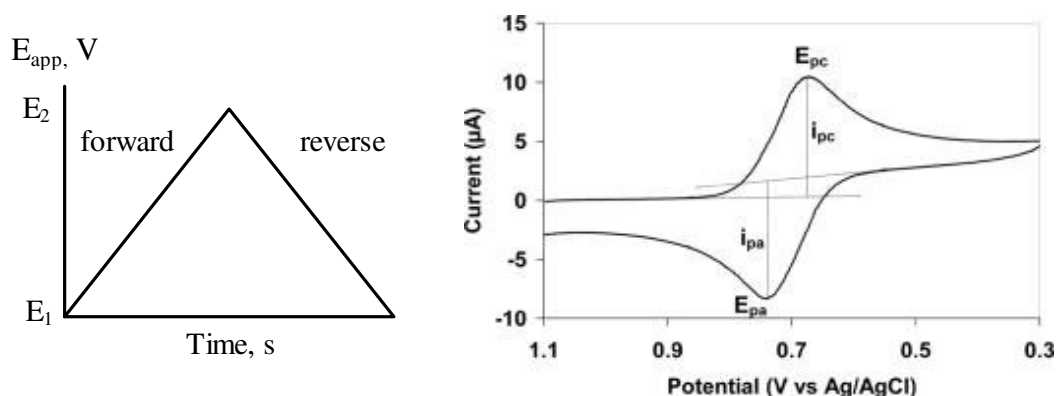


Figure 2-3. (Left panel) Cyclic voltammetry potential waveform. (Right panel) Typical cyclic voltammogram where i_{pc} , E_{pc} and i_{pa} , E_{pa} show the peak cathodic and anodic current and potential respectively for a reversible reaction (adapted from reference⁵⁷).

The expression of the peak current (in units A) for the forward sweep in a reversible system at 298 K is given by the Randles–Sevcik equation:

$$i_p = (2.69 \times 10^5) n^{3/2} A D^{1/2} \nu^{1/2} C^*$$

where n is the number of electrons exchanged during the redox process, A (cm^2) the active area of the working electrode; D ($\text{cm}^2 \text{ s}^{-1}$) and C^* (mol cm^{-3}) are the diffusion coefficient and the bulk concentration of the electroactive species, ν is the voltage scan rate (V s^{-1}).

Data interpretation

Reaction controlled by the mass transport- fast electron transfer kinetic

The current measured depends on the rate at which the analyte diffuses to the electrode. The current is said to be “diffusion controlled”, as given in the Cottrell equation:

$$i_p = nFAC \sqrt{\frac{D}{\pi t}}$$

where i_p is the peak current (A), n the stoichiometric number of electrons involved in the reaction, F the Faraday constant (96485 C/mol), A the area of the (planar) electrode (cm^2), C the initial concentration of electroactive species (mol/cm^3), D the diffusion coefficient of the electroactive species (cm^2/s), t time (s). In practice, the Cottrell equation simplifies to

$$i = kt^{-1/2}$$

where k is the collection of constants for a given system (n , F , A , c_j^0 , D_j). In general, the square root of scan rate (v)^{1/2} can be used in place of $t^{-1/2}$.

Reversible systems

For a so-called reversible system, the peak current intensity (i_p) is proportional to the square root of scan rate ($v^{1/2}$) according to the Randles-Sevcik equation. The ratio of anodic and cathodic peak current is approximately 1 ($\frac{i_{p,c}}{i_{p,a}} = 1$), independent on the potential scan rate (v).

The formal potential is the average of anodic and cathodic peak potential ($E_{p,a}$, $E_{p,c}$):

$$E_{\text{mid}} = \frac{1}{2} (E_{p,a} + E_{p,c})$$

The separation between peaks potential is given by:

$$\Delta E = |E_{p,c} - E_{p,a}| = \frac{59}{n} \text{ (mV)}$$

Thus, number of electrons transferred (n) can be determined by the peak separation (ΔE). A fast one-electron process exhibits a ΔE of about 59 mV. Both anodic and cathodic peak potentials are independent of scan rate.

Irreversible and Quasi-reversible systems

The Nernst equation for the quasi-reversible electrode process is modified and given by:

$$E_p = E^0 + \frac{RT}{\alpha n_a F} \left[\ln \left(\frac{k_s}{\sqrt{D}} \right) - 0.51 \ln \left(\frac{\alpha n_a F v}{RT} \right) - 0.78 \right]$$

where α is the electron transfer coefficient, n_a the number of electrons involved in the charge-transfer step, k_s the standard heterogeneous rate constant (cm/s), the other constants have the usual meaning as defined above.

The peak current is then given by:

$$i_p = (2.99 \times 10^5) n (\alpha n_a)^{1/2} A D^{1/2} v^{1/2} C^*$$

For quasi-reversible systems, the current is controlled by both the charge transfer and mass transport. A quasi- or irreversible system exhibits a larger separation of peaks potential $\Delta E > 59/n$ (mV), with the value increasing with increasing v .

2.1.2. Differential Pulse Voltammetry (DPV)

Differential pulse voltammetry (DPV), also known as differential pulse polarography (DPP), is a voltammetric technique, in which a series of regular voltage pulses is superimposed on the potential linear sweep or a staircase wave form. The advantage of pulse voltammetry is that the decay rate of the electrode charging current is considerably faster than the decay of the faradaic current. The measured current therefore consists solely of the faradaic current, resulting in a more precise analysis of electrode reactions and a lower detection limit.

In DPV the current is measured just prior to application of the pulse and at the end of the applied pulse. In this way the effect of the charging current can be minimized and high sensitivity is achieved. This technique is applied to study the redox properties of extremely small amounts of chemicals at a detection limit of about 10^{-8} M and is suitable for quantitative analysis. The difference between the two currents at the start and the end of the potential pulse is plotted as a function of potential.

The peak's height is directly proportional to the concentration of the corresponding analyte:

$$i_p = \frac{nFAD^{1/2}C}{\sqrt{\pi t_m}} \left(\frac{1 - \sigma}{1 + \sigma} \right)$$

where $\sigma = \exp[(nF/RT)(\Delta E/2)]$ (ΔE is the pulse amplitude), t_m is the time after application of the pulse where the current is sampled. The maximum absolute value of the quotient $(1-\sigma)/(1+\sigma)$ obtained for large pulse amplitudes, is unity.

The peak potential (E_p) can be used to identify the species, as it occurs near the half-wave potential:

$$E_p = E_{mid} - \Delta E/2$$

In DPV symmetric peaks are observed for reversible reactions and irreversible show asymmetric peaks.

2.1.3. Square-wave Voltammetry (SWV)

Square-wave voltammetry (SWV) is a large-amplitude differential technique, in which the current is measured at the end of each half-cycle (immediately before the potential direction is reversed). As a consequence, the contribution to the current signal resulting from charging

(referred to as non-faradaic or capacitive) current is minimal. The difference between current measured on the reverse half-cycle (i_r) and on the forward half-cycle (i_f) is displayed as a function of the applied potential. Peaks in the differential current vs. applied potential plot are indicative of redox processes, and the magnitudes of the peaks are proportional to the concentrations of the various redox active species according to:

$$\Delta i_p = \frac{nFAD_0^{1/2}C_0^*}{(\pi t_p)^{1/2}} \Delta \Psi_p$$

where Δi_p is the differential current peak value, A is the surface area of the electrode, C_0^* is the concentration of the species, D_0 is the diffusivity of the species, t_p is the pulse width, and $\Delta \Psi_p$ is a dimensionless parameter which gauges the peak height in SWV relative to the limiting response in normal pulse voltammetry.

Excellent sensitivity arises from the fact that the net current is larger than either the forward or reverse components (since it is the difference between them), and is in general higher than that of differential pulse polarography (in which the reverse current is not used). In SWV very low detection limits between 10^{-9} and 10^{-10} M can be attained.

The major advantage of square-wave voltammetry is its speed. The effective scan rate is given by $f \cdot \Delta E_s$. The term f is the square-wave frequency (in Hz) and ΔE_s is the step height. Frequencies of 1–100 cycles per second permit the use of extremely fast potential scan rates. For example, if $\Delta E_s = 10$ mV and $f = 50$ Hz, then the effective scan rate is 0.5 V/s. As a result, the analysis time is drastically reduced; a complete voltammogram can be recorded within a few seconds, as compared with about 2–3 min in differential-pulse voltammetry. Kinetic studies can also benefit from the rapid scanning capability and the reversal nature of square-wave voltammetry.

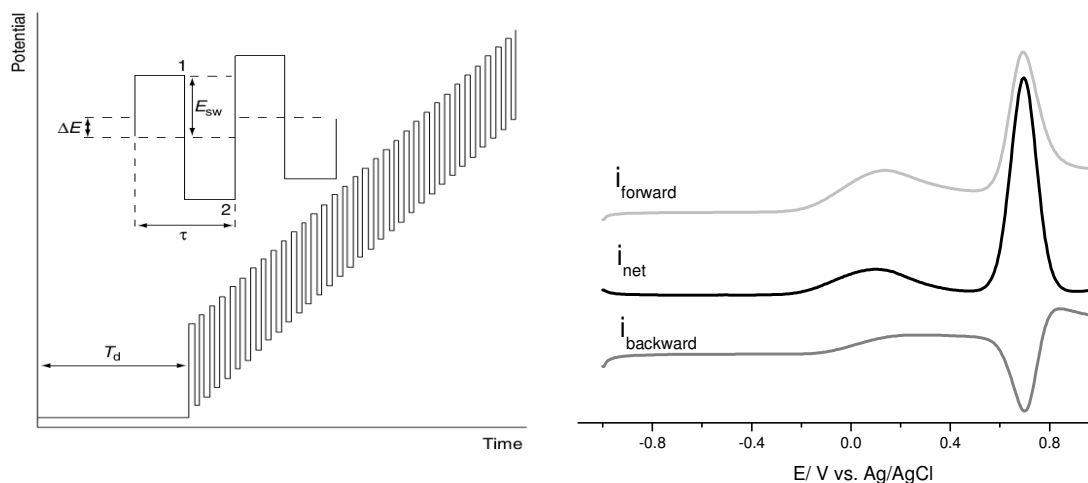


Figure 2-4. (Left panel) Square-wave waveform showing the amplitude E_{sw} , step height ΔE , square-wave period T , delay time T_d , and current measurement times 1 and 2 (adapted from⁵⁸). (Right panel) Square-wave voltammogram of two electrode reactions of CMH (2mM) in PB (pH 7.4, 50 mM), in which the net current is indicated in black, forward current in light grey and backward in grey. Parameters were amplitude 50 mV, step height (ΔE) 5 mV and frequency 10 Hz.

2.2. Electron Paramagnetic Resonance (EPR) Spectroscopy

Electron paramagnetic resonance (EPR), also called electron spin resonance (ESR) spectroscopy, is a basic method for investigation of paramagnetic particles, species with one or more unpaired electrons such as protein side chain radicals (Tyr \bullet , Trp \bullet , Gly \bullet , Cys \bullet), inorganic radicals (NO \bullet , O $_2^{\bullet-}$, HO \bullet), radical states of cofactors (semiquinones, flavins) and transition metal ions (Cu II , Co II , Fe III , Mn II , V VI , Mo V , W V). This non-destructive technique is applied in diverse fields of bio-inorganic chemistry, biology, medicine and physics to study the oxidation and reduction processes, reaction kinetics and particularly to examine the active sites of metalloproteins. In this section I refer to literature of John A. Weil, James R. Bolton, and John E. Wertz (1994) Electron paramagnetic resonance: Elementary theory and practical applications.

Quantum mechanics tells us that an electron spin will have only two possible orientations. In the absence of an external magnetic field (B), these orientations or spin states are of equal energy. When an external magnetic field B is applied, the two possible spin states are split to different energies (Scheme 2-1). The two states are labeled by the projection of the electron spin, m_s , on the direction of the magnetic field. The lower energy state $m_s = -1/2$ is adopted when the magnetic moment of the electron is aligned with the magnetic field (parallel) and a

higher energy state $m_s = +1/2$, when m_s is aligned against the magnetic field (antiparallel) (Scheme 2-1). Each alignment will have a specific energy due to the Zeeman effect:

$$E = m_s g_e \beta_e B = \pm \frac{1}{2} g_e \beta_e B$$

where g_e is the electron's so-called g-factor ($g_e = 2.0023$ for the free electron), β_e the Bohr magneton, a natural unit of electronic magnetic moment $\beta_e = |e|\hbar/2m_e = 9.2740154(31) \cdot 10^{-24} \text{ JT}^{-1}$; e electronic charge $|e| = 1.60217733(49) \cdot 10^{-19} \text{ C}$, Planck's constant $h = 6.6260755(40) \cdot 10^{-34} \text{ J s}$, $\hbar = h/2\pi = 1.05457266(63) \cdot 10^{-34} \text{ J s}$, m_e the mass of the electron $m_e = 9.1093897(54) \cdot 10^{-31} \text{ kg}$, B the external magnetic field in Tesla.

Using an oscillating electromagnetic field in the microwave range for a corresponding magnetic field, a transition can be induced from the lower to the higher energy state and *vice versa*, but only if the energy of this microwave exactly matches the difference between the energy levels with $\Delta m_s = \pm 1$.

The energy difference between two levels is therefore given by

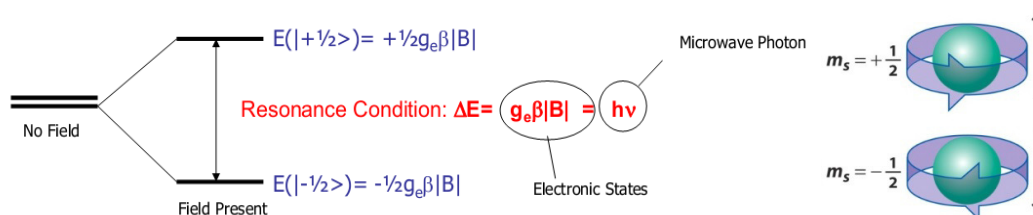
$$\Delta E = g_e \beta_e B$$

According to Planck's law, electromagnetic radiation may be absorbed if

$$\Delta E = h\nu$$

where ν is the frequency of radiation, which leads to the fundamental equation of EPR spectroscopy:

$$\Delta E = h\nu = g_e \beta_e B$$



Scheme 2-1. Energy level splitting diagram of an electron in an applied external field B . On the right is the projection of two electron spins orientations.⁵⁹

Like with most spectroscopic techniques, when radiation is absorbed, an absorption spectrum is produced as shown in Figure 2-5 (left spectrum). In EPR spectrometers modulation of the external field and a phase-sensitive detector is used, so that the recorded signal is displayed as the first derivative of the absorption intensity (Figure 2-5 right spectrum). The absorption

maximum corresponds to the point where the spectrum passes through zero that is used to determine the center of the signal.

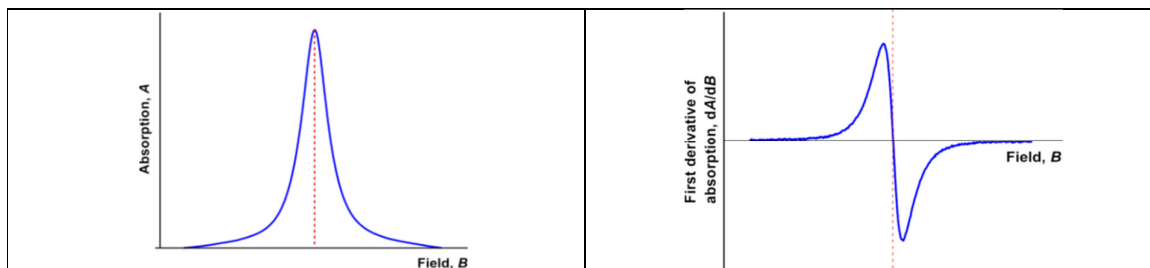


Figure 2-5. EPR absorption spectrum (left) and first derivative spectrum (right part). The red dotted line indicates the correspondence of absorption maximum and zero crossing of derivative spectrum.

Common EPR experiments are performed with microwaves in the 9–10 GHz frequency region (called X-band), with fields corresponding to about 3500 G (or 0.35 T with the correlation 1 T=10000 G, 1 mT=10 G). The magnetic field in EPR spectroscopy is usually measured in Gauss units, the SI unit, however, is Tesla. EPR spectra are usually generated by varying the magnetic field while holding the photon frequency incident on a sample constant, which is typical for continuous wave EPR. The reverse mode is also possible but technically more complicated for sweeping the microwave frequency and using highly sensitive resonant cavities. Also pulsed techniques are used in EPR in which at least part of the spectrum is excited by a very short microwave pulse (ns range). Then the absorption spectrum is obtained because no modulation and phase-sensitive detection is necessary.

Relaxation and saturation

In order to maintain steady state conditions during absorption there must be some mechanism operative, known as relaxation. This process occurs when electrons that have been excited to higher energy level lose energy and return to lower level. In practice, the spin system undergoes interactions with the surroundings. An extra energy δU_0 at $t = t_0$ is received thermodynamically and lost to its surroundings with an exponential decay

$$\delta U = \delta U_0 \exp[-(t - t_0)/\tau_1]$$

where δU_0 is the excess energy at time $t = t_0$.

τ_1 is the characteristic time for the energy flow from spin system into the surroundings. Relaxation time τ_1 reflects the degree to which the spin system is connected to its surroundings.

Relaxation occurs by two mechanisms:

- Spin-lattice relaxation τ_1 : interactions between an electron in an excited energetic level and surroundings.
- Spin-spin relaxation τ_2 : spinning electron in upper level transfers its energy to an electron in lower level exchanging the spin states. Here the total energy is conserved, but the correlation of spin states is diminishing.

The ratio of electrons in upper and lower energy levels is given by Boltzmann distribution

$$\frac{N_u}{N_l} = \exp(-\Delta U/k_b T_s) = \exp(-\frac{g\beta_B B}{k_B T_s})$$

where N_u and N_l are the occupancy numbers of the upper and lower levels, k_B the Boltzmann constant and T_s the absolute temperature of the spin system.

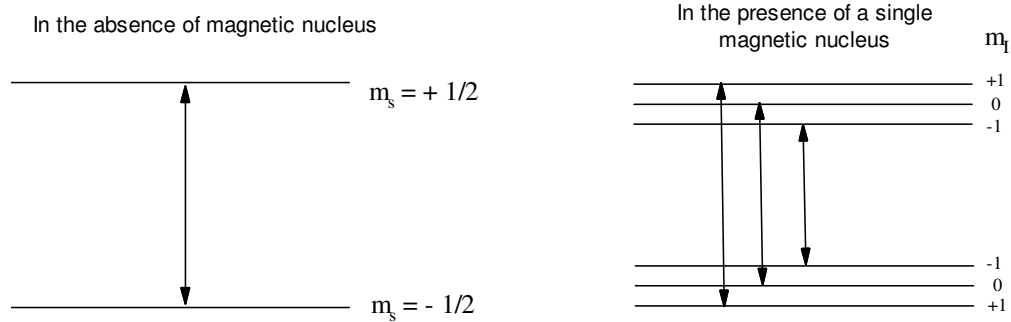
The magnitude of the EPR signal is proportional to the net polarization of the spin orientations of the set of paramagnetic species. Saturation occurs when the electron population in upper and lower levels is equal; then no net energy is transferred between microwave radiation and the spin system. When the system is saturated no further absorption, resonance or signal can be observed.

If the relaxation time τ_1 is very long (slow relaxation), one may have to set the parameter at very low microwave power to avoid saturation. With a short τ_1 (fast relaxation), the spectra are broadened, in some cases beyond detection. This difficulty is frequently observed with transition metal ions. It is usually dealt with by taking spectra at very low temperatures (< 77 K), since the value of τ_1 tends to increase dramatically with decreasing temperature.

Hyperfine splitting

The nuclei of atoms in a molecule or complex often have magnetic moments (m_I) which produce local magnetic fields experienced by the electron. The interaction between an unpaired electron and nuclei with non-zero nuclear spin is called the hyperfine interaction. This leads to splitting of the EPR line and is known as hyperfine spectrum, which occurs when the microwave energy exactly matches the difference between energy levels of the same nuclear substrate ($\Delta m_I = 0$) as indicated in Scheme 2-2.

Energy levels of an unpaired electron that is coupled to a single magnetic nucleus with spin quantum number 1



Electrons reside in either of the two levels.

Each energy level is split into $2I+1$ sublevels, so there are $2I+1$ stable orientations of the nucleus in external magnetic field.

Scheme 2-2. Energy diagram of systems having electron spin $S=1/2$ and additional nuclear spin $I=1$

Considering the effects of the isotropic hyperfine interaction, the appropriate spin-hamiltonian operator ($\hat{\mathcal{H}}$), which measures the magnetic interaction energy (in Joule) between the electron (spin operator S_z) and the nucleus (I_z), is expressed in general form:

$$\hat{\mathcal{H}} = A_0 S_z I_z$$

A_0 is the isotropic hyperfine coupling 'constant' which depends on the probability of the electron to be found at the nucleus ($|\Psi|^2$):

$$A_0 = \frac{2\mu_0}{3} g_e \beta_e g_n \beta_n |\psi(0)|^2$$

The spin-hamiltonian operator for the hydrogen atom (and other isotropic systems with one electron and one nucleus with $I = 1/2$) is obtained as:

$$\hat{\mathcal{H}} = g_e \beta_e B S_z - g_n \beta_n B I_z + A_0 S_z I_z$$

This is valid when B is sufficiently large. The nuclear Zeeman energy (the second term) has little effect on the transition energies because it is usually small compared to the hyperfine terms (third term) and shifts the corresponding energy levels of the transition in the same direction.

Powder EPR

g-anisotropy

The effect of the electronic environment on the unpaired electron is not the same in every direction. The shift in g-factor, Δg , depends on from which direction we look at the spin (the direction of the external magnetic field vector). The spin Hamiltonian becomes

$$\hat{\mathcal{H}} = \beta B \mathbf{g} S$$

and is expanded for the anisotropic Zeeman and nuclear hyperfine interactions to the form:

$$\hat{\mathcal{H}} = \beta B \mathbf{g} S + S_z \mathbf{A} I_z$$

Now \mathbf{B} is a row vector, S is a column vector operator, and \mathbf{g} and \mathbf{A} are 3 x 3 tensors. We can always choose a xyz-axis system such that \mathbf{g} is diagonal.

$$\begin{pmatrix} g_{xx} & g_{xy} & g_{xz} \\ g_{yx} & g_{yy} & g_{yz} \\ g_{zx} & g_{zy} & g_{zz} \end{pmatrix} \text{-----3 dimensional rotation} \rightarrow \begin{pmatrix} g_x & 0 & 0 \\ 0 & g_y & 0 \\ 0 & 0 & g_z \end{pmatrix}$$

Any spin system can be characterized by its g tensor and any g-factor can be calculated from the three principal values g_x , g_y and g_z according to the equation

$$g = \sqrt{g_x^2 \sin^2 \alpha \cos^2 \beta + g_y^2 \sin^2 \alpha \sin^2 \beta + g_z^2 \cos^2 \alpha}$$

where α and β are angles between magnetic field with respect to principle axes of g tensor.

Thus, we can determine the g tensor by evaluating the above equation, which can be achieved in single crystals measuring the angular dependence of g by rotating the crystal in the magnetic field. In most cases, single crystals are not available and the samples are used as powders or frozen solutions. For example, metalloproteins are commonly studied by EPR as frozen solutions. Then, all molecular tensors are randomly and statically oriented with respect to the magnetic field, so that we see all possible orientations when scanning an EPR spectrum. This is called powder EPR and the spectrum is reflecting the principal values of the g-tensor which can be directly read from the powder pattern. The directional information, however, is no longer available. According to the shape of the spectrum, one can distinguish three cases based on the observed g-tensor components:

Rhombic spectrum: $g_x \neq g_y \neq g_z$

Axial spectrum: $g_x = g_y \neq g_z \rightarrow g_x = g_y = g_{\perp}, g_z = g_{\parallel}$

Isotropic spectrum: $g_x = g_y = g_z = g_{\text{iso}}$

Zero-field splitting

For spin systems with more than one unpaired electron in the orbitals with a resulting group spin $S > 1/2$ the dipole-dipole interaction between individual electron spins removes the energetic degeneracy of the ground state. This zero-field splitting causes an energy splitting even in zero magnetic field and is expressed by

$$\mathcal{H}_{ZFS} = S^T \mathbf{D} S$$

with the symmetric and traceless zero-field interaction tensor \mathbf{D} and the group spin $S = \sum_k S_k$. Examples for such systems are transition metal ions with up to five unpaired d -electrons (e.g. high-spin Mn^{2+} , high-spin Co^{2+} or Fe^{3+}) often found in metal proteins or which are substituted in the active site of such a protein. In addition, two $S=1/2$ systems can couple to an $S=1$ system, for which then also zero field splitting may occur and drastically change the spectra of the individual moieties.

The total spin Hamiltonian for anisotropic g -tensor, hyperfine interaction and zero-field splitting thus completes to the expression

$$\hat{\mathcal{H}} = \beta_e B \mathbf{g} S_z - g_n \beta_n B I_z + S_z \mathbf{A} I_z + S^T \mathbf{D} S.$$

The first term includes the g -tensor (Zeeman interaction) while the second describes the nuclear Zeeman interaction which mostly is treated as an isotropic interaction. The third and fourth term represent the anisotropic hyperfine interaction with magnetic nuclei of the spin bearing molecule, and the interaction of several unpaired electrons (ZFS) within the system, respectively. Most EPR spectra can be analysed on the basis of this general Hamiltonian, but for many cases it can be simplified by omitting small or irrelevant terms. In the following paragraphs two examples will be presented in some detail.

EPR spectrum of TEMPOL

One example of solution EPR is given for the stable free nitroxide radical TEMPOL (2,2,6,6-tetramethyl piperidinol-1-oxyl), which can be directly transferred to the nitroxide radical formed upon reduction of CMH (1-hydroxy-3-methoxycarbonyl-2,2,5,5-tetramethyl-

pyrrolidine) applied in this study. TEMPOL is a one-electron radical which contains the unpaired electron mainly located on the nitroxide (N-O[•]) group. It belongs to a group of spin labels that possess an unpaired 2p electron, and can be attached to macromolecules such as proteins or membrane lipids. These spin labels are rather stable molecules and commonly used to obtain useful information on the molecules to which they are bound, for example on structural details, rate of motion of the macromolecule, on the amount of thermal motion in a membrane or even the polarity of its environment.

In nitroxide radicals, ¹⁴N has a nuclear spin $I = 1$ ($m_I = -1, 0, +1$) and the electron spin is $S = 1/2$ ($m_S = -1/2, +1/2$). According to the selection rules ($\Delta m_S = \pm 1, \Delta m_I = 0$), the interaction with a nitrogen atom results in a three line pattern (hyperfine couplings) with isotropic hyperfine splitting constant of nitrogen $A_N = 14\text{--}17$ G (Figure 2-6). On top of the interaction with nitrogen, there are also unresolved proton hyperfine interactions ($m_I = \pm 1/2, A_H = 0.2\text{--}0.5$ G⁶⁰) mainly arising from the adjacent methyl-protons. Their small couplings are strongly overlapping and broaden each peak in the nitroxide spectrum. In principle, a nitroxide radical exhibits anisotropy, so that the g-factor and hyperfine splitting are represented by 3x3 matrices referred to as g and A-tensors. Usually, for nitroxides a Cartesian molecule-fixed coordinate system [x, y, z] is defined, where the x-axis coincides with the N-O bond and the z-axis is along the 2p_z axis of the nitrogen atom, and the y-axis is perpendicular to both.

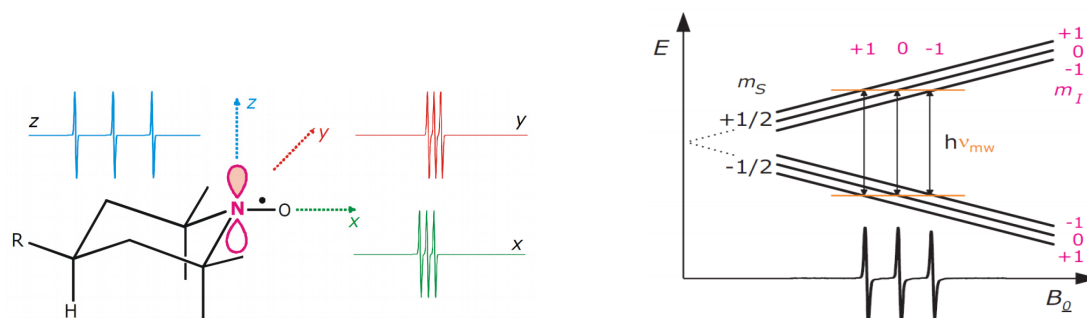


Figure 2-6. Nitroxide EPR single crystal spectra (left panel) along the principal axes show different field position due to anisotropic g-factor and variable hyperfine couplings of ¹⁴N nucleus ($m_I = -1, 0, +1$) for the anisotropic A-tensor. For a solution spectrum (right panel) the isotropic hyperfine splitting of the triplet signal is observed according to the transitions between the energy states (upper graph). (Taken from Bordignon-tutorial⁶¹).

Because of the symmetry of the 2p_z orbital, the [x, y, z] axes system coincides with the principal axes of the g and A-tensors, so g and A-tensors are diagonal in this axes system. The tensors for the 2,2,6,6-tetramethylpiperidin-1-oxyl (TEMPO) spin probe are represented by:⁶²

$$g = \begin{pmatrix} 2.0087 & 0 & 0 \\ 0 & 2.0061 & 0 \\ 0 & 0 & 2.0027 \end{pmatrix} \text{ and } A = \begin{pmatrix} 0.68 & 0 & 0 \\ 0 & 0.68 & 0 \\ 0 & 0 & 3.0 \end{pmatrix}, \text{ in mT}$$

These tensors and their orientation to the axis system can be obtained in single crystal experiments, whereas in frozen solution only the largest component of the hyperfine tensor can be derived, the other components being not sufficiently resolved. Also the g -anisotropy cannot be inferred directly from a spectrum at X-band frequencies, because the values are not sufficiently separated in field. This becomes possible when higher frequencies (and fields) are used, such as Q-band at 34 GHz or W-band at 94 GHz, which leads to a clear separation of the principal values of the g -tensor. Application of simulation programs help to determine the tensor parameters from powder type spectra.

In contrast to single crystals and frozen solutions, where the TEMPOL molecules are static and ordered (crystal) or are statistically disordered and static, they are rapidly tumbling in a disordered mode in liquid solution. When the tumbling is sufficiently fast the anisotropy of g - and A -tensor is averaged and one obtains the isotropic values $g_{\text{iso}}=(g_x+g_y+g_z)/3$ and $A_{\text{iso}}=(A_x+A_y+A_z)/3$. This is indicated in Figure 2-6 (right panel) for a solution of TEMPOL giving a three line signal (triplet) with an isotropic hyperfine coupling of 1.45 mT (=14.5 G) positioned at a magnetic field corresponding to an isotropic g -factor of 2.0058. Changes in tumbling rate or restriction in mobility of the label result in systematic modification of the triplet pattern, and allow for obtaining dynamic and structural information of the system in which the label is embedded.

Co-spectrum

Cobalt (Co) is a ferromagnetic transition metal with an electron configuration of $[\text{Ar}] 3d^7 4s^2$. In nature, Co has only one stable isotope, ^{59}Co . Oxidation states of Co include -1 , $+1$, $+2$, $+3$, $+4$, $+5$, in which Co^{2+} and Co^{3+} are the most common species occurring naturally. Co is known to be present in a relatively small number of enzymes and cofactors.⁶³ It is the active center of coenzymes called cobalamins, the most common example of which is vitamin B₁₂.^{64,65} Vitamin B₁₂ contains cobalt in a substituted corrin macrocycle (a porphyrin relative). The B₁₂ coenzyme possesses an axial Co(III)-alkyl (50-deoxyadenosine or methyl) group.

In the $+2$ oxidation state, Co^{2+} (d^7) is adopting two electron spin states, $S=3/2$ and $S=1/2$. For high spin Co^{2+} ($S=3/2$) the electron configuration results in a considerable g -anisotropy which

is overlaid by zero field splitting (zfs) effects. In addition, interaction of the electrons with the nuclear spin ($I=7/2$) can result in up to eight transitions located at various g-components. Therefore, high-spin Co^{2+} spectra at X-band expand over large field ranges (from high to rather low g-values) with broad features attributed to the zfs interaction and more or less resolved hyperfine lines. For example, broad resonances at $g=6.88$ with a hyperfine coupling constant of $A = 0.025 \text{ cm}^{-1} = 26 \text{ mT}$ were observed in the EPR spectrum of Co(II)-substituted phospholipase C [Co,Zn(PLC)] reported by R Bicknell⁶⁶ in 1986. The pronounced g anisotropy produces signals from $g= 6.88$ down to 1.99, which were interpreted as indicative for the distorted octahedral coordination, comparable to that observed for other Co(II) enzymes (Kennedy et al⁶⁷, 1972). The recent study of Co(II) in the Co-querectinase enzyme from *B. subtilis*, reported by Schaab⁹⁵ in 2005, also showed comparable spectra of high-spin Co^{2+} . The presence of zero field splitting for high-spin Co^{2+} in proteins makes the EPR spectra sensitive to changes in the metal's ligation sphere. The interaction of the unpaired electrons, and therefore also of the zfs parameter D, is sensing the changes of the ligand field via modified orbital energies upon binding different substrates or substituting a ligand. This dependence on the zfs parameter in some cases leads to strong changes in line width and resolution, because the ligand field may adopt many slightly different states (of e.g. ligand binding). It is mentioned, that the extremely short relaxation times of high-spin Co(II) requires low temperatures in the range from 4 to 20 K for observation of EPR spectra.

In comparison, for the low spin state of Co^{2+} ($S=1/2$) the anisotropy in g-factor is drastically reduced and resonances are found around $g=2$. Due to the absence of zfs effects the line width is generally much lower than in the high-spin state and the hyperfine coupling is well resolved. In this work no low-spin states of Co-querectinase were observed.

Evaluation of CMH and TAM measurements in enzyme reactions

The spin probe CMH is a one-electron reductant that effectively reacts with superoxide anion radical in a fast kinetic reaction ($k \sim 10^3\text{-}10^4 \text{ M}^{-1}\text{s}^{-1}$) to form the EPR accessible CM^\bullet radical, but it is also known to be susceptible to reaction with other oxidative species. Therefore, CMH is used in this study to follow the formation of oxidizing species which are expected to appear in the examined enzymatic reaction (see below). The emerging CM^\bullet radical is very stable and elicits a typical 3-line EPR spectrum whose temporal evolution was recorded for certain time periods (Figure 2-7 left panel).

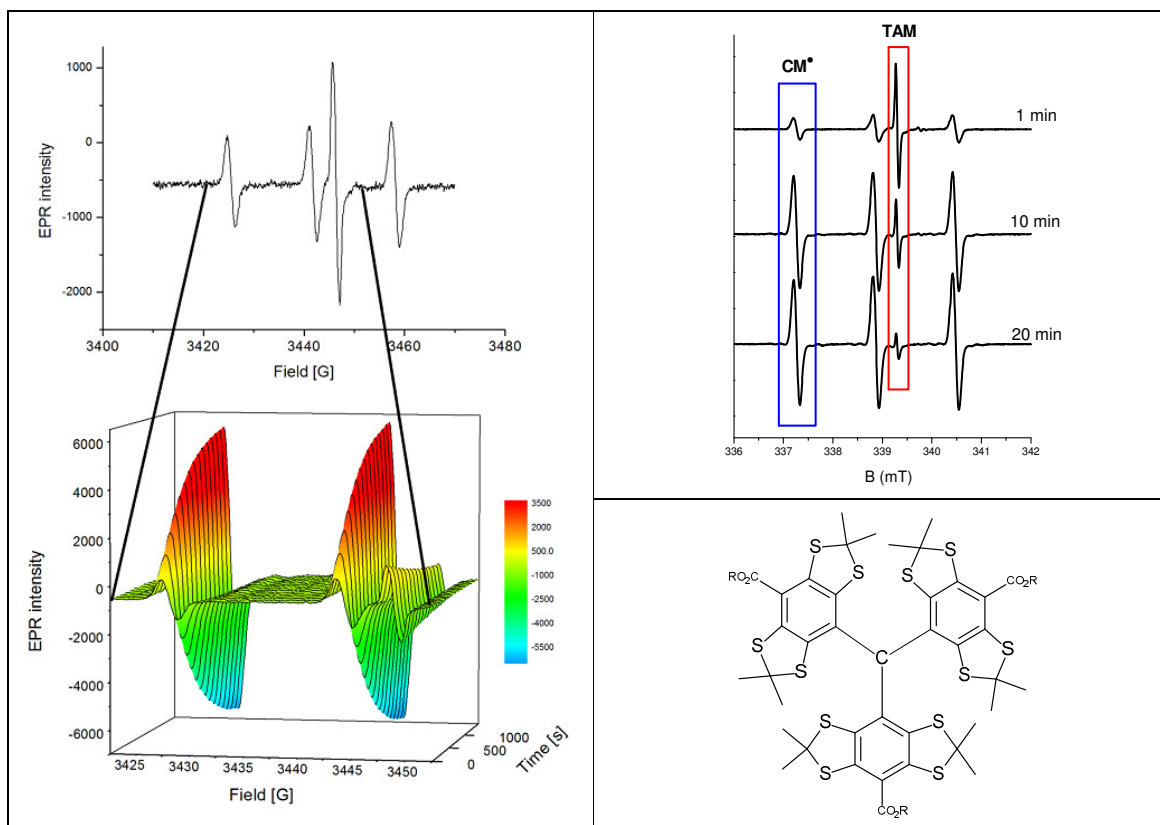


Figure 2-7. (Left panel) Temporal evolution of EPR spectra in the HodC reaction with BHOQ. The single spectrum (top) indicates the spectral segment used for presentation of intensity changes of CM and TAM radical signals. (Right panel, top) EPR spectra of CM and TAM radicals for different reaction time. While the intensity of CM is increasing, the TAM signal is attenuated for the decrease in concentration of dissolved oxygen. The blue and red rectangles indicate the lines of both radicals used for evaluation of concentration. The chemical structure of TAM (tetrathiatriarylmethyl radical) is shown in lower right panel.

Because the enzymes studied are consuming oxygen, the TAM radical ($4 \mu\text{M}$ in H_2O) was added to measure the change of oxygen concentration in the reaction mixture. The TAM oximetric probe is a sterically protected trivalent carbon bearing four sulfur atoms on the phenyl ring (Figure 2-7 lower right panel), and can be monitored by EPR displaying a narrow single line which is not overlapping with the signals of the CM^\bullet radical. In the presence of dissolved oxygen, a paramagnetic species, the TAM radical is relaxing quite fast and the signal is not saturating for the microwave power applied. When oxygen is consumed and not replenished, the TAM relaxation becomes slower and the signal intensity is diminished due to saturation effects. The observed TAM signal intensity is then proportional to the amount of dissolved oxygen.

For observing the formation of the CM^\bullet and loss of the TAM^\bullet (as an indicator for oxygen consumption), each recorded spectrum of the time series was saved with the associated time of the internal computer clock (resolution 1s). All individual spectra were then evaluated with the home made program g-medeia with which the spectra were sorted according to time, and the peak to peak intensity of a selected line was automatically measured for spectra and saved in an input file for Origin8.5 for further processing and presentation. A standard solution of 100 μM TEMPOL (4-hydroxy-2,2,6,6-tetramethylpiperidine-1-oxyl), showing an identical three-line EPR spectrum, was used to determine the concentrations of CM^\bullet in the samples.

An example of an EPR experiment of 2-butyl-3-hydroxy-4(1*H*)-quinolone (BHOQ) substrate converted by HodC enzyme in presence of CMH and TAM is given in Figure 2-7 left panel. The formation of oxidizing species in the reaction is followed by the formation of CM^\bullet , while the oxygen consumption is measured with TAM^\bullet signals. The top spectrum is the first in the time series after starting the reaction, showing the three lines of CM^\bullet and the more intense signal of TAM^\bullet . Because of the time delay for sequentially recording the CM^\bullet hyperfine lines, the 2nd and 3rd line is increasing in intensity during the ongoing reaction. The bottom graph presents the change in signal intensity for the indicated spectral segment. While the CM^\bullet signals are increasing towards saturation, the TAM^\bullet signal drops to its minimal intensity when oxygen is completely consumed.

The CM^\bullet and TAM^\bullet signals, evaluated from the peak to peak intensity of spectra, were plotted against time (Figure 2-8). Because of the non-linear behavior observed on the signal (radical) formation, non-linear regression was performed to measure reaction kinetic of CM^\bullet and rate of oxygen consumption. The fitting was performed in Origin8.5 with various appropriate fitting functions, such as sigmoidal Weibull1, exponential BoxLucas, and new derived (modified) exponential-linear growth function, dependent on the curve behavior.

These functions are shown in their explicit forms:

Weibull1 function:
$$y = A(1 - e^{-(k(x-x_c)^d)})$$

BoxLucas1 function:
$$y = a(1 - e^{-bx})$$

exponential-linear function:
$$y = A(1 - e^{-k_1x}) + k_2x$$

sequential reaction (integral form):
$$y = \frac{A_0 e^{-(k_2(t-t_0))} (e^{((k_2-k_1)(t-t_0))-1})k_1}{(k_2-k_1)}$$

For example, the fitting of a CM^\bullet formation curve (Figure 2-8) was performed with a Weibull1 function, from which the saturation concentration of CM^\bullet is determined by the fit parameter A (in this case $38.5 \pm 0.02 \mu\text{M}$). The characteristic time t , at which 63% of maximal concentration is reached is derived from k value, $t = k^{-1}$. To measure the rate of CM^\bullet formation and the decay of TAM^\bullet signals (or rate of oxygen consumption), linear fits were applied for the initial phases of the corresponding reaction for the first 2 minutes (Figure 2-8). The slopes derived from fit equation were $3.15 \pm 0.06 \mu\text{M}/\text{min}$ of CM^\bullet formation and gave a rate of $11.3 \pm 0.02 \mu\text{M}/\text{min}$ of O_2 consumption.

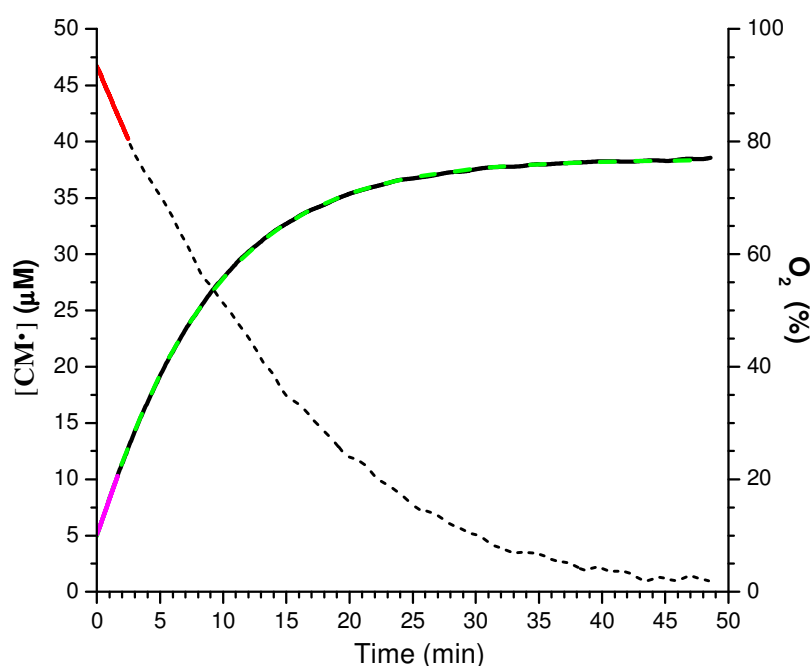


Figure 2-8. Evolution of CM^\bullet signal (solid black line) and decay curve of TAM^\bullet (dotted black line) in the conversion of BHOQ by HodC. The CM^\bullet signal is referenced to the left y-axis, while TAM signal is related to the right y-axis (100% O_2 corresponds to about $220 \mu\text{M}$ dissolved oxygen). The maximal (saturated) CM^\bullet concentration of $38.4 \pm 0.02 \mu\text{M}$ and characteristic time t of $540.5 \pm 2.5 \text{ s}$ are determined from the Weibull fit (green dashed trace). Initial rates of CM^\bullet formation ($3.15 \pm 0.06 \mu\text{M}/\text{min}$) and O_2 consumption ($11.3 \pm 0.02 \mu\text{M}/\text{min}$) are derived from linear fits (red and magenta solid lines).

2.3. Dioxygenases

Dioxygenases are oxidoreductase enzymes that catalyse the direct incorporation of both atoms of dioxygen into substrates. Dioxygenases originate from bacteria or fungi, and play a key role in biodegradation of aromatic compounds in the environment. They can be divided into

three subgroups, the iron- and copper-containing and cambialistic dioxygenases, both harboring metal cofactors, and the cofactor-independent dioxygenases.

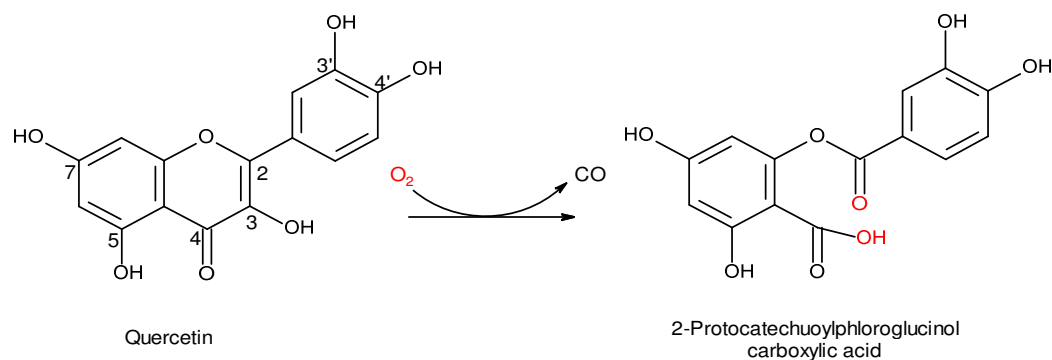
Cofactor-dependent dioxygenases usually employ a transition metal or an organic cofactor to mediate dioxygen activation. The most observed cofactors involved in the dioxygenation are iron and copper. These metals, in their lower oxidation states, can form complexes with dioxygen, organic substrate, or both, and affect the electronic structure of the bound compound to alter its reactivity. Organic cofactors like dihydroflavin and tetrahydropterin are thought to donate an electron to dioxygen, generating an activated oxygen species. Well-studied dioxygenases are iron- or copper- containing dioxygenases^{68,69,70,71,72,89} and flavin- or pterin-cofactor dioxygenases.^{40,73,74}

In contrast to cofactor-dependent enzymes, several dioxygenases have been identified which neither contain nor require any cofactor⁷⁵. The crystal structures of different families of cofactor-independent oxygenases made evident that different protein folds can provide the catalytic scaffold for oxygenation and dioxygen reduction.^{76,77,78,79,80,81,82,83,84,85,86,87,88} To date, the details of catalytic functions of these enzymes are still an open question.

2.3.1. Metal-cofactor of quercetinases

Quercetinases (QueD) are metal-containing flavonol 2,4-dioxygenases that catalyze the 2,4-dioxygenolytic cleavage of the flavonol quercetin (3,5,7,3',4'-pentahydroxyflavone) to 2-protocatechuoyl-phloroglucinol carboxylic acid and release of carbon monoxide (Scheme 2-3). In this study, the nomenclature of flavonol 2,4-dioxygenase is used instead of 2,3-dioxygenase which often is inconsistently used in literature. The 2,3-dioxygenolytic cleavage that refers for the catalytic reaction of 2,3-dioxygenases can break only one C-C bond of the flavonol (C-2 and C-3 of the center ring) and therefore is unable to release carbon monoxide as identified for the catalytic reaction of quercetinase protein.

Quercetinases from *Aspergillus japonicus* and *Bacillus subtilis* have a bicupin scaffold, each subunit consisting of 337 and 350 amino acids, respectively, which form two cupin domains.^{89,90} Quercetinase of *Streptomyces* sp. strain FLA encodes a small protein of 186 amino acids that is 35.9 and 29.0% identical in sequence to the C-terminal and N-terminal cupin domains of *B. subtilis* quercetinase, respectively, which is supporting the hypothesis that QueD of *Streptomyces* sp. strain FLA is a single-domain cupin.¹³⁰



Scheme 2-3. QueD catalytic reaction. QueD cleaves two carbon-carbon bonds of the flavonol quercetin. During the reaction both atoms of molecular oxygen are incorporated into the product, 2-protocatechuoylphloroglucinol carboxylic acid (red oxygen atoms). The reaction is fairly unique in that each molecule of quercetin produces one molecule of carbon monoxide.

Crystal structures of *A. japonicas* QueD⁸⁹ with Cu²⁺ and *B. subtilis* QueD⁹⁰ with Fe²⁺ in the active sites are shown in Figure 2-9. These two bicupin proteins have two regions of beta-barrels of N- and C-terminal domains. Comparison of these two structures shows the different number of metal binding sites, in which *B. subtilis* QueD has two Fe²⁺ binding in both core domains while *A. japonicas* QueD contains only one Cu²⁺ binding in the N-terminal core domain. Although the *A. japonicas* QueD is a bicupin enzyme, only the N-terminal domain has the 3 His and 1 Glu residues for metal-binding.

Mechanisms have been proposed for both fungal and bacterial quercetinases. For both reactions the first step is deprotonation of the 3-OH of quercetin by a nearby glutamate residue allowing quercetin to bind to the metal through its 3-oxygen. In case of quercetin 2,4-dioxygenase from *Aspergillus japonicas*, a single electron is drawn from quercetin to Cu²⁺ cofactor, thus forming the enzyme-substrate E-S complex, which is attacked by molecular oxygen at C2 of flavonol to form the peroxide. After nucleophilic attack of the peroxide on the C4 atom the endoperoxide is generated that easily releases the carbon monoxide and forms the depside-bound product (Scheme 2-4, Steiner et al⁹¹).

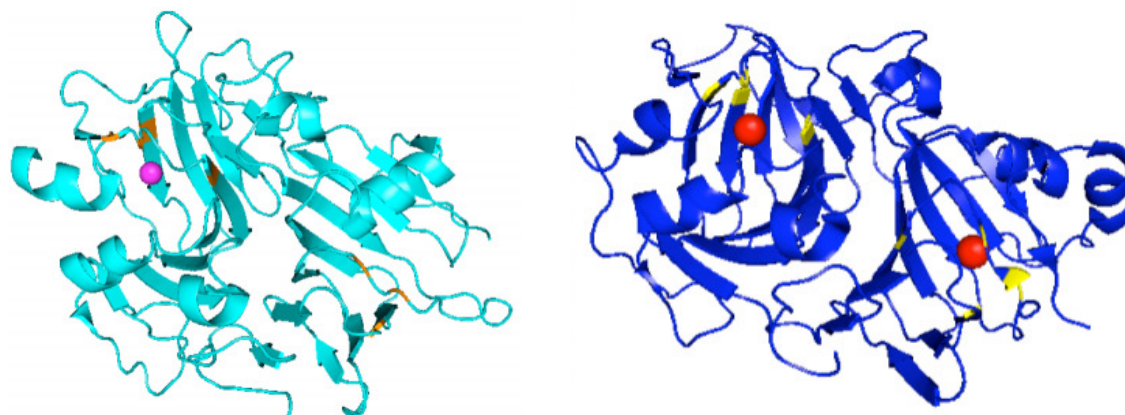
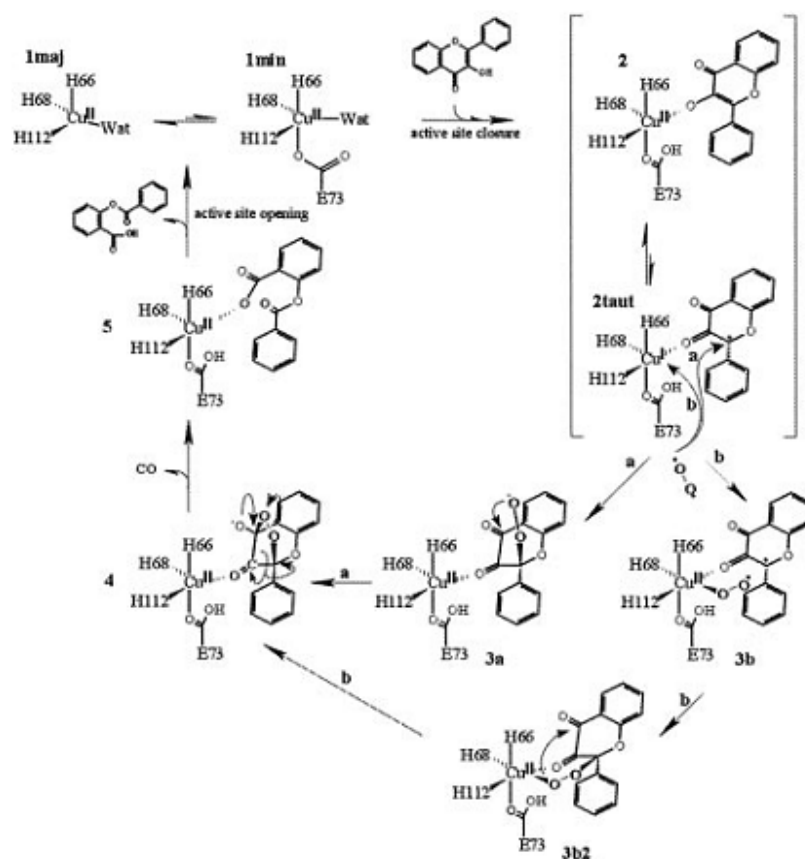
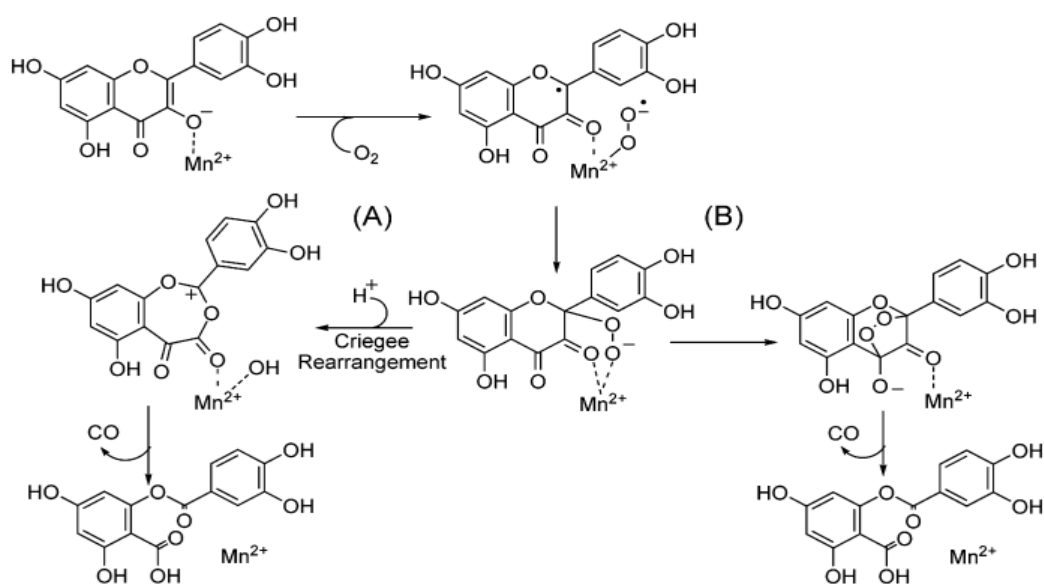


Figure 2-9. Crystal structure of *A. japonicas* QueD (cyan) and *B. subtilis* QueD (blue).^{89,90} In each structure, two beta-barrel folds can be seen, but in *A. japonicas* QueD only one domain contains a metal ion. Copper ions are shown in magenta; iron ions are shown in red. Some residues of the cupin domain are colored orange and yellow. These residues are metal-binding (HHEH) in both domains of *B. subtilis* QueD and the N-terminal domain of *A. japonicas* QueD, but they are non-metal-binding (FFNF) in *A. japonicas* QueD's C-terminal domain (adapted from⁹²).



Scheme 2-4. Substrate activation of QueD from *A. japonicas* and reaction with oxygen (adapted from Steiner et al⁹¹).

In contrast, the QueD from *Bacillus subtilis* was proposed to activate the oxygen for reaction with the substrate by binding molecular oxygen through the Mn^{2+} cofactor which is proceeding via two pathways (Scheme 2-5, Schaab M R⁹⁵); either (A) a dioxolane intermediate is formed and decomposes into the deposite and carbon monoxide, similar to the mechanism proposed for the *Aspergillus* flavonol 2,4-dioxygenase;⁹¹ or (B) the superoxide intermediate reacts with the flavonoxyl radical to form a lactone intermediate and a hydroxide ion via a Criegee intermediate, a Baeyer-Villiger rearrangement with alkyl migration would then generate the final products; this is identical to the mechanism proposed for extradiol catechol dioxygenases⁹³ and aci-reductone dioxygenase⁹⁴.



Scheme 2-5. Oxygen activation of QueD from *B. subtilis* and reaction with quercetin. Note that the metal binds both substrate and oxygen before creating the free radical that causes the oxygen bridge intermediate (adapted from Schaab et al⁹⁵).

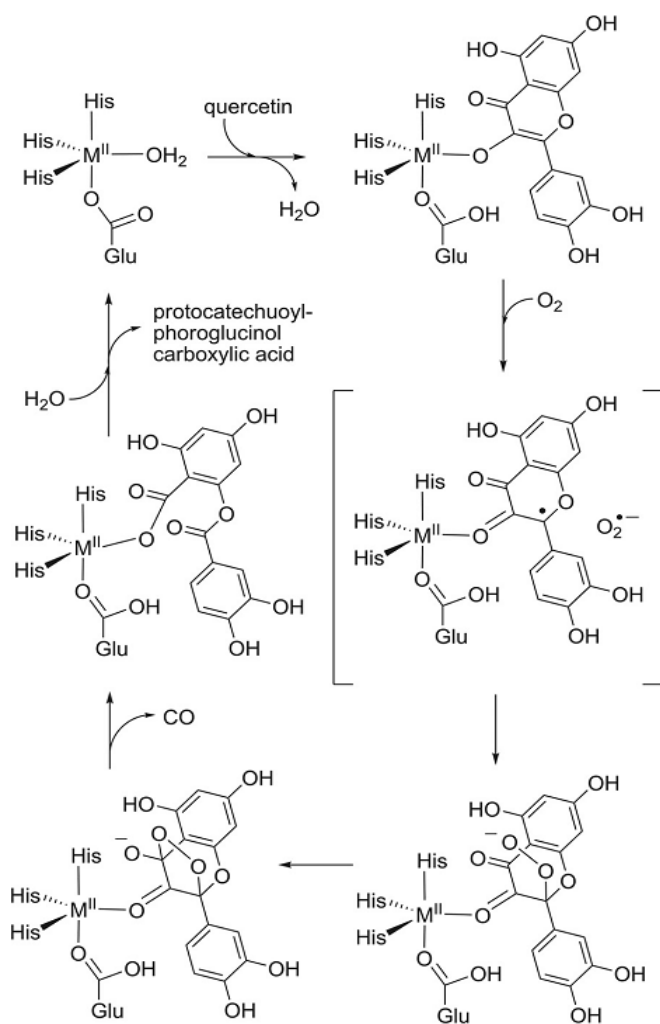
In contrast to the *Aspergillus* spp. and *B. subtilis* QueD which are most active with Cu^{2+} and Mn^{2+} , respectively, quercetinase from *Streptomyces* sp. strain FLA is very interesting as a cambialistic quercetinase. *Streptomyces* QueD is a monocupin enzyme and is most active with Ni^{2+} ions as cofactor, followed by Co^{2+} .⁹⁵ A variety of other metals Cu^{2+} , Fe^{2+} , Mn^{2+} can afford for the catalytic reaction of this enzyme.^{129,130} Considering the wide range of reduction potentials (>1.5 V, Table 2-1), the redox properties of bound metals are suspected rather non-decisive for the reaction. Recent EPR studies of Co^{2+} and Ni^{2+} metal centers of quercetinases

and model complexes⁹⁶ suggested that the accessibility of redox states other than the divalent metal M^{II} -state is debatable.^{129,130} This leads to the suggestion that the M^{II} -flavonolate complex is oxidized by an outer-sphere electron transfer to dioxygen, generating the superoxide anion radical along with the M^{II} -[flavonoxy radical] without valence change of the metal (Figure 2-10). The major role of the divalent metal ion in the active site of quercetinases could be to orient the substrate and to stabilize transition states and intermediates rather than to mediate electron transfer.

Although mechanisms have been proposed for 2,4-QueD from *A. japonicas* and *B. subtilis*, some detailed aspects of the catalytic pathway, in particular the formation of a radical pair or the peroxo intermediate state, have been not yet confirmed. This part of the study on 2,4-QueD from *Streptomyces* sp. strain FLA, following up earlier studies of Ni- and Co-QueD (Merkens et al. 2008¹²⁹), aims to achieve a more detailed insight into the catalytic reaction of this enzyme species containing various metal cofactors.

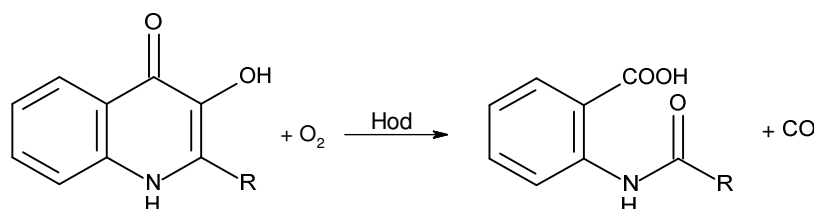
Table 2-1. Standard reduction potentials of selected transition metal cations (adapted from Fetzner S.⁷¹).

Redox pair	eV
$\text{Cu}^{3+}/\text{Cu}^{2+}$	2.4
$\text{Ni}^{3+}/\text{Ni}^{2+}$	2.3
$\text{Co}^{3+}/\text{Co}^{2+}$	1.92
	1.81
$\text{Mn}^{3+}/\text{Mn}^{2+}$	1.56
	1.5415
	1.51
$\text{Fe}^{+3}/\text{Fe}^{2+}$	0.771
$\text{Cu}^{2+}/\text{Cu}^{1+}$	0.153

Figure 2-10. Hypothetical reaction mechanism of bacterial quercetinases (*Streptomyces* QueD) (adapted from Fetzner S.⁷¹).

2.3.2. 1H-3-Hydroxy-4-oxoquinaldine 2,4-dioxygenase (Hod)

Apart from metal-cofactor quercetinase, the cofactor-free 1H-3-Hydroxy-4-oxoquinaldine 2,4-dioxygenase (Hod) was also object of a part of this study. Hod is one of several oxygenases, described so far, which have been shown to neither contain nor require any cofactor for catalysis.^{48,75} Hod is involved in the quinaldine (2-methylquinoline) degradation by *Arthrobacter* sp. Rue61a.^{97,98} It catalyzes the dioxygenolytic cleavage of two C-C bonds of its *N*-heteroaromatic substrates, releasing carbon monoxide and the corresponding *N*-acylanthranilate (Scheme 2-6). The analogy of this reaction to that of quercetinases is motivating a comparison of the structural and mechanistic prerequisites of the catalytic processes in these two groups of enzymes.



Scheme 2-6. Reaction catalyzed by 1H-3-Hydroxy-4-oxoquinaldine 2,4-dioxygenase (Hod). R = H, CH₃, or C₂ to C₉ *n*-alkyl.⁹⁹

Hod belongs to the α/β -hydrolase fold superfamily of proteins that often employ a catalytic triad consisting of a nucleophilic residue (Ser or Asp), a strictly conserved histidine, and an acidic residue (Asp or Glu) for catalysis.^{78,100,101,102} Remarkably, such a triad is structurally conserved in the dioxygenase Hod, comprising the residues S101, H251, and D126 (Figure 2-11).⁷⁸ Whereas in canonical α/β -hydrolases the nucleophilic residue is essential for catalysis, S101 of Hod is not required for substrate turnover, but rather is involved in binding of the organic substrate. In contrast, H251 and D126, which form a charge-relay tandem, have a key role in catalysis.⁷⁸ Steady state kinetic and UV spectroscopic data indicated that upon initial binding of the physiological substrate 3-hydroxy-2-methyl-4(1H)-quinolone (MHOQ) to the enzyme, H251 acts as a general base to form an MHOQ anion.^{78,104} From the crystal structure of Hod in complex with MHOQ, it can be deduced that deprotonation by the His/Asp dyad selectively occurs at the 3-OH group of the substrate, while the substrate's NH group is hydrogen bonded to the backbone carbonyl oxygen atom of W36.⁷⁸ However, the hypothesis of a general base mechanism does not address the key question of how the enzyme is activating dioxygen and thus satisfying the quantum rule.

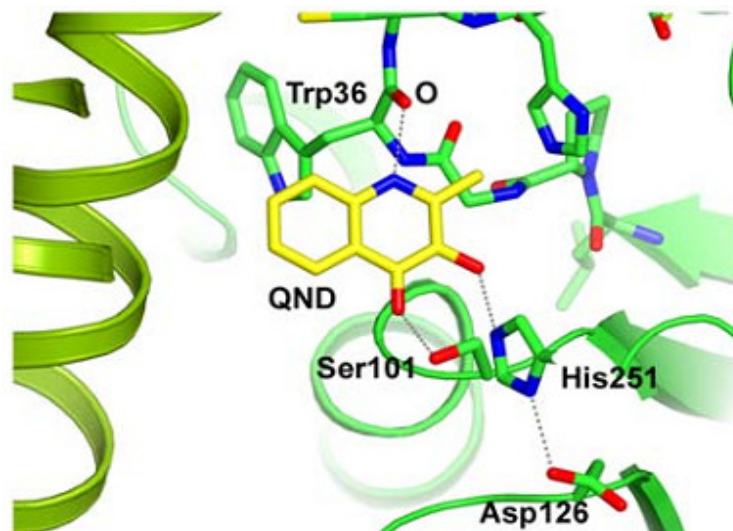


Figure 2-11. Catalytic dyad residues in the active site of dioxygenase Hod, the substrate is shown in yellow (adapted from Fetzner S.⁴¹)

In this part of the study, our major concern was to thoroughly understand the catalytic mechanism of this enzymatic reaction. Two possible catalytic mechanisms have been proposed for cofactor-independent enzymatic O_2 activation. For urate oxidase, it was recently reported that activation of the enzyme-bound urate dianion to a urate monoanion radical and enzyme radical (EH^\bullet) occurs without participation of dioxygen.¹⁰³ In 2004, U. Frerichs-Deeken¹⁰⁴ proposed that the catalytic mechanism of cofactor-less 2,4-dioxygenase Hod involved a single-electron transfer from enzyme-bound substrate anion to dioxygen to form a [substrate radical-anion superoxide radical] pair. Radical recombination would then form a peroxide anion or hydroperoxide. This alternative mechanism is analogous to the reduction of reduced flavins with dioxygen. In the Hod reaction pathway, a subsequent intramolecular reaction would afford a C2-C4-endoperoxide, which collapses to release the products CO and *N*-acetylthranilate. However, except for initial proton abstraction by H251 to form the enzyme-bound substrate anion, the proposed reaction pathway is still hypothetical. This presumption agrees well with the hypothesis of bacterial metabolism of quinoline and derivatives under aerobic redox condition which was discussed in 1997 by S. Fetzner.¹⁰⁵

Using EPR and analytical spectroscopic methods, our major interest was to address the question of how a cofactor-independent enzyme works in catalysis, using the available 1*H*-3-Hydroxy-4-oxoquinoline 2,4-dioxygenase (Hod) system.

3. MATERIALS AND METHODS

3.1. Materials

The cyclic hydroxylamine 1-hydroxy-3-methoxycarbonyl-2,2,5,5-tetramethyl-pyrrolidine (CMH) and 1-hydroxy-3-carboxy-2,2,5,5-tetramethylpyrrolidine (CPH), the oximetry probe NOX-15.1-OS (a tetrathiatriarylmethyl radical (TAM)), the spin label radical TEMPOL (4-hydroxy-2,2,6,6-tetramethylpiperidine-1-oxyl), deferoxaminemethanesulfonate (DF) and diethylthiocarbamate (DETC) were obtained from Noxygen GmbH (Denzlingen, Germany).

Potassium phosphate monobasic (K_2HPO_4), potassium phosphate dibasic (KH_2PO_4) Trace-SELECT (≥ 99.995 and 99.999 %), as well as quercetin, rhamnetin, myricetin, 3-hydroxyflavone, potassium dioxide (KO_2), stabilized hydrogen peroxide (H_2O_2), type VI-A horseradish peroxidase (HRP) and the NO-donor 3-(Aminopropyl)-1-hydroxy-3-isopropyl-2-oxo-1-triazene (NOC-5) were purchased from Sigma-Aldrich (Seelze, Germany).

Dimethyl sulfoxide (DMSO) (≥ 99.9 %) was purchased from Sigma-Life Science (Germany) and ethanol absolute (≥ 99.8 %) was obtained from Sigma-Aldrich (Seelze, Germany).

3-Hydroxy-2-methyl-4(1*H*)-quinolone (MHOQ) and 2-Butyl-3-hydroxy-4(1*H*)-quinolone (BHOQ) were synthesized by S. R.Chhabra following the procedure reported by Ilangovan *et al.*¹⁰⁶

1*H*-3-Hydroxy-4-oxoquinaldine 2,4-dioxygenase (Hod) wild type and Hod-C69S variant (HodC) enzymes were purified by S. Thierbach (WWU-Münster) from growing of *E. coli* M15 [pREP4, pQE30-*hodC69S*] and -derivatives, and purification of the His₆-tagged Hod proteins.¹⁰⁷

Quercetin-2,4-dioxygenase (Quercetinase, QueD) of *Streptomyces* sp. FLA, expressed from *queD* gene in *Escherichia coli*, was grown and supplemented with various metal salts of $MnCl_2$, $FeCl_2$, $CoCl_2$, $NiCl_2$. All metal substituted QueD wild type and E76H, I66A and Y117A variants enzymes were prepared by D. Nianios (WWU-Münster).

Millipore water was used in the preparation of all aqueous solutions.

Stock solutions of potassium phosphate buffer (pH 7.4) were made from K_2HPO_4 and H_2PO_4 TraceSELECT. NaOH and HCl were used to adjust the pH.

3.2. Methods

3.2.1. Electron Paramagnetic Resonance (EPR)

Liquid phase EPR experiments were performed on a Bruker ESP300e spectrometer interfaced to a computer with the in-house LilaQ software system for controlling the spectrometer and recording of spectra. The spectrometer was equipped with a standard ST9010 or a specialized TMH8603 cavity holding the quartz capillary or the flat cell. Temperature control was achieved with a GTC-III gas-temperature controller (Noxygen) ($T = 25 \pm 1^\circ\text{C}$).

EPR parameters were set for all solution (liquid) measurements with modulation amplitude 0.1 mT, microwave power 10 mW and time constant 20 ms for the optimal detection of the nitroxide radical (CM^\bullet).

Stock solutions of CMH (10 mM) and TAM (40 μM , 5 μM) were prepared in degassed (de-aerated) water containing DF (25 μM) and DETC (5 μM).

Stock solutions of BHOQ, MHOQ (2 mM) and Quercetin (5 mM) were prepared in DMSO or ethanol (absolute 99.99%).

Stock solutions of 1.0 mg mL^{-1} HRP were prepared in 100 mM potassium phosphate buffer (PB) (pH 6.0) and aliquots were stored at -20°C .

Sample preparation for anoxic measurements was done in an anaerobic glove box (Coy), using nitrogen-flushed buffer and substrate solutions. Protein stock solutions, after being degassed under reduced pressure, were overlaid with moistened argon gas and equilibrated overnight. Samples were transferred into glass capillaries which were sealed gas-tight for solution experiments, or frozen in liquid nitrogen inside the glove box in quartz glass EPR tubes (Wilmad) for low temperature experiments.

To measure the formation of oxidizing species during the enzymatic reaction, 0.6 mM of CMH was added to every measured probe. Consumption of O_2 during the enzymatic reaction was followed with the oximetry probe TAM. For experiments with quercetin, 4 μM of TAM was used and the amount of QueD in the samples was adjusted to the corresponding activities. In each case, 50 μL of the respective sample was transferred into a glass capillary immediately after mixing the solutions, and spectra of accumulating radicals were recorded with a scan time of 60 s. Each spectrum consists of a 3-line EPR signal of the nitroxide radical CM^\bullet and a single signal of TAM well separated from the triplet signal.

To monitor the kinetic behavior, time-resolved spectra were analyzed by calculating the line's peak-to-peak intensity of both TAM and CM^\bullet . A standard solution of 100 μM TEMPOL (4-hydroxy-2,2,6,6-tetramethylpiperidine 1-oxyl) radical spin label, showing an identical three-line EPR spectrum, was used to calibrate the EPR spectrometer and determine the concentrations of CM^\bullet in the samples.

EPR spectra were recorded at low temperature (5K – 70K) with an ELEXSYS E680 spectrometer (Bruker) using an ESR900 cryostat and an ITC504 temperature controller (Oxford Inst.). All spectra were background corrected by using Bruker WinEpr and XEPRView computer softwares.

EPR experiments of CMH with KO_2

Stock solutions of potassium superoxide (KO_2) were freshly prepared with corresponding KO_2 concentrations (2, 5, 10, 30, 50, 70, 90, 110 mM) in 5 ml phosphate buffer (PB) (20 mM, pH 7.4). In this step, weighed powder of KO_2 was added in a quiescent solution of PB just prior experiment. Stock solution of CMH (50 mM, H_2O) was prepared in anaerobic solution. Probes of CMH (1 mM) and KO_2 (0.2, 0.5, 1, 3, 5, 7, 9, 11 mM) in PB (20 mM, pH 7.4) were then immediately prepared for EPR measurements to minimize the offset time of either decaying time of KO_2 in solution or CMH oxidation.

3.2.2. Voltammetry

Voltammetric measurements were carried out using a Potentio-Galvanostat PGSTAT12 (Autolab PGSTAT12 Potentio Galvanostat AUT72957, Netherland) running with GPES (General Purpose Electrochemical System) software.

All experiments were performed at room temperature (ca. $25\pm 1^\circ\text{C}$) under quiescent condition by using a three-electrode configuration in a one-compartment cell. A glassy carbon (GC) (0.000314 cm^2 exposed area, 2 mm diameter) was used as the working electrode, a saturated silver chloride Ag/AgCl as the reference electrode, a Platinum wire as the auxiliary electrode. The working electrode was polished with 0.3 μm alumina powder, cleaned with Millipore water in an ultrasonic bath for about 5 seconds, then again rinsed with Millipore water before use.

Cyclic voltammograms were recorded at potential scan rate of 10, 25, 50, 100, 200, 350, 500 mV/s. Differential pulse voltammetry parameters used were pulse width 50 ms, scan rate 5 mV/s, pulse amplitude 5, 7.5, 10, 15, 20, 25, 30 and 50 mV. Square wave voltammetry con-

ditions were amplitude 50 mV, frequency 10, 25, 50, 100, 200, 350 and 500 Hz. The electrochemical measurements were carried out in deaerated solutions in a pure nitrogen atmosphere.

Stock solution of CMH (50 mM) was prepared in deoxygenated Millipore water and diluted to 1mM or 2 mM final concentration for voltammetric experiments.

BHOQ, MHOQ, quercetin, myricetin, rhamnetin and 3-hydroxyflavone were dissolved in dimethyl sulfoxide (DMSO) to 10 mM concentration and diluted to 0.4 mM in phosphate buffer systems containing 50% volume of ethanol for voltammetric measurements.

HCl and NaOH were added to phosphate buffer to adjust the pH of solutions (pH 3 – 11).

3.2.3. Nuclear Magnetic Resonance (NMR)

^1H - and ^{13}C -NMR spectroscopy was performed with a Bruker Advance 500 spectrometer equipped with a 5 mm TCI cryoprobe for dilute samples. CMH and CPH, purchased from Noxygen GmbH (Denzlingen, Germany), was dissolved in deuterated phosphate buffer (pD of 1, 3, 8 and 13) and measured at 298 K. Deuterated water (D_2O) and substances (KD_2PO_4 , K_2DPO_4 , DCl, NaOD) were used to prepare CMH, CPH solutions and adjust their pD. The chemical shifts were relative to D_2O at δ 4.8 (^1H -NMR) using the standard δ notation in parts per million (ppm). Expected chemical shifts and J -couplings for suggested structures were calculated with the prediction tool of ACD/ChemSketch 7.00 release.

3.2.4. Fluorescence Spectroscopy

All the fluorescence measurements with the AmplexUltraRed assay for determination of hydrogen peroxide concentration were performed on the Tecan Infnit M200Pro with 96 wells plate. For calibration purposes, a precise determination of H_2O_2 concentration from purchased or prepared stock solution was performed with the oxidation-reduction method using potassium permanganate (for details see Appendix).¹⁰⁸

4. RESULTS

4.1. CMH

The application and role of cyclic hydroxylamines for the detection of reactive oxygen species (ROS), in particular superoxide, have been discussed in many biochemistry and physiology papers.^{23,24,25,26,27,28,29,30} In several studies S. Dikalov reported on using cyclic hydroxylamines as EPR spin probes for the *intra*- and *extracellular* superoxide ($O_2^{\bullet-}$) radical measurement in cultured cells, tissue, *in vivo* and in mitochondria. Cyclic hydroxylamines are oxidized in a fast reaction ($k \sim 10^3$ - 10^4 $M^{-1}s^{-1}$, pH 7.4) to form EPR-detectable stable nitroxides with half-lives of several hours in cell cultures. As compared to nitron spin traps which have a much slower reaction kinetic with $O_2^{\bullet-}$ radical ($k \sim 35$ - 75 $M^{-1}s^{-1}$, pH 7.4),¹⁹ cyclic hydroxylamines are therefore highly efficient for $O_2^{\bullet-}$ radical detection. Moreover, the oxidation of cyclic hydroxylamine is inhibited in the presence of antioxidant enzymes like superoxide dismutase (SOD),³¹ or substrates like ascorbate and glutathione.³² Due to these aspects, the knowledge of the redox properties of cyclic hydroxylamines is of fundamental interest, but only a few studies of the redox reaction of cyclic hydroxylamines were reported.^{32,109,110,111} Most of them focus on studying the reactions with other redox reactants, for instance, ascorbate or glutathione,³² but do not clarify fully the redox behavior of the cyclic hydroxylamines. For example, S. Morris reported on the influence of substituents on the five-membered pyrrolidine and pyrroline nitroxides on the reaction rate constants for the reduction of ascorbate.³² In a comparative study, S. Manda described the electrochemical redox behavior of five β -substituted nitroxyl radicals with different electron-donating or -withdrawing groups on the ring to understand the electronic influence of a substituent altering the redox potentials and the electrophilicity of the host compound, which would help to design new compounds with controlled chemical as well as biological activity.¹¹¹ In this study, we performed a thorough electrochemical examination of the redox properties of the cyclic hydroxylamine 1-hydroxy-3-methoxycarbonyl-2,2,5,5-tetramethyl-pyrrolidine (CMH) which is applied for the radical detection in both biochemical and physiological systems of our work. In the course of this study, the redox behaviour of 1-hydroxy-3-carboxy-2,2,5,5-tetramethylpyrrolidine (CPH), product from the hydroxyl substitution of CMH, a relative of five-member pyrrolidine cyclic hydroxylamine, was also examined. This knowledge is essential for us to understand the redox processes that might be relevant for enzymatic mechanisms and in cellular systems as well as for competitive reactions in such complex systems.

4.1.1. Redox properties and reactions of CMH

Redox behaviour of CMH

Cyclic voltammetry was used for studying the redox behavior of CMH. A typical cyclic voltammogram (CV) recorded for CMH at a glassy carbon electrode immersed in phosphate buffer (PB) solution (50 mM, pH 7) containing 2 mM of CMH is given in Figure 4-1. The electrochemical behavior of CMH exhibited two well-separated redox couples, nitroxide CM^\bullet /hydroxylamine CMH (transition I) and oxoammonium cation CM^+ /nitroxide CM^\bullet (transition II). The mid-peak potentials, $E_{\text{mid}} = \frac{1}{2} (E_{\text{p,a}} + E_{\text{p,c}})$, determined from the respective anodic ($E_{\text{p,a}}$) and cathodic ($E_{\text{p,c}}$) peak potentials for $\text{CM}^\bullet/\text{CMH}$ and $\text{CM}^+/\text{CM}^\bullet$, were +0.15 V and +0.91 V (vs. SHE), respectively. The value for transition II agrees well with that given by Manda et al.,¹¹¹ whereas their value for transition I was not determined from CV directly and showed a more negative value. Because in our case oxidation and reduction waves of both transitions were well developed, the derived mid-peak potentials are very reliable.

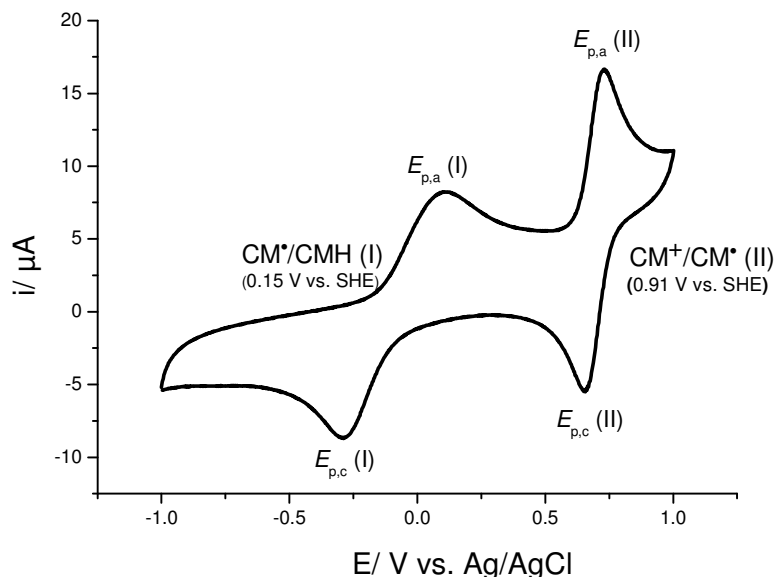


Figure 4-1. Cyclic voltammogram (CV) of CMH (2 mM) in PB (50 mM, pH 7) at 100 mV/s scan rate shows two well separated redox transitions, $\text{CM}^\bullet/\text{CMH}$ (I) and $\text{CM}^+/\text{CM}^\bullet$ (II). $E_{\text{p,a}}$ and $E_{\text{p,c}}$ stand for oxidation and reduction peak potentials, respectively. The mid-peak potentials, $E_{\text{mid}} = \frac{1}{2} (E_{\text{p,a}} + E_{\text{p,c}})$, of transition I and II are +0.15 V and +0.91 V (vs. SHE), respectively.

To understand if the processes occurring on the glassy carbon electrode are under diffusion or adsorption control, CVs were conducted for the peak current and peak potential of CMH with scan rates ranging from 10 to 500 mV/s (Figure A 1 in appendix). The observed linear depen-

dence of anodic ($i_{p,a}$) and cathodic currents ($i_{p,c}$) with the square root of scan rate ($v^{1/2}$) of two redox couples CM^{\bullet}/CMH and CM^+/CM^{\bullet} indicated that the processes are diffusion controlled (Figure 4-2A,B), according to the Cottrell equation

$$i_p = nFAC \sqrt{\frac{D}{\pi t}}$$

where i_p is the peak current (A), n the stoichiometric number of electrons involved in the reaction, F the Faraday constant (96485 C/mol), A the area of the (planar) electrode (cm^2), C the initial concentration of electroactive species (mol/cm^3), D the diffusion coefficient of the electroactive species (cm^2/s), and t time (s), (scan rate v)^{1/2} can be used in place of $t^{-1/2}$.

In addition, a linear relationship of anodic and cathodic potentials with the logarithm of the scan rate ($\log v$) of redox couple CM^{\bullet}/CMH revealed that the processes are quasi-reversible (Figure 4-2C,D) which follows from the systematic shift of the anodic and cathodic potentials to more positive and more negative values, respectively. The quasireversible nature of the electrode process of CM^{\bullet}/CMH is further supported by the large potential separation of the anodic and cathodic peak increasing linearly with logarithm of the scan rate. In contrast, the anodic and cathodic potential of redox couple CM^+/CM^{\bullet} are independent on the scan rate v indicating that this process is electrochemically reversible. Both, the anodic and cathodic currents of redox couple CM^+/CM^{\bullet} , derived from the voltammogram of CMH (2 mM) in PB (50 mM, pH 7) in Figure 4-1, gave a ratio of $\frac{i_{p,c}}{i_{p,a}} = 1$ independent on applied scan rates which also confirmed the reversibility of the processes.

Furthermore, the number of electron transferred for the redox couple CM^{\bullet}/CMH is determined by the modified Nernst equation for the quasi-reversible electrode process:

$$E_p = E^0 + \frac{RT}{\alpha nF} \left[\ln \left(\frac{k_s}{\sqrt{D}} \right) - 0.51 \ln \left(\frac{\alpha nFv}{RT} \right) - 0.78 \right]$$

where α is the electron transfer coefficient, k_s the standard heterogeneous rate constant (cm/s), R the gas constant (8.314 (VC)/(Kmol)), T the temperature (K), n the stoichiometric number of electrons involved in the process, F the Faraday constant (96485 C/mol), D the diffusion coefficient of the electroactive species (cm^2/s), and v the potential scan rate (V/s).

The factor αn can be calculated from the linear slope of peak potential as a function of the logarithm of scan rate ($\log v$) for the redox couple CM^{\bullet}/CMH . The dependence of E_p vs. $\log v$ of oxidation and reduction processes was derived from Figure 4-2C with the equations

$E_{p,a} = 0.02844 + 0.11626 \log v$ ($R^2 = 0.9446$), $E_{p,c} = -0.23285 - 0.08184 \log v$ ($R^2 = 0.99266$). The electron transfer number n in the oxidation and reduction processes of redox couple CM^\bullet/CMH was calculated to be 1, implying for the factor $\alpha n = 0.27$ as required for the electron transfer coefficient α ($0 < \alpha < 1$) which agrees well with the value of 0.35 theoretically derived by our co-worker Prof. Dr. Valentin Mirceski (data not shown).

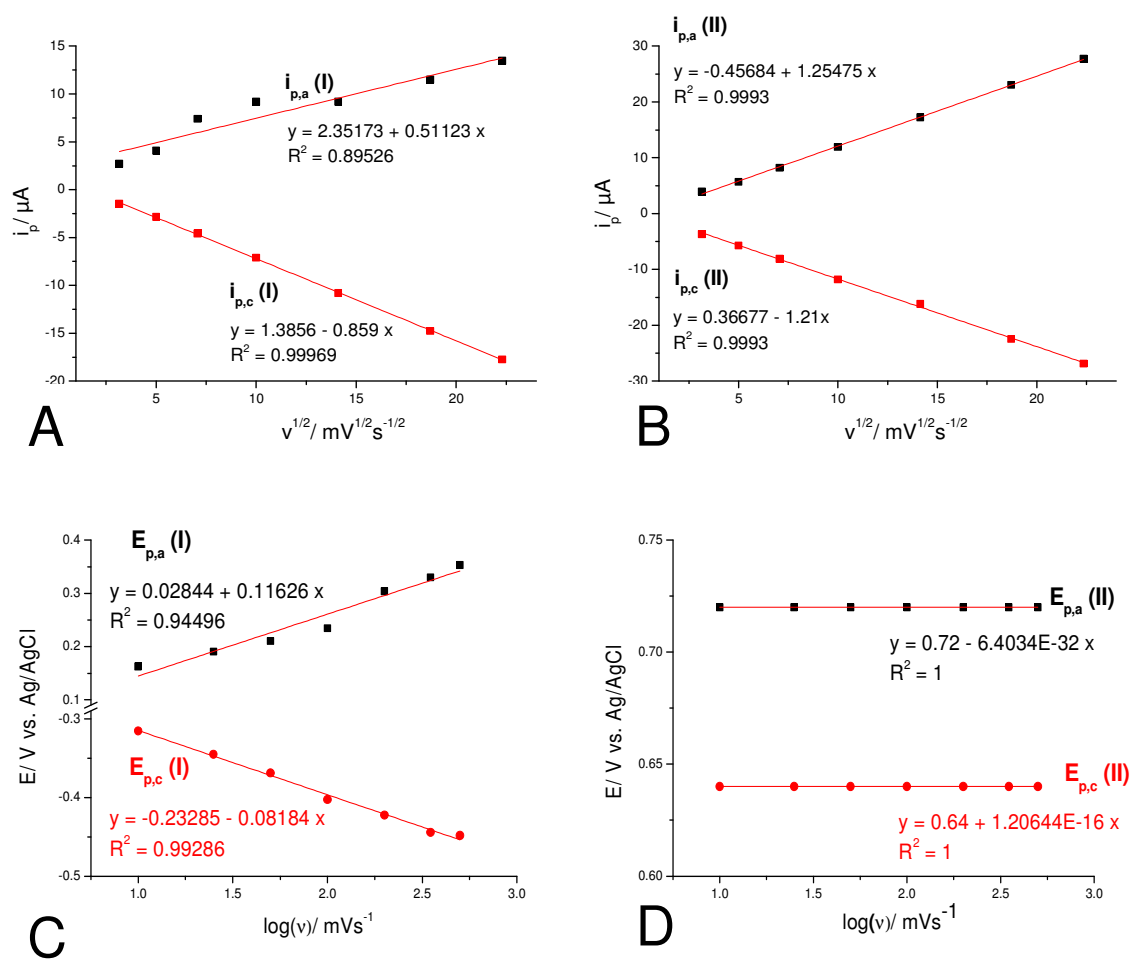


Figure 4-2. Oxidation and reduction currents of redox couple CM^\bullet/CMH (A) and CM^+/CM^\bullet (B) vs. square root of scan rate ($v^{1/2}$) in PB (50 mM, pH 7). Oxidation and reduction potentials of redox couple CM^\bullet/CMH (C) and CM^+/CM^\bullet (D) vs. logarithm of scan rate ($\log v$) in PB (50 mM, pH 7). All values were derived from CVs of scan rate variation (10, 20, 50...500 mV/s) (Figure A 1 in Appendix). Red lines are linear fits and the corresponding functions are given. Both transitions are diffusion controlled as described by the linear correlation of i_p vs. $v^{1/2}$, transition I is quasi-reversible with one electron transfer derived from linear fit function of E_p vs. $\log v$, whereas transition II is fully-reversible with independent potential vs. $\log v$.

For the redox couple CM^+/CM^\bullet , the electron transfer number was derived from the peak separation potential (ΔE) of anodic and cathodic processes (which is defined as $\Delta E = |E_{p,c} - E_{p,a}| = \frac{0.059}{n}$ (V) (at 25°C) for reversible (Nernstian) reaction) and gave a value

of 0.080 (V) ($\Delta E = |E_{p,c} - E_{p,a}| = |0.72 - 0.64| = 0.08$ (V) (Figure 4-2D). The electron transfer of redox couple CM^+/CM^\bullet was thus calculated to be 1 for oxidation and reduction processes.

Effect of pH on CMH redox behavior

In the present study the redox properties of CMH were investigated in a pH range from 1-14. Typical cyclic voltammograms recorded at 100 mV/s scan rate at various pH are given in Figure 4-3 left panel. At pH 1 no waves are observed. Above pH 2 peaks evolve for transition I and shift with increasing pH toward more negative potentials. In contrast, peaks of transition II are not affected by pH, only at very high pH peak positions and shapes are changing drastically. The midpotentials (E_{mid}) of redox couples CM^\bullet/CMH (I) and CM^+/CM^\bullet (II), determined from the anodic and cathodic potentials in CVs were plotted against pH (Figure 4-3 right panel).

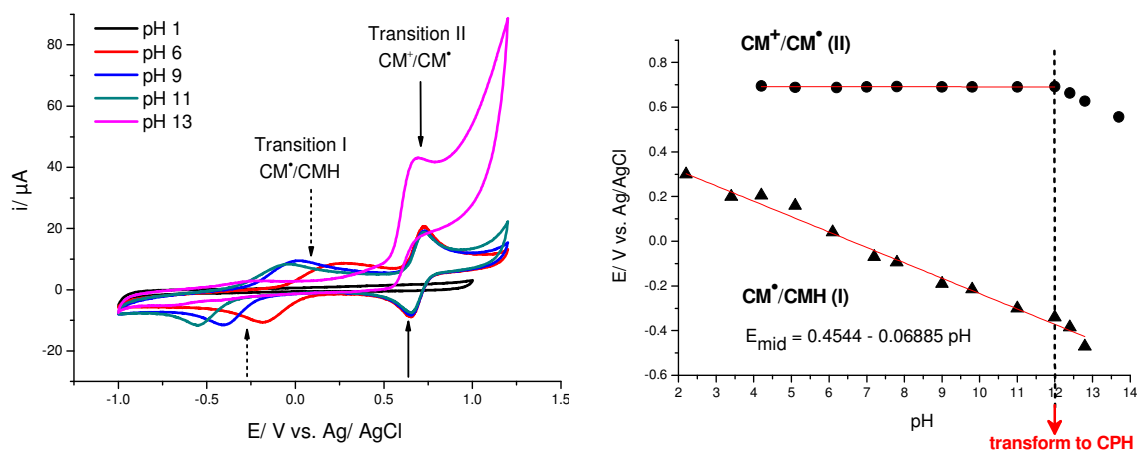
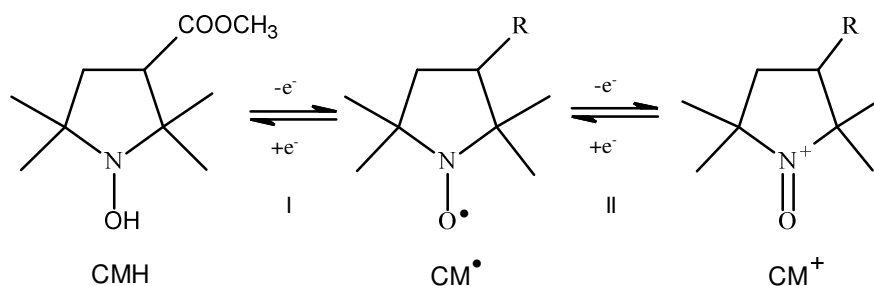


Figure 4-3. (Left panel) Selected CVs of CMH (2 mM) in PB (50 mM) in the range of pH 1-14 at 100 mV/s scan rate show the shift in potential of transition I, whereas transition II remains unaffected. Color code in figure legend indicates pH of solution. Arrows indicate the oxidation/reduction waves of the variable transition I (dotted arrows) and stable transition II (solid arrows). (Right panel) pH dependence of mid-peak potentials (E_{mid}) of redox couples CM^\bullet/CMH (I) and CM^+/CM^\bullet (II) in pH 1-14, E_{mid} was derived from the CVs in the left panel. In pH range 2-12 transition I is linearly dependent on pH with a shift of -68.8 mV of E_{mid} per pH unit while transition II is pH independent. At pH > 12 CMH is assumed to transform to CPH (see NMR data below in Figure 4-4, Figure 4-5).

Over the wide pH window of 2 – 12, the midpotential E_{mid} of redox couple CM^\bullet/CMH (I) shifted to more negative potential with increasing pH which indicates that hydrogen ions are involved in the electrode reaction. As pH increases, the hydroxyl groups gradually dissociate so that the protonation state affects the redox equilibrium. A linear relationship of E_{mid} vs. pH

was observed with a slope of -68 mV per pH unit, according to the equation $E_{\text{mid}} = 0.4544 - 0.06885\text{pH}$ (Figure 4-3 right panel). Based on the Nernst equation $E_{\text{mid}} = E - 2.303RT\text{pH} \frac{m}{\alpha nF}$ (m is the proton number, and n the number of electrons) and the linear pH-dependence, the proton number involved in this electrode reaction is calculated as 1 for the redox couple $\text{CM}^\bullet/\text{CMH}$.

Conversely, the midpotential E_{mid} of redox couple $\text{CM}^+/\text{CM}^\bullet$ (II) remained constant in the same pH window 2 – 12 implying that hydrogen ions do not participate in the electrode reaction or influence the reaction rate. These detailed observations are in agreement with the sequential redox reactions found for six-membered piperidine and saturated and non-saturated five-membered pyrrolidine nitroxides in earlier studies.^{31,109,112,113,114} As reported, CMH is first oxidized to CM^\bullet via the proton dissociation. It is followed by the second oxidation of CM^\bullet to form the oxoammonium CM^+ cation (Scheme 4-1).



Scheme 4-1. Redox reactions of two electron transfer steps of CMH. Cyclic hydroxylamine CMH is deprotonated and oxidized by one electron to nitroxide radical CM^\bullet , a second electron is abstracted from CM^\bullet forming oxoammonium cation CM^+ by further oxidation.

However, the CVs of CMH performed at very high pH ($\text{pH} > 12.5$) in strong basic solutions showed a peculiar behavior. Both oxidation and reduction peaks of redox couple $\text{CM}^\bullet/\text{CMH}$ (I) were strongly diminished, whereas the oxidation peak current of redox couple $\text{CM}^+/\text{CM}^\bullet$ (II) increased drastically but the reduction peak current virtually vanished (Figure 4-3 left panel). Additionally, in the CVs of CMH recorded in the extreme acidic solution ($\text{pH} < 2$) very weak oxidation and reduction peak currents for both redox couples $\text{CM}^\bullet/\text{CMH}$ (I) and $\text{CM}^+/\text{CM}^\bullet$ (II) were observed. To understand these new observations and to correlate them to possible structural changes, we performed $^1\text{H-NMR}$ measurements of CMH (5 mM) at 4 different pD values of 1, 3, 8 and 13. Deuterated water (D_2O) and substances (KD_2PO_4 , K_2DPO_4 , DCl , NaOD) were used to prepare CMH solutions and adjust their pD.

The corresponding ^1H -NMR spectra of CMH are shown in Figure 4-4. At pD8 the ^1H spectrum is containing four well-resolved signal groups: 4 singlet lines of totally 12 protons of 4 methyl CH_3 groups (δ 1.1-1.4), 2 multiplet lines of methylene CH_2 group (δ 2.0-2.2), 1 doublet of doublet pattern of CH group (δ 3.0-3.1) and a singlet line of 3 protons of methyl CH_3 of methoxy group (δ 3.7). The appearance of multiplet line patterns for the ring protons is indicative for an inequivalence of the methylene protons. All data are compiled in Table 4-1.

At low pD (pD 3) the spectral pattern and the proton numbers are conserved, but the groups are shifted to higher ppm-values (Table 4-1) and show broader lines. For the extreme pD 1 the ^1H spectrum showed additional symmetric splitting of all proton groups except the methoxy-protons conserving the count of protons (Table 4-1). This spectral splitting with respect to the typical ^1H spectrum pattern of CMH at pD 8 is associated with two different CMH configurations at low pD. In going through a transition state at pD 3 to the extreme pD 1 the increasingly higher concentration of deuterium ion (D^+) is inducing attachment of the D^+ ion to the lone electron pair of the nitroxide group of CMH forming an asymmetric CMH-D^+ moiety which causes the observed steric effects.

However, at pD 13 the spectral pattern changes drastically with new additional signals indicative for a second molecular species (marked with balls in Figure 4-4). In the methyl-proton region (δ 1.1-1.4 ppm) seven singlet lines are present as well as additional lines at shifts of 2.82 and 3.35 ppm. Comparing the methyl-proton resonances to the spectrum at pD 8, it becomes evident that four lines are at nearly identical positions and thus have to be correlated to CMH (marked with asterisks in Figure 4-4). Normalizing the number of protons with the methoxy group protons (at 3.745 ppm) three of these methyl peaks correspond to three protons each and that with the highest intensity to 7.4 protons. This latter finding points to a superposition with a second methyl-signal. Inspection of the new resonance at 2.82 ppm shows the same splitting pattern as the line of CMH at 3.06 ppm with an intensity of 1.37 protons. Associating this resonance to the CH-proton of the new species it is possible to calculate the protons contributing to the new methyl signals which in each case give around 3 contributing protons as listed in Table 4-1. With this procedure the CH_2 lines around 2.1 ppm also correspond now to two protons indicating that multiplet signals of CMH and the new species are superimposing. Finally, the new signal at 3.35 ppm is typical for methyl-protons of methanol, which obviously is formed under alkaline conditions. The methoxy side group of CMH is the only candidate which could result in methanol as a leaving group upon substitution with hy-

droxyl anion. This reaction then yields a new structure which is represented by the hydroxyl-amine CPH (1-hydroxy-3-carboxy-2,2,5,5-tetramethylpyrrolidine) having a carboxyl-side chain.

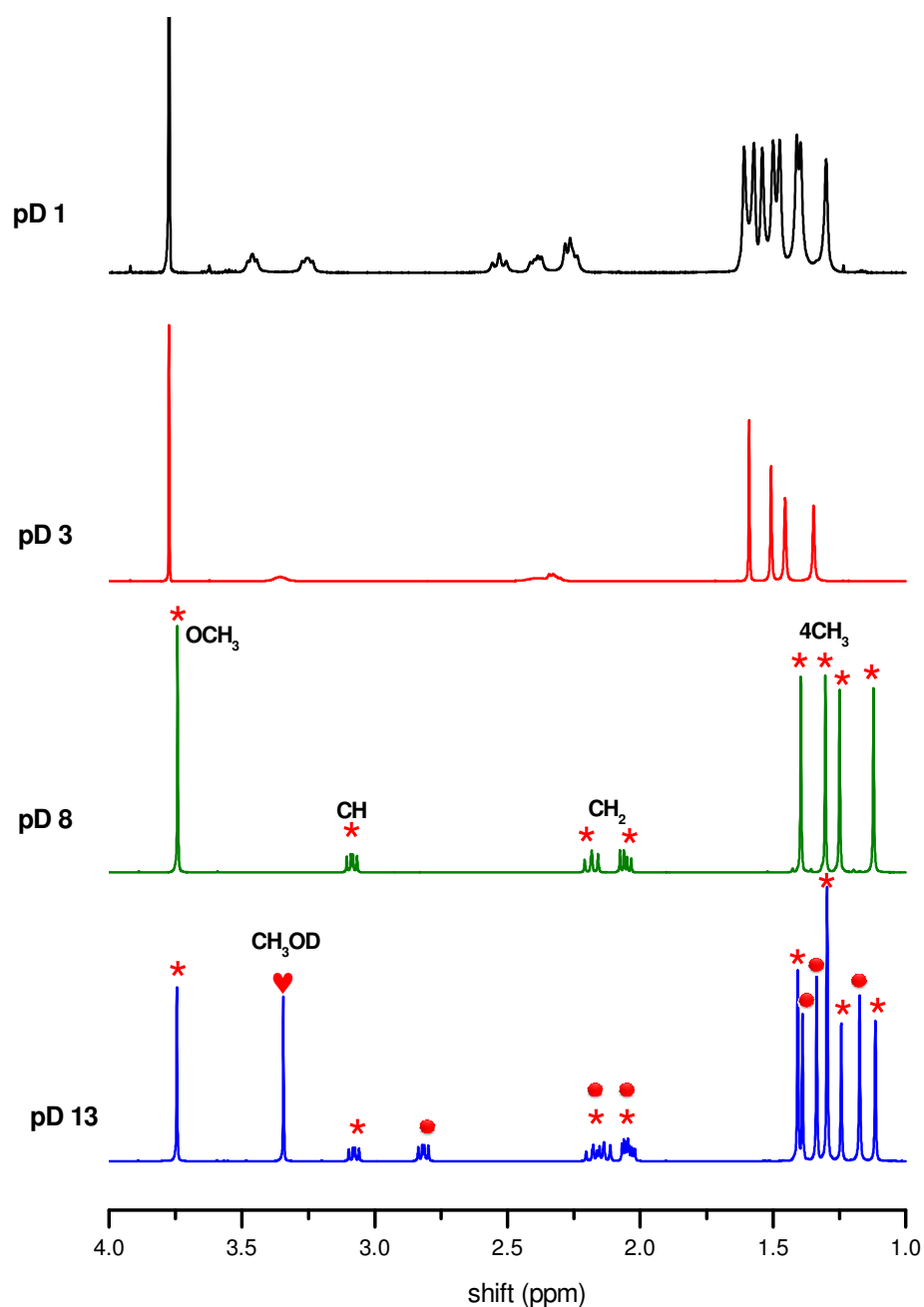


Figure 4-4. $^1\text{H-NMR}$ data of CMH (5 mM) in pD 1, pD 3, pD 8 and pD 13. The asterisks are indicative for the signals of CMH observed at pH 8, 12 protons of 4 methyl CH_3 groups (δ 1.1-1.4), 2 multiplet lines of methylene CH_2 group (δ 2.0-2.2), 1 doublet of doublet pattern of CH group (δ 3.0-3.1) and a singlet line of 3 protons of methyl CH_3 of methoxy group (δ 3.7), which remained identically at pD 13. At pD 13, CMH transforms to CPH in the hydroxyl-substitution reaction with an inequivalent ratio, the balls represent signals of CPH, the heart indicates the methoxy group which was released after the hydroxyl group attack. At pD 3 spectral pattern and proton number are maintained, but all signals shift to higher ppm and become broader, whereas at extreme pD 1 the spectrum shows a symmetrical splitting with respect to two different CMH configurations, most probably due to the steric effect caused by the attachment of deuterium ion (D^+) to the lone electron pair of the nitroxide group.

In order to confirm this hypothesis, ^1H -NMR measurements of CPH were performed for the same pD values which are shown in Figure 4-5. At pD 8, the ^1H spectrum consists of the same signals as in CMH with four methyl CH_3 groups (δ 1.3-1.5), two methylene CH_2 (δ 2.1-2.3) and one CH group (δ 2.7-3.1) consistent with proton counts (Table 4-1). As expected the methoxy-methyl protons are absent. Lowering the pD down to 1, the signals undergo a similar shift, and, for pD1, also show the splitting of resonances as observed for CMH. At pD 13 the same pattern as for pD 8 is found showing a slight shift and line broadening, which indicates that the structure of CPH is conserved for this alkaline condition. Comparing the methyl-proton resonances for CMH and CPH and adjusting slightly different chemical shifts, it becomes evident that the pattern of CMH at pD13 is composed of contributions of CMH at pD8 and of CPH at pD13 as demonstrated in Figure 4-6A. The three additional lines of CMH pD13 spectrum are arising from CPH methyl protons, and one is superimposing with a CMH resonance. Inspection of the ring protons also gives clear evidence that the new line (2.82 ppm) in CMH at pD13 can be associated to the corresponding CPH CH-ring proton. The same holds for the methylene protons of CPH (apart from line width) (Figure 4-6B).

The drastic changes in oxidation waves of CVs, the appearance of a methanol signal and the similarity of signals to CPH in NMR give clear evidence for a loss of the methoxy-group of CMH at high pH values. This finding is explained via the nucleophilic substitution reaction, in which the nucleophilic hydroxyl (OH^-) group is attached to the polarized carbon of the side group and methoxy (CH_3O) is the leaving group in this case (Scheme 4-2). In alkaline environment with high concentration of hydroxyl (OH^-) anion, the acetate (CH_3COO) groups are surrounded by hydroxyl groups which enable a $\text{S}_{\text{N}}1$ or $\text{S}_{\text{N}}2$ nucleophilic substitution reaction to occur as proposed in literature. Due to the steric effect of the bulky methoxy group, the reaction is more in favor of the $\text{S}_{\text{N}}1$ mechanism, in which the methoxy group heterolytically breaks the bond and leaves the carbon center with the electron pair in a slow process forming a carbocation. Then in a very fast process, the hydroxyl group attacks making a new bond with the carbocation and complete the substitution reaction. The released methoxy group combines with hydrogen ions in the solution forming methanol (CH_3OH) (or remains in the deprotonated state).

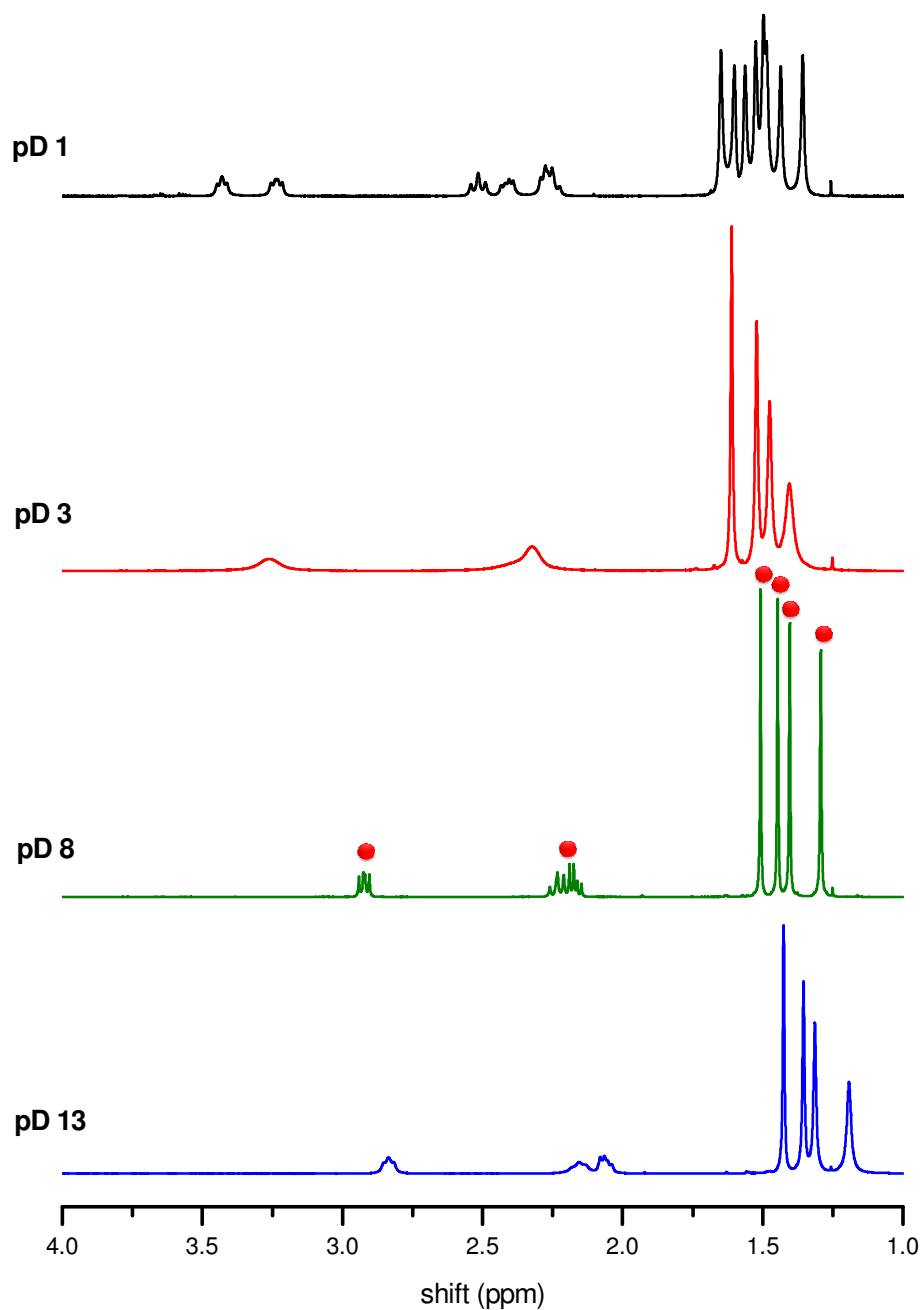


Figure 4-5. $^1\text{H-NMR}$ data of CPH (5 mM) in pD 1, pD 3, pD 8 and pD 13. The red balls display the signals of CPH at pD 8, which is identical to signals found in CMH pD 13 (Figure 4-4), four methyl CH_3 groups (δ 1.3-1.5), two methylene CH_2 (δ 2.1-2.3) and one CH group (δ 2.7-3.1). As observed for CMH, the signals shift to higher ppm, get broader at pD 3 and show a splitting at pD 1, whereas the spectrum is conserved at pD 13 with only a slight shift and line broadening.

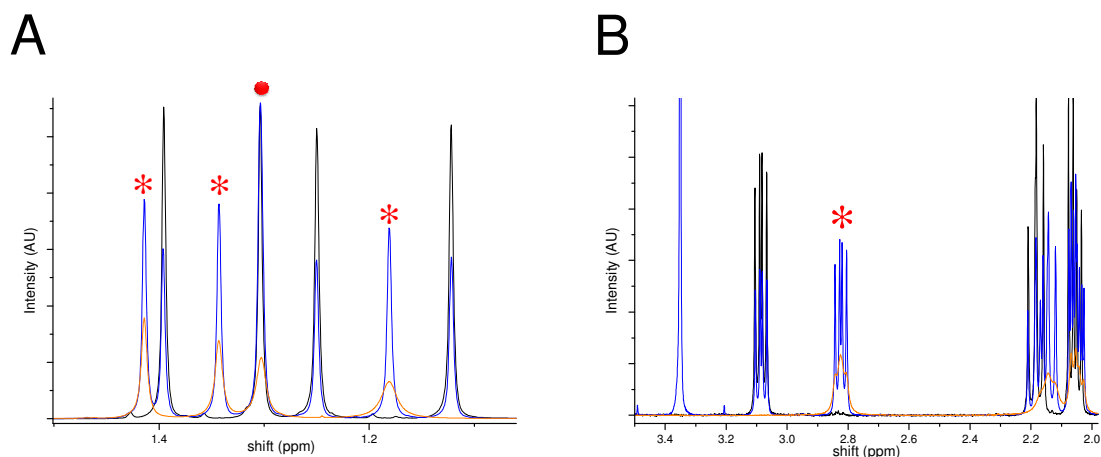
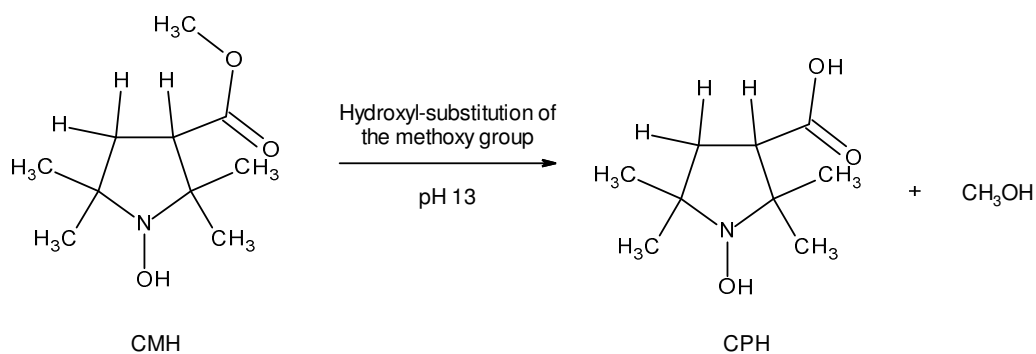


Figure 4-6. Enlarged ¹H-NMR signals of (A) methyl-proton resonance and (B) methylene- and methine (methanetriyl)proton resonance patterns of CMH (pD 8 – black line, pD 13 – blue line), CPH (pD 13 – red line). In panel A, the methyl-proton pattern, the blue lines (CMH, pD13) are composed of black lines (CMH, pD8) and red lines (CPH, pD13). The three additional lines (marked with asterisk) of CMH pD13 spectrum are arising from CPH methyl protons, and one (marked with ball) is superimposing with a CMH resonance. In panel B the new line (2.82 ppm) (marked with asterisk) in CMH at pD13 is associated to the corresponding CPH CH-ring proton. The same holds for the methylene protons of CPH (apart from line width).



Scheme 4-2. Transformation of CMH to CPH via the nucleophilic substitution reaction at pH 13, methanol (CH₃OH) is released in the reaction.

For a complete understanding of the complex redox behavior of CMH at high pH, cyclic voltammetric measurements of CPH were performed with scan rate variation of 50 – 900 mV/s (Figure A 1 in appendix). The voltammograms of CPH showed two well-separated redox couples associated with nitroxide CP[•]/hydroxylamine CPH (I) and oxoammonium cation CP⁺/nitroxide CP[•] (II) pairs, but the redox couple CP[•]/CPH was pronounced only for scan rates above 250 mV/s. This implies that the CP[•]/CPH transition is governed by a very low kinetic of the electrode reaction. The mid-peak potentials, $E_{\text{mid}} = \frac{1}{2} (E_{\text{p,a}} + E_{\text{p,c}})$ determined from the respective anodic ($E_{\text{p,a}}$) and cathodic ($E_{\text{p,c}}$) peak potentials for CP[•]/CPH and CP⁺/CP[•], were –0.05 V and +0.87 V (vs. SHE), respectively.

Table 4-1. Experimental chemical shifts of CMH and CPH in neutral and alkaline solutions (pD 8, 13).

	CMH			CPH		
		δ_H (ppm)	Normalized proton number		δ_H (ppm)	Normalized proton number
pD 8	4CH ₃	1.1-1.4 (<i>s</i>)	13.0	4CH ₃	1.3-1.5 (<i>s</i>)	12.2
	CH ₂	2.0-2.2 (<i>m</i>)	2.2	CH ₂	2.1-2.3 (<i>m</i>)	2.0
	CH	3.0-3.1 (<i>dd</i>)	1.0	CH	2.7-3.1 (<i>dd</i>)	1.0
	OCH ₃	3.7 (<i>s</i>)	3.0			
pD 13	4CH ₃	1.2-1.4 (<i>s</i>)	12.7	4CH ₃	1.1-1.4 (<i>s</i>)	12.6
	CH ₂	2.0-2.2 (<i>m</i>)	2.1	CH ₂	2.0-2.2 (<i>m</i>)	2.0
	CH	2.8-2.9 (<i>dd</i>)	1.0	CH	2.8-2.9 (<i>t</i>)	1.0
	OCH ₃ (CH ₃ OD)	3.3 (<i>s</i>)	2.5			
	4CH ₃	1.1-1.4 (<i>s</i>)	12.5			
	CH ₂	2.0-2.2 (<i>m</i>)	2.0			
	CH	3.0-3.1 (<i>dd</i>)	1.0			
	OCH ₃	3.7 (<i>s</i>)	3.0			

s singlet, *m* multiplet, *dd* doublet of doublet, *t* triplet

With this information, it is possible to interpret the redox behavior of CMH at high pH. When CMH is transformed to CPH at pH>12.5, the CVs of CMH recorded in high pH solutions at 100 mV/s showed a depletion of oxidation and reduction peaks of the first electron transfer step (Figure 4-3 left panel), because of significant depletion of the CMH concentration due to transformation to CPH, as well as the response attributed to the first oxidation of the formed CPH is not pronounced at this scan rate (Figure 4-7). The second transition with high oxidation peak current is therefore correlated to the redox couple CP⁺/CP[•]. On the other hand, the midpotentials E_{mid} observed for the redox couples CM[•]/CMH and CP⁺/CP[•] were +0.15 V and +0.87 V, respectively. Thus, the potential separation $\Delta E = +0.15 - 0.87 = -0.72$ V of both pairs CM[•]/CMH and CP⁺/CP[•] thermodynamically allows an electron to be driven from unreacted CMH to CP⁺. Consequently, the CP⁺ formed at high potential was possibly reduced by CMH regaining CP[•] that increased the oxidation peak current.

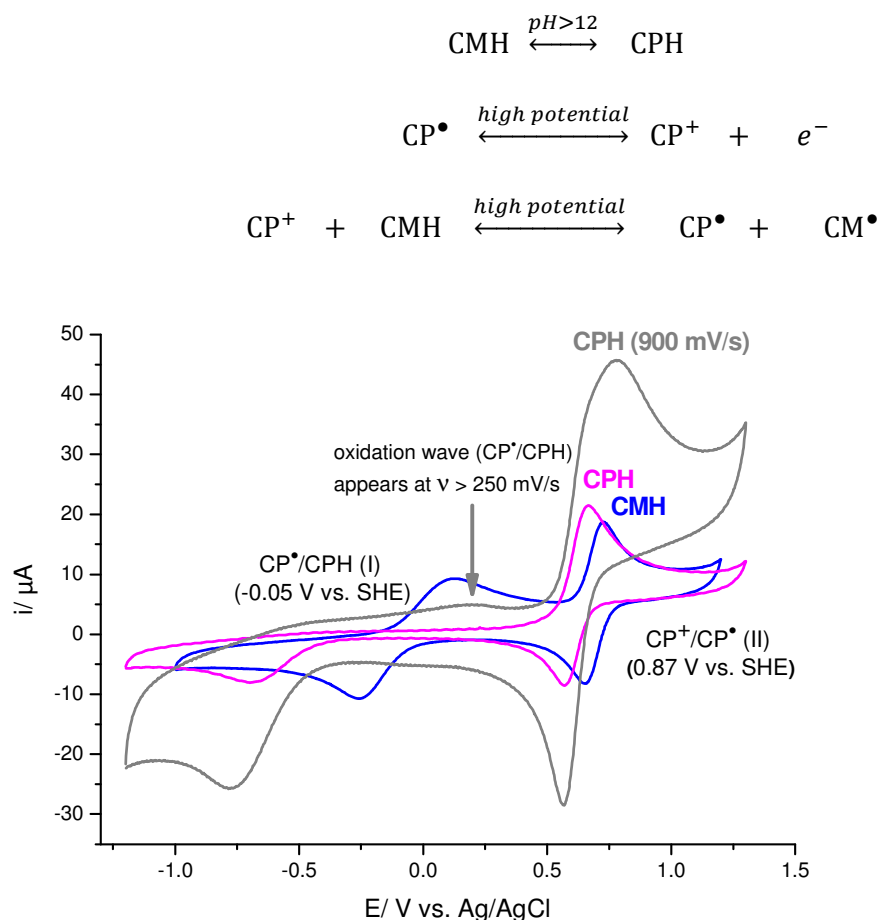


Figure 4-7. CVs of 2 mM CMH (blue line) and CPH (magenta line), both recorded at 100 mV/s scan rate, and CPH at 900 mV/s (grey line) in PB (50 mM, pH 7.4). The arrow points at the oxidation wave of CPH (900 mV/s) (transition I) which is only pronounced at high scan rate (>250 mV/s). The mid-peak potentials E_{mid} of redox couples $\text{CP}^\bullet/\text{CPH}$ and $\text{CP}^+/\text{CP}^\bullet$ were -0.05 V and $+0.87$ V (vs. SHE), respectively. The absence of the first oxidation wave of CPH (pH 7.4, 100 mV/s) is consistent with the diminishing current of transition I in CMH at pH 13, associated with the transformation of CMH to CPH at high pH (>12.5) (refer to Figure 4-3).

Because of the transformation of CMH to CPH at high pH, the pK_a of CMH could not be determined directly by CV, but is suggested to be above 14 as found in the modeling of CMH protonation states (Figure 4-8).

The pK_a - modeling is also in agreement with the experimental findings for acidic conditions. The CVs of CMH recorded at $\text{pH} < 2$ showed only very weak oxidation and reduction peak currents for both redox couples $\text{CM}^\bullet/\text{CMH}$ (I) and $\text{CM}^+/\text{CM}^\bullet$ (II). As confirmed with $^1\text{H-NMR}$ of CMH at $\text{pD} 1$ mainly doubly protonated CMH-H^+ species are present, which are also the major population in the pK_a -modeling (Figure 4-8). This protonated form of CMH is electrochemically inactive, as the free electron pair at the nitrogen, which plays a critical role

in stabilizing the CM[•] radical, is engaged in covalent bonding of the proton. With increasing pH the inactive species is gradually replaced with the active single protonated species (CMH) above pH 2 associated with the emerging redox waves for higher pH values. The modeling of CMH protonation states given in Figure 4-8 was obtained from webpage calculation (<http://aceorganic.pearsoncmg.com/epoch-plugin/public/pKa.js>).

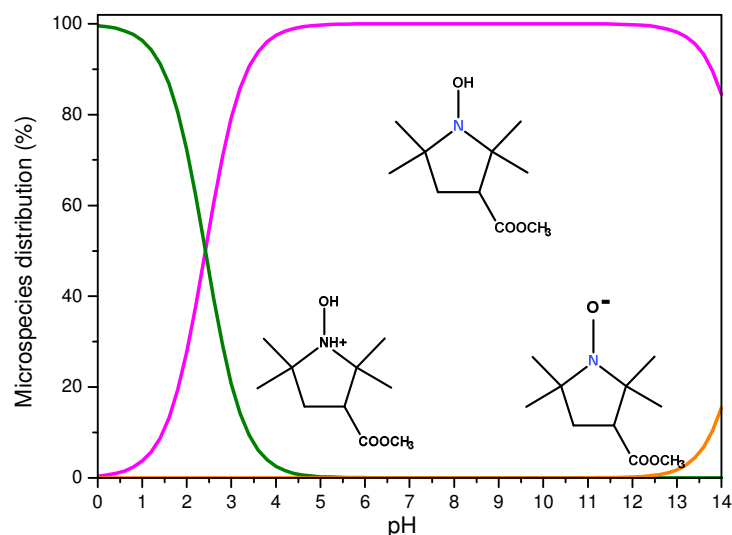


Figure 4-8. Modeling of CMH protonation states was obtained from webpage calculation <http://aceorganic.pearsoncmg.com/epoch-plugin/public/pKa.js> - doubly protonated CMH-H⁺ at pH<2, mono-protonated CMH at 2<pH<12 and deprotonated CM⁻ at pH>12.

Reaction of CMH with oxygen (O₂)

It is known from literature¹¹⁵ that CMH undergoes autoxidation in the presence of oxygen (O₂) and/or transition metal ions in an aqueous solution. As a consequence, CMH is oxidized to CM[•], which is responsible for formation of a usually small background EPR signal. In this part of our study we focus on the parameters of the CM[•] background formation related to its redox properties for its application as a spin probe in electron paramagnetic resonance (EPR) spectroscopy.

EPR measurements were performed in solutions at different pH with and without oxygen (O₂) at room temperature (25 ± 1°C). EPR parameters were set to 0.02 mT modulation amplitude, 0.63 mW microwave power, 20 ms time constant for all shown EPR experiments. The kinetics of CM[•] formation from CMH (2 mM) in solutions of pH 2, 7 and 13 are given in Figure 4-9.

Regardless of the presence of O₂, the EPR measurement of CMH solutions of pH 2 showed nearly no CM[•] formation as read from the very small slope of the fit equation $y = 6.15 - 2.33E-5 x$. This matches well with the inert redox behavior of the doubly protonated CMH-H⁺ existing at pH < 2 as described in the preceding section.

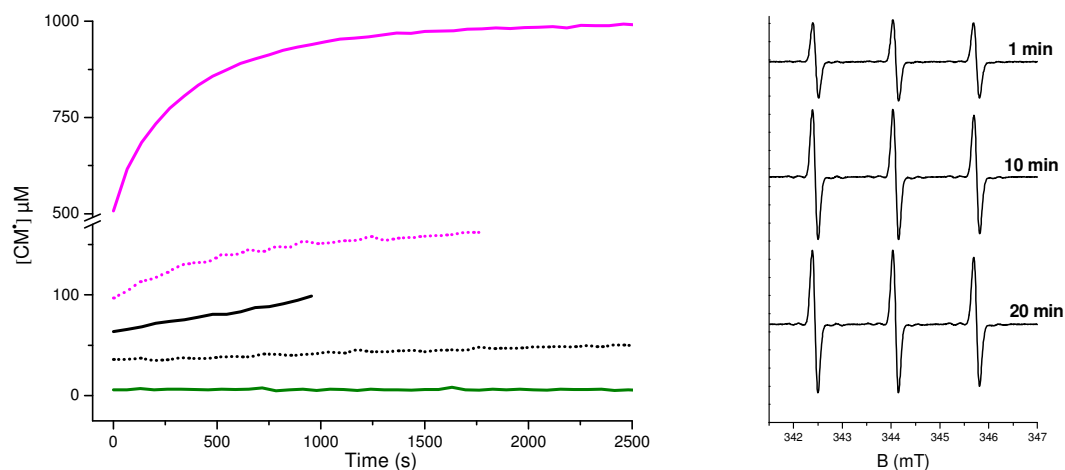


Figure 4-9. (Left panel) CM[•] background formation of CMH (2 mM) in solutions of pH 2 (olive), pH 7 (black) and pH 13 (magenta). Condition with O₂ presence is shown as solid curves and without O₂ as dotted curves. The initial formation of CM[•] was observed by linearly fitting the initial phase of all curves (conditions, or measurements). pH 13 shows a massively high increase of CM[•] and saturates when O₂ is consumed. The same behavior with much smaller signal is observed for pH 7 while nearly no CM[•] formation is seen for pH 2. Right panel shows the evolution of CM[•] at pH 13. Parameters were set to 0.02 mT modulation amplitude, 0.63 mW microwave power, 20 ms time constant for all measurements.

At pH 7, we observed two different kinetics of CM[•] formation depending on O₂. In the presence of O₂, CM[•] signals increased in a linear kinetic mode (slope of 0.03 μM/s), according to the fit equation $y = 63.66 + 0.0344 x$. However, when O₂ is absent, the slope of CM[•] signals dropped to a value of 5.8E-3 which is about 6-fold less than in the presence of O₂ (fit equation $y = 35.85 + 5.87E-3 x$). This observation is in line with the growing electrochemical activity of CMH above pH 2.

Furthermore, large CM[•] formation was surprisingly obtained at pH 13 in the presence of oxygen. CM[•] signals increased massively in the initial linear phase (slope of 1.3 μM/s), from fit equation $y = 543.87 + 1.305 x$, which is about 38 times more than at pH 7. The reaction was hindered when the limited O₂ supply (ca. 200 μM) in the capillary was consumed. Similar to findings at pH 7, in the absence of oxygen the CM[•] signals dropped down drastically to an initial linear slope of 0.12 μM/s at pH 13, which is about 10.7-fold less than with O₂ (fit equation $y = 95.74 + 0.124 x$).

The pH-dependent behavior of CMH in EPR experiments is closely correlating to the redox properties. At low pH CMH is inert for oxidation, and the presence of oxygen has no additional effect. In the physiological important range around pH 7 the small background signal without O₂ is mainly due to oxidation by traces of metal ions (and/or to residual oxygen still present even after careful preparation in the anaerobic tent). The background clearly increases in the presence of oxygen, which can be explained by Haber-Weiss- and Fenton-type reactions occurring under these conditions. As a consequence, metal chelators such as deferoxamine (DF) or diethylthiocarbamate (DETC) are used for physiological buffers to reduce background signal formation (Dikalov S, Fink B¹¹⁶). At pH above 12 CMH is gradually transformed to CPH in a slow kinetic mode, so that both species concomitantly exist. As reported, the midpotentials E_{mid} of redox couples CM[•]/CMH and CP[•]/CPH are 0.15 V and -0.05 V at pH 7, respectively. Since both processes are pH sensitive, the midpotentials of CM[•]/CMH and CP[•]/CPH at pH 13 are stepping down by -0.408 V (-0.068 V per pH unit) to -0.258 V and -0.458 V, respectively. With such low potential CMH (and also CPH) can possibly reduce O₂ to O₂^{•-} (E_{mid} of -0.329 V), which in turn can efficiently oxidize CMH to CM[•] leading to the observed dramatic increase of EPR signals. A further reaction potentially may occur, in which CPH could reduce CM[•] to regain the CMH and forming CP[•] then keeping the EPR signal constant. For full clarification of the complex reactions at high pH further experiments with variable reactant concentrations and ¹⁵N-substituted CMH or CPH would be necessary.

Reaction of CMH with superoxide (KO₂) and hydrogen peroxide (H₂O₂)

CMH is known to readily react with O₂^{•-} forming H₂O₂. Therefore, we examined reactions of CMH with KO₂ chemically liberating O₂^{•-} as well as with H₂O₂ by EPR and cyclic voltammetry. CVs of CMH (2 mM) and KO₂ (2, 4, 6 mM) in PB (50 mM, pH 7) recorded at 100 mV/s scan rate are given in Figure 4-10A. As observed, the redox couple CM[•]/CMH was not affected by addition of KO₂, but the redox couple CM⁺/CM[•] was strongly increasing in oxidation and reduction peak currents depending on concentrations of KO₂, exhibiting a typical behavior of a catalytic regenerative EC' (Electrochemical-Catalytic chemical) mechanism, in which the electrochemically formed CM⁺ at the electrode surface is reduced back to the initial form (CM[•]) in the course of the voltammetric experiment. In addition, a new reduction peak at -0.55 V associated with reduction of O₂ was observed on the reverse scan of CV. The observed change of CV pattern can be explained by the following rationale. As the experiments are conducted at equal or higher amount of O₂^{•-} compared to CMH, the total amount of CMH

is converted to CM[•], yielding additionally an equivalent amount of H₂O₂ and an excess of unreacted O₂^{•-}. Thus, the intensity of the voltammetric response corresponding to the couple CM[•]/CMH remains unaffected by the amount of added O₂^{•-}, as it is limited by the initial concentration of CM[•] radical formed in the bulk of the solution, which in turn is limited by initial concentration of CMH. Note that although the bulk solution contains only CM[•], the voltammetric pattern of the couple CM[•]/CMH has its common morphology (compare Figure 4-10 and Figure 4-1) due to the chemical reversibility of the electrode reaction and formation of CMH at the electrode surface at the starting potential of the voltammetric experiment (i.e. -1.0 V), which is significantly more negative than $E_{\text{mid}}(\text{CM}^{\bullet}/\text{CMH})$. The electrocatalytic properties of the voltammetric response of the CM⁺/CM[•] couple clearly reveals that CM⁺ is reduced back to CM[•] by the excess of O₂^{•-} in the course of the voltammetric experiment to form O₂. The latter causes the new reduction wave found in the reverse scan ascribed to O₂ at potential of -0.5 V reduction. The slope of the dependence $i_{\text{p,a}}(\text{II})$ vs. concentration of O₂^{•-} reflects the kinetics of the redox reaction between CM⁺ and O₂^{•-}.

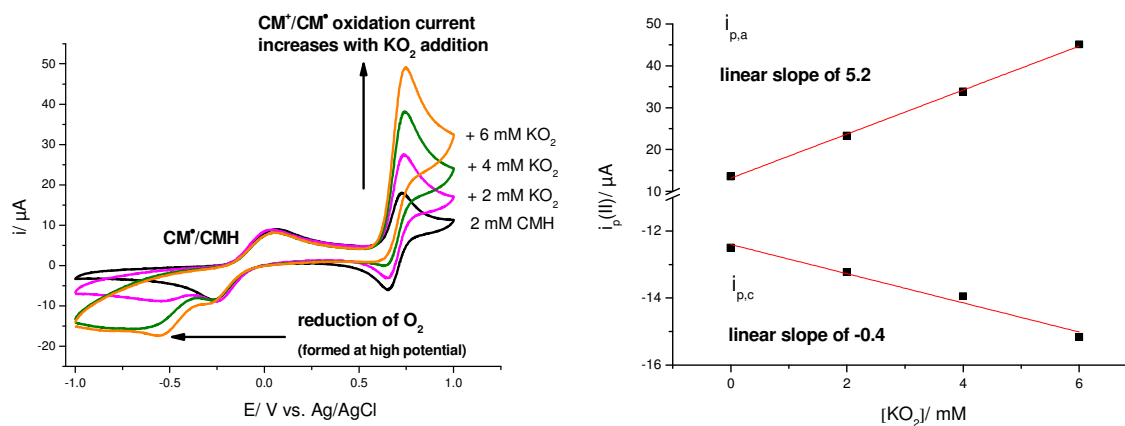


Figure 4-10. (Left panel) CVs of CMH (2 mM) with increasing concentrations of KO₂ in PB (50 mM, pH 7) at 100 mV/s scan rate. By addition of KO₂, the redox couple CM[•]/CMH is not affected, whereas the current of redox couple CM⁺/CM[•] is increased with oxidation ($i_{\text{p,a}}$) and reduction current ($i_{\text{p,c}}$) depending on the KO₂ concentration added (shown in the right panel). Both currents increase linearly but unequally with increasing KO₂ concentration, the oxidation peak current shows a slope of 5.2 μA per 1 mM KO₂, which is 13-fold higher than the reduction current (slope of -0.4). A new reduction peak at -0.55 V, observed on the reverse scan of CV, is associated to the reduction of O₂.

In addition, the corresponding EPR experiment was performed to follow CM[•] formation in the reaction of CMH with KO₂. First, background formation of CM[•] was measured for 1 mM CMH in PB (50 mM, pH 7). Then the reaction kinetics of CMH (1 mM) upon addition of 0.2, 0.5, 1, 3, 5, 7, 9 and 11 mM KO₂ in PB (50 mM, pH 7) was recorded for more than 2.5 hours.

The resulting curves after CM[•] background subtraction are given in Figure 4-11A. All reaction curves showed two different kinetics, an initial steep increase of CM[•] signal within the first 10 – 20 minutes and (with exception of the curve for 0.2 mM KO₂) a later slow decay of the CM[•] signal. Apparently, the maximum concentrations of CM[•] increase up to roughly equimolar condition and then decrease with higher KO₂ concentrations. It is noted here, that the measured CM[•] concentrations should be considered only semi-quantitative because of difficulties to apply exact concentrations of KO₂. The error for concentrations lower than 3 mM was estimated with 30 – 50%, for values above with 20 – 30% due to the small masses used and the strong hygroscopic properties of KO₂. Details of experimental preparation are explained in Methods 3.2.1. Nevertheless some clues on ongoing reactions can be derived. The liberated O₂^{•-} oxidizes CMH to CM[•] reaching full conversion of CMH for approximately equimolar concentration. For a substantial excess of superoxide formation of CM[•] is lowered which can be caused by further oxidation of CM[•] by O₂^{•-} forming diamagnetic CM⁺ and H₂O₂, a reaction thermodynamically possible as indicated by the midpotentials E_{mid} of redox couples CM⁺/CM[•] and O₂^{•-}/H₂O₂ of +0.91 V and +0.94 V, respectively. Furthermore, excess of O₂^{•-} also can reduce CM[•] back to CMH producing O₂ which is also possible according to redox potentials ($E_{\text{mid}}[\text{O}_2/\text{O}_2^{\bullet-}] = -0.3 \text{ V}$ vs. $E_{\text{mid}}[\text{CM}^{\bullet}/\text{CMH}] = +0.15 \text{ V}$). Apart from the curve for lowest KO₂ concentration, the behavior is typical for a sequential chemical reaction (E→I→P) governed by the constant of formation (k_1) and the decay constant (k_2). The experimental curves can be well fit by the integrated function for the intermediate product (see Methodology 2.2) as shown in Figure 4-11A. The formation constant k_1 is in the range 0.003 – 0.0016 s⁻¹, whereas k_2 is about two orders of magnitude smaller (see Figure 4-11B) varying slightly with KO₂ concentration (however, it has to be kept in mind, that this shows only a tendency, because of the mentioned uncertainties in KO₂ concentration). Assuming that O₂^{•-} is completely consumed or is disproportionate to H₂O₂ and O₂ in the decay regime, the slow loss of CM[•] signals can be associated to disproportionation reaction of CM[•] forming CMH and CM⁺. The latter may react with available H₂O₂ to form again CMH and O₂ in a two-step process (via CM[•]/O₂^{•-}) further decreasing the EPR signal. Both reactions, disproportionation and backward reaction for high CM[•] concentration, are sufficiently slow to explain the observed behavior. To clarify, if these and possibly other reactions are occurring, would require a detailed product analysis of the reaction processes.

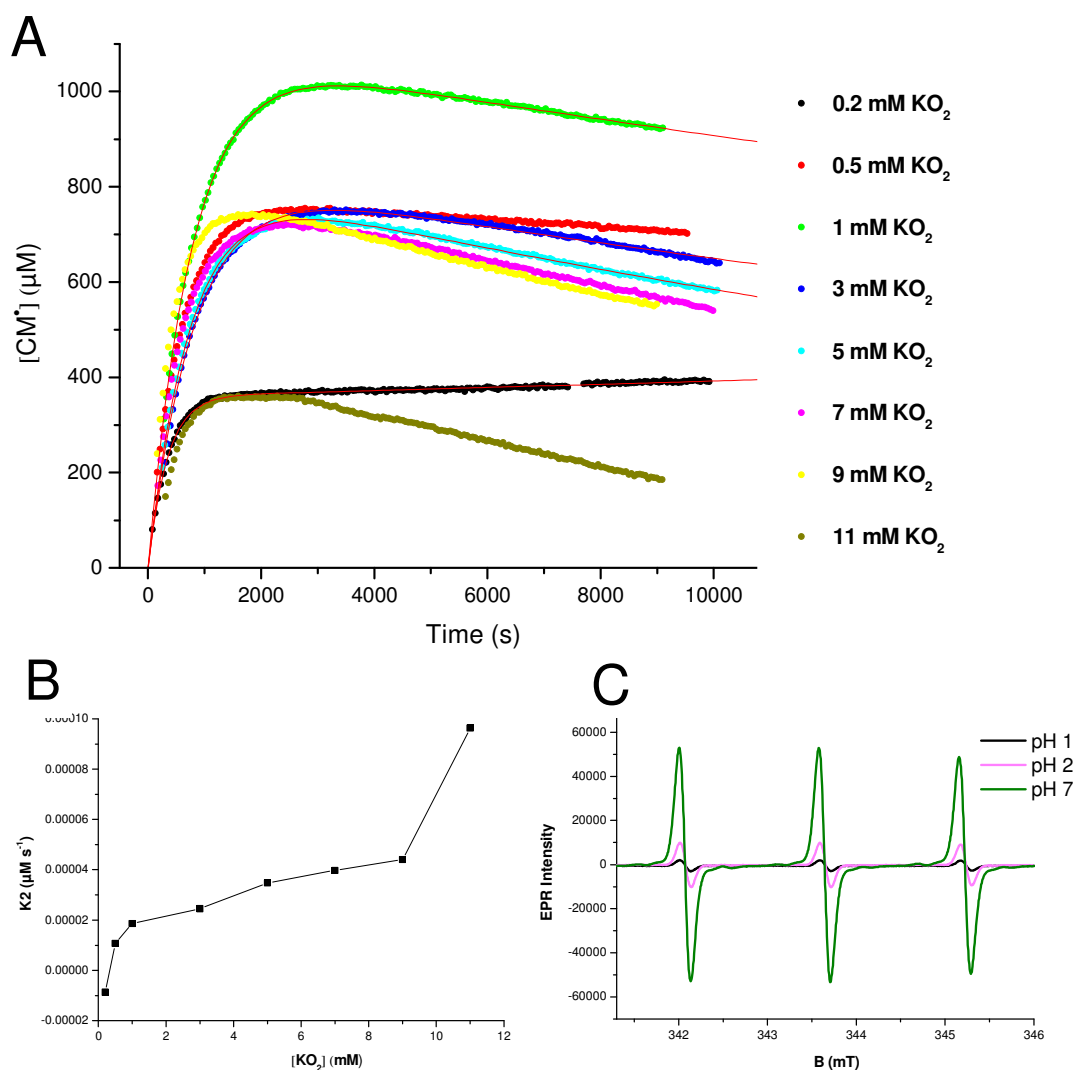


Figure 4-11. (A) Reaction kinetics of CMH (1 mM) with added KO_2 in PB (50 mM, pH 7) forming CM^\bullet is shown in dots. Color code indicates addition of different concentrations KO_2 (0.2, 0.5, 1 to 11 mM). Integrated fits are shown in red curves. EPR parameters were set to 0.02 mT modulation amplitude, 0.63 mW microwave power, 20 ms time constant. In the first 10 – 20 minutes an initial step increase of CM^\bullet signal is observed, the maximum concentrations of CM^\bullet (1 mM) increase up to roughly equimolar condition (1 mM KO_2 addition) and then decrease with higher KO_2 concentrations (with exception of 0.2 mM KO_2 addition). The rate constant k_2 of the later slow decay, as derived from the integrated fit functions of panel A, are plotted against KO_2 concentration and shown in panel B. (C) Individual spectra of CM^\bullet formed at different pH (1, 2, 7) in the reaction of 2 mM CMH and 4 mM KO_2 .

In order to study the pH-dependence of CM^\bullet formation from reaction of CMH with $\text{O}_2^{\bullet-}$, EPR experiments were performed for pH 1-7 as shown in Figure 4-11C. A drastic increase of

CM[•] signal intensity is observed for higher pH, which agrees well with the pH-dependent change of electrochemical activity measured by CV (see Figure 4-3).

A further important aspect concerns the possible reaction of CMH with H₂O₂ which was also examined by EPR and CV. Upon addition of 0.05 to 3 mM H₂O₂ to CMH (0.5 mM) in PB (50 mM, pH 7), all EPR measurements showed only small signals around the CM[•] background regardless of H₂O₂ concentration (Figure 4-12). This implies that CMH is not oxidized by H₂O₂, as is already reported in literature^{117,118}, and which is related to the result that both reactants are in the reduced form within the redox couples CM[•]/CMH and O₂^{•-}/H₂O₂ as indicated in Figure 4-14. An alternative reaction between CMH and H₂O₂ would involve formation of water and hydroxyl radical, which thermodynamically could be feasible according to the redox potentials (see Figure 4-14), but appears not to occur for kinetic reasons, as no CM[•] is observed in EPR. A comparison of the midpotentials of redox couples CM[•]/CMH (+0.15 V) and O₂^{•-}/H₂O₂ (+0.94 V) indicates that not only CMH but also CM[•] is not reacting with H₂O₂ for thermodynamic reasons.

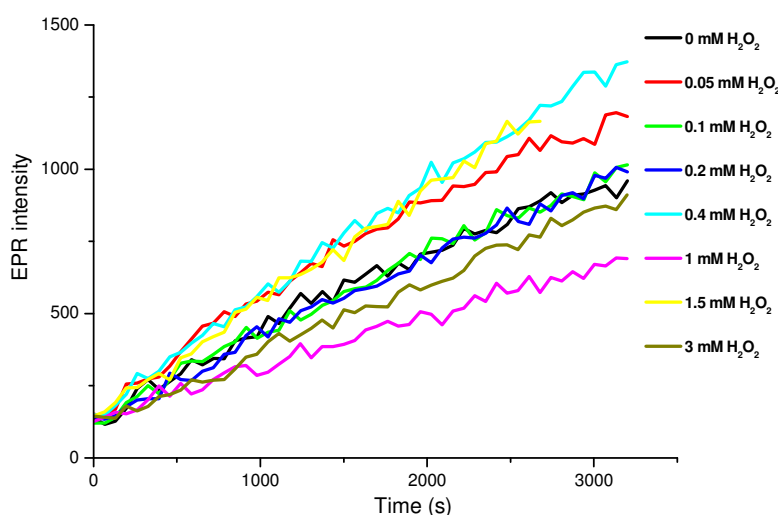


Figure 4-12. Reaction kinetics of 0.5 mM CMH with different concentrations of H₂O₂ (0, 0.05, up to 3 mM) in PB (50 mM, pH 7). EPR parameters were set to 0.02 mT modulation amplitude, 0.63 mW microwave power, 20 ms time constant. Only small signals around the CM[•] background are observed independent on H₂O₂ concentration.

Applying CV, quite similar voltammograms were obtained for the reaction of CMH with H₂O₂ as compared with KO₂, which are shown in Figure 4-13 (left panel) for 1 mM CMH and up to 3 mM H₂O₂ in PB (50 mM, pH 7) recorded at 100 mV/s scan rate. Once more, the redox

couple CM[•]/CMH remained unaffected, and an asymmetric increase of the oxidation and reduction peak currents of redox couple CM⁺/CM[•] with increasing H₂O₂ concentration was observed, typical for the catalytic regenerative EC' mechanism, together with a new reduction peak at -0.55V, assigned to the oxygen reduction. Because it was proven by EPR experiments that CMH is not oxidized by H₂O₂, its effect on the redox couple CM⁺/CM[•] in the voltammograms can only be explained by the reduction of CM⁺, which is electrochemically formed at the electrode surface at high potential to CM[•]. This results in the observed increase of the oxidation peak current of redox couple CM⁺/CM[•] and a depletion of the reduction peak current since CM⁺ is consumed in the course of the voltammetric experiment. According to mid-peak potentials of CM⁺/CM[•] and O₂/H₂O₂ (+0.91 V and +0.695 V) an electron transfer from H₂O₂ to CM⁺ is thermodynamically possible, which most probably proceeds via intermediate formation of O₂^{-•}. Note that O₂^{-•} is again able to reduce further CM⁺ to CM[•] producing finally O₂. This two fold action of H₂O₂ on CM⁺ is responsible for the larger concentration dependent slopes of oxidation and reduction currents (Figure 4-13 right panel) when compared to CM⁺ reduction by O₂^{-•} alone (see Figure 4-10), and also causes the new reduction peak at -0.55 V developing on the reverse scan from reduction of O₂.

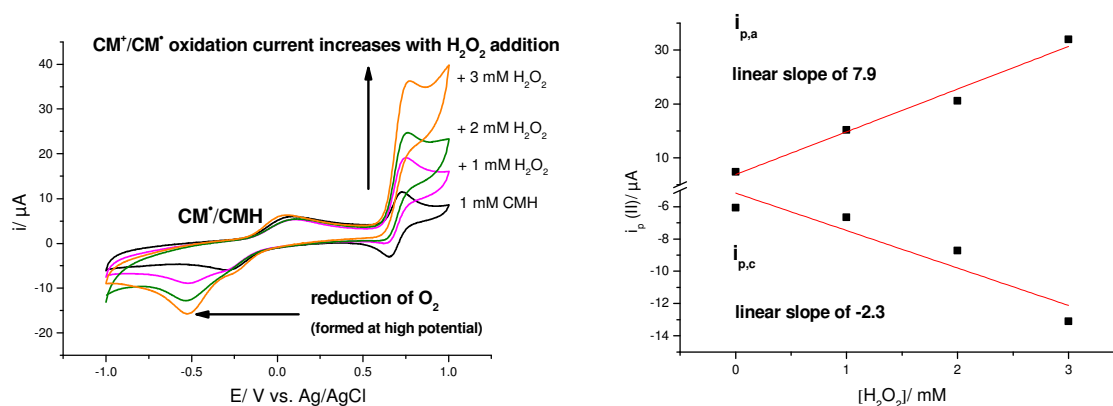


Figure 4-13. (Left panel) CVs of CMH (1 mM) with increasing concentrations of H₂O₂ in PB, pH 7 at 100 mV/s scan rate. Similar behavior is observed as for the KO₂ addition, the redox couple CM[•]/CMH is unaffected, but both oxidation (*i*_{p,a}) and reduction current (*i*_{p,c}) of redox couple CM⁺/CM[•] are increased by adding H₂O₂ as shown in the right panel. However, again the increment of current is unsymmetrical; the oxidation peak current shows a slope of 7.9 μA per 1 mM H₂O₂, which is 3.4-fold higher than the reduction current (slope of -2.3). A new reduction peak at -0.55 V again associated to the reduction of O₂ is observed on the reverse scan.

Summing up, it was possible to determine precise redox potentials of the two electron transfer steps, their pH-dependence and the reactions of oxygen, superoxide and hydrogen peroxide for both hydroxylamines CMH and CPH with CV. From the measured mid-peak potentials

the concentration dependence of the redox behavior (versus SHE at pH7) can be established, which is shown in Figure 4-14 together with some other relevant redox couples taken from literature (Halliwell B, Gutteridge J M 1999¹¹⁹). In this representation electrons flow from the reduced species located on the right side of the curves from a more negative potential to the oxidized species located on left side at higher potential, so that thermodynamically favorable reactions can be predicted. Of course, it cannot take into account kinetic considerations important for reaction, such as steric hindrance or charge effects. Nevertheless, it is a tool to discuss some of the observed reactions particularly related to EPR. It also allows visualizing the pH (or proton)-dependent redox reactions by shifting the curves up in potential or down in going to lower or higher pH with increment of 68 mV/pH-unit for ratio of one electron transferred per proton. Some reaction of redox couples can immediately be inferred such as the reduction of O₂^{•-} by CMH (arrow 1) essential for its detection by EPR. For high concentration of CM[•] and high flux of O₂^{•-} formation of CM⁺ is a possible reaction albeit with a smaller driving force (arrow 2). On the other hand, reaction of CMH with H₂O₂ appears possible (arrow 3), but homolytic splitting to form the OH[•] seems to be hindered. Dismutation of CM[•] even at high concentration is not favored in this scheme (dashed arrow 1') which explains the high stability of CM[•] in solution and the slow decay of EPR signal after reaction with excess of KO₂. An important aspect concerns interaction with redox active additives such as ascorbate (AscH⁻), which, as stated in literature, indeed is not reacting with CMH, both being in the reduced state. However, CMH may be oxidized by the ascorbyl radical (Asc[•]) as well as ascorbyl radical may destroy the CM[•]. This implies that great care has to be taken to safely conclude on the presence of superoxide radicals, when other redox active species are present in the reaction solution. Therefore, careful studies on the redox behavior of the substrates of the dioxygenases described in the next chapters had to be performed.

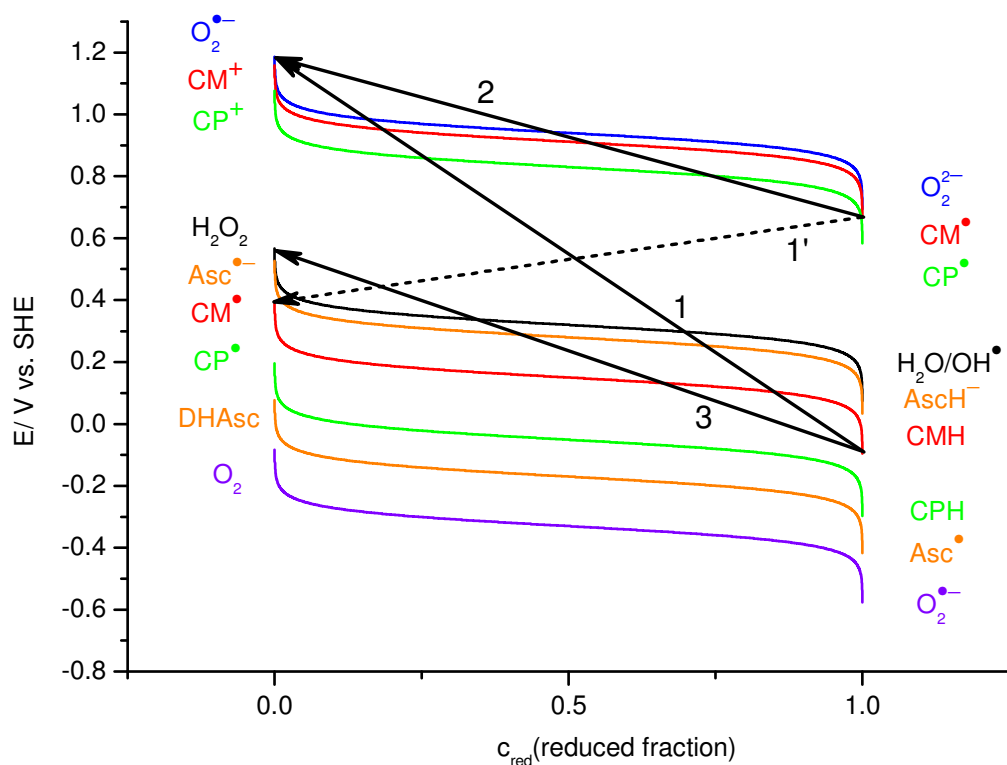


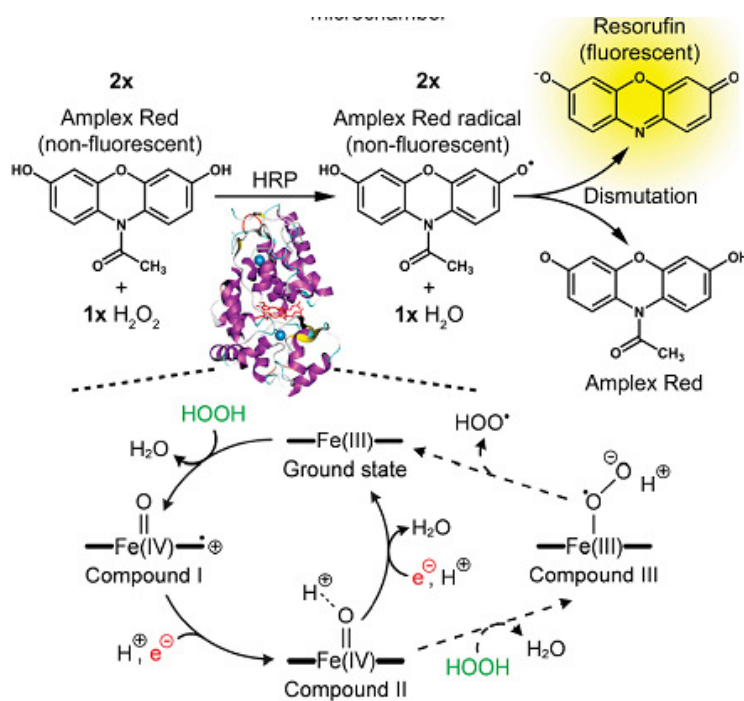
Figure 4-14. Concentration dependence of redox potentials for some relevant redox couples. By definition, the possible electron transfer is driven from a reduced species (more negative potential on the right hand side) to an oxidized species (more positive potential on the left hand side) and can occur thermodynamically. In this diagram, CMH can be reduced to CM[•] by O₂^{•-}/O₂²⁻ (arrow 1), or also by H₂O₂/H₂O, OH[•] (arrow 3), but is not affected by ascorbate (AscH⁻). On the other hand, CM[•] is possibly oxidized to CM⁺ by high flux of O₂^{•-} albeit with a smaller driving force (arrow 2), as well as being reduced to CMH by ascorbyl radical (Asc[•]). However, the dismutation of CM[•] is not favored in this diagram (dashed arrow 1').

4.1.2. CMH application for H₂O₂ quantification in HRP assay

In the course of characterizing the physico-chemical properties of the cyclic hydroxylamines CMH and CPH and the work on dioxygenases (see next chapters) the necessity of an EPR-based method to monitor presence of hydrogen peroxide (or O₂²⁻) was arising. In analogy to the widely used fluorescence based AmplexRed assay the idea was followed to test CMH as a potential electron donor to horseradish peroxidase (HRP). In short, the Amplex Red assay uses N-acetyl-3,7-dihydroxyphenoxazine (AmplexRed) as a substrate for HRP for the detection of hydrogen peroxide (H₂O₂).³⁴ Catalyzed by HRP, AmplexRed reacts with H₂O₂ in a stoichiometry of 1:1 to form a colored and highly fluorescent compound resorufin. The assay has been successfully (practically) applied to measure the activity of NADPH oxidase, monoamine oxidase and glucose oxidase, and permits detection of 50 nM to 20 μM of H₂O₂ con-

centration.³⁴ In 2002, Berglund G I described the catalytic pathway of HRP showing the redox chemistry of HRP involved in the reduction of H₂O₂.¹²⁰ The catalyzed reduction occurs via two sequential steps of one-electron oxidation of AmplexRed, forming two intermediate radicals which are dismutated to regain one AmplexRed and form one colored, fluorescent resorufin (Scheme 4-3).¹²¹ As discussed in literature, this method is limited of H₂O₂ detection (less than 20 μ M due to the fluorescent instrumental limit) and the instability of resorufin that can be further oxidized by HRP to non-fluorescent, colorless product(s).^{122,123,124} In addition, the concentration of H₂O₂ can be underestimated if a biological sample contains high levels of other peroxidase substrates, which may be endogenous compounds or exogenous compounds such as drugs, as these will compete with AmplexRed for oxidation by H₂O₂/HRP, resulting in less H₂O₂ available for the oxidation of AmplexRed.¹²⁴

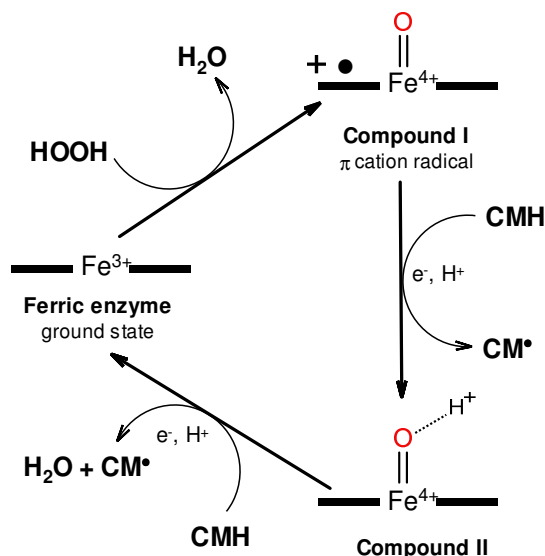
Also because of these limitations, the new HRP assay was established which utilizes the cyclic hydroxylamine CMH as a substrate for the catalyzed reduction of H₂O₂.



Scheme 4-3. Substrate turnover by HRP. HRP (purple structure) catalyzes two one-electron oxidations of non-fluorescent AmplexRed to nonfluorescent AmplexRed radicals. The formation of fluorescent resorufin (yellow background) from two AmplexRed radicals is an enzyme independent dismutation reaction. The overall reaction stoichiometry between AmplexRed and H₂O₂ (green) is 1:1³⁴ only if all AmplexRed radicals are converted to resorufin. The lower part of the scheme shows the activation cycle of HRP by H₂O₂ to CpDI and two successive electron uptakes from substrate. The dashed reaction arrows show the possible oxypoxidase pathway (adapted from reference¹²¹).

Reaction stoichiometry of H₂O₂ with CMH

A suggested EPR-based approach for detecting H₂O₂ is working in an analogous way as the AmplexRed assay using acetamidphenol (AAP) as co-substrate of HRP. After electron donation to HRP by AAP the formed radical is oxidizing CPH to its stable radical form which is detectable by EPR.¹²⁵ With the knowledge of the redox potentials of CPH and CMH for the two sequential electron steps, the new assay uses CMH as a single and direct electron donor to the catalytic cycle of HRP. For the catalyzed-reduction of H₂O₂, two electrons are needed from substrate to recycle the enzyme activity of HRP according to the proposed Scheme 4-4. Therefore, the double concentration of CM[•] should be measured by EPR for a certain amount of H₂O₂.



Scheme 4-4. Proposed electron donation of CMH substrate in the catalytic pathway of HRP enzyme. In this cycle, hydrogen peroxide (H₂O₂) is reduced by the two-electron oxidation of the ferric ground-state HRP to Compound I, which is a porphyrin- π -cation radical. To close the catalytic cycle of HRP, two single-electron transfers from CMH donor reduce Compound I first to Compound II and then back to the ground, forming two CM[•] as a consequence.

For proof of principle, the reaction stoichiometry of the HRP-catalyzed reduction of H₂O₂ with CMH was determined after a series of optimizing experiments and independent determination of the H₂O₂ concentration (see Methods 3.2.1 and Appendix). The latter tests were necessary, because deviations of up to 25% of given concentrations were observed depending on the source and the age of hydrogen peroxide stock solutions. H₂O₂ concentration was varied between 0.1 to 100 μ M with adjusted HRP concentrations to keep reactions in a reason-

ble time window. The CM[•] signal showed a typical linear initial increase and later saturation (Figure 4-15A, B). In the increasing phase CM[•] was generated from the oxidation of CMH by HRP for catalyzing the H₂O₂ reduction, and, once the reduction was complete, CM[•] formation was saturating. As controls, background formation of CM[•] was also monitored in only PB, H₂O₂ or HRP solutions that showed very small CM[•] signals, and was subtracted to obtain the reaction curves. For H₂O₂ concentrations up to 8 μM the CM[•] saturation concentration was higher than expected, whereas from 10 μM on it reproduced the stoichiometry. This can also be seen when plotting CM[•] saturation against the H₂O₂ concentration (Figure 4-15C) showing a curvature for the low concentrations. Applying a linear fit, a slope of 2.1 is obtained which is close to the expected 2:1 stoichiometry. Further ongoing studies are designed to explore the observed deviation from strict stoichiometry considering purity of HRP and the possibility of an effect of the oxygenase cycle on the results (right part of reaction sequence in Scheme 4-3). For a comparison, the fluorescence-based method was used to verify the H₂O₂ concentration, employing the HRP assay with Amplex UltraRed as an indicator dye. For the use of the assay, the calibration experiment was performed with variation of low levels of H₂O₂ concentration (0.1 to 10 μM) due to the instrumental detection limit. The Amplex UltraRed oxidation, correlated to the fluorescent intensity of resorufin, induced by the HRP-catalyzed reduction of H₂O₂ is shown in Figure 4-16 left panel. After subtracting the background signals (obtained for controls), all reaction curves show an initial increase and later saturation as also observed for EPR measurements. The calibration curve obtained by plotting the fluorescence intensities, derived from the saturating signals of resorufin on the left panel, against H₂O₂ concentration shows a perfect linear fitting (R^2 0.9988, Figure 4-16 right panel).

Taken together, the suggested method for measuring H₂O₂ is simpler than the approach by Dikalov¹²⁵ because it is not necessary to add an additional reactant to the complex mixtures. In addition it provides an amplification factor giving doubled signal intensity. The developed HRP assay using CMH as substrate was successfully applied for quantifying the amount of H₂O₂ released during catalytic turnover of BHOQ substrate by HodC-W160A enzyme as will be described in section 4.2. Recalling that CMH is reducing superoxide to H₂O₂, the suggested method could be used to measure superoxide formation, and, after addition of HRP, total formation of H₂O₂ in physiological samples of superoxide and hydrogen peroxide forming cells such as monocytes or other immune cells containing NADPH oxidases. Such studies are presently performed in our group and compared to the fluorescence-based method.

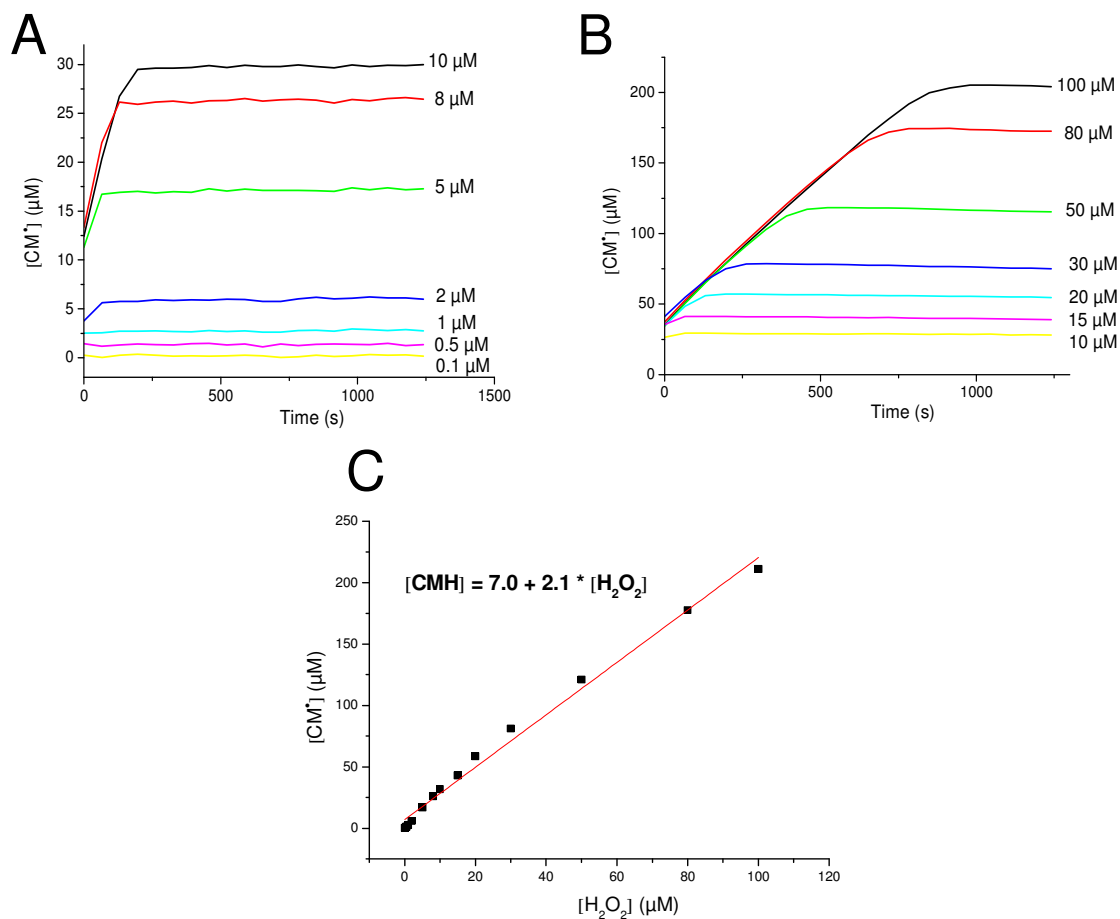


Figure 4-15. Reaction kinetics of CMH oxidation in the assay of HRP with H₂O₂ concentration of 0.1-10 μM (A) and 10-100 μM (B). The H₂O₂ concentrations are given for each trace and were added to the assay mixture of CMH (600 μM) and HRP (1 U/ml (catalyzed for 0.1- 2 μM H₂O₂), 5 U/ml (5-10 μM H₂O₂) and 50 U/ml (10-100 μM H₂O₂)) in PB (50 mM, pH 7.4) solution. The parameters of EPR measurements were set at 0.1 mT modulation amplitude, 0.2 mW microwave power. All reaction curves were background corrected and show a typical linear initial increase and later saturation of CMH• signal. (C) Calibration curve of H₂O₂ and CMH in the HRP assay (black scatter) as shown by plotting the saturating CMH• concentrations, derived from reaction curves in panel A-B, against H₂O₂ concentration. The slope of 2.1, derived from the linear equation, represents the reaction stoichiometry of CMH:H₂O₂ which is close to the expected 2:1 stoichiometry.

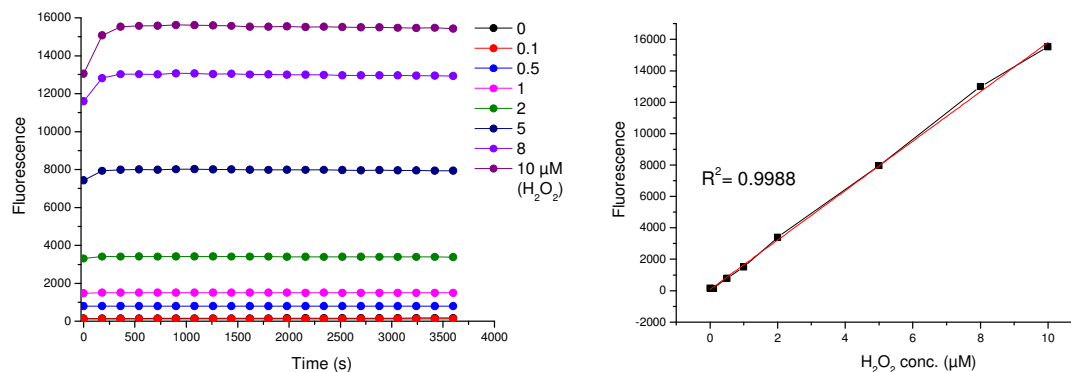
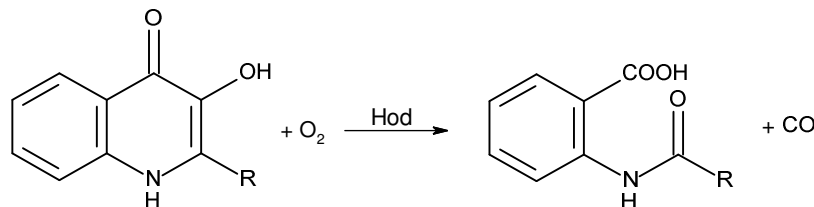


Figure 4-16. Kinetic analysis of fluorescent signal of resorufin caused by Amplex UltraRed oxidation in the assay of HRP with H₂O₂ concentrations of 0.1-10 μM (left panel). Color code identifies the H₂O₂ concentration that was added to the assay mixture of 15 μM Amplex UltraRed and 25 mU/ml HRP in PB (50 mM, pH 7.4) solution. All reaction curves were background subtracted and partly show a typical linear initial increase and later saturation of fluorescent resorufin signals. The right panel shows the calibration curve, plotting the fluorescence signals, derived from the saturating signals of resorufin on the left panel, against H₂O₂ concentration (black scatter). An excellent linearity, as judged from the coefficients of determination (R^2) of 0.9988, is observed for the linear fit of calibration curve (red line). Fluorescence was measured with a fluorescence-based 96-well plate reader using excitation at 535 ± 9 nm and emission at 590 ± 20 nm. Data are the mean of triplicate readings. Experiments were performed with E. Slowik.

4.2. Cofactor-independent 1*H*-3-Hydroxy-4-oxoquinaldine 2,4-dioxygenase (Hod)

The study of cofactor-independent 1*H*-3-Hydroxy-4-oxoquinaldine 2,4-dioxygenase (Hod) was incorporated with the Molecular Microbiology and Biotechnology group of Professor Susanne Fetzner (WWU-Münster). The results have been published recently as “Substrate-Assisted O₂ Activation in a Cofactor-Independent Dioxygenase” in *Chemistry and Biology Journal* 2014.¹⁰⁷ As mentioned in section 2.3.2, this enzyme is involved in the quinaldine (2-methylquinoline) degradation by *Arthrobacter* sp. Rue61a. Hod catalyzes the dioxygenolytic cleavage of two C-C bonds of its *N*-heteroaromatic substrates, releasing carbon monoxide and the corresponding *N*-acylanthranilate (Scheme 4-5).

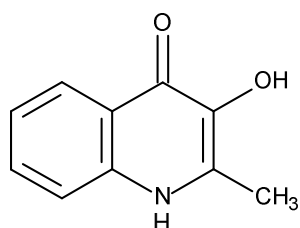


Scheme 4-5. Reaction catalyzed by 1*H*-3-Hydroxy-4-oxoquinaldine 2,4-dioxygenase (Hod). R = H, CH₃, or C2 to C9 *n*-alkyl.⁹⁹

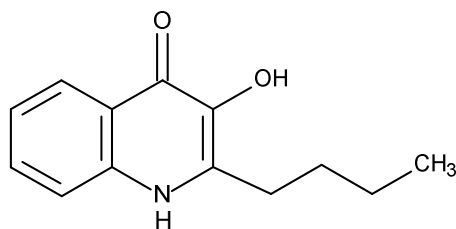
In contrast to cofactor-dependent enzymes that usually employ transition metals or organic cofactors for catalysis, several oxygenases and oxidases have been identified that neither contains nor require any cofactor⁴¹ which raises the question of how these enzymes work. However, in this group of enzymes, for which the catalytic mechanism of urate oxidase has been studied in great detail,^{83,84,126,103} the catalytic function of Hod is still an open question. Urate oxidase was proposed to catalyze an initial monoelectron activation of the bound substrate dianion, without participation of dioxygen, resulting in a urate radical monoanion and an enzyme-H[•] state; subsequent dioxygen activation is thought to occur via single electron transfer from the enzyme radical to form the superoxide anion radical.¹⁰³ For Hod, the catalytic reaction for the 2,4-dioxygenolysis has been proposed in 2004 work via a single-electron transfer from enzyme-bound substrate anion to dioxygen, forming a [substrate radical-anion superoxide radical] pair.¹⁰⁴ To thoroughly understand the complete catalytic pathway of Hod, this study was followed the earlier work of U. Frerichs-Deeken,¹⁰⁴ and attempted to address the question of how this cofactor-independent enzyme functions in catalysis, and in particular to demonstrate activation of oxygen in a radical pair.

In the course of this work, analytical and spectroscopic methods were utilized to investigate the Hod-catalyzed conversion of two substrates, the natural substrate 3-hydroxy-2-methyl-4(1H)-quinolone (MHOQ) and modified substrate 2-Butyl-3-hydroxy-4(1H)-quinolone (BHOQ) (Scheme 4-6).

3-hydroxy-2-methyl-4(1H)-quinolone
(MHOQ)



2-Butyl-3-hydroxy-4(1H)-quinolone
(BHOQ)



Scheme 4-6. Chemical structure of Hod substrates.

Transient radicals were detected with CMH for the enzymatic reaction pathway identification.

This part of studies was performed by S. Thierbach¹⁰⁷ (Münster group) and is summarized here briefly. By using EPR spectroscopy, he was able to measure the formation of oxidizing

species and O₂ consumption during the enzyme-catalyzed Hod reaction by adding the redox-activated cyclic hydroxylamine CMH spin probe and oximetry probe TAM, respectively.

The natural substrate MHOQ (methyl-) and a modified substrate BHOQ (butyl-), with better accessibility for the active site of enzyme, were prepared. Hod-C69S variant (or HodC) having the identical catalytic activity was used instead of wild-type Hod, because of a more effective preparation. In comparison the catalytic activity of HodC-W160A variant enzyme is clearly lower for both substrates (Table 4-2).

Table 4-2. Apparent Steady-state Kinetic Parameters of HodC and HodC-W160A

Protein	K_M (μM)		k_{cat} (s^{-1})	
	MHOQ	BHOQ	MHOQ	BHOQ
HodC	2.7 (0.3) ^a	29.4 (5.3) ^a	38.4 (0.3) ^a	41.2 (2.5) ^a
HodC-W160A	272.1 (27.7)	167.6 (22.4)	0.93 (0.05)	0.12 (0.01)

^a data from ref.⁷⁸ The average of at least 3 independent experiments is given with the standard deviation in parentheses.

Figure 4-17 shows CM[•] formation and O₂ consumption during HodC- and HodC-W160A-catalyzed conversion of MHOQ and BHOQ. From what has been observed, significant amounts of CM[•] were obtained for HodC-W160A-catalyzed conversion (Figure 4-17, black traces), but not so for HodC (Figure 4-17, red traces), suggesting that wild-type protein efficiently shields its active site, whereas the mutant protein may have a more open or more flexible active-site pocket. Moreover, the modified substrate BHOQ exhibited a much faster (higher) conversion (Figure 4-17B, black and red traces) than natural substrate MHOQ (Figure 4-17A, black and red traces), most probably due to the long butyl chain attachment that facilitates accessibility. Formation of the reactive CMH-oxidizing species was strictly dependent on the presence of both the organic substrate and O₂. Possibly released hydroperoxides that may escape from the enzymatic reaction are not responsible for CM[•] formation. CMH oxidation was not affected by H₂O₂, catalase, SOD or TPP, a reagent selective for organic hydroperoxides (Figure 4-17B, gray traces). Low temperature and room temperature EPR experiments with high protein and substrate concentrations showed that interaction of

MHOQ with Hod does not generate a stable radical species, which is an essential difference to the reaction of urate oxidase.¹⁰³

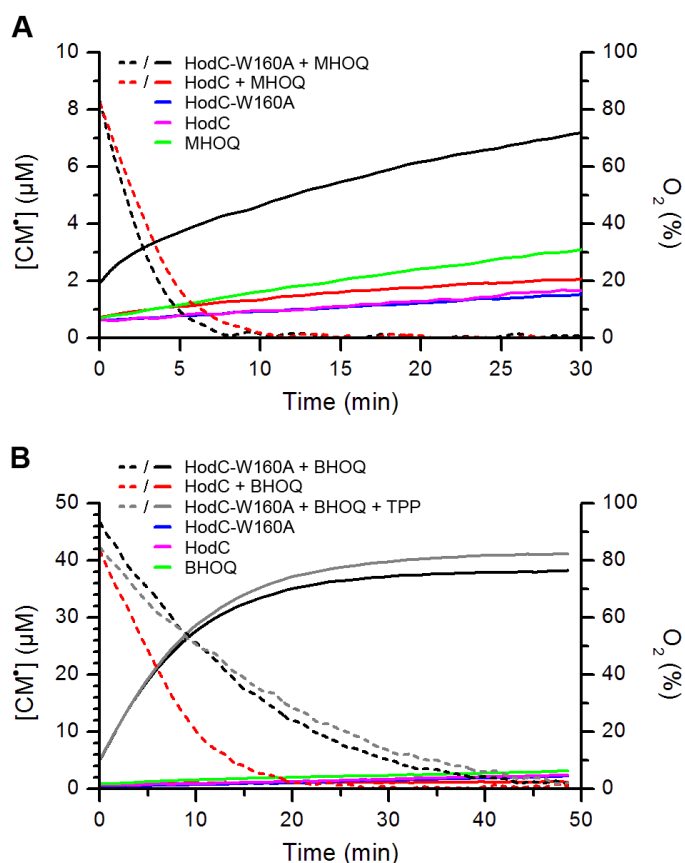


Figure 4-17. Kinetics of CM• formation and O₂ consumption during the enzyme-catalyzed conversion of MHOQ (A) and BHOQ (B). The contents of the assay mixtures are indicated in the insets. Solid lines: formation of CM•; dashed lines: consumption of dioxygen, as deduced from the time course of the TAM signals. Constant intensities of the TAM signal from control experiments were defined to correspond to 100% of dissolved O₂. The stable minimum of the TAM intensity after conversion of MHOQ and BHOQ by HodC or HodC-W160A, respectively, was assumed to represent 0% O₂. Traces are the means of at least 3 replicates. Experiments were performed by S. Thierbach.

The Stoichiometry of the Products of CMH Oxidation Reveals that Two Radical Species are Formed in the Hod Reaction.

During the enzyme-catalyzed conversion, the possibly formed superoxide O₂^{•-} is reduced by CMH to hydrogen peroxide H₂O₂, which can be accurately quantified with the developed HRP assay (see 4.1.2). Using CMH as a co-substrate in the assay, two equivalents of CMH were quantitatively measured to yield one equivalent of H₂O₂ during the conversion of BHOQ

by HodC-W160A, independent of the amount of substrate converted by the enzyme (Figure 4-18). This suggests that CMH seems to come close enough to the active site pocket for allowing an electron transfer, reducing superoxide in the active site to form O_2^{2-} or HO_2^- , whereas neither the bulky SOD nor the *N*-oxide spin traps appear to be able to sufficiently approach the active site pocket for reaction.

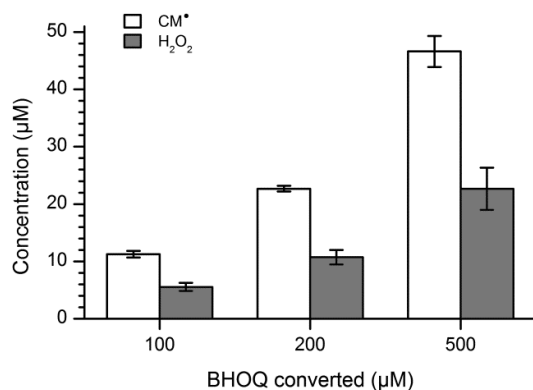


Figure 4-18. Concentrations of CM^* and H_2O_2 , formed during the HodC-W160A catalyzed oxidation of different concentrations of BHOQ. All reactions were incubated until full conversion of the organic substrate. Final CM^* concentrations were corrected for background oxidation, and the corresponding H_2O_2 concentrations were corrected for the spontaneous decay of H_2O_2 as deduced from control experiments.

A single-electron transfer from enzyme-bound substrate anion to dioxygen, forming a [substrate radical-anion superoxide radical] pair has been proposed for Hod-catalyzed reaction.¹⁰⁴ According to this hypothesis, the catalytic reaction was postulated to involve redox processes for which a more detailed understanding demanded detailed studies of redox properties of the used substrates 3-Hydroxy-2-methyl-4(1*H*)-quinolone (MHOQ) and 2-Butyl-3-hydroxy-4(1*H*)-quinolone (BHOQ).

The following redox studies of substrates were performed by the author, which decisively contributed to a thorough understanding of the catalytic mechanism of cofactor-free Hod dioxygenase.

Redox behavior of MHOQ and BHOQ was studied with cyclic voltammetry.

CVs of MHOQ (black, solid) and BHOQ (black, dashed) both of 0.4 mM in PB (50 mM, pH 7) recorded at 100 mV/s scan rate are given in Figure 4-19A. The arrows indicate the first oxidation and reduction peaks which were used to estimate the midpotential E_{mid} for MHOQ. The response of the buffer is given as the dashed olive line. The pH dependence of the first

oxidation peak of MHOQ is shown in Figure 4-19B (small wine dots with line). The derived midpotentials E_{mid} (vs. Ag/AgCl) of this substrate (named Hod) are represented by the larger black dots which were fit with a linear function (black dashed line). The two black lines correspond to the potential change induced by a 10^5 -fold excess of the reduced or oxidized species as calculated from the Nernst equation ($[\text{Hod}^\bullet]_{\text{max}}$ indicates the one electron oxidized radical species, $[(\text{HodH})\text{Hod}^-]_{\text{max}}$ stands for the protonated or deprotonated reduced substrate MHOQ). The olive squares and dashed lines represent the behavior of redox couple $\text{CM}^\bullet/\text{CMH}$ with pH, which is quite similar in slope to that of MHOQ. The olive lines are the 10^5 -fold excess potential limits. The midpotential E_{mid} of redox couple $\text{CM}^+/\text{CM}^\bullet$ is independent on pH as discussed. The midpotential of $\text{O}_2/\text{O}_2^{\bullet-}$ and the potential change for excess oxygen is given in blue. The black arrow visualizes the driving force for the electron transfer from Hod^- to O_2 , the olive arrow from CMH to substrate radical with a potential marked by the x.

The very similar CVs in Figure 4-19 indicate that the electronic properties of MHOQ and BHOQ are only slightly affected by the alkyl substituent at C-2 (methyl vs. butyl). Therefore, a similar redox behavior of the butyl-substrate is expected for the protein reaction. For MHOQ the pH dependence was derived, showing a linear behavior with a slope of -75 mV/pH-unit, so that the potential is eventually sufficiently negative for an electron transfer from substrate Hod or Hod^- to O_2 . Indeed, the straight line for $[(\text{Hod})\text{Hod}^-]_{\text{max}}$ crosses the $[\text{O}_2]_{\text{max}}$ level around pH 7, so that an electron transfer to oxygen is in principle (i.e. thermodynamically) possible. However, the driving force remains rather low, so that only very small concentrations of oxidized substrate and reduced oxygen might be formed.

In contrast, for higher pH, say pH 13, the potential difference is about 0.45 V (black arrow in Figure 4-19) and considerable equilibrium concentrations of Hod^\bullet and superoxide are expected. This was observed in model reactions, where in a pH range between 13 and 14 formation of the substrate radical was detected.

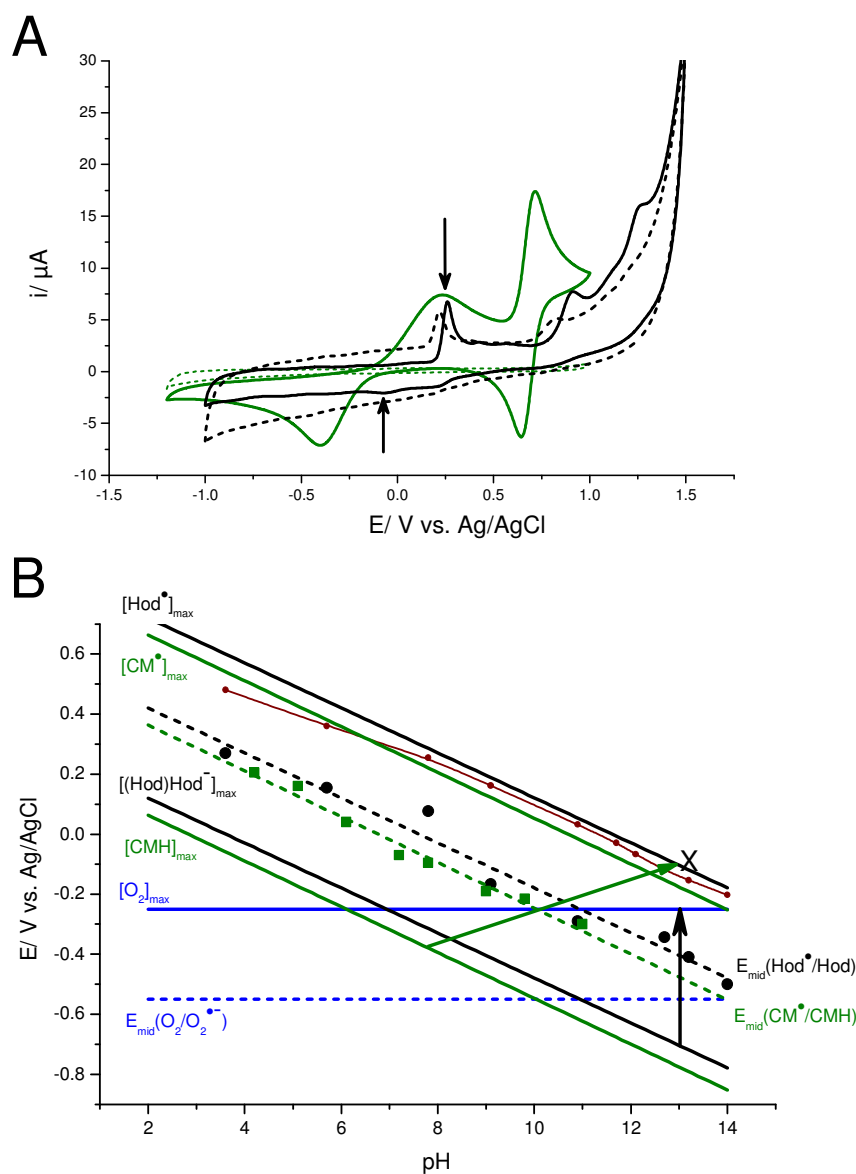


Figure 4-19. Cyclic voltammograms and pH-dependence. Graph A shows the CV of 0.4 mM MHOQ (black, line) and BHOQ (black, dashed) recorded with a scan rate of 100 mV/s at pH 7.8 and 7.4 (PB 50 mM), respectively. The arrows indicate the first oxidation peak and the less intense reduction peak which were used to estimate the mid-peak redox potential for MHOQ. The CV of CMH (olive) is shown for comparison. The response of the buffer is given as the dashed black line. The pH dependence of the first oxidation peak of MHOQ is shown in graph B (small wine dots with line). The derived midpoint potentials E_{mid} (vs. Ag/AgCl) of this substrate (Hod) are represented by the larger black dots which were fit with a linear function (black dashed line). The two black lines correspond to the potential change induced by a 10^5 -fold excess of the reduced or oxidized species as calculated from the Nernst equation. $[\text{Hod}^\bullet]_{\text{max}}$ indicates the one electron oxidized radical species, $[(\text{Hod})\text{Hod}^-]_{\text{max}}$ stands for the protonated or deprotonated reduced substrate MHOQ. The olive squares and dashed lines represent the behavior of transition $\text{CM}^\bullet/\text{CMH}$ of CMH with pH, which is quite similar to that of Hod. The olive lines are the 10^5 -fold excess potential limits. The midpotential E_{mid} of $\text{O}_2/\text{O}_2^{\bullet-}$ and the potential change for excess oxygen are given in blue. The black arrow visualizes the driving force for the electron transfer from Hod^- to O_2 , the olive arrow from CMH to substrate radical with a potential marked by the x.

The increase in pH is expected to cause deprotonation of the nitrogen N-1 and the 3-OH group until a dianionic form of the substrate prevails. In the CVs the midpotential E_{mid} ($\text{Hod}^{\bullet}/\text{Hod}^-$) clearly is a linear function up to pH 14 with a slope being consistent with transfer of an electron and a proton (generally, same number of protons and electrons). This means that the dianionic substrate, which would not show pH dependence in the CV, is formed at $\text{pH} \geq 14$. For all lower pH values either two protons or one proton have to be available as origin of the pH dependence. Using web-based pKa-calculators, the pH behavior of MHOQ was simulated yielding pK_a values of 9.6 and 11.9, or 10.6 and 13.7. The latter pair is closer to the result obtained from CV and is modeled in Figure 4-20, showing the protonation state of the structures. Up to a pH of 9 the protonated species S1 (S stands for MHOQ substrate) is present which is replaced by the monoanionic 3-OH deprotonated and the N1-deprotonated forms S2 and S3, with S3 prevailing. Above pH 12 the dianionic species S4 is appearing reaching about 68% at pH 14.

Considering the redox behavior of MHOQ (Figure 4-19), the monoanionic form appears to have a sufficient low potential to reduce oxygen. Therefore, deprotonation at N1 or 3-OH should suffice to form an adequately reducing substrate species in the protein. This assumption is supported by EPR measurements at pH 12, in which immediately after adding the substrate to the alkaline solution the typical pattern of the substrate radical is seen.

At pH 7 however, actually no signal is observed even after prolonged spectra accumulation. Of course, double deprotonation at higher pH would further increase the reducing power of the substrate. As can be inferred from Figure 4-19, CMH is displaying the same pH-dependence as the substrate with E_{mid} potentials shifted by ca. 70 mV to lower values. For a pH above 13, CMH is not stable, so that data up to pH 11 are shown. Around neutral pH it definitely is reducing the superoxide radical whose redox pair $\text{O}_2^{\bullet-}/\text{O}_2^{2-}$ has a mid-peak potential of 0.74 V (vs. Ag/AgCl). With respect to the reduction of the substrate radical by CMH in the protein reaction, one can again refer to Figure 4-19. After electron transfer to O_2 , the substrate radical can adopt a potential approximately 0.3 V above E_{mid} when sensing a local pH around 13 (marked by the cross in Figure 4-19). When the local pH is decreasing, then the potential is shifted to even more positive values. A CMH molecule, sufficiently close to the substrate radical, is able to transfer an electron even if sensing a pH around 7 or 8, i.e., being not exposed to the active site environment of the protein, because there still is a considerable potential difference (indicated by the olive arrow). This process regains the substrate mono- or dianion. It is important to note here, that CMH in a protein solution is not activating oxy-

gen and forming a CM radical in the absence of the substrate, as shown by the EPR control experiments (see Figure 4-17).

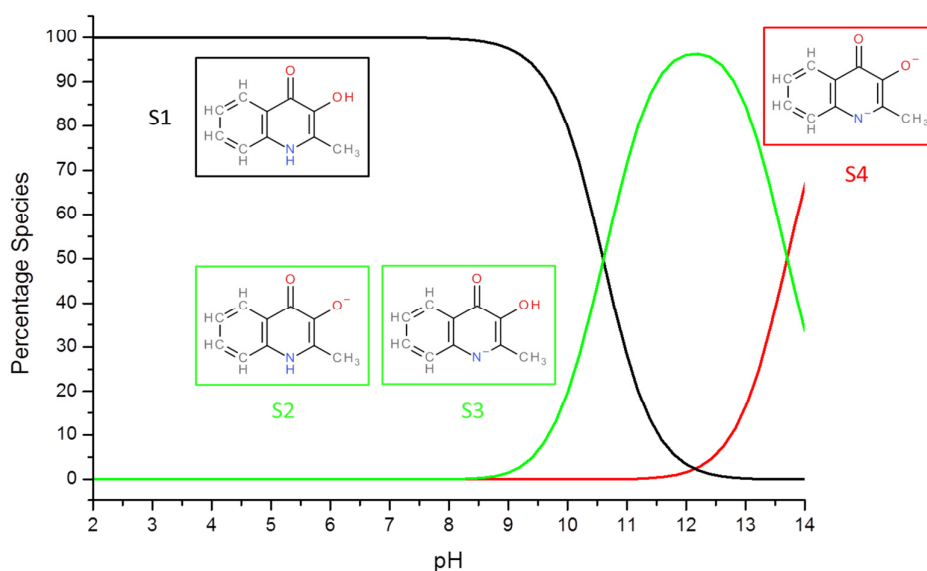
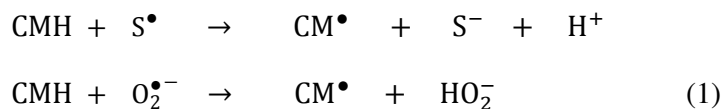


Figure 4-20. Modeling of the MHOQ substrate protonation states. The color code of the inset structures relates them to the pH curves.

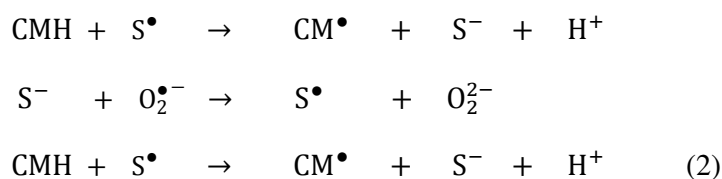
These considerations, based on the analysis of redox potentials, clearly show that one CMH is able to reduce the substrate radical and a second one the superoxide in the protein reaction, so that two CM radicals and one H_2O_2 are finally formed in strictly conserved stoichiometry as measured. Because the redox behavior of the couple $\text{S}^\bullet/\text{S}^-$ resembles that of $\text{CM}^\bullet/\text{CMH}$, an alternative electron transfer pattern in the protein appears plausible: After formation of the radical pair, CMH is reducing S^\bullet to produce S^- . This regained substrate anion has a sufficiently low potential to reduce $\text{O}_2^{\bullet-}$ to O_2^{2-} , forming again the substrate radical which is then reduced once more by a second CMH. This two-step reduction of S^\bullet yields again the observed stoichiometry of one equivalent of H_2O_2 from two equivalents of CMH oxidized. In this model, it is not necessary that two CMH molecules approach the substrate radical and superoxide radical independently, but, instead, the substrate radical is used as an electron relay for superoxide reduction.

Accounting that oxygen is presumed to be located in the bottom part of the active-site cavity shielded by the substrate; the suggested two-step electron transfer via the substrate seems very probable.

Considering the redox behavior of the organic substrate and CMH, the observed stoichiometry of one H_2O_2 and two CM^\bullet formed during BHOQ oxidation by HodC-W160A can be explained by the reaction of CMH with substrate radical as well as superoxide, according to the equations:



Alternatively, after reduction of S^\bullet by CMH to regain the substrate anion, an electron can be transferred from S^- , whose reduction potential is sufficiently low, to nearby $\text{O}_2^{\bullet-}$ to produce O_2^{2-} and again the substrate radical, which in turn is reduced by a second CMH molecule:



Reduction of the substrate radical by CMH, as suggested in equation 1 and 2, regenerates the substrate. This should result in an apparently lower rate of substrate consumption in the enzymatic reaction if CMH is present. The effect of CMH (600 μM) on BHOQ turnover by HodC-W160A was determined in a spectrophotometric assay, measuring BHOQ at 337 nm. The initial rate of BHOQ consumption was reduced by about 10%, supporting the proposal of substrate recycling in the presence of CMH.

This shows the importance of redox studies for CMH and MHOQ and BHOQ substrates which were very helpful to conclude on the prevailing mechanism of Hod enzyme, in which Hod-bound substrate anion itself activates dioxygen by single electron transfer forming the [substrate radical - superoxide anion radical] pair.

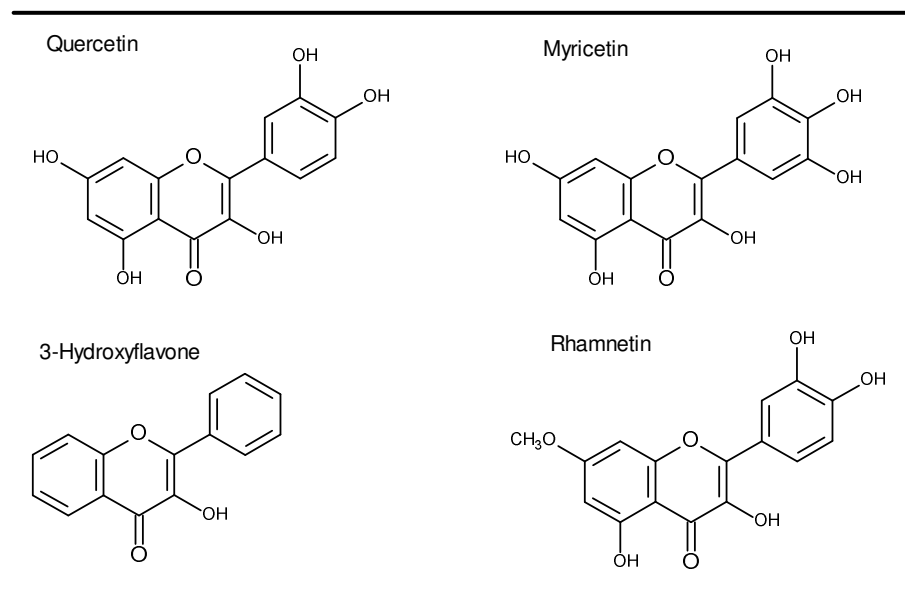
4.3. Metal-cofactor Quercetin-2,4-dioxygenase (Quercetinase, QueD)

Although mechanisms have been proposed for 2,4-QueD from *A. japonicas* and *B. subtilis*, the catalytic pathway of 2,4-QueD from *Streptomyces* sp. strain FLA has been not yet confirmed (see section 2.3.1). This part of the study aimed to achieve an insight into the catalytic reaction of 2,4-QueD, particularly by addressing the question of possible radical intermediate states. In analogy to the HOD-enzyme, we followed the approach to monitor presence of oxidizing radical species through oxidation of the cyclic hydroxylamines CMH or CPH. The en-

zyme preparation and biochemical characterization was performed by the group in Münster. The quercetinase samples were generally less stable than HOD and always showed several types of metal occupation (active or inactive) of the metal-binding center albeit grown in minimal metal containing media. The maximal occupations were about 0.7 for a single metal such as Co^{2+} as determined by the group in Münster, where also the enzyme activities were measured. In a first step, the redox behavior of the different chosen substrates was examined by voltammetric methods. Then, the working hypothesis that substrate and/or oxygen are activated by the enzyme forming intermediate radicals should be tested by using CMH as a radical spin probe. The possibility of participation of the metal-center in the catalytic process also was of concern and addressed by employing EPR to observe changes in metal oxidation state or spin state. These experiments were usually performed at low temperature (< 60 K).

4.3.1. Redox properties of flavonol substrates (Quercetin, Myricetin, Rhamnetin, 3-Hydroxyflavone)

The proposed mechanisms include several possible pathways, in which always transfer of electrons is involved in substrate activation, particularly in the first oxidation step of flavonol substrates. Therefore, the knowledge of redox properties of flavonol substrates is essential to achieve insight in all redox processes which possibly occur in the enzyme-catalyzed reaction. The main substrate quercetin (3,5,7,3',4'-pentahydroxyflavone) is a polyphenolic compound belonging to the class of flavonols. It is a very common flavonoid, and is found in many nutrients such as onions, apples and tea. It contains five hydroxyl-groups and its electron-rich character is the origin of antioxidant properties assigned to it (see Scheme 4-7). Related flavonols as substrates for quercetinase are characterized by a different number of attached or modified hydroxy-groups as shown in Scheme 4-7.



Scheme 4-7. Chemical structure of flavonols used in this study.

Cyclic voltammetry was applied for deriving the redox properties of the four (potential) flavonol substrates, quercetin, myricetin, rhamnetin and 3-hydroxyflavone. Cyclic voltammograms of the reference substrate quercetin recorded in the large and narrow potential windows are given in Figure 4-21, which are in agreement with previously reported studies.^{127,128} Three oxidation peaks (I, II, III) occurred at +0.48 V, +0.81 V and +1.2 V (vs. SHE) in the large potential window (Figure 4-21 black line) but on the reverse scan no reduction peak was recorded. However, a reduction peak I' at +0.33 V (vs. SHE) was observed when the potential scan was inverted before peak II in the narrow window (Figure 4-21 green line). This observation exhibits a reversible character of the first electron transfer reaction corresponding to the first redox couple $\text{Quer}^\bullet/\text{Quer}$, which actually would correspond to the pair involved in the activation step of the enzyme reaction. The absence of reduction peak I' in the large potential window is explained by the formation of an unstable or electrochemically active product from the first oxidation (peak I). This product can be further oxidized at higher potential (peak II), whereas it is reduced if the potential scan is reversed right after its generation. In addition, quercetin was adsorbed strongly on the electrode surface and the final oxidation product blocks the electrode surface, as found from the rapid decrease of the quercetin oxidation peak (data not shown). This process causes an inactive electrode surface inhibiting the electron transfer.

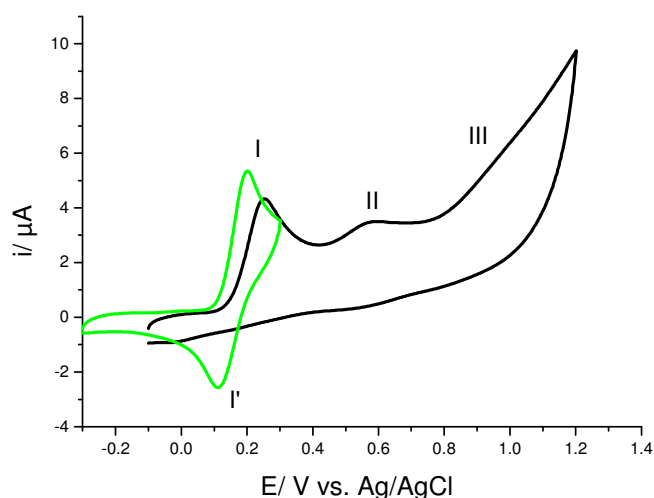


Figure 4-21. CVs of quercetin (0.4 mM) in 50% EtOH: PB (50 mM, pH 7.4) at 100 mV/s scan rate. Three oxidation peaks I, II and III are observed at +0.48 V, +0.81 V and +1.2 V (vs. SHE) respectively in the large potential window (black). Whereas in the narrow potential window (green) a reduction peak I', associated to oxidation peak I, is observed at +0.33 V (vs. SHE) exhibiting a reversible character of the first electron transfer $\text{Quer}^{\bullet}/\text{Quer}$.

Effect of pH

The influence of pH on the redox behavior of quercetin was also investigated with cyclic voltammetry. CVs of quercetin in different solutions of pH 4 – 13 were recorded in the narrow potential window (Figure 4-22 left panel). The derived midpotentials E_{mid} of redox couple $\text{Quer}^{\bullet}/\text{Quer}$, determined from the anodic $E_{\text{p,a}}$ and cathodic $E_{\text{p,c}}$ potential, were plotted against pH (Figure 4-22 right panel).

In the pH range of 4 – 13 the midpotential E_{mid} of redox couple $\text{Quer}^{\bullet}/\text{Quer}$ shifted to more negative potential with increasing pH which indicates that hydrogen ion transfer is involved in the electrode reaction. As pH increases, the hydroxyl group gradually dissociates so that the protonation state affects the reaction rate. A linear relationship of E_{mid} (pH) was observed with a slope of -48 mV per pH unit, according to the equation $E_{\text{mid}} = 0.54 - 0.048 \text{ pH}$ (Figure 4-22 right panel). Based on the Nernst equation $E_{\text{mid}} = E - 2.303RT\text{pH} \frac{m}{anF}$ (m , the proton number), the slope of -48 mV/pH demonstrates that the numbers of electron and proton transferred in this electrode reaction are equal, as can be assumed to be 1 for the first redox reaction of $\text{Quer}^{\bullet}/\text{Quer}$.

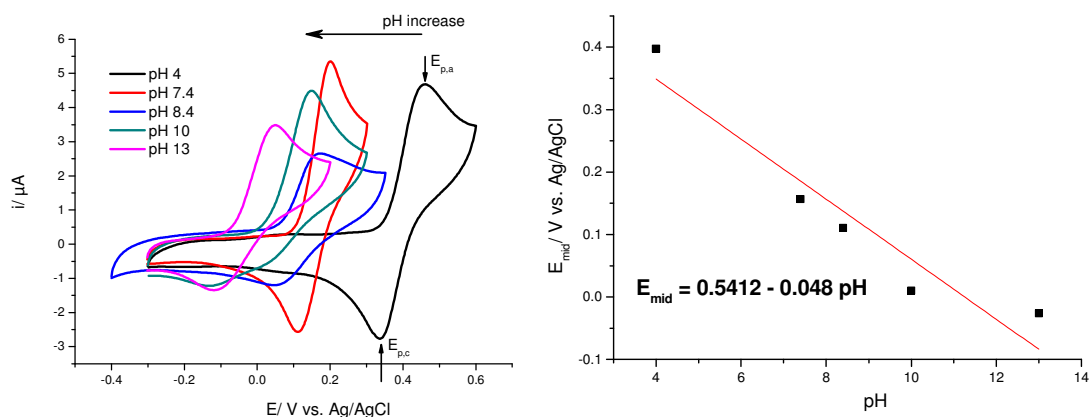


Figure 4-22. (Left panel) CVs of the first redox couple $\text{Quer}^\bullet/\text{Quer}$ of quercetin (0.4 mM) in 50% EtOH:PB (50 mM) in the pH range of 4-13 at 100 mV/s scan rate. Arrows indicate the oxidation ($E_{p,a}$) and reduction peak potential ($E_{p,c}$) at pH 4. The pH-dependence of midpotentials E_{mid} of $\text{Quer}^\bullet/\text{Quer}$, derived from the CVs on the left panel, is shown in the right panel. The derived midpotentials E_{mid} were fit with a linear function (red line). A linear relationship of E_{mid} (pH) is observed with a slope of -48 mV per pH unit, implying one proton number is involved in this reaction according to the Nernst equation $E_{\text{mid}} = E - 2.303RT\text{pH} \frac{m}{\alpha nF}$ (m, proton number).

As for Hod substrate, the pH-dependence of redox potential was also obtained for quercetin substrate showing a similar behavior (Figure 4-23). Together with those of CMH and O_2 , the derived midpotentials E_{mid} (vs. Ag/AgCl) of quercetin (red dots) were plotted against pH and fit with a linear function (red dashed line). The potential change induced by a 10^5 -fold excess of the reduced or oxidized species as calculated from the Nernst equation is represented as the two red lines ($[\text{Quer}^\bullet]_{\text{max}}$ indicates the one electron oxidized radical species, $[(\text{Quer})\text{Quer}^-]_{\text{max}}$ stands for the protonated or deprotonated reduced substrate quercetin) is represented as the two red lines. The olive squares and dashed lines represent the behaviour of redox couple $\text{CM}^\bullet/\text{CMH}$ with pH, the olive lines are once more the 10^5 -fold excess potential limits. The midpotential of $\text{O}_2/\text{O}_2^{\bullet-}$ and the potential change for excess oxygen is given in blue. The red arrow visualizes the driving force for the electron transfer from Quer^- to O_2 for a local pH of 12, the olive arrow from CMH to substrate radical.

The diagram shows clearly that an electron transfer from Quer or Quer^- to O_2 is only possible at high pH (e.g. pH 12, red arrow), while it is thermodynamically unfavorable at lower or neutral pH. As indicated by the crossing of the straight lines $[\text{Quer}^-]_{\text{max}}$ and $[\text{O}_2]_{\text{max}}$ at about a pH of 9, only potentials at higher pH are in principle sufficiently negative to allow electron moving from Quer or Quer^- to O_2 . However, the potential difference of 140 mV at pH 12 remains

rather low, so that only very small concentrations of oxidized substrate Quer^\bullet and reduced oxygen superoxide might be formed.

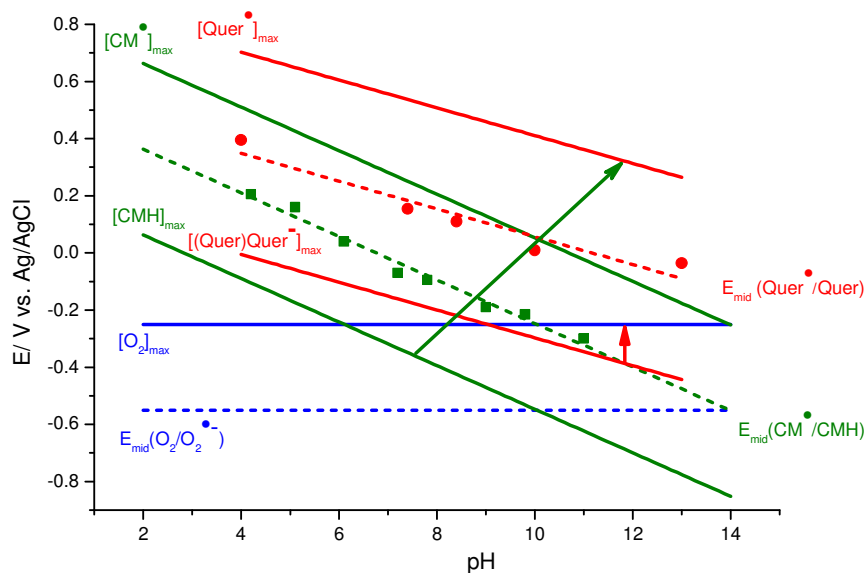


Figure 4-23. pH-dependence of the mid-peak potentials E_{mid} (vs. Ag/AgCl) of quercetin substrate (red dots) and CMH (olive squares). The derived mid-peak potentials E_{mid} were fit with a linear function (olive and red dashed lines). The olive (CMH) and red solid lines (quercetin) correspond to the potential change induced by a 10^5 -fold excess of the reduced or oxidized species as calculated from the Nernst equation ($[\text{CM}^\bullet]_{\text{max}}$ and $[\text{Quer}^\bullet]_{\text{max}}$ indicate the one electron oxidized radical species, $[\text{CMH}]_{\text{max}}$ and $[(\text{Quer})\text{Quer}^-]_{\text{max}}$ stand for the protonated or deprotonated reduced CMH and quercetin). The mid-peak potential of $\text{O}_2/\text{O}_2^{\bullet-}$ and the potential change for excess oxygen are given in blue. The red arrow visualizes the driving force for the electron transfer from Quer or Quer^- to O_2 , the olive arrow from CMH to substrate radical.

For CMH, as discussed in chapter 4.1, the pH-dependence of E_{mid} potentials (ca. -70 mV/pH -unit) obtained for the redox couple $\text{CM}^\bullet/\text{CMH}$ is also given in Figure 4-23, olive dashed line. At neutral pH, with a midpotential E_{mid} of -0.07 V (vs. Ag/AgCl) CMH is instantly reducing the superoxide radical to hydrogen peroxide ($E_{\text{mid}} \text{O}_2^{\bullet-}/\text{O}_2^{2-}$ of 0.74 V (vs. Ag/AgCl)). On the other hand, the quercetin radical, after being oxidized by O_2 , can adopt a potential approximately 0.3 V above E_{mid} . In analogy to the Hod reaction, CMH in the QueD enzyme reaction should be able to reduce the quercetin substrate radical Quer^\bullet either at neutral or higher pH (local pH in enzyme pocket) without being exposed to the active site environment of the QueD protein, because there still is a considerable potential difference (indicated by the olive arrow). In protein solution, without substrate, CMH is not activating oxygen to form a CM radical, as shown by the EPR control experiments.

The CV experiments on quercetin suggested that CMH should be a possible electron donor to any of the oxidizing intermediate species in the reaction of quercetinase.

The redox properties of other flavonol substrates such as myricetin, rhamnetin and 3-hydroxyflavone were also studied by cyclic voltammetry. Their obtained CVs recorded in different pH solutions are shown in Figure 4-24A, B and C, respectively. The derived midpotential E_{mid} , determined from anodic $E_{\text{p,a}}$ and cathodic potential $E_{\text{p,c}}$, plotted against pH are shown as inset of these plots. Among these flavonols, myricetin exhibits the highest oxidative property as indicated by the smallest E_{mid} value of 0.33 V of the first redox pair (Table 4-3). A linear dependence of midpotential E_{mid} vs. pH was observed for the first redox couple of all three substrates. According to fits, the proton number involved in the first redox couple of all three flavonols was calculated to be 1, as demonstrated for quercetin.

Table 4-3. Midpotential E_{mid} (vs. SHE) of flavonols in PB (50 mM, pH 7.4).

Flavonol	Quercetin	Myricetin	Rhamnetin	3-Hydroxyflavone
E_{mid} (V)/ SHE	0.39	0.33	0.42	0.76

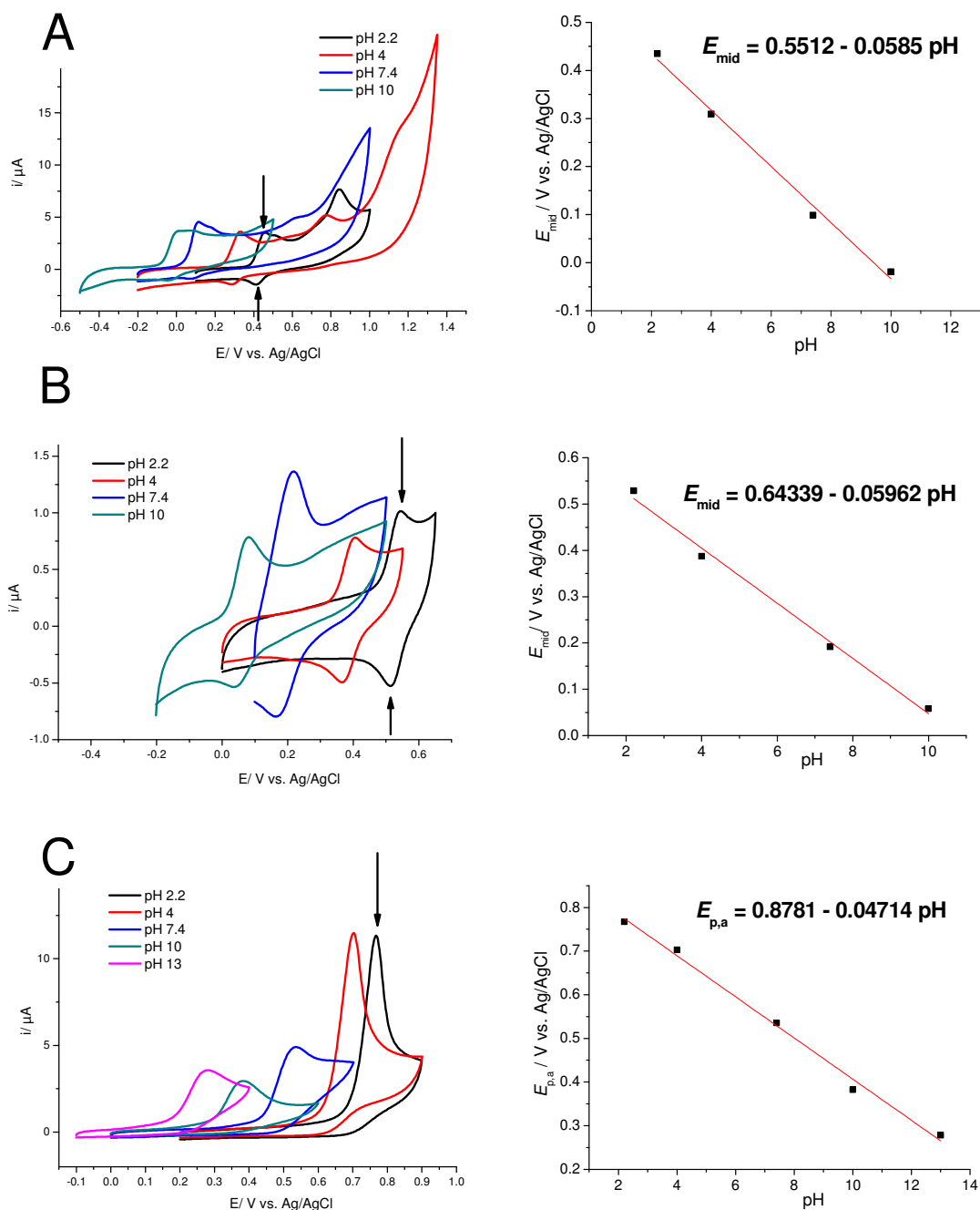


Figure 4-24. On the left side are the CVs of the first redox pair of 0.4 mM myricetin (A), rhamnetin (B) and 3-hydroxyflavone (C) in 50% EtOH:PB (50 mM) in the pH range 2.2-13 at 100 mV/s scan rate. On the right side is the respective pH dependence of the midpotentials E_{mid} of given flavonols, which were derived from CVs. The arrows indicate the first redox pair (oxidation and reduction peaks, except for 3-hydroxyflavone showing only oxidation peak) at pH 2.2, color code identifies other pH values. The derived midpotentials E_{mid} were fit with a linear function (red lines).

4.3.2. Roles of the metal-binding site and transient radical detection with CMH in the enzymatic reaction pathway of Quercetinase

Quercetinase (QueD) of *Streptomyces* sp. FLA, expressed from *queD* gene in *Escherichia coli*, was grown and supplemented with various metal salts of MnCl₂, FeCl₂, CoCl₂, NiCl₂, CuCl₂ and ZnCl₂. All this biochemical work, enzyme expression, purification and characterization were done by D. Nianios from Molecular Microbiology and Biotechnology group of Professor Susanne Fetzner (WWU-Münster). The Ni²⁺ and Co²⁺ substituted QueD exhibited a rather high specific activity with the apparent kinetic constants for quercetin of Ni-QueD ($k_{\text{cat}} = 40.1 \text{ s}^{-1}$, and $K_{\text{m}} = 5.75 \text{ }\mu\text{M}$) and Co-QueD ($k_{\text{cat}} = 7.6 \text{ s}^{-1}$, $K_{\text{m}} = 0.96 \text{ }\mu\text{M}$).¹²⁹ Other metals (e.g. Fe²⁺) had delivered preliminary values for k_{cat} lower than 1.5 s^{-1} and 30 to 8 fold lower specific activity vs. Ni²⁺ and Co²⁺. Therefore, in a first step Mn²⁺ and Fe²⁺-substituted QueD were available and examined with respect to their properties. In the second step we focused on the Ni²⁺- and Co²⁺-QueD for addressing details of the catalytic mechanism of QueD reaction. During the project period crystallographic information on flavonolato complexes of Ni(II) performed in Berlin by H. Dobbek's group became available, which disclosed the coordination mode of the flavonolate ligand, and geometries around the metal ions (see Methodology 2.3.1). The crystal structure of Ni-QueD suggested that the glutamic acid Glu76 as a direct metal-binding ligand, and neighboring amino acids tyrosine Tyr117 and isoleucine Ile66 residues played important roles for the activity, respectively accessibility of quercetin substrate to the active site, and also for the stability of the quercetin-binding pocket (data not published, supplied by H. Dobbek). In this respect, QueD variants were prepared by substituting Glu76 with histidine (His) residue to have QueD-E76H, Tyr117 and Ile66 with alanine (Ala) residue to yield QueD-Y117A and QueD-I66A. These QueD mutants were prepared with various metal ion substitution (Ni, Co, Fe, Mn).

Electron paramagnetic resonance (EPR) spectroscopy was used to study the reaction of QueD in the 2,4-dioxygenolytic cleavage of quercetin as well as myricetin, rhamnetin and 3-hydroxyflavone which allows to monitor the paramagnetic ions Co²⁺, Mn²⁺, Fe³⁺, usually at low temperatures (8 K to 60 K). In particular, changes in the metal ligand sphere upon substrate binding, and changes in valence state or spin state of the metal ions become accessible with this method. It is noted here, that metal occupancy of the various metal substitutions was variable reaching maximal values of 0.7 atoms/ subunit for Co and Ni as determined by ICP-OES (Münster group). The rest was occupied with metal ions such as Zn, Cu, Mn and Fe.

Therefore, always additional signals of paramagnetic ions appeared in the EPR spectra of Ni^{2+} - or Co^{2+} -substituted proteins, which in unfavorable cases were superimposing. In addition, the QueD-catalyzed reaction of quercetin was followed by using the cyclic hydroxylamine 1-hydroxy-3-methoxycarbonyl-2,2,5,5-tetramethyl-pyrrolidine (CMH) spin probe in an analogous way as for HOD (see Results 4.2) to detect radical formation or other oxidative intermediates.

Fe- and Mn-QueD

Having prepared Fe-QueD in sufficient amounts, good purity and with high occupancy (0.65 to 0.79) it was first examined by low temperature EPR. Experiments were performed with and without quercetin showing the typical signal of high-spin ($S = 3/2$) Fe^{3+} species as a sharp line at low-field around 150 mT ($g \approx 4.3$) and broad additional features around 75 mT ($g \approx 9.8$) in all samples of Fe-QueD protein under anoxic or oxic condition (Figure 4-25 left panel-A). When quercetin was added under oxygen free conditions the signal intensity of Fe^{3+} was smaller and the line changed its shape reflecting some alteration in ligand sphere and relaxation properties.

Exposing this reaction mixture to oxygen resulted in a recovery of Fe^{3+} signal intensity (Figure 4-25 left panel-B-D). However, the analysis of these experiments led to a contradiction. Only divalent metal ions can be incorporated into the active site so that no EPR spectrum should be visible (Fe^{2+} is diamagnetic or has integer spin, which both are inaccessible by EPR). If Fe^{3+} were the active species then an electron withdrawn from the substrate should result in a loss of Fe^{3+} -signal. Consequently, the long term increase of Fe^{3+} -signal appears not to be associated with a substrate conversion but might be due to autoxidation and, additionally, by relaxation effects caused by presence of paramagnetic oxygen.

To address this problem, EPR measurements were also performed at room temperature for Fe- and Mn-QueD with both wild-type (WT) and E76H variant samples. CMH was added to the reaction mixture of QueD and quercetin to monitor presence of oxidizing species that might be formed in the reaction. CM^\bullet formation during conversion of quercetin by wild-type or E76H variant of Mn- or Fe-QueD in the presence of oxygen was extremely slow, followed a linear kinetics and showed only background behavior as measured in oxic quercetin, Mn- or Fe-QueD protein (WT and E76H) solution (Figure 4-25 right panel). This indicates that no

substantial amounts of oxidizing species can be detected in the Fe- and Mn-QueD-catalyzed conversion of quercetin.

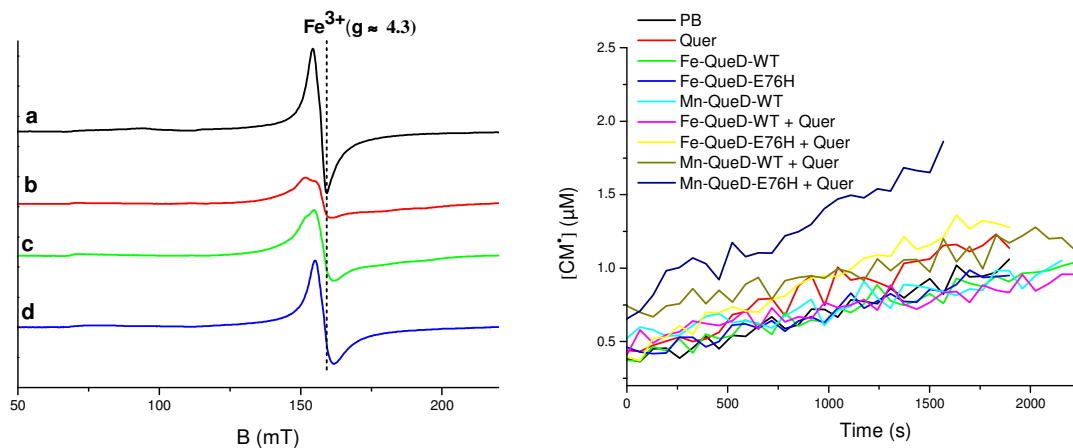


Figure 4-25. (Left panel) EPR spectra of (a) anoxic Fe-QueD (1.57 mM), (b) addition of 2-fold molar excess of quercetin, (c) exposing for 30 min and (d) 90 min to air. Signal of high-spin ($S = 3/2$) Fe^{3+} species as a sharp line at around 150 mT ($g \approx 4.3$, dashed line) and broad additional features around 75 mT ($g \approx 9.8$) are observed for the Fe-enzyme (a), diminish with quercetin addition (b) and recover again when exposing to air (c,d). Spectra were recorded at 8 K, microwave power 2 mW and modulation amplitude 0.5 mT. Kinetics of CM^\bullet formation in the quercetin conversion catalyzed by Fe- and Mn-substituted enzymes (wild type and E76 variant) is shown in the right panel. Only small signal of CM^\bullet formation following a linear kinetic is observed for reactions and controls. The assay contained enzyme (0.1 U/ml), quercetin (400 μM in DMSO) and 600 μM CMH. The contents of the assay mixtures are given in the figure legend.

In order to assure that we were not dealing with a non-working system, the catalytic reaction of Fe-QueD with quercetin was carefully reexamined by spectrophotometry. It was indeed verified that our Fe-QueD samples were not catalyzing the dioxygenolytic reaction of quercetin, because the product (2-protocatechuoyl-phloroglucinol carboxylic acid) as well as carbon monoxide were not detected (done by our co-worker D. Nianios (WWU-Münster)). In addition, Mn^{2+} -QueD was found to have a very low occupancy (0.17) with large contributions of other metals (ca. 0.30, Fe, Zn, Ni, Cu). From this point, we decided to move to Ni^{2+} - and Co^{2+} -substituted quercetinases which have been confirmed to show a high catalytic efficiency for quercetin¹²⁹ and good active site occupancy.

Ni and Co-QueD

Nickel and cobalt as the most active metal ion cofactors for QueD protein from *Streptomyces* sp. FLA,^{129,130} showed good occupancies ranging from 0.55 to 0.8 with rather low values for other metal ions (<0.03 total) for both the wild type and the E76H variant. Therefore, EPR

experiments of Ni- and Co-QueD and their variants were performed at low temperature (8-20 K) to monitor effects of ligand binding and formation of intermediate states.

Ni-QueD

EPR spectra of Ni-QueD-WT and -E76H are presented in Figure 4-26A-B. In none of the spectra any signal indicative of a paramagnetic Ni species (Ni^{1+} , Ni^{3+}) was detected under anoxic or oxic condition, or in the presence or absence of quercetin. Only signals of trace metal Mn^{2+} , Cu^{2+} are seen in the high-field region around 330 mT ($g \approx 2.05$) and some Fe^{3+} species at the low-field around 150 mT ($g \approx 4.3$) that are present in the enzyme preparation.

For detecting oxidizing species possibly formed in enzyme-catalyzed conversion of quercetin by Ni-QueD-WT and -I66A variant, EPR measurements were performed at room temperature with CMH (Figure 4-26C-D). A slight curvature of CM^\bullet formation, observed for the reaction mixtures (blue traces) and induced by oxygen consumption in the sample, was a hint on the ongoing reaction as derived from a comparison with controls, for which the signal formation in oxic quercetin or protein solutions was very slow and followed a strict linear kinetic as observed in Fe-QueD reaction. Despite the Ni-enzymes were active, obviously only an extremely small fraction of oxidizing species can be detected. Possibly the reaction kinetics was so fast that the transient radicals were concomitantly formed and reacted away locally in the active site of enzyme, so that CMH was not able to approach the reaction site and perform the oxidation.

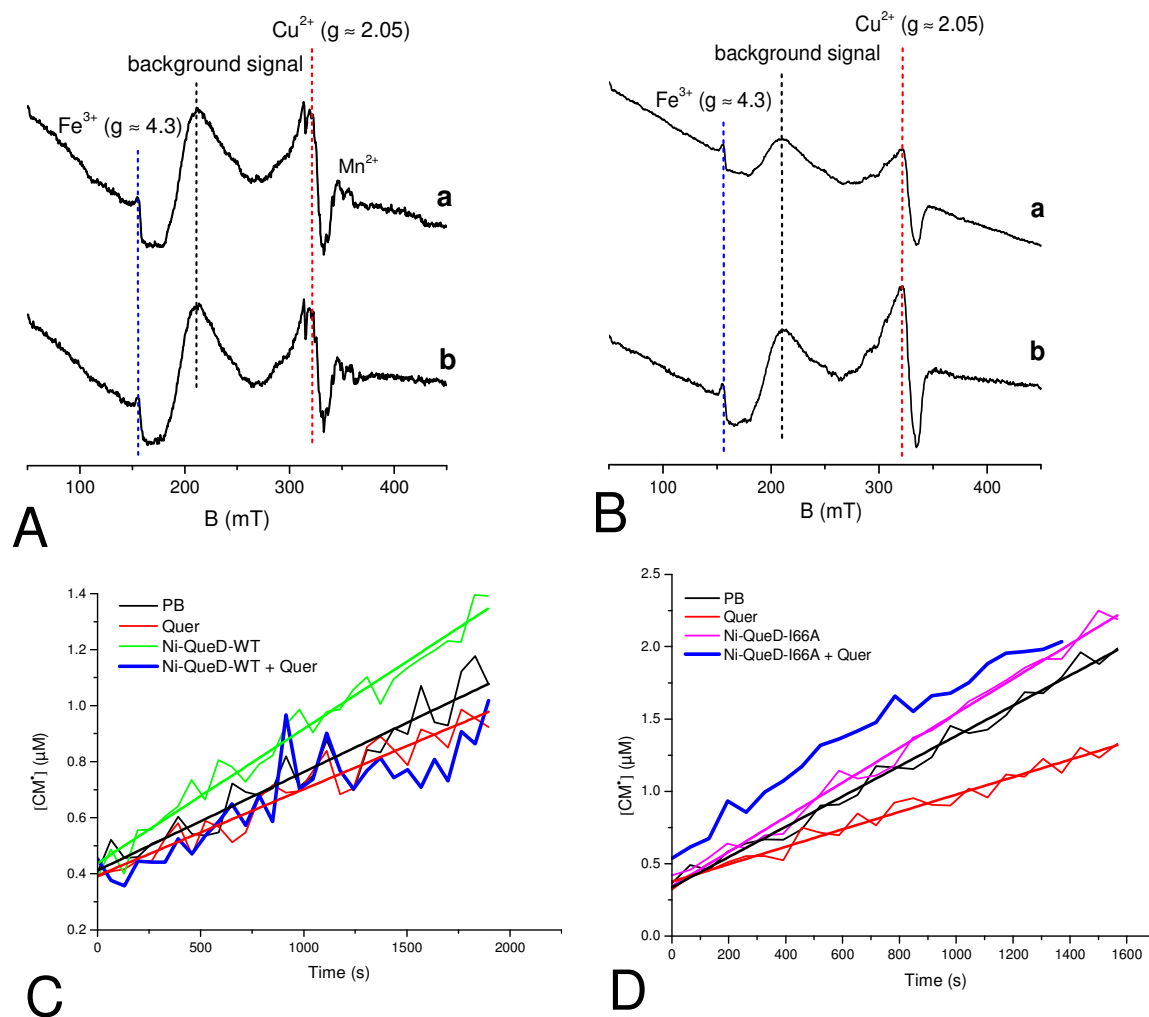


Figure 4-26. No signals indicative for Ni species (Ni^+ , Ni^{3+}) is observed in the EPR spectra of anoxic Ni-QueD-WT (A-a) and -E76H variant (B-a) at the resting state, and after addition of 2-fold molar excess of quercetin (A-b, B-b). The dashed lines indicate the signals of trace metal Mn^{2+} , Cu^{2+} (around 330 mT, $g \approx 2.05$, red), Fe^{3+} (around 150 mT, $g \approx 4.3$, blue) and broad signal arises from background (at 200 mT, black). Spectra are not background corrected. EPR spectra were recorded at 8-15 K, modulation amplitude 0.7 mT and microwave power 2 mW. The kinetics of CM^\bullet formation in the conversion of quercetin catalyzed by Ni-QueD-WT and -I66A variant is shown in panel C and D, respectively. Controls in C, D are fit with straight lines. As compared to the controls, a slight curvature of the small CM^\bullet signal is indicative for a reaction of both Ni-WT and I66A variant (blue traces). The assay contained enzyme (0.1 U/ml), quercetin (200 μM in DMSO) and CMH (600 μM in H_2O). The contents of the assay are indicated in figure legends.

Co-QueD

Similarly, the role of Co^{2+} in QueD-WT and -E76H, -Y117A, -I66A variants was examined by performing EPR experiments at low temperature (8-60 K) for anoxic and oxic condition, and with and without quercetin addition.

EPR signals of anoxic Co-QueD-WT were visible in the region between 50 and 250 mT containing a pattern with multiple lines around 100 mT ($g \approx 6$), a line at $g \approx 4.3$ and a broad line around 180 mT ($g \approx 3.8$). Above 250 mT quite intense signals of bound Cu^{2+} and particularly Mn^{2+} are present (Figure 4-27 a) which are overlaying a very broad additional Co^{2+} -signal ($g \approx 2.3$) observed in previous experiments¹²⁹. When quercetin was added to the anoxic Co-QueD-WT and subsequently exposed to air, spectral changes of the Co^{2+} signals were induced showing a change in symmetry of the spectrum and a characteristic change of hyperfine pattern at $g \approx 6$ (Figure 4-27 b-d). These findings agree with a previous paper of our groups (Merkens et al)¹²⁹ in which a high-spin ($S = 3/2$) Co^{2+} -species was assigned to the active site, and the spectral changes to binding of substrate and conversion to bound product based on the analysis of six different hyperfine patterns with up to eight lines arising from the nuclear spin of $I=7/2$ for Co^{2+} . No alteration of the Co^{2+} -valence state is observed during the reaction.

EPR spectra recorded for Co-QueD-E76H are presented in Figure 4-27B. The signal of Co^{2+} species found in the anoxic spectra of Co-QueD-E76H exhibits a weak multiple line pattern in the region around 100 mT ($g \approx 6$) but shows a significantly smaller width and altered symmetry as compared to wild type protein (Figure 4-27B-a). In addition, a new line was found around 217 mT ($g \approx 3.1$) which was suspected to be a second Co^{2+} species, because this signal is highly sensitive to temperature and behaves differently with respect to the main components at $g \approx 6$ to 3.8 as shown in Figure 4-27B-c. With increasing temperature, the line was broadened, shifted to higher field and was visible up to 40 K indicating that it has a different relaxation behavior. However, the signal disappeared when quercetin was added to Co-QueD-E76H under oxygen free condition. Remarkably, a new doublet line was also found in the high-field region at 337 mT ($g \approx 2.0$) with line splitting of about 2.0 mT, both parameters being indicative for an organic radical (Figure 4-27A-b). This organic radical signal appeared with quercetin addition and gained some intensity when the thawed sample was shortly exposed to air (30 s) (Figure 4-27B-c). After a further exposure (5 minutes) the signal was falling off (Figure 4-27B-d) and finally vanished after about 10 minutes (Figure 4-27B-e). Apparently, a reaction occurred in the protein active site when oxygen was present consuming

the organic radical. Apart from loss of the Co^{2+} -signal at $g \approx 3.1$, the signals at $g \approx 6$ also showed some changes in the course of reaction. Upon substrate binding the signal intensity was lowered, but increased slightly in presence of oxygen due to effects of relaxation. In particular, the width of the signal increased due to hyperfine lines in the region between 50 and 100 mT for longest exposure to oxygen (marked with arrow in Figure 4-27B-e). For the quite different wild type Co-QueD spectral pattern the signals in that range were assigned to a product bound state.¹²⁹ No significant change of valence state of Co was detected. Quite intense signals of mainly Cu^{2+} metal ions were found in this preparation (marked by asterisk in Figure 4-27B-a).

For a detailed analysis of the organic radical signal, the EPR spectra of the anoxic mixture of Co-QueD-E76H and quercetin were recorded with higher resolution in a narrow field window of 300-353 mT. Microwave power and temperature were varied from 0.2 – 20 mW and 15-60 K, respectively. As presented in Figure 4-28 left panel, signal intensity of the organic radical is strongly increasing with higher microwave power. With respect to temperature the signal loses intensity increasing this parameter (Figure 4-28 right panel), and seems to vanish above 70K. Such a dependence on microwave (mw) power and temperature is very unusual for organic radicals. In general, at high power organic radical signals are saturating and losing intensity when measured in our applied low temperature range, or vice versa, gain intensity when going to higher temperatures for a given mw power. The observed behavior can only be explained by an interaction and energy exchange effect with a fast relaxing paramagnetic species in the vicinity of the radical, which, of course, is the Co^{2+} -ion in the active site (c.f. Figure 4-30; the relaxation behavior of the Co^{2+} -species has been explicitly studied, but the data are not shown here). It is concluded that the organic radical has to be located close to the Co^{2+} -ion or may even be attached to it. This raises the question on the origin of the radical signal.

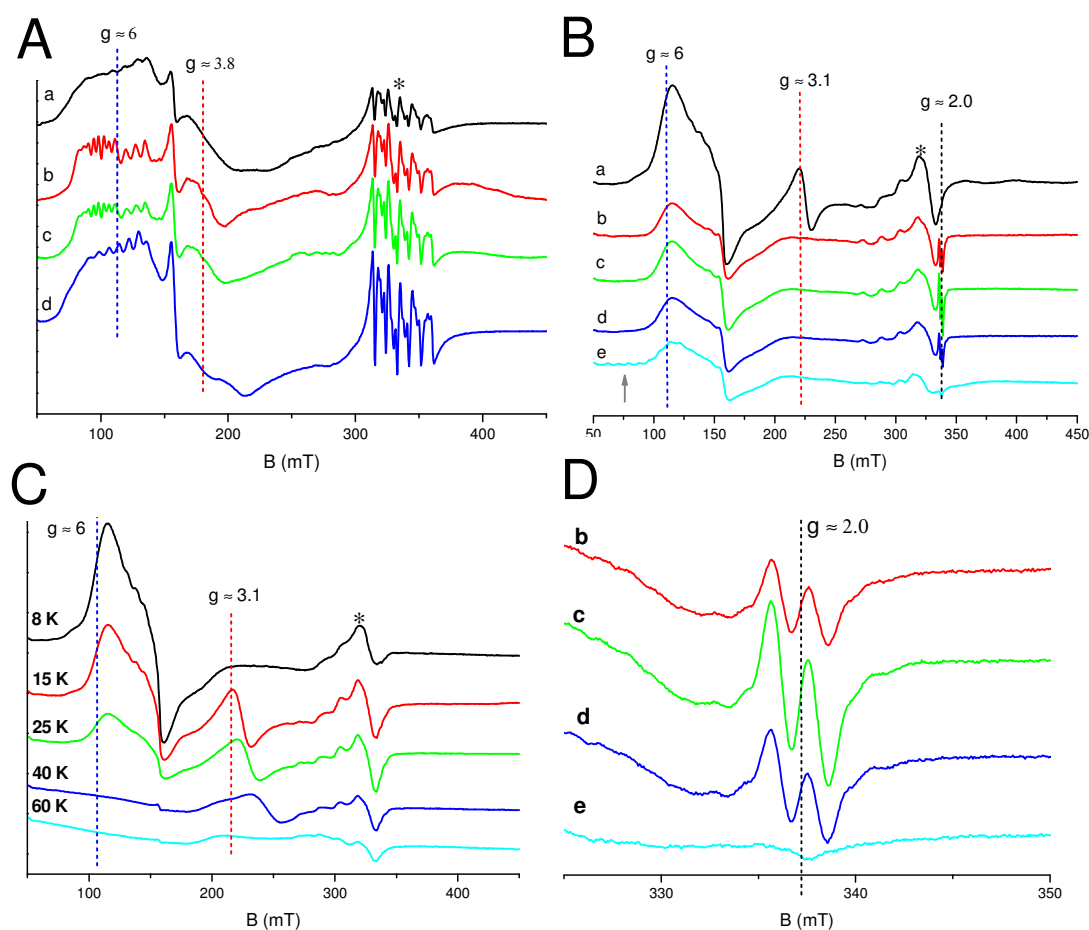


Figure 4-27. (A) EPR spectra of anoxic Co-QueD wild type (1.13 mM) at 8 K in the resting state (a), after addition of a 2-fold molar excess of quercetin (3 mM) (b), and after exposure to air for 60 s (c) and 10 minutes (d). (B) EPR spectra of anoxic Co-QueD-E76H (2.8 mM) at 15 K in the resting state (a), after addition of a 2-fold excess of quercetin (5 mM) (b), and after being exposed in air for 30 s (c), 5 minutes (d), and 10 minutes (e). (D) EPR spectra of the organic radical signal recorded in narrow field window with the same condition in color code of panel A. (C) Temperature dependence of the Co²⁺ signals of oxidic Co-QueD-E76H in the resting state. Parameters settings were microwave power 2 mW, modulation amplitude 0.7 mT (panel A, B, C) and 0.4 mT (panel D). The signals marked with asterisks arise from some amount of Mn²⁺ ($g \approx 2.005$), and (or) Cu²⁺ ($g \approx 2.05$). The dashed lines indicate the signal of Co²⁺ at $g \approx 6$ (blue in A, B and C), $g \approx 3.8$ and $g \approx 3.1$ (red in A, B and C) and the signal of the organic radical at $g \approx 2$ (black in B, D).

A full analysis of the organic radical signal is hampered by the fact, that it was not observed in high concentration and was varying in intensity for different preparation batches, so that no additional techniques such as high frequency EPR or other high resolution techniques could be applied. From the spectral signature in Figure 4-28 (top spectrum) some information can be derived. Next to the strong doublet lines (separated by 2.0 mT), at least two pairs of weak and broad signals with splitting of about 1.5 mT are symmetrically visible at higher and lower field. The strong difference in intensity compared to the doublet argues against a single radi-

cal species. In addition, the weak signals are stretching over nearly 9 mT which is very atypical for a carbon centered radical interacting with protons. For such a wide extension interactions with minimum two nitrogens having hyperfine couplings between 1.6 and 2 mT are necessary as was inferred from test simulations. The all histidine ligation of Co-QueD-E76H would, in principle, provide such an environment. The doublet signal then would be assigned to a second radical with a strong hyperfine interaction with nucleus of $I=1/2$, i.e. a proton. Another possibility is that a spin coupled system with $S=1$ is present, in which a zero field splitting of about 4.4 mT is approximately reproducing the observed pattern showing deviation of 0.2 to 0.4 mT of calculated splittings as shown in Figure 4-29. A more elaborate approach including variability and orientation dependence of the zero field splitting parameters needs to be applied for further improvement of simulation. For the moment, the most plausible explanation is that two independent radicals are present or that two radicals are coupled to spin system of $S=1$, which may include or interact with the Co^{2+} -center.

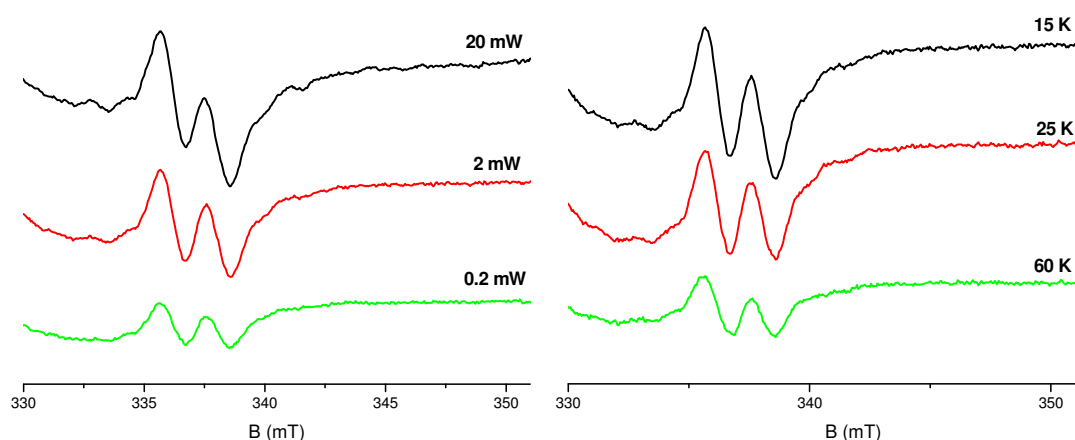


Figure 4-28. Unusual behavior in signal intensity is observed for the organic radical formed in the anoxic mixture of Co-QueD-E76H and quercetin (2-fold molar excess) by applying different microwave powers (left panel) and temperatures (right panel). Modulation amplitude was set at 0.4 mT, temperature 15K (left panel) and microwave power 2 mW (right panel).

We also examined QueD variants with amino acid modifications in the immediate vicinity of the active site to obtain Co-QueD-I66A and -Y117A (explained in introductory paragraph of this chapter). Their spectra are given in Figure 4-30 showing again Cu^{2+} and Mn^{2+} signals above 250 mT. In the anoxic state, the overall pattern of the Co^{2+} -resonances at low field resembled that of the wild type protein, apart from lower signal intensity and resolution of the Co^{2+} hyperfine lines (Figure 4-30A-a, B-a). Addition of the substrate also caused comparable spectral changes as in the wild type protein (Figure 4-30A-b, B-b). Exposure to oxygen in-

duced further changes (not shown) similar to the wild type protein confirming the catalytic activity of these variants as determined by the Münster group. However, no indication of presence of an organic radical was observed.

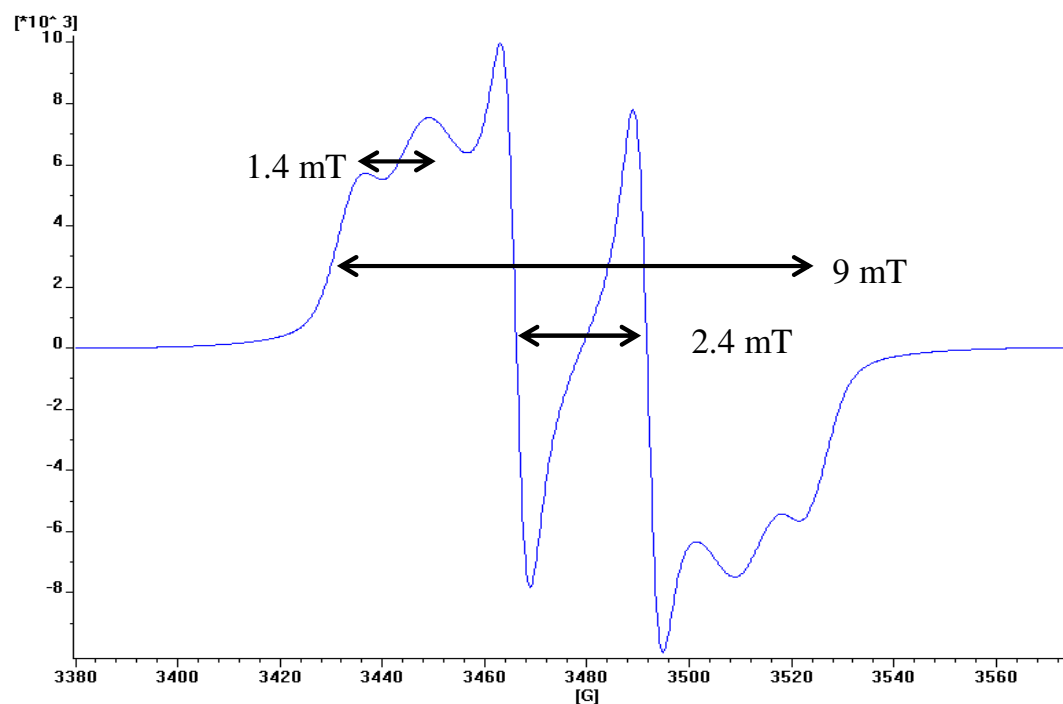


Figure 4-29. Simulation trial with an $S=1$ spin system approximately reproducing the experimental pattern (see Figure 4-28). Isotropic g -tensor was assumed with a zero field splitting of $D=44\text{G}$ ($=4.4\text{ mT}$) and a rhombic parameter $E=6\text{ G}$ ($=0.6\text{ mT}$). The pattern is shifted to higher field because a higher mw-frequency was used. Arrows are indication of line splittings.

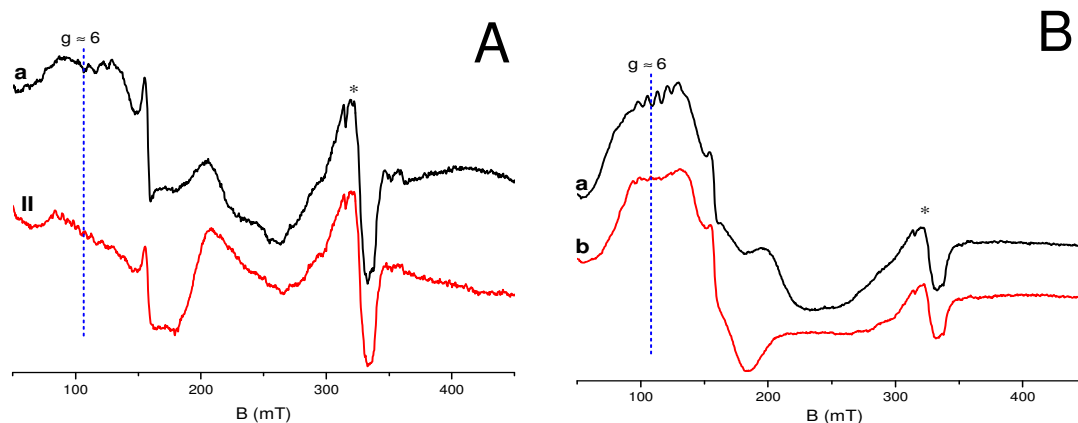


Figure 4-30. EPR spectra of anoxic Co-QueD-I66A (A-a) and -Y117A (B-a) at 8 K in the resting state, and no observation of organic radical after addition of a 2-fold excess of quercetin (A-b, B-b). The dashed lines indicate the signal of Co^{2+} at $g \approx 6$ (blue). The signal marked with asterisk arises from small amounts of Cu^{2+} and Mn^{2+} . Parameter settings: are of microwave power 2 mW, modulation amplitude 0.7 mT. Spectra in A are not baseline corrected.

To detect oxidizing species possibly generated in the enzymatic reaction, EPR experiments at room temperature were conducted using again the spin probe CMH. Co-QueD protein and substrate were dissolved in phosphate buffer solution and transferred to 50 μl EPR-capillaries.

Similar to Ni-enzymes, the wild type protein with Co substitution also showed indications for ongoing reaction as seen in the bending curve of reaction (Figure 4-31A, blue trace). As compared to the very small CM^\bullet signals observed for the controls that followed linear kinetic, once more no significant increase in CM^\bullet arising from reaction of CMH with oxidizing intermediate species could be observed.

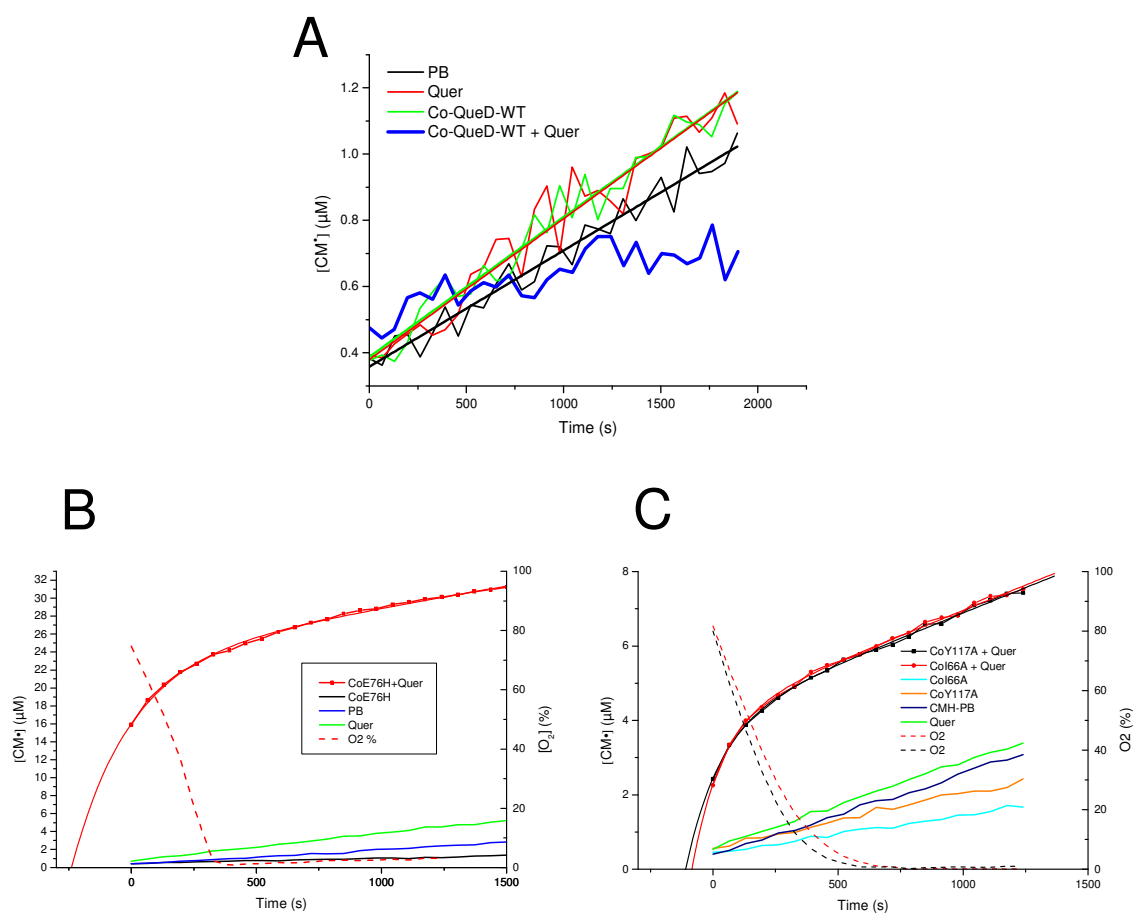


Figure 4-31. Oxidation of CMH by QueD enzymes produces very low yields for CoQueD-WT (A) and much higher signals for CoQueD-E76H (B) and CoQueD-I66A and -Y117A (C). Controls in A are fit with linear, reactions in B, C with exponential-linear functions. The dashed lines monitor oxygen consumption by TAM radical. Constant intensities of the TAM signal from control experiments were defined to correspond to 100% of dissolved O_2 . The stable minimum of the TAM intensity after conversion of quercetin was assumed to represent 0% O_2 . Concentrations: enzyme (0.6 U/ml in A, 0.1 U/ml in B, C), 400 μM quercetin, 600 μM CMH and 4 μM TAM. The contents of the assay mixtures are indicated in the insets.

However, in case of Co-QueD variants E76H, Y117 and I66A, significant amounts of CM^\bullet which followed a nonlinear kinetics were observed for conversion of quercetin. As shown in Figure 4-31B, the CM^\bullet formation increased drastically in the reaction of Co-QueD-E76H (solid red line-symbol), so that the CM^\bullet signal starts at high CM^\bullet concentration produced in the short time (1-4 min) elapsing between start of the reaction and the first spectrum recorded. The experimental points can be well fit with an exponential-linear growth function, which is interpolated to the start of the reaction (at negative times, solid red line). From the initial increase there, a fast kinetic can be estimated ($k = 0.089 \mu\text{M}/\text{sec} = 5.3 \mu\text{M}/\text{min}$). For longer times, the CMH oxidation rate was decreasing and leveled out to linear behavior, which can be attributed to the decelerating enzymatic reaction, caused by substrate depletion, in this case oxygen. As illustrated by the kinetics of the signal of the tetrathiatriarylmethyl radical (TAM) oxygen probe, which reached its minimum at about 400 s, oxygen in the solution is completely consumed for reaction time above 500 s. The linear slope at longer times ($0.0048 \mu\text{M}/\text{sec}$) corresponds roughly to the slopes found for quercetin and protein controls.

From the fitting procedure a maximal CM^\bullet concentration of $24.1 \pm 0.21 \mu\text{M}$ was obtained, which is associated with a characteristic time of $228.5 \pm 5.8 \text{ s}$ for reaching 63% of the maximal value under oxygen limitation. For a given concentration of about $220 \mu\text{M}$ of dissolved oxygen, approximately 10% of oxidizing species formed during reaction of Co-QueD-E76H are intercepted by CMH. Whereas the CM^\bullet signal monitors the oxidation of CMH in the course of reaction, the TAM signal provides an approximate measure of oxygen consumption, and, indirectly, of substrate conversion. The initial rates of O_2 consumption (Figure 4-31B, red dashed trace) and CM^\bullet formation (Figure 4-31B, red solid trace) were $23.6 \mu\text{M}/\text{min}$ and $5.3 \mu\text{M}/\text{min}$, respectively. For the other protein variants, Co-QueD-I66A and -Y117A, we found nearly identical saturation concentrations from the fitting of about $4.2 \pm 0.07 \mu\text{M}$ (Figure 4-31C, black and red traces), and initial slopes of CM^\bullet formation of about $1.6 \mu\text{M}/\text{min}$, which both are clearly lower than for the E76H variant. In addition, the characteristic times for the reaction curves are only about half the value (116 and 135 s) as found for E76H variant. The slopes in the linear end part of reaction curves are similar to those of the protein and substrate controls. Using again the TAM signal, the initial oxygen consumption amounted up to 29 and $35 \mu\text{M}/\text{min}$ for the I66A and Y117A variants, respectively, which decayed completely above 500 s (Figure 4-31C, red and black dashed trace). The initial rates of O_2 consumption observed in these assays approximately corresponded to the rates of substrate conversion, measured spectrophotometrically under conditions identical to those of the EPR experiments.

In order to verify that the catalytic reaction is observed in the described experiments, the enzyme activity at constant substrate concentration, and the amount of substrate at constant enzyme concentration were varied. As shown in Figure 4-32 (left panel) for Co-QueD-E76H, the conversion rate increases with the enzyme activity reaching similar saturation levels. The controls clearly differ from the reaction curves. For substrate variation the initial increase is comparable, and the saturation levels are different as expected for the catalytic conversion (Figure 4-32 right panel). Once more, the controls are found at clearly lower intensities. Therefore, CM^{\bullet} formation is monitoring the catalytic process of the enzyme.

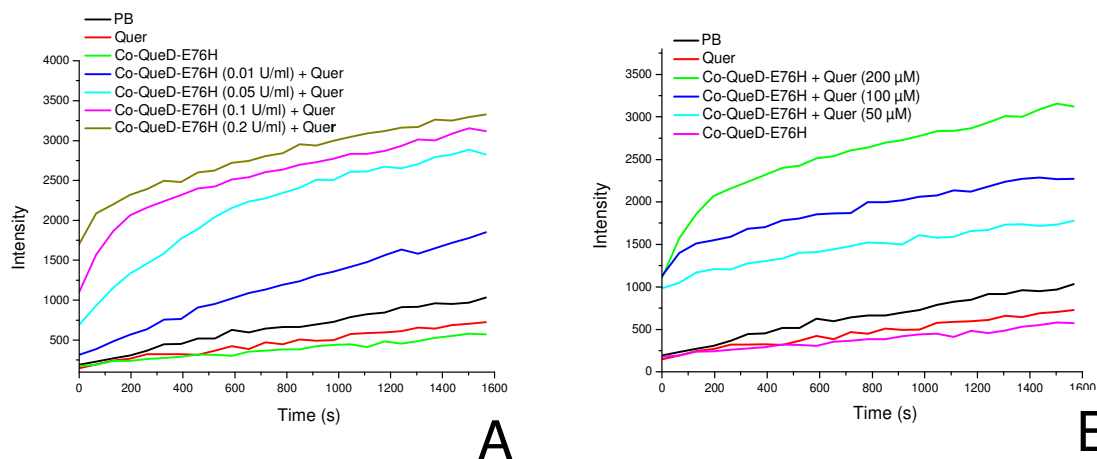


Figure 4-32. Dependence of the catalytic conversion of quercetin on the enzyme activity (A) and substrate concentration (B). The assays contain quercetin (500 μ M, panel A), Co-QueD-E76H (0.1 U/ml, panel B) and CMH (600 μ M) in PB pH 7.4 (20 mM). The contents of assay mixtures are given in figure legends. Note that the EPR signal intensity is used as y-axis scale.

Summing up, the experiments using CMH spin probe gave clear evidence for presence of oxidizing species in the reaction of Co-QueD variants E76H, I66A and Y117A. It appears that the variants show a different degree of shielding of the active site for interaction with CMH. For Co-QueD-E76H about 10% of the maximally possible substrate conversions are detectable but only about 1.9% in case of Y117A and I66A variants. Obviously, the wild type protein controls the reaction perfectly by shielding the active site against any interaction with CMH. The mutation (E76H) in the ligand sphere of the Co^{2+} -ion induces a much more pronounced interaction mode with CMH than the mutations Y117A and I66A in the active site environment. In part, this is also reflected by the low temperature spectra, showing that the ligation sphere of Co^{2+} in the E76H variant is strongly affected. Further Co^{2+} -QueD protein

variants, in which single phenylalanines located in the path towards the active site and probably involved in proper orientation of the substrate, were exchanged with alanines, did not improve accessibility or reactivity for CMH (data not shown). It may be speculated that multiple phenylalanine substitution might improve the rate for intercepting radical intermediates by CMH provided that the possible disturbance of structure is not too pronounced.

So far, the reaction of Co-variants were considered, when all components, i.e. enzyme E, substrate S and oxygen, are present in the solution. It is of interest to analyze the behavior when substrate or oxygen is absent recalling that for the E76H-variant an organic radical signal was observed under anoxic conditions. In oxic protein solutions without a flavonol substrate, formation of CM^\bullet was negligible (Figure 4-31, cyan and orange traces in panel B and black in panel A) being in the range of background signal formation. This observation is disproving the possibility that the CMH oxidation observed during the reaction is due to an oxidizing species which might be formed by direct O_2 activation by the enzyme. Anoxic mixtures of Co-QueD variants I66A or Y117A with substrate likewise showed only background formation of CM^\bullet (comparable to that observed in oxic substrate reference solutions) (Figure 4-33A, cyan and magenta solid traces), which argues against the possibility that the CMH oxidizing species derives from direct substrate activation to a radical by the enzyme. For these two Co-QueD variants, I66A and Y117A, the results clearly indicate that formation of the reactive oxidizing species was strictly dependent on the presence of both the quercetin substrate and O_2 . However, in the case of Co-QueD-E76H, a remarkable amount of CM^\bullet was monitored in the anoxic state in presence of quercetin which followed an apparently linear kinetic (Figure 4-33A, blue solid trace). It is far above any background formation of CM^\bullet as observed in anoxic substrate or enzyme reference solutions (Figure 4-33A, green and black solid traces), and also small residual amounts of oxygen in the solution cannot be responsible because oxygen concentration measured by TAM signal was zero (Figure 4-33A, blue dashed trace). The signal formation in anoxic environment is also depending on the protein concentration as shown in the right panel of Figure 4-33B for 100, 50 and 10 μM of two Co-QueD batches. Hence, the CM^\bullet formation is apparently emerging from an oxidizing species formed in the anoxic mixture of the E76H-variant and quercetin. As was shown previously by UV-Vis absorption spectroscopy (and very recently by the available X-ray crystallographic data of the Berlin group) under anoxic conditions,¹²⁹ formation of ES complexes does not require the presence of dioxygen, so that the oxidizing species might be related to the radical observed in low temperature EPR for Co-QueD-E76H.

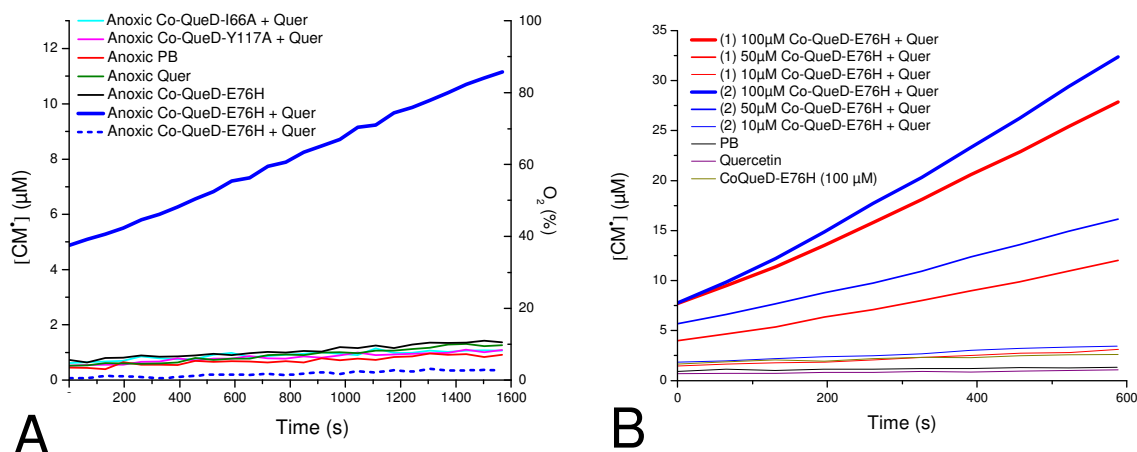


Figure 4-33. (A) Oxidation of CMH in anoxic reaction of CoQueD variants with quercetin. Only CoQueD-E76H variant shows a notable amount of CM^{\bullet} following a linear kinetic (blue solid trace), oxygen consumption was monitored by TAM signal (blue dashed trace). (B) CM^{\bullet} formation in anoxic reaction of different concentration of CoQueD-E76H (two different batches, numbered with (1) and (2) in figure legend). The assay contains of CoQueD-E76H (10, 50, 100 μM), CMH (600 μM) and quercetin (500 μM in DMSO) in PB (pH 7.4, 20 mM). The contents of the assay mixtures are indicated in the insets.

The observed CM^{\bullet} formation under anoxic condition led to further experiments using limiting amounts of CMH or protein to study long term effects and possible saturation. For this purpose, small limiting concentrations of CMH of up to 50 μM were added to the assay mixtures containing 100 μM Co-QueD-E76H and 500 μM quercetin recording an extended time period (~ 3 hours) under oxygen free conditions. Indeed, the reaction curves for 10, 20 and 50 μM CMH showed nonlinear kinetics of CM^{\bullet} formation approaching saturation (Figure 4-34A). Fitting these curves with an exponential growth function (Weibull2) the saturation values can be approximated with 9.2, 18.9 and 47.2 μM close to the applied concentrations (it is noted that the used function gives very good agreement for the 10 and 20 μM curves with corrected R^2 of 0.9989 and 0.9996, and a somewhat less good fit for 50 μM curve with 0.9986 not reproducing the sigmoidal curvature at early times perfectly). From fit parameters of the growth functions rather similar characteristic times are obtained in a range 2730 to 2820 s. This implies that the anoxic oxidation reaction is about 12 and 23 times slower than the conversion under oxic conditions (116 s, 135 s and 228 s). The analogous anoxic experiment with limiting enzyme concentration of the E76H variant (50 μM) and excess concentrations of CMH (600 μM) and quercetin (500 μM) is presented in B showing a saturation behavior (black symbols). In this case, several growth fit procedures (BoxLucas, Weibull2) gave a saturation value of 49.2 ± 0.14 μM (corrected R^2 of 0.997) but the fitting curves did not perfectly reproduce the initial sigmoidal curvature as well as a small slope at the end of the graph. Because

CMH is used in a large excess, this final slope arises from a background oxidation and is slightly larger than for the CMH control (magenta line). Using the slope and the initial CM[•] signal of the control, a linear function is set up and subtracted from the original data yielding the corrected curve (blue symbols). A sigmoidal fit (Weibull2) to this curve results in a saturation value of $39.2 \pm 0.03 \mu\text{M}$ (corrected R^2 of 0.9995) as shown by the overlaid fit curve, for which a characteristic time of 2400 s is measured that is quite similar to the values for limited CMH concentrations. Notably, the smaller saturation value would more closely correspond to an expected value of $35 \mu\text{M}$ considering a metal occupancy of about 0.7 for these samples.

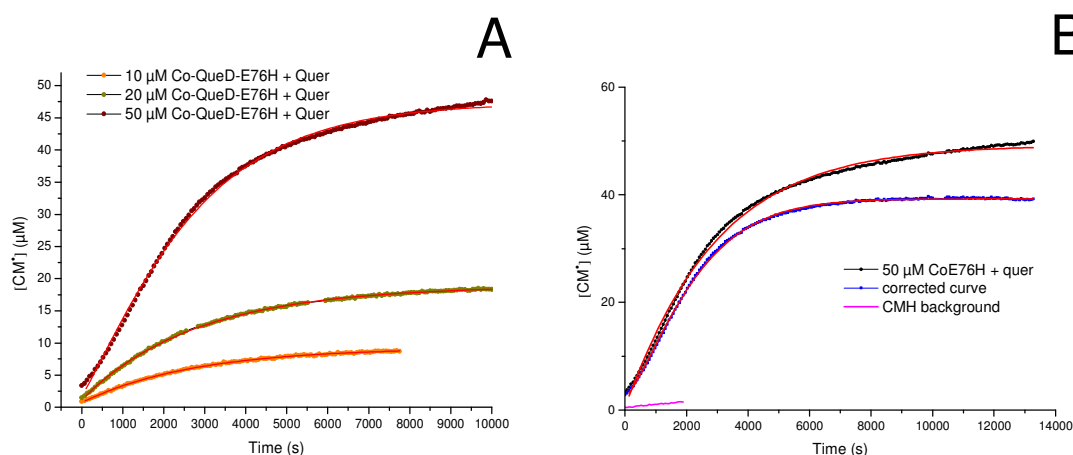


Figure 4-34. Kinetics of CM[•] formation in anoxic ES complex of CoQueD-E76H under limited CMH (A), and protein concentration (B). Red lines are fit of curves; in B background of CM[•] formation in control was subtracted. Concentrations are (A) protein 100 μM, quercetin 500 μM, and (B) quercetin 500 μM, CMH 600 μM in PB pH 7.4 (20 mM). The contents of the assay mixtures are indicated in the insets.

The results for CoQueD-E76H clearly indicate that, in absence of oxygen, an electron acceptor for oxidation of CMH must be present which is correlated to active enzyme concentration. This implies that CM[•] is formed in a slow reaction, and in 1:1 stoichiometry. Because quercetin is used in high concentration, the ES complex is prevailing (low dissociation constant K_d) in which the substrate is deprotonated and may be annotated as Co(II)-QueD-S^- . In this state, S is transferring an electron either to enzyme thus forming S^\bullet and E^\bullet or, formally, onto the Co-ligand moiety which can then be described as $[\text{Co(II)-QueD}]^- \text{-S}^\bullet$. In the first case, CMH needs to reduce either S^\bullet or to give $\text{S}^-/\text{E}^\bullet$, or E^\bullet , which is less probable requiring a second reduction of enzyme radical to yield $\text{S}^\bullet/\text{E}^-$. Both combinations have to be locked dead-end states to fulfill the observed stoichiometry. However, no signals of a radical are observed in the anoxic liquid phase experiments. In the second scenario, starting from state $[\text{Co(II)-}$

QueD]⁻S[•], CMH would reduce S[•] in a slow process finally yielding a state [Co(II)-QueD]⁻S⁻, which again is a dead end state. The behavior of the additional electron on this moiety is not clear at present. It could be delocalized on the four ligating histidines (or even to further amino acids) or might be localized onto the metal which formally is then reduced to a diamagnetic state. First low temperature EPR experiments, performed to address this question, were not yet successful.

The conversion of other flavonols with additional hydroxyl groups (see section 4.3.1) by CoQueD-E76H was also studied to search for hints on the origin and nature of the oxidizing species. However, assays with 3-hydroflavone and rhamnetin showed very slow reaction rates with a linear kinetic close to CM[•] background formation (Figure 4-35A). For myricetin, a burst of CM[•] signal was observed in the reaction with Co-QueD-E76H- following a nonlinear kinetic (Figure 4-35B, blue trace) which, however, was found to basically arise from spontaneous background formation of CM[•] in the oxidic myricetin reference solution (Figure 4-35B, green trace). Because from the four used flavonol substrates myricetin is most easily oxidized ($E_{1/2} = 0.33$ V) (and has two inseparable and irreversible further oxidation steps), this substrate possibly was spontaneously oxidized in the presence of oxygen inducing a massive amount of CM[•]. The clearly diminished but still relative high amount of CM[•] perceived in the conversion by Co-QueD-WT (Figure 4-35B, light blue trace) compared to the E76H variant (and oxidic background of myricetin alone) is likely to be caused by effective consumption of myricetin in the Co-QueD-WT-catalyzed conversion. Unfortunately, the use of other substrates did not contribute to clarify details of the conversion reaction; however, the experiments demonstrate the importance to qualify all possible redox related interactions in these complex solutions.

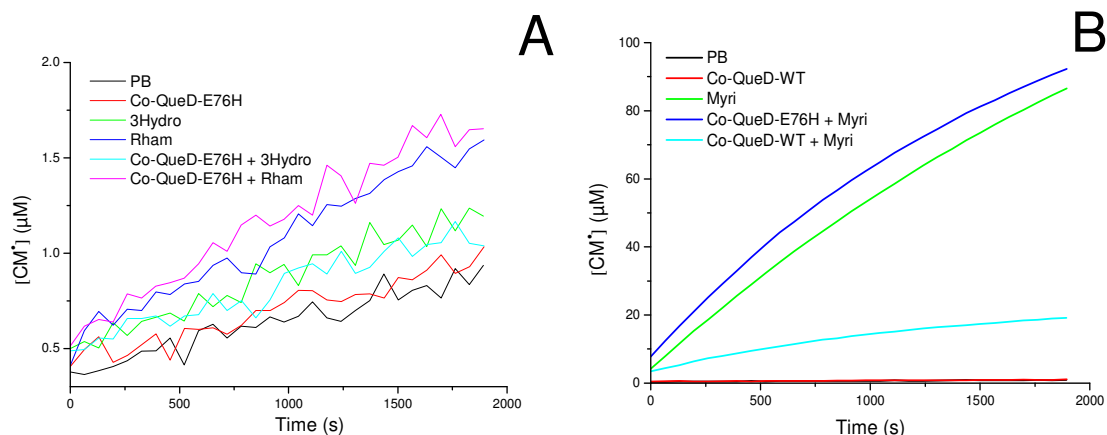


Figure 4-35. Formation of CM^\bullet during the conversion of other flavonol substrates, 3-hydroxyflavone, rhamnetin (A) and myricetin (B), catalyzed by Co-QueD-E76H enzyme. Only very small CM^\bullet formation following a linear kinetic is observed for 3OH-hydroxyflavone and rhamnetin around background CM^\bullet formation, whereas a burst of CM^\bullet arises nonlinearly for myricetin. The assay composition: enzyme (0.6 U/ml), substrate (400 μM) and CMH (600 μM) in PB pH 7.4 (20 mM). The contents of the assay mixtures are indicated in the figure legends.

Nitroxide as oxygen mimic

In studies of anoxic QueD enzyme reaction we found an organic radical in the enzyme-substrate mixture of Co-QueD-E76H and quercetin under anaerobic condition. Exposition with oxygen results a depletion of the signal with time. Apparently, a reaction occurred with oxygen in the protein active site consuming the organic radical. In an attempt to search for the location of dioxygen in the reaction site and how it engages in the depletion reaction of the organic radical, nitric oxide (NO) was used as an analogue for oxygen, because it may occupy the position of oxygen in the active site of QueD according to the similar size of both molecules. In biology, the nitric oxide is involved in the two important reactions, S-nitrosation of thiols and nitrosylation of transition metal ions. S-nitrosation involves the conversion of thiol groups, including cysteine residues in proteins, to form S-nitrosothiols (RSNOs)¹³¹, while nitrosylation involves the binding of NO to a transition metal ion like iron or copper. Typical cases are the nitrosylation of heme proteins, in which hemoglobin is a prominent example that can be modified by NO in both pathways: NO may attach directly to the heme in the nitrosylation reaction, and independently form S-nitrosothiols by S-nitrosation of the thiol moieties¹³². In the first reaction, it is known that NO can bind to heme in a manner similar to O_2 . Therefore, we used EPR spectroscopy to study the effects of NO interaction with the ES complex (QueD-quercetin) for a comparison with O_2 . According to NO-binding modes to metal ions, it is expected that EPR spectra may vanish or alter due to a change in valence state, or the spin state of the metal. Likewise, if no binding occurs and the NO molecule is positioned

somewhere in the environment of the metal center, a magnetic interaction appears possible, which, in principle, is monitored by a change of the EPR spectrum. In a similar way, also QueD with diamagnetic metal substitution can be exposed to NO to follow the appearance of EPR spectra. For this experiment, NOC-5 (3-(Aminopropyl)-1-hydroxy-3-isopropyl-2-oxo-1-triazene (NOC-5) was used as NO-donor that releases nitric oxide spontaneously in a rate-controlled manner with half-life of about 93 min in solution.

When anoxic CoQueD-E76H-quercetin is exposed to NO, the organic radical is instantly quenched (Figure 4-36 c). For prolonged exposure extended Co^{2+} -hyperfine structures appear which are also observed in CoQueD wt reaction indicating that binding of substrate and further reaction are proceeding in an analogous way as for the wt protein (Figure 4-36 c, d, e). A search for nitrosylated products has not been successful so far, so that a final proof on the mode of reaction is not available. It turned out that kinetic experiments at room temperature with CMH in the NO reaction assay are problematic because multiple redox reaction seems to occur, so that a clear interpretation is hampered.

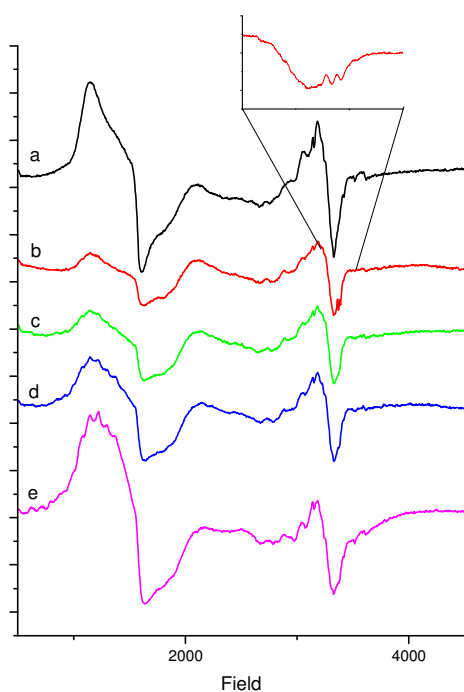


Figure 4-36. EPR spectra shows loss of organic radical in CoQueD-E76H ES-complex upon release of NO from NO-donor NOC-5 at different concentrations (c, 1 mM; d, 2 mM; e, 3 mM), trace a is the oxidic state and b the anoxic state with quercetin, the inset shows close-up of organic radical 1mM of NOC5 (nitroxide source) in addition. Parameters settings: microwave power 2 mW and modulation amplitude 0.7 mT.

5. DISCUSSION

Redox properties and reactivity of cyclic hydroxylamines

Cyclic hydroxylamines EPR spin probes are of great interest for the detection of reactive oxygen species (ROS), in particular superoxide ($O_2^{\bullet-}$).^{23,24,25,26,27,28,29,30} In cell systems, they are used to detect *extra* and *intracellular* superoxide^{29,133} and react with it in a much faster kinetic as compared to nitrene spin traps (CMH is ca. 200 fold better than DEPMPO).²⁵ Therefore, they are considered a valuable addition to the tool box for following the formation and reaction of this ROS species. Superoxide dismutase (SOD) and other antioxidants such as ascorbate and glutathione are involved in competitive reaction with superoxide and cyclic hydroxylamine oxidation so that their effects and efficacy can be measured.^{31,32,33} Despite of the fundamental interest of redox properties of cyclic hydroxylamines, only few studies were reported which mostly focus on the reaction of cyclic hydroxylamines with other redox substances.^{109,110,111} Variation of substitution at β -position on the five-membered pyrrolidine and pyrrolidine nitroxides was shown to influence the reaction rate constants for the reduction of ascorbate, which was also compared to the more rapid reduction of six-membered nitroxides (piperidines) and correlated to the inductive effects of substituents.¹¹⁰ In an analogous study, the redox potential of nitroxyl radicals was found to directly correlate to the electro-negativity of the β -substituted group, in which an electron-donating group causes a negative shift in the redox potential while an electron-withdrawing group behaves oppositely.¹¹¹

Our study describes the thorough electrochemical examination of the redox properties of the cyclic hydroxylamines CMH and CPH, which is of key importance for us to understand the redox processes that might be relevant for enzymatic mechanisms and cellular systems as well as competitive reactions in such complex systems.

Using cyclic voltammetry, the redox potentials of two electron transfer steps, their pH-dependence, and the reactions with oxygen, superoxide and hydrogen peroxide for both CMH and CPH were determined. For CMH, the first electron transfer from hydroxylamine CMH to nitroxide CM^{\bullet} is strongly pH dependent, whereas the second electron transfer from CM^{\bullet} to oxoammonium cation CM^+ is not affected by pH of solution. In aqueous solution CMH protonation states are altered depending on pH, i.e., doubly protonated $CMH-H^+$ at $pH < 2$, mono-protonated CMH at $2 < pH < 12$ and deprotonated CM^- at $pH > 12$. The doubly protonate

CMH-H⁺ form showed an inert redox behavior at pH < 2 being an electrochemically inactive species. In the range pH 2-12 two well-separated redox couples of CM[•]/CMH and CM⁺/CM[•] are consistently visible with a well-resolved NMR spectrum at pD 8 defined for mono-protonated CMH. At higher pH > 12, CMH transforms to CPH in a hydroxyl-substitution reaction releasing methanol (CH₃OH). NMR spectra at pD 13 showed not only the pattern of CMH but also of a second molecular species indicative for CPH (having the identical NMR signals of CPH), and, especially, signals of methanol leaving from the substitution. The elimination of the first redox potential wave (CM[•]/CMH) and the drastic increase of second oxidation current from CVs agreed with the transformation of CMH to CPH at pH 13. CVs of CPH also showed two well-separated redox couples associated with nitroxide CP[•]/hydroxylamine CPH (I) and oxoammonium cation CP⁺/CP[•] (II) pairs, in which the first pair CP[•]/CPH is governed by a very slow kinetic of the electrode reaction. This explains the much slower kinetics for reaction of CPH with superoxide as compared to CMH. From this aspect it becomes evident that for CPH kinetics is important for reaction behavior, although CPH is thermodynamically favored for reaction, having the lower midpotential compared to CMH.

Correlated to its redox properties, CMH can undergo autoxidation in presence of O₂ and/or transition metal ions in aqueous solution. A small EPR background is a consequence of CMH oxidation, giving variable amounts of CM[•] signals. CMH oxidation is inert at low pH (pH 2) as expected, but shows a considerable background of CM[•] in the physiological important range around pH 7 due to oxidation by, e.g., Haber-Weiss- and Fenton-type reactions. Therefore, metal chelators such as deferoxamine (DF) or diethylthiocarbamate (DETC) are used for physiological buffers to reduce background signal formation (Dikalov S, Fink B¹¹⁶). However, massive amounts of CM[•] were surprisingly observed at pH 13 (with O₂), being much larger than at pH 7, and showing saturation when O₂ was consumed (ca. 200 μM in the capillary). At pH above 12, when CMH transforms to CPH, O₂ can possibly be reduced to O₂^{•-} according to the low measured mid-peak potentials of CPH, and superoxide in turn can efficiently oxidize CMH to CM[•]. This is demonstrated in Figure 5-1 panel A by arrows 1 (dashed) and 3, respectively, helping to visualize the thermodynamic driving force with respect to the concentration ratio and pH. On the other hand, CPH can also reduce CM[•] (arrow 2) to regain the CMH and forming CP[•]. The large background of CMH oxidation at high pH is requiring attention when working with chemical systems at higher pH values. Of course, such extreme pH conditions hardly occur in the bulk solution of biological samples but might well be valid on a microscopic scale inside a protein pocket.

Superoxide ($\text{O}_2^{\bullet-}$) is known to be reduced by CMH to hydrogen peroxide (H_2O_2). Performing EPR experiments of CMH with KO_2 (as a source of $\text{O}_2^{\bullet-}$, liberated in solution) several possible reactions could be derived. In all probes two different kinetics regimes, an initial steep increase and a later slow decay of CM^\bullet signal, were observed. The liberated $\text{O}_2^{\bullet-}$ oxidizes CMH to CM^\bullet reaching full conversion of CMH for approximately equimolar concentration (Figure 5-1 panel B, solid arrow). Substantial excess of $\text{O}_2^{\bullet-}$ can further oxidize CM^\bullet to diamagnetic CM^+ and H_2O_2 (or O_2^{2-}), which is thermodynamically possible as indicated by the midpotentials E_{mid} of redox couples $\text{CM}^+/\text{CM}^\bullet$ and $\text{O}_2^{\bullet-}/\text{H}_2\text{O}_2$ of +0.91 V and +0.94 V, respectively (Figure 5-1 panel B, dotted arrow). Furthermore, excess of $\text{O}_2^{\bullet-}$ also can reduce CM^\bullet back to CMH producing O_2 which is also possible according to redox potentials ($E_{\text{mid}}[\text{O}_2/\text{O}_2^{\bullet-}] = -0.3$ V vs. $E_{\text{mid}}[\text{CM}^\bullet/\text{CMH}] = +0.15$ V), (Figure 5-1 panel B, dashed arrow). Assuming that $\text{O}_2^{\bullet-}$ is completely consumed or is disproportionated to H_2O_2 and O_2 in the decay regime, the slow loss of CM^\bullet signals can be associated to disproportionation reaction of CM^\bullet forming CMH and CM^+ which is not favored thermodynamically. The latter may react with available H_2O_2 to form again CMH and O_2 in a two-step process (via $\text{CM}^\bullet/\text{O}_2^{\bullet-}$) further decreasing the EPR signal. Both reactions, disproportionation and backward reaction for high CM^\bullet concentration, are sufficiently slow to explain the observed behavior. CM^\bullet formation in reaction of CMH with $\text{O}_2^{\bullet-}$ was pH dependent, increasing drastically for higher pH. CV experiments of CMH and KO_2 showed that CMH reduces superoxide $\text{O}_2^{\bullet-}$ to H_2O_2 , while superoxide $\text{O}_2^{\bullet-}$ can reduce oxoammonium CM^+ back to CM^\bullet , forming oxygen O_2 that caused the new reduction wave on reverse scan of CVs.

Examining the reaction of CMH and H_2O_2 by EPR again confirmed that CMH is not oxidized by H_2O_2 , as already reported in literature, because only CM^\bullet background signals were observed regardless of H_2O_2 concentration. Although the reaction of $\text{CM}^\bullet/\text{CMH}$ and $\text{H}_2\text{O}, \text{OH}^\bullet/\text{H}_2\text{O}_2$ is thermodynamically feasible (Figure 5-1 panel B, dashed-dotted arrow), it does obviously not occur for kinetic reason as no CM^\bullet was observed in EPR. Our CV experiments of CMH and H_2O_2 also showed that H_2O_2 does not react with CMH but thermodynamically reduces oxoammonium CM^+ to CM^\bullet , forming $\text{O}_2^{\bullet-}$ which is able to further reduce CM^+ to CM^\bullet finally producing O_2 , which is causing the new reduction peak at -0.55V in CVs typical for oxygen.

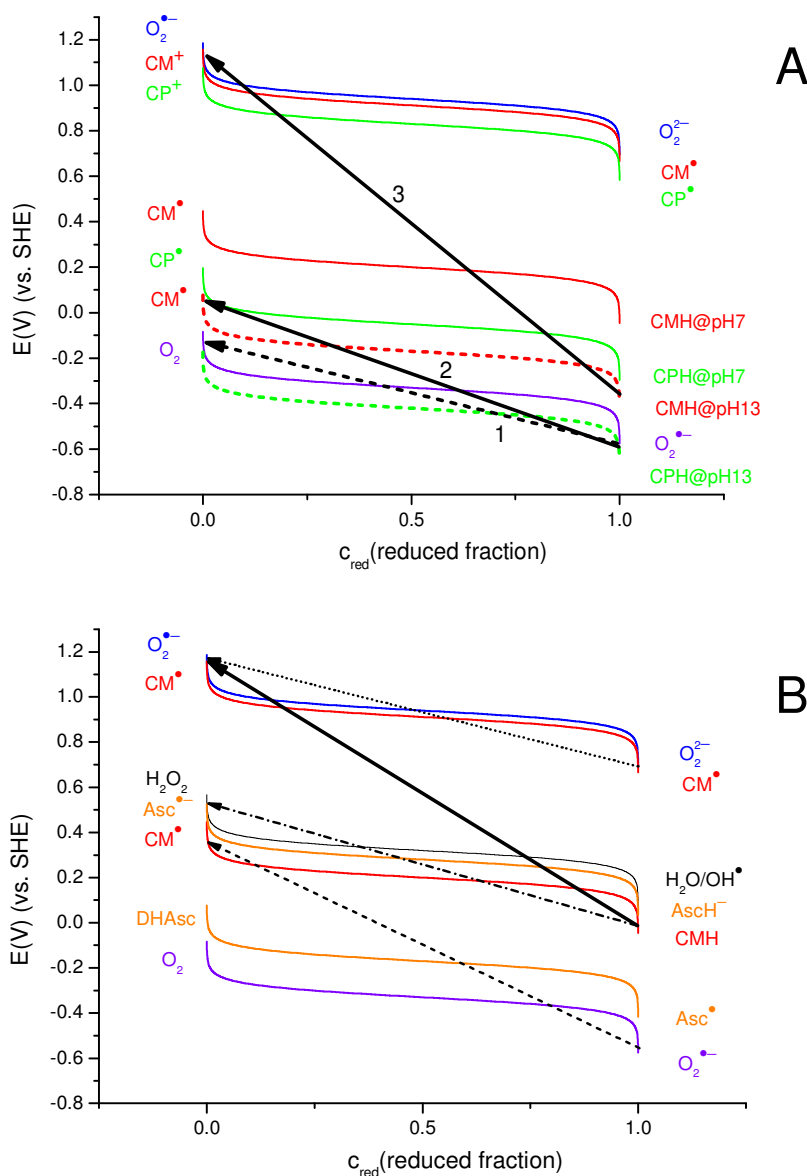


Figure 5-1. Concentration dependence of redox potentials for some relevant redox couples. By definition, the electron transfer is thermodynamically possible from a reduced species (more negative potential on the right hand side) to an oxidized species (more positive potential on the left hand side). Diagram A demonstrates the thermodynamically favored electron transfer with respect to concentration ratio and pH. At pH 7, both CMH and CPH are not able to reduce O_2 . However, at pH above 12, O_2 can possibly be reduced to $\text{O}_2^{\bullet-}$ by CPH according to the lower measured mid-peak potentials (arrow 1, dashed), superoxide in turn can efficiently oxidize CMH to CM^{\bullet} (arrow 3), and CPH can also reduce CM^{\bullet} (arrow 2) to regain the CMH and forming CP^{\bullet} . In diagram B, CMH can be reduced to CM^{\bullet} by $\text{O}_2^{\bullet-}/\text{O}_2^{2-}$ (solid arrow) or also by $\text{H}_2\text{O}_2/\text{H}_2\text{O}$, OH^{\bullet} (dotted-dashed arrow), but is not affected by ascorbate (AscH^-). On the other hand, CM^{\bullet} is possibly oxidized to CM^+ by high flux of $\text{O}_2^{\bullet-}$ albeit with a smaller driving force (dotted arrow), as well as being reduced back to CMH by ascorbyl radical (Asc^{\bullet}) forming DHAsc or by $\text{O}_2^{\bullet-}$ producing O_2 (dashed arrow). However, the dismutation of CM^{\bullet} is not favored in this diagram.

Taken together, we established the concentration dependence of the redox behavior of CMH and CPH (vs. SHE at pH7) from their measured mid-peak potentials and can relate it with some other relevant redox couples taken from literature¹¹⁹ by implementing in the redox couple diagram of Figure 5-1. In this type of diagram kinetic properties arising from steric or charge effects are not considered but thermodynamically favorable reactions can be predicted, if the potential of the reduced species located on the right side is more negative than the oxidized species located on left side, and thus is a very helpful tool to discuss some of the observed reactions particularly related to EPR. It also allows visualizing the pH (or proton)-dependent redox reactions by shifting the curves up in potential or down in going to lower or higher pH with increment of 68 mV per pH-unit for a ratio of one electron transferred per proton. Some possible reactions of redox couples can immediately be inferred such as the reduction of $O_2^{\bullet-}$ by CMH essential for its detection by EPR. For high concentration of CM^{\bullet} and high flux of $O_2^{\bullet-}$ formation of CM^+ is a possible reaction albeit with a smaller driving force. On the other hand, reaction of CMH with H_2O_2 appears possible, but homolytic splitting to form the hydroxyl radical OH^{\bullet} seems to be kinetically hindered. Dismutation of CM^{\bullet} even at high concentration is not favored in this scheme which explains the high stability of CM^{\bullet} in solution and the slow decay of EPR signal after reaction with excess of KO_2 . An important aspect concerns interaction with redox active additives such as ascorbate ($AscH^-$), which, as stated in literature, indeed is not reacting with CMH, both being in the reduced state. However, CMH may be oxidized by the ascorbyl radical (Asc^{\bullet}) as well as ascorbyl radical may destroy the CM^{\bullet} as can be inferred from Figure 5-1 panel B. This implies that great care has to be taken to safely conclude on the presence of superoxide radicals, when other redox active species are present in the reaction solution. Therefore, careful studies on the redox behavior of the substrates of the dioxygenases had to be performed.

Development of an EPR-based hydrogen peroxide assay

With the knowledge obtained from the redox properties of cyclic hydroxylamines CMH and CPH and the necessity for the dioxygenase projects, an EPR-based method to monitor the presence of hydrogen peroxide (or O_2^{2-}) was established. In the fluorescence based Amplex Red assay, commonly used for detection of hydrogen peroxide (H_2O_2), Amplex Red (N-acetyl-3,7-dihydroxyphenoxazine) reacts with H_2O_2 (catalyzed by horseradish peroxidase HRP) in a stoichiometry of 1:1 to form the colored and highly fluorescent compound resoru-

fin. In an analogy to the Amplex Red assay, an EPR-based approach using acetamidphenol (AAP) as co-substrate for HRP has been proposed. After electron donation to HRP by AAP the formed radical is oxidizing CPH to its stable radical form which is detectable by EPR. With the knowledge of the redox potentials of CPH and CMH for the two sequential electron steps, the new assay uses CMH as a single and direct electron donor to the catalytic cycle of HRP. For the catalyzed reduction of H_2O_2 , two electrons are needed from substrate to recycle the enzyme activity of HRP according to the proposed Scheme 4-4. Therefore, the double concentration of CM^\bullet should be measured by EPR for a certain amount of H_2O_2 . For proof of principle, the reaction stoichiometry of the HRP-catalyzed reduction of H_2O_2 with CMH was determined after a series of optimizing experiments and independent determination of the H_2O_2 concentration. The reaction stoichiometry is obtained from the calibration curve of H_2O_2 and CMH having a slope of 2.1 close to the expected 2:1 stoichiometry, which tends to be higher for H_2O_2 concentrations lower than $10 \mu\text{M}$. Further comparative experiments with Amplex Red assay and physiological detection of superoxide and hydrogen peroxide in cellular systems such as HyPer biosensor^{134,135} (Hyper protein is used to detect intracellular H_2O_2 , sensitive to pH and insensitive to $\text{O}_2^{\bullet-}$) are currently performed in our group.

Towards the reaction mechanism of Hod and quercetinase enzymes

The comprehensive knowledge of redox behavior of CMH was decisively important to access the details of the catalytic pathway of Hod and quercetinase enzymes. The transient phase of an enzyme-catalyzed reaction usually occupies a very short period of time (usually fractions of a second) and has very low product concentrations. Therefore, special techniques must be used for investigating this phase of the reaction. In the common rapid-mixing (or stopped-flow) technique, enzyme and reactants are mixed together at relatively high velocities so that time courses for reactions occurring on time scales as short as a few milliseconds can be assessed. However, this limit of milliseconds time scale prevents detection of faster reactions. In our experiments, the rapid-mixing spectrophotometry failed completely to detect transient intermediate species during Hod- and Quercetinase-catalyzed reactions. In the course of this work, the anion substrate as well as final product was detected in Hod enzyme reaction by means of optical (absorption) spectroscopy, but the detection was not successful for QueD enzyme. Redox activation of CMH forming stable CM radicals (CM^\bullet) has the big advantage that very short-lived intermediates can be trapped, because for electron transfer, being extremely rapid (approximately 10^{-15} s), time does not need to be considered and direct contact

is not necessarily required. The electron can go over long distances up to approximately 15-20 Å,¹³⁶ and may pass many other groups until it meets the proper reactant on which it occupies the lowest energy orbital. Of course, kinetics also needs to be taken into account in addition to the thermodynamic driving force. Considering the properties of electron transfer, CMH oxidation even does not need to take place inside the enzyme's active site but the molecule only has to approach close enough to transfer electron independent on conditions (pH, temperature,...) into the enzyme pocket.

Reaction intermediates in Hod enzyme and mechanistic details

The Hod enzyme, supplied and biochemically characterized by the Münster group, is one of cofactor-free dioxygenases that have been identified to neither contain nor require any cofactor for catalysis. The available crystal structures of cofactor-less oxygenases and oxidases confirmed that different protein folds provide the catalytic scaffold for cofactor-independent O₂ activation.^{78,79,80,81,82,83,84,85,86,87,88} For several members, formation of a (carb)-anion intermediate was proposed to occur as initial catalytic step.^{79,81,82,104} The ability of the deprotonated substrates to form resonance-stabilized radicals seems to be common to all the reaction. For MHOQ¹⁰⁴ and also for anthrones,¹³⁷ which are substrates of quinone-forming monooxygenases, radical formation from the respective anion was observed in chemical model reactions. In case of urate oxidase, the detection of two radical species in the enzyme-substrate complex under anaerobic conditions suggests an initial monoelectron activation of the bound substrate dianion, without participation of dioxygen, resulting in a urate radical monoanion and an enzyme-H• (radical-) state.¹²⁶ Subsequent dioxygen activation is thought to occur via single electron transfer from the enzyme radical to form the superoxide anion radical. However, as in our study, spin trapping of superoxide or other oxygen radicals failed, suggesting that superoxide, if produced during the enzymatic reaction, is not released from the enzyme. In order to detect possible radical species formed during the Hod reaction, our coworker S. Thierbach of the Münster group used the spin probe CMH for a spectroscopic analysis.¹⁰⁷ Under our assay conditions CMH does not react with H₂O₂ or with the organic hydroperoxide that may escape from the enzymatic reaction. Significant amounts of CM• were formed during the reaction when the mutant protein HodC-W160A was the catalyst, but not during HodC-catalyzed conversions, suggesting that wild-type protein efficiently shields its active site, whereas the mutant protein may have a more open or more flexible active-site pocket and/or a slower decaying intermediate state.

CMH oxidation was not detected in anoxic mixtures of enzyme and substrate, arguing against the possibility of initial S^\bullet production by the enzyme. The observation that CMH oxidation only occurs during the ongoing Hod reaction also indicates that the enzyme is not able to directly activate the organic substrate (or dioxygen). This hypothesis is supported by EPR studies on the anoxic complex of HodC and MHOQ, which – in contrast to the anoxic urate oxidase-urate complex – did not reveal any radical species.

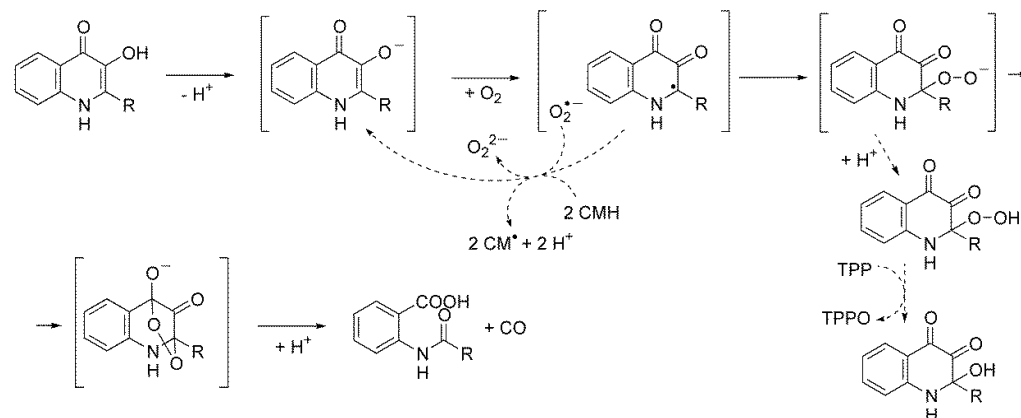
The observed exact stoichiometry of 1 H_2O_2 formed from the oxidation of 2 CMH does hardly conform to a possible reaction pathway via a peroxy radical intermediate, but rather supports the hypothesis of 1:1 formation of substrate radical S^\bullet and superoxide radical $O_2^{\bullet-}$ in the Hod reaction. Based on our analysis of redox potentials, sequential transfer of two electrons from two CMH to the substrate and via the substrate as an electron relay to superoxide appears most plausible not requiring the independent approach of two CMH to both initial radicals.

The [substrate radical - superoxide anion radical] pair formed by direct electron transfer from the enzyme-bound substrate anion to dioxygen requires that the Hod-bound substrate anion itself activates dioxygen by single electron transfer (Scheme 5-1). This view is again supported by the CV results which indicate that the substrate mono- and dianions have sufficient low potentials to thermodynamically allow electron transfer to oxygen. In the protein, the substrate anion, deprotonated at its 3-OH by H251, is hydrogen bonded with its N1 proton to the carbonyl oxygen of W36, which additionally facilitates the delivery of an electron from substrate anion to dioxygen. Considering the close proximity of substrate to oxygen in the active site pocket of Hod (as suggested by distances of 2.51 and 2.63 Å of a chloride mimic to the substrate's C2 and C4 atoms, respectively), the transfer appears to be kinetically feasible.

Recombination of the [substrate radical - superoxide radical] pair has been suggested to yield a C2-peroxide anion (Scheme 5-1), which presumably is stabilized by the “oxyanion hole” of the α/β -hydrolase fold of Hod. When using the non-physiological substrate BHOQ, trace amounts of organic hydroperoxide indeed were released from the Hod reaction, as indicated by the oxidation of TPP to TPPO. Identification of the alcohol produced from the reaction of the hydroperoxide with TPP as 2-butyl-2-hydroxy-1,2-dihydroquinoline-3,4-dione verified that hydroperoxide formation had occurred at C-2 of the substrate (Scheme 5-1). In the Hod reaction, subsequent intramolecular attack of the C2-peroxide anion at the C4 carbonyl forms

an endoperoxide (anion) that collapses to the reaction products carbon monoxide and *N*-acylanthranilic acid (Scheme 5-1).

In summary, data support the hypothesis that a major role of Hod, besides activating the substrate by general base catalysis and besides stabilizing transition states along the reaction pathway by electrostatic interactions and hydrogen bonding, is to provide an environment that facilitates electron transfer from the substrate anion to dioxygen. We conclude that the cofactor-independent 1*H*-3-hydroxy-4-oxoquinoline 2,4-dioxygenase Hod is a “substrate-assisted oxygenase”, which utilizes the intrinsic reactivity of its enzyme-bound substrate anion towards electrophiles for dioxygen activation .



Scheme 5-1. Proposed Reaction Pathway of the Hod-catalyzed 2,4-Dioxygenolysis of 2-Alkyl-3-hydroxy-4(1*H*)-quinolones, and Side Reactions of Intermediates.^a

^a R = H, *n*-alkyl (C1 to C9). Brackets indicate enzyme-bound reaction intermediates. The italicized numbers refer to equations defined in the results section.¹⁰⁷

Detection of oxidative intermediates and mechanistic implication for Quercetinase

In contrast to Hod, quercetinase is a metal-dependent enzyme that catalyzes the 2,4-dioxygenolytic cleavage of flavonol quercetin (3,5,7,3',4'-pentahydroxyflavone) to 2-protocatechuoyl-phloroglucinol carboxylic acid and release of carbon monoxide. In this work we focused on the catalytic pathway of 2,4-QueD from *Streptomyces* sp. Strain FLA, particularly to address the question of possible radical intermediate states. For this question, cyclic hydroxylamine CMH was used in an analogous approach as for Hod to monitor presence of oxidizing radical species. While the enzyme preparation and biochemical characterization was done by the group in Münster, our work dealt with the redox studies of flavonol substrates, testing the formation of intermediate radicals by using CMH redox spin probe and addressing the role of the metal-center in the catalytic process by looking at changes in metal oxidation

state or spin state in EPR spectra. It is noted that some of the EPR experiments were becoming more complicated by the observed metal promiscuity of QueD and the incomplete occupancies of the metal binding sites.

The importance of studying the redox properties of substrates by voltammetry arises from the fact that substrate activation is always involved in several possible mechanistic steps, particularly in the first oxidation step of substrate. Therefore, this knowledge is essential to understand possible redox processes in the enzyme-catalyzed reaction. The redox properties of the main flavonol substrate quercetin as well as three related substrates with a different number of attached or modified hydroxyl-groups were characterized by cyclic voltammetry. CVs of quercetin showed three oxidation peaks (I, II, III), in which only the first peak exhibits a reversible character corresponding to the first redox couple $\text{Quer}^\bullet/\text{Quer}$, which actually should be the relevant redox couple in the enzyme reaction. However, in the large potential window the first electron transfer loses its reversibility by being further oxidized at higher potential (peak II). In the physiological pH range, the midpotential E_{mid} of redox couple $\text{Quer}^\bullet/\text{Quer}$ is dependent on pH with a shift of -48 mV per pH unit. For other substrates myricetin, rhamnetin and 3-hydroxyflavone, redox potentials of the first electron transfer were also observed that are all pH dependent. Among these flavonols, myricetin exhibits the highest oxidative property as indicated by the smallest E_{mid} value of the first redox pair which is probably the reason for the strong EPR background of CM^\bullet signals in the oxidic controls.

For the ESR experiments we used, besides trials with classical spin traps (e.g. DEPMPO), mainly the redox activated CMH to search for formation of possible intermediate radicals in the catalytic reaction of 2,4-QueD. In addition, low temperature EPR was performed to observe changes in metal oxidation or spin state of the metal-center of various wild type QueD enzymes containing mainly Fe, Mn, Ni and Co in the active site. Several protein variants, E76H, I66A and Y117A with different metal occupation were also examined, which were produced by the Münster group according to functional considerations derived from the preliminary crystal structure of Ni-QueD (data not published, performed and supplied by H.Dobbek's group).

In the attempt to detect oxidizing species formed during the QueD reaction with CMH, apart from Co and Ni, no radical formation was observed for Fe, Mn substituted QueD. Low temperature EPR spectra of Fe-QueD showed some changes in the intensity of high-spin ($S=3/2$) Fe^{3+} signal with the sequentially addition of quercetin substrate and oxygen, which mostly

related to the autoxidation of Fe^{3+} and relaxation effects caused by the paramagnetism of oxygen, but was not at all related to the divalent Fe^{2+} active center. In this respect, reexamination of Fe-QueD reaction by spectrophotometry indeed confirmed that Fe-QueD is not active. In case of Ni-QueD no low temperature EPR signals indicative of paramagnetic Ni species (Ni^{1+} , Ni^{3+}) formed by a valence change during reaction were observed giving spectra only containing signals of accompanying trace metals of Fe^{3+} , Cu^{2+} and Mn^{2+} . In contrast to Mn that delivered preliminary low values for turnover number, specific activity and a very low occupancy, the active Ni-enzymes showed a rather high specific activity and apparent kinetic constant for quercetin. Nevertheless, only a minimal production of oxidizing species in the Ni-enzyme could be detected by CMH suggesting a very fast reaction kinetics, in which the transient radicals formed immediately reacted away locally in the active site of enzyme, and/or an efficient tight pocket obstructed any interaction with CMH.

For Co-substituted enzymes, significant spectral changes of high spin ($S=3/2$) Co^{2+} species with sequential addition of quercetin substrate and oxygen were observed for all samples, wild type and variants E76H, I66A, Y117A at low temperature. For wild type Co-QueD, the changes resemble those previously reported by our group, for which a high-spin ($S=3/2$) Co^{2+} -species was assigned to the active site, and the spectral changes to binding of substrate and conversion to bound product based on the analysis of six different hyperfine patterns with up to eight lines arising from the nuclear spin of $I=7/2$ for Co^{2+} . A valence state change was not observed for wt- Co^{2+} -QueD. An important finding for the available E76H variant was the appearance of an organic radical in the anoxic mixture with quercetin substrate. The unusual properties of this organic radical with respect to microwave (mw) power and temperature, it vanished above 70K and increased in intensity with higher mw power, can only be explained by an interaction and energy exchange effect with a fast relaxing paramagnetic species in the vicinity of the radical. This strongly indicates that the organic radical has to be located close to the Co^{2+} -ion or may even be attached to it. However, this organic radical was not observed in the two variants I66A and Y117A, and also varied considerably in intensity for different preparation batches of Co-QueD-E76H. This restricted its further analysis by additional techniques such as high frequency EPR and other high resolution techniques. Spectral simulation of the organic radical signal disclosed of two possibilities: (i) two independent radicals are present or (ii) two radicals couple to a spin system of $S=1$, which may include the Co^{2+} -center or at least interact with it. The experiments with Co-QueD- E76H clearly show the involvement of the organic radical in the reaction of quercetin. Whether the formation of the organic

radical is a general rule and is also valid for the other variants I66A and Y117A remains unclear at present. It may well be, that the variation of a glutamate ligand of Co^{2+} (E76) to histidine creates a ligation sphere which enables the stabilization of the organic radical as a special case only for this variant whereas the other variants with amino acid variation close to but not at the Co-center do not necessarily form such persistent radical.

Significant amounts of CM^\bullet were formed in the reaction of Co-variants E76H, I66A and Y117A which gave clear evidence for presence of oxidizing species, but only very little signal was found during conversion by wt-QueD. This suggests that the wild type protein controls the reaction perfectly by shielding the active site against any interaction with CMH, whereas the mutant proteins I66A and Y117A may have a more open flexible and therefore better accessible active-site pockets. According to the available crystallographic data of Ni-QueD, substitution of amino acids tyrosine Tyr117 and isoleucine Ile66 by the less bulky alanine residues may indeed play an important role for access and accommodation of substrate in the active site. The Co-site is only little affected by these substitutions as seen from the similarity of low temperature EPR patterns to the wild type Co-QueD. In contrast, the mutation E76H concerns the Co-ion directly and this new 4-histidine ligation induces clear changes in the symmetry of the Co-EPR signals. Most probably, this alteration in ligation also changes the interaction of the Co-center with the substrate which eventually leads to the stabilization of the organic radical at low temperature. Its detailed structure remains elusive to date in absence of further spectroscopic or crystallographic data. The stabilized radical in Co-QueD-E76H and the modification of interaction with CMH for the Y117A and I66A variants are responsible for the detection of oxidizing intermediates making up to 10% of the maximally possible substrate conversion for the E76H variant and still well detectable 1.9% in case of Y117A and I66A variants.

Under anoxic condition Co-QueD-E76H and quercetin represent the ES complex which is characterized by the formed organic radical. Nitroxide released from donors mimics the action of oxygen and also quenches the radical immediately. For prolonged reaction times Co^{2+} -EPR spectra exhibit very similar changes as found for the reaction with oxygen. A nitrosylated product as an independent proof for the ongoing reaction with NO has not yet been isolated. Kinetic experiments releasing NO in presence of CMH in solution turned out to be very complex due to multiple redox reaction possibly occurring between several reactants, so that an interpretation is hampered and needs more detailed approaches.

The organic radical present in the (anoxic) ES complex is very likely the oxidative species which leads to slow formation of CM-radicals and finally to a dead-end state of the Co-QueD-E76H enzyme as deduced from the strict correlation of CM[•] formation to limited enzyme or CMH concentration in excess of substrate. The essential properties of the organic radical can be summarized: (i) it is always found in CoQueD-E76H variant with batch dependent intensities, (ii) it is rapidly lost in presence of oxygen and nitroxide, (iii) for the Y117A- and I66A-variant and the Co wt-protein no traces are observed, and (iv) no signal is detected in Ni-enzymes (wt and variants). Because CM[•] formation as a monitor for presence of a reactive oxidizing species was strictly dependent on the presence of both the quercetin substrate and O₂ in Co-QueD Y117A- and I66A-variants and to a much lower extent in wt Co-QueD and Ni-QueD, the reaction pathways should differ to some extent between Co-QueD-E76H and the Y117A- and I66A-variants. A schematic summary of the proposed mechanism for *Streptomyces* QueD with the two ligation states 3His/1Glu and 4His of the central metal ion is presented in Figure 5-2 including the structural proposal adapted from reference⁷¹.

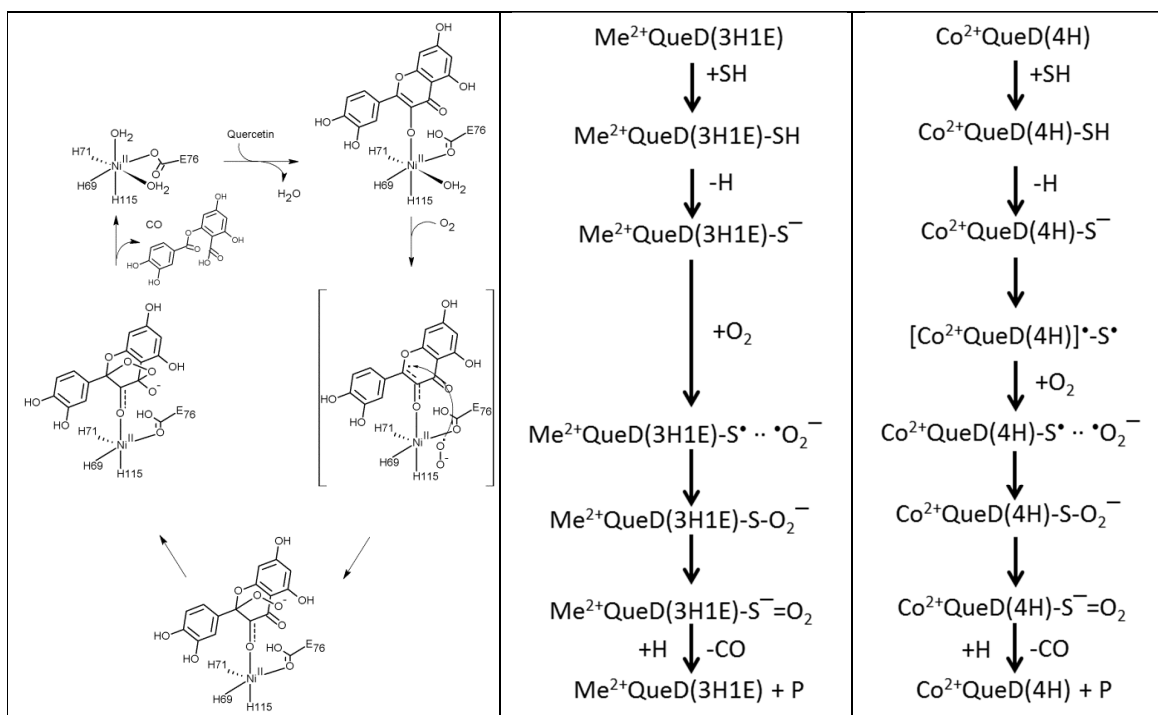


Figure 5-2. Proposed reaction mechanism of wild-type QueD protein and QueD-E76H. (3H1E) and (4H) denote the 3His/1Glu and 4His-ligand sphere, respectively; the organic substrate quercetin is abbreviated as SH, and Me²⁺ stands for Ni and Co ions.

As shown in the crystal structure of the NiQueD-quercetin complex under anoxic conditions the initial step of the reaction involves ES complex formation without the presence of mole-

cular oxygen. The glutamine E76 is found in a position allowing to deprotonate the 3-OH group of quercetin, and the significantly decreased catalytic activity of the NiQueD-E76H and CoQueD-E76H proteins is strongly supporting its essential catalytic function. Because the reaction of triplet oxygen with singlet substrate is a spin-forbidden process, activation of O₂ is the critical reaction step. Polarization of the substrate by the metal ion and lowering of the substrate's redox potential within the microenvironment of the binding site may facilitate single electron transfer from the organic substrate to O₂ which results in an [S[•]- O₂^{•-}] radical pair. Evidence for radical formation during catalysis is obtained for CoQueD-Y117A and -I66A variants from oxidation of CMH, which also occurs in the CoQueD wt and NiQueD forms, albeit at a very low level hardly detectable. Just before this oxygen activation step, modification of the ligand sphere in CoQueD-E76H has an additional impact of the activation of substrate in the ES complex in absence of oxygen producing a magnetically coupled pair probably located on substrate and the metal-ligand complex. From here, oxygen is then activated so that an intermediate peroxide is subsequently collapsing to the endoperoxide which breaks down to carbon monoxide and 2-protocatechuoyl-phoroglucinol carboxylic acid.

Based on the generation of CM[•] signals by oxidative species, the mechanism suggested for Co²⁺ and Ni²⁺ substituted QueD with 3His/1Glu ligation basically resembles that of the cofactor-independent 1*H*-3-hydroxy-4-oxoquinaldine dioxygenase (Hod). From spectroscopic and biochemical data this enzyme was characterized as a “substrate-assisted” dioxygenase, for which the catalytic reaction proceeds via a radical mechanism initiated by single electron transfer (SET) from the enzyme-bound substrate anion to O₂ for its activation and to form a radical pair (Thierbach *et al.*, 2014¹⁰⁷). Because no change in valence state is observed for QueD, the metal is proposed not to directly participate in SET but may help to stabilize both reactants, substrate and oxygen, and to support SET by polarization of substrate and possibly lowering its redox potential. An interesting aspect on the role of the metal ion arises from a comparison of the pH dependent redox behavior of quercetin and Hod substrate. Over the pH range the midpoint potential of quercetin is at least 150 mV higher than for Hod substrate, which implies that the thermodynamic driving force for reduction of oxygen to superoxide, i.e. the activated reactive species, is less pronounced. This is schematically visualized in Figure 5-3. For an assumed local effective pH of about 12 in the active site pocket the potential difference for reduction of O₂ by deprotonated Hod⁻ substrate is about 380 mV but only 140 mV for quercetin (quer⁻) as indicated by the black and red arrows. It appears plausible that, besides orientation of substrate and oxygen, an important function of the metal ion is to assist

activation of substrate by sufficiently lowering the redox potential for effective transfer of an electron onto oxygen. Considering the high reactivity of quercetin towards O_2 in presence of a base catalyst in model system studies (Balogh-Hergovich and Speier, 2001¹³⁸) and the presence of radical intermediate states, substrate-mediated oxygen activation could be proposed also for the quercetinase reaction. In terms of activity, the ranking Ni>Co>Mn indicates that the Ni ion is optimal for *Streptomyces* QueD and may be the preferred metal for the wild type enzyme.

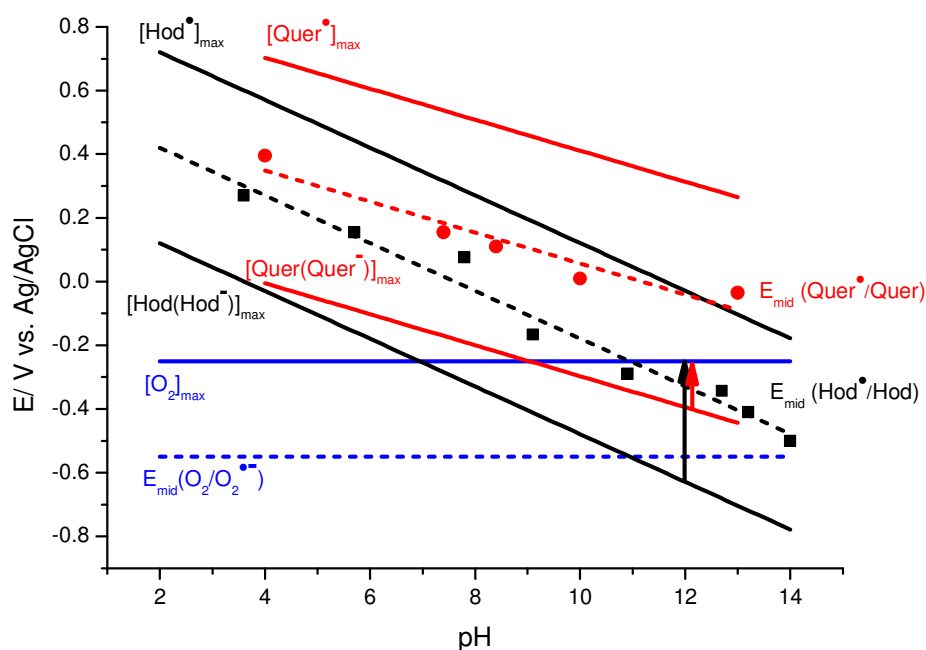


Figure 5-3. pH-dependence of the mid-peak potentials E_{mid} (vs. Ag/AgCl) of Hod substrate (black squares) and quercetin substrate (red dots). The derived mid-peak potentials E_{mid} of these substrates were fit with a linear function (black and red dashed lines). The black (Hod) and red solid lines (quercetin) correspond to the potential change induced by a 10^5 -fold excess of the reduced or oxidized species as calculated from the Nernst equation ($[Hod\bullet]_{max}$ and $[Quer\bullet]_{max}$ indicate the one electron oxidized radical species, $[Hod(Hod\bullet)]_{max}$ and $[Quer(Quer\bullet)]_{max}$ stand for the deprotonated reduced substrates Hod and quercetin. The mid-peak potential of $O_2/O_2\bullet^-$ and the potential change for excess oxygen are given in blue. The black arrow visualizes the driving force for the electron transfer from $Hod\bullet$ to O_2 , and the red arrow from $Quer\bullet$ to O_2 .

A drastic change in the coordination sphere of the Co^{2+} ion in case of Co-QueD-E76H with 4 ligating histidines is not only lowering the enzyme activity significantly compared to the wild type, but also seems to modify the mode of activation as derived from the formation of the organic radical signal and the slow oxidation of CMH in the anoxic ES complex. In this case a radical associated to the enzyme is formed (cf. Figure 5-2 right panel) so that probably a

magnetically coupled system is developing which interacts with the Co^{2+} -ion in a fast relaxation mode. Further details of the structure of the radical system were not resolvable due to its complex behavior being accessible only at very low temperatures and concentration. The inserted mechanistic step of an enzyme based radical state is reminiscent of urate oxidase enzyme, in which the two intermediate radical species were detected in the enzyme-substrate complex under anaerobic conditions. In this context, it may be speculated for Co-QueD-E76H that the enzyme based electron is dislocated from the substrate to one or several histidines. From a spectroscopic point of view such an activated complex in the vicinity of a paramagnetic metal ion is an interesting and novel but intricate object for detailed analysis.

APPENDIX

Oxidation-reduction method using potassium permanganate to standardize H₂O₂ concentration

Preparation:

Add 7.5 mL of stock H₂O₂ solution (e.g., ACS reagent, stabilized 30 wt % in water) to a 2 L volumetric flask, dilute to volume with deionized water, and mix well. The target concentration of H₂O₂ in this solution is 1000 mg/L.

Potassium permanganate solution (0.1 N): Dissolve 3.2 g of KMnO₄ in 400 to 600 mL of deionized water placed in a 1 L volumetric flask. Adjust the volume to the mark.

Sulfuric acid solution: Slowly add 50 mL of concentrated sulfuric acid (density, 1.84 g/mL) to 450 mL of demineralized water placed in a 1 L beaker. Continuously stir during the process and then allow the solution to cool.

Procedure:

Using measuring cylinders, add 10 mL of sulfuric acid solution and 50 mL of deionized water to a 250 mL Erlenmeyer (or conical) flask. Pipette 10.0 or 50 mL of H₂O₂ stock solution into the flask and titrate drop-wise with solution potassium permanganate (0.1 N) to the appearance of a faint permanent pinkness (initially, the pinkness of added permanganate will fade in the initial phase of titration, but it appears at the end point).

Calculate the weight concentration of H₂O₂ in the stock solution using the following formula:

$$[H_2O_2]_{stock} = \frac{T_{MnO_4} \times N_{MnO_4} \times 17 \times 1000}{V_{stock}} \left(\frac{mg}{L} \right)$$

In this formula, T_{MnO_4} is the volume of potassium permanganate titrant (in milliliters), N_{MnO_4} the normality of potassium permanganate titrant (nominally 0.1 N), and V_{stock} the volume of stock solution of H₂O₂ subject to titration (in milliliters).

For 10-mL and 50-mL aliquots of H₂O₂ stock solution, the above formula can be rewritten as:

$$\text{For a 10-mL aliquot } [H_2O_2]_{stock} = 1700 \times T_{MnO_4} \times N_{MnO_4} \left(\frac{mg}{L} \right)$$

$$\text{For a 50-mL aliquot } [H_2O_2]_{stock} = 340 \times T_{MnO_4} \times N_{MnO_4} \left(\frac{mg}{L} \right)$$

Additionally, the concentration of KMnO_4 solution was quantitatively determined by the oxidation-reduction reaction with sodium oxalate. The titration is carried out in acid medium.



Procedure

Preparation of 1000 mL of 0.1 N KMnO_4 solution:

Weigh out approximately the appropriate amount of potassium permanganate (3.2 g, mol. wt. 158.0 g/mol) using a watch-glass. Transfer into a 250-mL beaker containing water and stir thoroughly breaking up the crystals with a glass-rod for effective solution. Allow to stand for at least 2 days. Filter the solution through a small plug of glass-wool supported in a funnel, into a 1 L volumetric flask, leaving the un-dissolved residues in the beaker and repeat the process several times until all the potassium permanganate has dissolved. Fill the solution up to the graduation mark by addition of water, and shake well to ensure thorough mixing, store in a dark container.

Standardization

Accurately weigh 0.2 g of anhydrous sodium oxalate (mol. wt. 134 g/mol) previously dried to 110°C about 1 hour and dissolve it in 100 mL of water, add 7 mL of sulfuric acid (99.999% wt, Aldrich-Sigma, density 1.84 g/ml) and heat to about 70°C . Then slowly add the permanganate solution from the burette with a constant shaking. The first few drops result in a pink color persisting for about 20 seconds. Wait until the color disappears and then continue the titration in the usual manner. The end point is reached when a faint pink color persists for about 30 seconds upon shaking the flask. Note that the temperature of the medium should not be less than 60°C throughout the titration. Record the volume of KMnO_4 solution used and calculate the normality using the following equation:

$$N \times V = \frac{\text{wt.}}{\text{eq.wt.}} \times 1000$$

where N is the normality of KMnO_4 solution to be calculated, V the volume of KMnO_4 solution used (in mL), wt. the weight of sodium oxalate (in g), eq. wt. the equivalent weight of sodium oxalate (67).

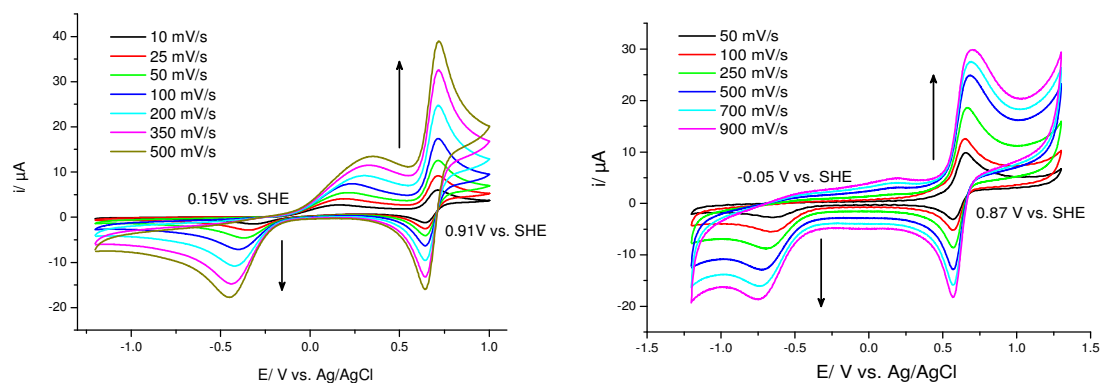


Figure A 1. CVs of scan rate variation of CMH (2 mM) (left panel) and CPH (1 mM) (right panel) in PB (50 mM, pH 7). Color codes define the scanning speed. The arrows show the increase of currents (oxidation and reduction) with increasing scan rate.

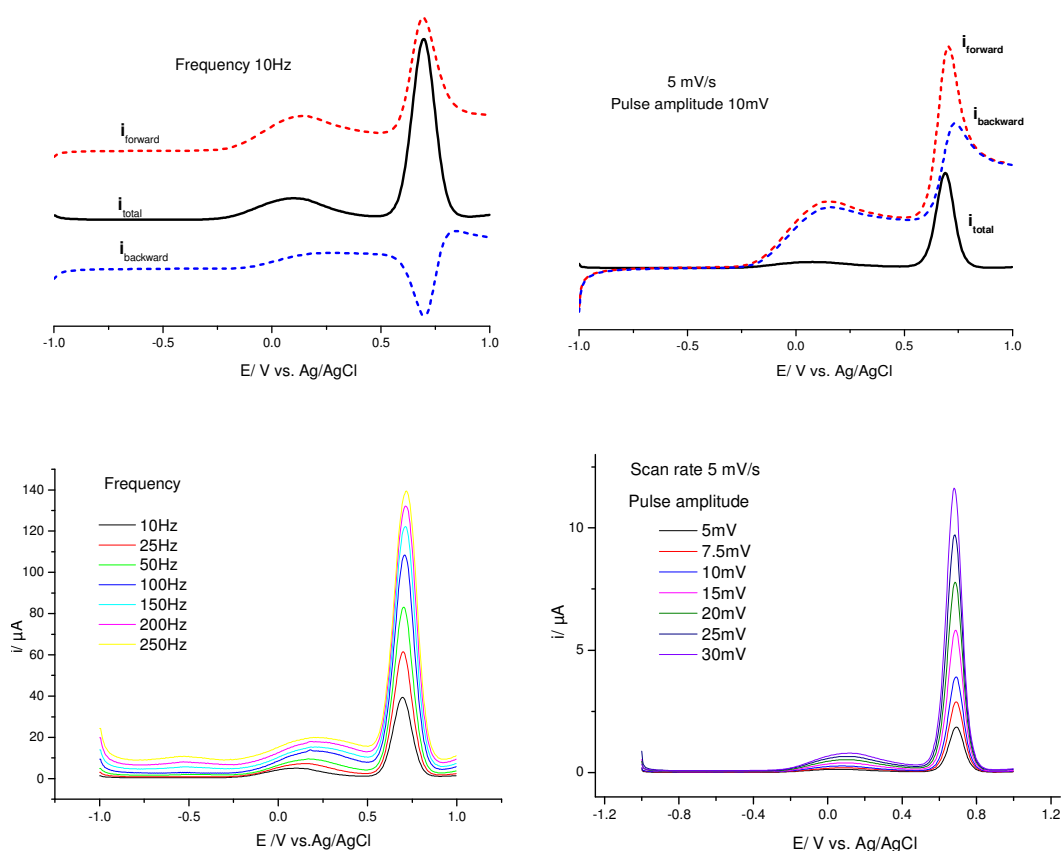


Figure A 2. Square wave (upper left) and differential pulse voltammograms (upper right panel) of CMH (2 mM) in PB (50 mM, pH 7.4). Frequency variation of SWV and pulse amplitude variation of DPV are shown in lower left and right figures, respectively. Parameters were set to pulse width 50 ms, scan rate 5 mV/s for DPV and amplitude 50 mV, step height ΔE 5 mV for SWV measurements. The frequency and pulse amplitude are identified in figure legends.

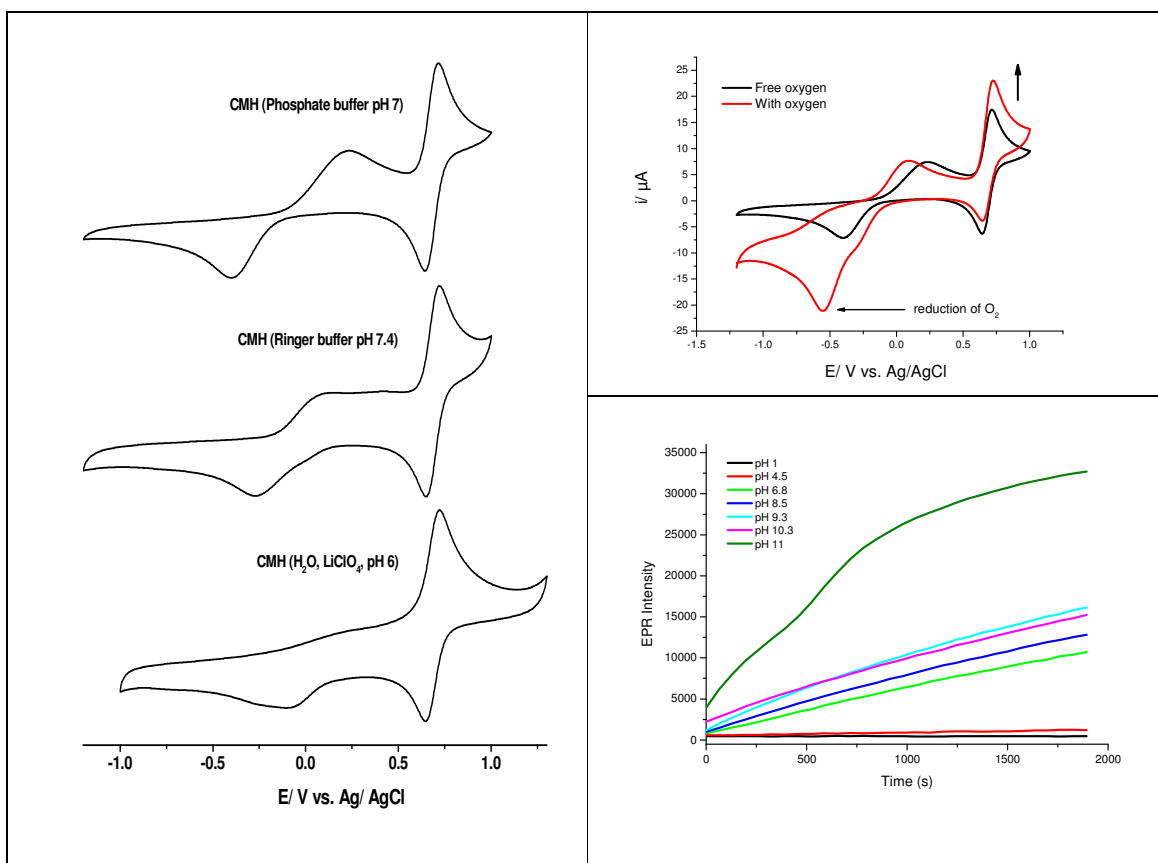


Figure A 3. The influence of solvent on the redox reactions of CMH (left panel). The first electron transfer $\text{CM}^\bullet/\text{CMH}$ is affected by changing the solvent from phosphate buffer to ringer buffer or water solution (with LiClO_4 as supporting electrolyte), while the second transition $\text{CM}^+/\text{CM}^\bullet$ remains unchanged. The upper right panel shows the effect of dissolved oxygen on the CV of CMH, in which an additional peak was observed in the red line (oxygen is present) with respect to the reduction of oxygen (about -0.5 V vs. Ag/AgCl). In addition, the black arrow shows the increase of second oxidation current that is associated to the regeneration of CM^\bullet by reaction of CM^+ and superoxide $\text{O}_2^{\bullet-}$ (formed by oxygen reduction). CVs were recorded in different solvents of CMH (2 mM) at 100 mV/s scan rate. The lower right panel shows the effect of pH on CMH oxidation. As seen in the figure, the CM^\bullet formation can be divided in pH regions, low (<4.5), neutral (6~10) and high pH (≥ 11). In presence of oxygen, and with increasing pH, the background formation of CM^\bullet clearly increases which can be explained by pH dependence of CMH oxidation with respect to Haber-Weiss- and Fenton-type reactions. The assay contains CMH (2 mM) in the presence of O_2 . Color code identifies the pH of solution. Parameters were set at modulation amplitude 0.2 G and microwave power 0.63 mW.

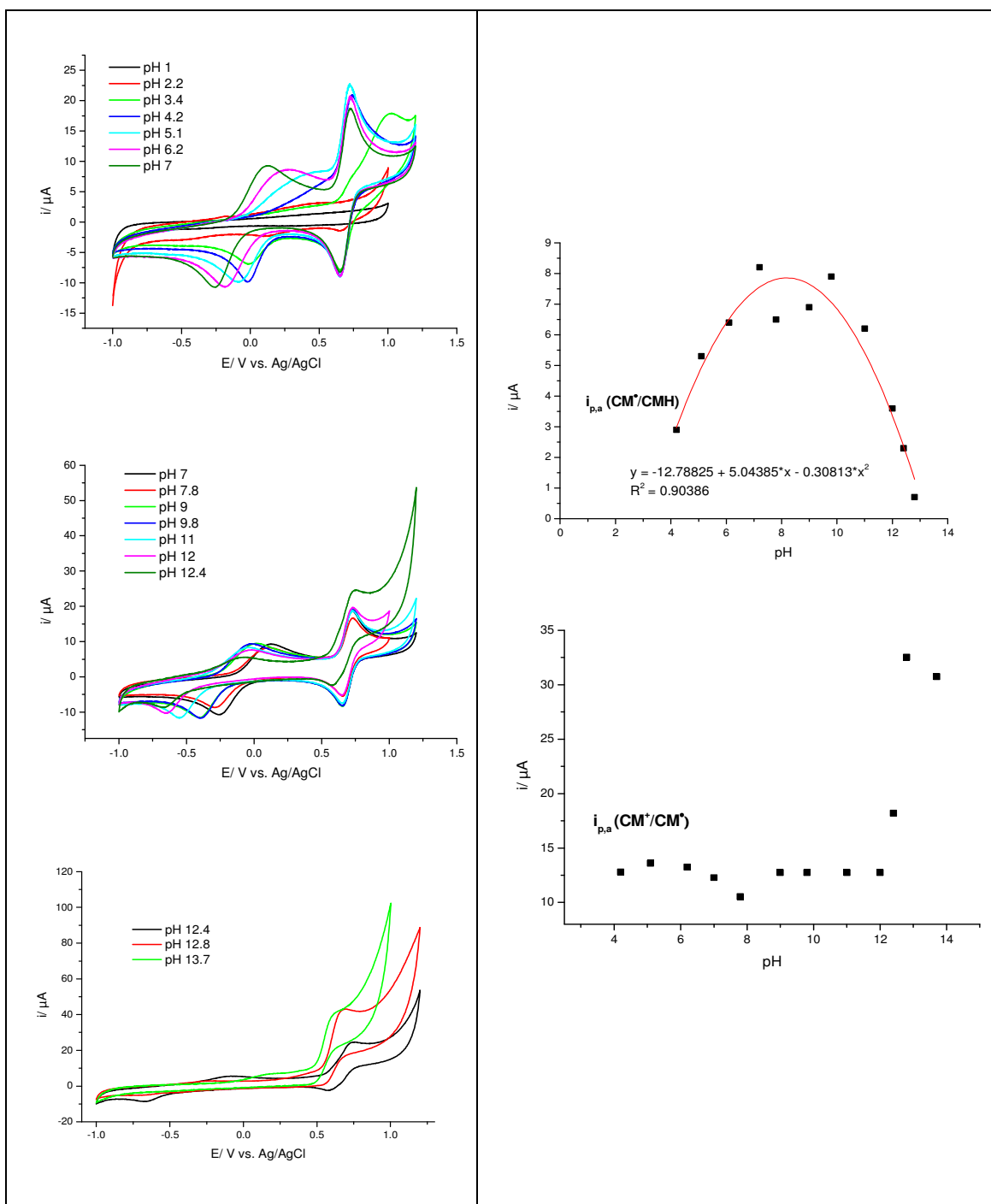


Figure A 4. The left figures show CVs of CMH (2 mM) in different pH solutions (pH 1 – 14). The right figures describe the pH dependence of oxidation currents of transition I (upper) and II (lower), derived from CVs on the left. Color codes identify the pH of solution. CVs were recorded at 100 mV/s scan rate.

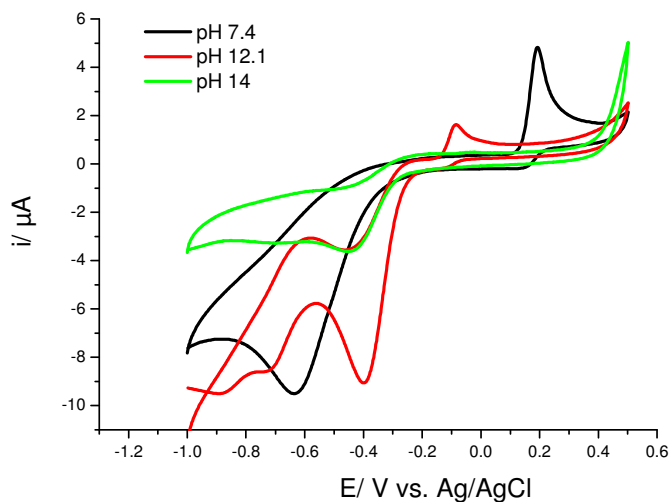


Figure A 5. pH dependence of redox reaction of MHOQ substrate. CVs show the first oxidation peak of MHOQ (0.4 mM) in solutions (pH 7.4, 12.1, 14) with oxygen (O_2) present. As pH increased, the negative shift in potential of the oxidation peak displays the pH dependence, while the diminishing in current confirmed the substrate reaction with O_2 . At high pH substrate is consumed in the chemical reaction with oxygen leading to a loss of current intensity (pH 12, red line) or even a complete vanishing at extreme pH (pH 14, green line). The reduction peak of O_2 (around -0.6 V) was found on the reverse scan at pH 7.4 (black line) but drastically reduced and slightly shifted to more negative at higher pH (12.1 and 14) (red and green lines); meanwhile, a new reduction peak (-0.4 V) appeared at pH 12.1 that might be associated with the formation of oxidized species from reaction of substrate and O_2 , either the oxidized substrate or the bound [substrate-oxygen]. Further experiments are required to confirm this hypothesis. Inset indicates the pH of solution.

REFERENCES

-
- ¹ D'Autreaux, B., and Toledano, M. B. (2007) ROS as signalling molecules: mechanisms that generate specificity in ROS homeostasis, *Nature reviews. Molecular cell biology* 8, 813-824.
- ² Muller, F. (2000) The nature and mechanism of superoxide production by the electron transport chain: Its relevance to aging, *AGE* 23, 227-253.
- ³ Han, D., Williams, E., and Cadenas, E. (2001) Mitochondrial respiratory chain-dependent generation of superoxide anion and its release into the intermembrane space, *Biochemical Journal* 353, 411-416.
- ⁴ Brieger, K., Schiavone, S., Miller, F. J., Jr., and Krause, K. H. (2012) Reactive oxygen species: from health to disease, *Swiss medical weekly* 142, w13659.
- ⁵ Krause, K. H., and Bedard, K. (2008) NOX enzymes in immuno-inflammatory pathologies, *Seminars in immunopathology* 30, 193-194.
- ⁶ Edens, W. A., Sharling, L., Cheng, G., Shapira, R., Kinkade, J. M., Lee, T., Edens, H. A., Tang, X., Sullards, C., Flaherty, D. B., Benian, G. M., and Lambeth, J. D. (2001) Tyrosine cross-linking of extracellular matrix is catalyzed by Duox, a multidomain oxidase/peroxidase with homology to the phagocyte oxidase subunit gp91phox, *The Journal of Cell Biology* 154, 879-892.
- ⁷ Finkel, T. (2011) Signal transduction by reactive oxygen species, *J Cell Biol* 194, 7-15.
- ⁸ Wyche, K. E., Wang, S. S., Griendling, K. K., Dikalov, S. I., Austin, H., Rao, S., Fink, B., Harrison, D. G., and Zafari, A. M. (2004) C242T CYBA polymorphism of the NADPH oxidase is associated with reduced respiratory burst in human neutrophils, *Hypertension* 43, 1246-1251.
- ⁹ Gavazzi, G., Banfi, B., Deffert, C., Fiette, L., Schappi, M., Herrmann, F., and Krause, K. H. (2006) Decreased blood pressure in NOX1-deficient mice, *FEBS letters* 580, 497-504.
- ¹⁰ Qin, B., Cartier, L., Dubois-Dauphin, M., Li, B., Serrander, L., and Krause, K. H. (2006) A key role for the microglial NADPH oxidase in APP-dependent killing of neurons, *Neurobiology of aging* 27, 1577-1587.
- ¹¹ Zhang, Y., Dawson, V. L., and Dawson, T. M. (2000) Oxidative stress and genetics in the pathogenesis of Parkinson's disease, *Neurobiology of disease* 7, 240-250.
- ¹² Dhalla, N. S., Temsah, R. M., and Netticadan, T. (2000) Role of oxidative stress in cardiovascular diseases, *Journal of hypertension* 18, 655-673.

-
- ¹³ Sorce, S., and Krause, K. H. (2009) NOX enzymes in the central nervous system: from signaling to disease, *Antioxidants & redox signaling* 11, 2481-2504.
- ¹⁴ Block, M. L., Zecca, L., and Hong, J. S. (2007) Microglia-mediated neurotoxicity: uncovering the molecular mechanisms, *Nature reviews. Neuroscience* 8, 57-69.
- ¹⁵ Waris, G., and Ahsan, H. (2006) Reactive oxygen species: role in the development of cancer and various chronic conditions, *Journal of Carcinogenesis* 5, 14-14.
- ¹⁶ Liao, D., Corle, C., Seagroves, T. N., and Johnson, R. S. (2007) Hypoxia-inducible factor-1alpha is a key regulator of metastasis in a transgenic model of cancer initiation and progression, *Cancer research* 67, 563-572.
- ¹⁷ Bartsch, H., and Nair, J. (2006) Chronic inflammation and oxidative stress in the genesis and perpetuation of cancer: role of lipid peroxidation, DNA damage, and repair, *Langenbecks Arch Surg* 391, 499-510.
- ¹⁸ Dikalov, S. I., and Harrison, D. G. (2014) Methods for detection of mitochondrial and cellular reactive oxygen species, *Antioxidants & redox signaling* 20, 372-382.
- ¹⁹ Dikalov, S. I., Dikalova, A. E., and Mason, R. P. (2002) Noninvasive diagnostic tool for inflammation-induced oxidative stress using electron spin resonance spectroscopy and an extracellular cyclic hydroxylamine, *Archives of biochemistry and biophysics* 402, 218-226.
- ²⁰ Zielonka, J., and Kalyanaram, B. (2010) Hydroethidine- and MitoSOX-derived red fluorescence is not a reliable indicator of intracellular superoxide formation: another inconvenient truth, *Free radical biology & medicine* 48, 983-1001.
- ²¹ Zhang, H., Joseph, J., Vasquez-Vivar, J., Karoui, H., Nsanzumuhire, C., Martasek, P., Tordo, P., and Kalyanaram, B. (2000) Detection of superoxide anion using an isotopically labeled nitron spin trap: potential biological applications, *FEBS letters* 473, 58-62.
- ²² Frejaville, C., Karoui, H., Tuccio, B., Moigne, F. L., Culcasi, M., Pietri, S., Lauricella, R., and Tordo, P. (1995) 5-(Diethoxyphosphoryl)-5-methyl-1-pyrroline N-oxide: A New Efficient Phosphorylated Nitron for the in Vitro and in Vivo Spin Trapping of Oxygen-Centered Radicals, *Journal of Medicinal Chemistry* 38, 258-265.
- ²³ Dikalov, S., Skatchkov, M., and Bassenge, E. (1997) Spin trapping of superoxide radicals and peroxynitrite by 1-hydroxy-3-carboxy-pyrrolidine and 1-hydroxy-2,2,6,6-tetramethyl-4-oxo-piperidine

and the stability of corresponding nitroxyl radicals towards biological reductants, *Biochem Biophys Res Commun* 231, 701-704.

²⁴ Dikalov, S., Griendling, K. K., and Harrison, D. G. (2007) Measurement of reactive oxygen species in cardiovascular studies, *Hypertension* 49, 717-727.

²⁵ Dikalov, S. I., Li, W., Mehranpour, P., Wang, S. S., and Zafari, A. M. (2007) Production of extracellular superoxide by human lymphoblast cell lines: comparison of electron spin resonance techniques and cytochrome C reduction assay, *Biochemical pharmacology* 73, 972-980.

²⁶ Dikalov, S. I., Kirilyuk, I. A., Voinov, M., and Grigor'ev, I. A. (2011) EPR detection of cellular and mitochondrial superoxide using cyclic hydroxylamines, *Free radical research* 45, 417-430.

²⁷ Dudley, S. C., Jr., Hoch, N. E., McCann, L. A., Honeycutt, C., Diamandopoulos, L., Fukai, T., Harrison, D. G., Dikalov, S. I., and Langberg, J. (2005) Atrial fibrillation increases production of superoxide by the left atrium and left atrial appendage: role of the NADPH and xanthine oxidases, *Circulation* 112, 1266-1273.

²⁸ Dikalov, S., Fink, B., Skatchkov, M., and Bassenge, E. (1999) Comparison of glyceryl trinitrate-induced with pentaerythrityl tetranitrate-induced in vivo formation of superoxide radicals: effect of vitamin C, *Free radical biology & medicine* 27, 170-176.

²⁹ Dikalova, A., Clempus, R., Lassegue, B., Cheng, G., McCoy, J., Dikalov, S., San Martin, A., Lyle, A., Weber, D. S., Weiss, D., Taylor, W. R., Schmidt, H. H., Owens, G. K., Lambeth, J. D., and Griendling, K. K. (2005) Nox1 overexpression potentiates angiotensin II-induced hypertension and vascular smooth muscle hypertrophy in transgenic mice, *Circulation* 112, 2668-2676.

³⁰ Piskernik, C., Haindl, S., Behling, T., Gerald, Z., Kehrer, I., Redl, H., and Kozlov, A. V. (2008) Antimycin A and lipopolysaccharide cause the leakage of superoxide radicals from rat liver mitochondria, *Biochimica et biophysica acta* 1782, 280-285.

³¹ Goldstein, S., Merenyi, G., Russo, A., and Samuni, A. (2003) The role of oxoammonium cation in the SOD-mimic activity of cyclic nitroxides, *J Am Chem Soc* 125, 789-795.

³² Bobko, A. A., Kirilyuk, I. A., Grigor'ev, I. A., Zweier, J. L., and Khramtsov, V. V. (2007) Reversible reduction of nitroxides to hydroxylamines: roles for ascorbate and glutathione, *Free radical biology & medicine* 42, 404-412.

-
- ³³ Ganini, D., Canistro, D., Jiang, J., Stadler, K., Mason, R. P., and Kadiiska, M. B. (2012) Ceruloplasmin (ferroxidase) oxidizes hydroxylamine probes: deceptive implications for free radical detection, *Free radical biology & medicine* 53, 1514-1521.
- ³⁴ Zhou, M., Diwu, Z., Panchuk-Voloshina, N., and Haugland, R. P. (1997) A Stable Nonfluorescent Derivative of Resorufin for the Fluorometric Determination of Trace Hydrogen Peroxide: Applications in Detecting the Activity of Phagocyte NADPH Oxidase and Other Oxidases, *Analytical Biochemistry* 253, 162-168.
- ³⁵ Jones, K. C. (1991) Contaminant trends in soils and crops, *Environmental pollution (Barking, Essex : 1987)* 69, 311-325.
- ³⁶ Wild, S. R., Harrad, S. J., and Jones, K. C. (1994) The influence of sewage sludge applications to agricultural land on human exposure to polychlorinated dibenzo-p-dioxins (PCDDs) and -furans (PCDFs), *Environmental pollution (Barking, Essex : 1987)* 83, 357-369.
- ³⁷ Perera, F. P. (1997) Environment and cancer: who are susceptible?, *Science* 278, 1068-1073.
- ³⁸ W. C. Evans (1968) The microbiological degradation of aromatic compounds, *J. gen. Microbiol.* 32, 177-184.
- ³⁹ Arora, P. K., Kumar, M., Chauhan, A., Raghava, G. P., and Jain, R. K. (2009) OxDBase: a database of oxygenases involved in biodegradation, *BMC research notes* 2, 67.
- ⁴⁰ Bugg, T. D. H. (2003) Dioxygenase enzymes: catalytic mechanisms and chemical models, *Tetrahedron* 59, 7075-7101.
- ⁴¹ Fetzner, S., and Steiner, R. A. (2010) Cofactor-independent oxidases and oxygenases, *Applied microbiology and biotechnology* 86, 791-804.
- ⁴² Hattori, S., and Noguchi, I. (1959) Microbial Degradation of Rutin, *Nature* 184, 1145-1146.
- ⁴³ Oka, T., and Simpson, F. J. (1971) Quercetinase, a dioxygenase containing copper, *Biochemical and Biophysical Research Communications* 43, 1-5.
- ⁴⁴ Krishnamurty, H. G., and Simpson, F. J. (1970) Degradation of Rutin by *Aspergillus flavus* : studies with oxygen 18 on the action of a dioxygenase on quercetin, *Journal of Biological Chemistry* 245, 1467-1471.
- ⁴⁵ Westlake, D. W. S., Roxburgh, J. M., and Talbot, G. (1961) Microbial Production of Carbon Monoxide from Flavonoids, *Nature* 189, 510-511.

-
- ⁴⁶ Oka, T., Simpson, F. J., and Krishnamurty, H. G. (1972) Degradation of rutin by *Aspergillus flavus*. Studies on specificity, inhibition, and possible reaction mechanism of quercetinase, *Canadian journal of microbiology* 18, 493-508.
- ⁴⁷ Hund, H. K., Breuer, J., Lingens, F., Huttermann, J., Kappl, R., and Fetzner, S. (1999) Flavonol 2,4-dioxygenase from *Aspergillus niger* DSM 821, a type 2 CuII-containing glycoprotein, *European journal of biochemistry / FEBS* 263, 871-878.
- ⁴⁸ Bauer, I., de Beyer, A., Tshisuaka, B., Fetzner, S., and Lingens, F. (1994) A novel type of oxygenolytic ring cleavage: 2,4-oxygenation and decarbonylation of 1H-3-hydroxy-4-oxoquinoline and 1H-3-hydroxy-4-oxoquinoline, *FEMS Microbiol. Lett.* 117, 299-304.
- ⁴⁹ Bauer, I., Max, N., Fetzner, S., and Lingens, F. (1996) 2,4-Dioxygenases catalyzing N-heterocyclic ring cleavage and formation of carbon monoxide. Purification and some properties of 1H-3-hydroxy-4-oxoquinoline 2,4-dioxygenase from *Arthrobacter* sp. Ru61a and comparison with 1H-3-hydroxy-4-oxoquinoline 2,4-dioxygenase from *Pseudomonas putida* 33/1, *European Journal of Biochemistry* 240, 576-583.
- ⁵⁰ Myers, R. W., Wray, J. W., Fish, S., and Abeles, R. H. (1993) Purification and characterization of an enzyme involved in oxidative carbon-carbon bond cleavage reactions in the methionine salvage pathway of *Klebsiella pneumoniae*, *The Journal of biological chemistry* 268, 24785-24791.
- ⁵¹ Wray, J. W., and Abeles, R. H. (1995) The methionine salvage pathway in *Klebsiella pneumoniae* and rat liver. Identification and characterization of two novel dioxygenases, *Journal of Biological Chemistry* 270, 3147-3153.
- ⁵² Cynthia G. Zoski, (2007) *Handbook of Electrochemistry*, 1st ed., Elsevier: Amsterdam, The Netherlands.
- ⁵³ J. Newman, C. W. Tobias (1967) *Advances in Electrochemistry and Electrochemical Engineering*, Ed., Wiley: New York, Vol. V.
- ⁵⁴ J. J. Lingane, (1958) *Electroanalytical Chemistry*, 2nd ed., Wiley: New York.
- ⁵⁵ <http://www.ceb.cam.ac.uk/research/groups/rg-eme/teaching-notes/introduction-403>.
- ⁵⁶ Zhang, L. L., and Zhao, X. S. (2009) Carbon-based materials as supercapacitor electrodes, *Chemical Society Reviews* 38, 2520-2531.
- ⁵⁷ https://en.wikipedia.org/wiki/Cyclic_voltammetry

-
- ⁵⁸ Wang, J. (2006) *Analytical Electrochemistry*, 3rd ed., Wiley: New Jersey.
- ⁵⁹ Ebsworth, E. A. V. (1991) *Structural methods in inorganic chemistry*, (Rankin, D. W. H., and Craddock, S., Eds.) 2nd ed. ed., CRC Press, Boca Raton, Fla.
- ⁶⁰ Kao, J. P. Y., Barth, E. D., Burks, S. R., Smithback, P., Mailer, C., Ahn, K.-H., Halpern, H. J., and Rosen, G. M. (2007) Very-Low-Frequency Electron Paramagnetic Resonance (EPR) Imaging of Nitroxide-Loaded Cells, *Magnetic resonance in medicine : official journal of the Society of Magnetic Resonance in Medicine / Society of Magnetic Resonance in Medicine* 58, 850-854.
- ⁶¹ www.epr.ethz.ch/news/Bordignon_tutorial_Nitroxide_spectrum_analysis.pdf.
- ⁶² Windle, J. J. (1981) Hyperfine coupling constants for nitroxide spin probes in water and carbon tetrachloride, *Journal of Magnetic Resonance (1969)* 45, 432-439.
- ⁶³ Kobayashi, M., and Shimizu, S. (1999) Cobalt proteins, *European journal of biochemistry / FEBS* 261, 1-9.
- ⁶⁴ Battersby, A. R. (1993) Biosynthesis of vitamin B12, *Accounts of Chemical Research* 26, 15-21.
- ⁶⁵ Smith, D. M., Golding, B. T., and Radom, L. (1999) Understanding the Mechanism of B12-Dependent Methylmalonyl-CoA Mutase: Partial Proton Transfer in Action, *Journal of the American Chemical Society* 121, 9388-9399.
- ⁶⁶ Bicknell, R., Hanson, G. R., Holmquist, B., and Little, C. (1986) A spectral study of cobalt(II)-substituted *Bacillus cereus* phospholipase C, *Biochemistry* 25, 4219-4223.
- ⁶⁷ Kennedy, F. C., Hill, H. A., Kaden, T. A., and Vallee, B. L. (1972) Electron paramagnetic resonance spectra of some active cobalt(II) substituted metalloenzymes and other cobalt(II) complexes, *Biochem Biophys Res Commun* 48, 1533-1539.
- ⁶⁸ Pang, H., Bartlam, M., Zeng, Q., Miyatake, H., Hisano, T., Miki, K., Wong, L. L., Gao, G. F., and Rao, Z. (2004) Crystal structure of human pirin: an iron-binding nuclear protein and transcription co-factor, *The Journal of biological chemistry* 279, 1491-1498.
- ⁶⁹ Sariaslani, F. S. (1989) Microbial enzymes for oxidation of organic molecules, *Critical reviews in biotechnology* 9, 171-257.
- ⁷⁰ Leitgeb, S., and Nidetzky, B. (2008) Structural and functional comparison of 2-His-1-carboxylate and 3-His metallocentres in non-haem iron(II)-dependent enzymes, *Biochemical Society transactions* 36, 1180-1186.

-
- ⁷¹ Fetzner, S. (2012) Ring-Cleaving Dioxygenases with a Cupin Fold, *Appl. Environ. Microbiol.* 78, 2505-2514.
- ⁷² Ryle, M. J., and Hausinger, R. P. (2002) Non-heme iron oxygenases, *Current opinion in chemical biology* 6, 193-201.
- ⁷³ Massey, V. (1994) Activation of molecular oxygen by flavins and flavoproteins, *The Journal of biological chemistry* 269, 22459-22462.
- ⁷⁴ Palfey, B., Ballou, D., and Massey, V. (1995) Oxygen Activation by Flavins and Pterins, In *Active Oxygen in Biochemistry* (Valentine, J., Foote, C., Greenberg, A., and Liebman, J., Eds.), pp 37-83, Springer Netherlands.
- ⁷⁵ Fetzner, S. (2002) Oxygenases without requirement for cofactors or metal ions, *Applied microbiology and biotechnology* 60, 243-257.
- ⁷⁶ Dierks, T., Dickmanns, A., Preusser-Kunze, A., Schmidt, B., Mariappan, M., von Figura, K., Ficner, R., and Rudolph, M. G. (2005) Molecular basis for multiple sulfatase deficiency and mechanism for formylglycine generation of the human formylglycine-generating enzyme, *Cell* 121, 541-552.
- ⁷⁷ Phillips, J. D., Whitby, F. G., Warby, C. A., Labbe, P., Yang, C., Pflugrath, J. W., Ferrara, J. D., Robinson, H., Kushner, J. P., and Hill, C. P. (2004) Crystal structure of the oxygen-dependant coproporphyrinogen oxidase (Hem13p) of *Saccharomyces cerevisiae*, *The Journal of biological chemistry* 279, 38960-38968.
- ⁷⁸ Steiner, R. A., Janssen, H. J., Roversi, P., Oakley, A. J., and Fetzner, S. (2010) Structural basis for cofactor-independent dioxygenation of N-heteroaromatic compounds at the alpha/beta-hydrolase fold, *Proceedings of the National Academy of Sciences of the United States of America* 107, 657-662.
- ⁷⁹ Sciarra, G., Kendrew, S. G., Miele, A. E., Marsh, N. G., Federici, L., Malatesta, F., Schimperna, G., Savino, C., and Vallone, B. (2003) The structure of ActVA-Orf6, a novel type of monooxygenase involved in actinorhodin biosynthesis, *European Molecular Biology Organization journal* 22, 205-215.
- ⁸⁰ Loening, A. M., Fenn, T. D., and Gambhir, S. S. (2007) Crystal Structures of the Luciferase and Green Fluorescent Protein from *Renilla reniformis*, *Journal of Molecular Biology* 374, 1017-1028.
- ⁸¹ Widboom, P. F., Fielding, E. N., Liu, Y., and Bruner, S. D. (2007) Structural basis for cofactor-independent dioxygenation in vancomycin biosynthesis, *Nature* 447, 342-345.

-
- ⁸² Grocholski, T., Koskiniemi, H., Lindqvist, Y., Mantsala, P., Niemi, J., and Schneider, G. (2010) Crystal structure of the cofactor-independent monooxygenase SnoaB from *Streptomyces nogalater*: implications for the reaction mechanism, *Biochemistry* 49, 934-944.
- ⁸³ Colloc'h, N., el Hajji, M., Bachet, B., L'Hermite, G., Schiltz, M., Prange, T., Castro, B., and Mornon, J. P. (1997) Crystal structure of the protein drug urate oxidase-inhibitor complex at 2.05 Å resolution, *Nature structural biology* 4, 947-952.
- ⁸⁴ Colloc'h, N., Gabison, L., Monard, G., Altarsha, M., Chiadmi, M., Marassio, G., Sopkova-de Oliveira Santos, J., El Hajji, M., Castro, B., Abraini, J. H., and Prange, T. (2008) Oxygen pressurized X-ray crystallography: probing the dioxygen binding site in cofactorless urate oxidase and implications for its catalytic mechanism, *Biophysical journal* 95, 2415-2422.
- ⁸⁵ Juan, E. C., Hoque, M. M., Shimizu, S., Hossain, M. T., Yamamoto, T., Imamura, S., Suzuki, K., Tsunoda, M., Amano, H., Sekiguchi, T., and Takenaka, A. (2008) Structures of *Arthrobacter globiformis* urate oxidase-ligand complexes, *Acta crystallographica. Section D, Biological crystallography* D64, 815-822.
- ⁸⁶ Schwarzenbacher, R., Stenner-Liewen, F., Liewen, H., Reed, J. C., and Liddington, R. C. (2004) Crystal structure of PqqC from *Klebsiella pneumoniae* at 2.1 Å resolution, *Proteins* 56, 401-403.
- ⁸⁷ Lee, D. S., Flachsova, E., Bodnarova, M., Demeler, B., Martasek, P., and Raman, C. S. (2005) Structural basis of hereditary coproporphyrinuria, *Proceedings of the National Academy of Sciences of the United States of America* 102, 14232-14237.
- ⁸⁸ Carlson, B. L., Ballister, E. R., Skordalakes, E., King, D. S., Breidenbach, M. A., Gilmore, S. A., Berger, J. M., and Bertozzi, C. R. (2008) Function and structure of a prokaryotic formylglycine-generating enzyme, *The Journal of biological chemistry* 283, 20117-20125.
- ⁸⁹ Fusetti, F., Schroter, K. H., Steiner, R. A., van Noort, P. I., Pijning, T., Rozeboom, H. J., Kalk, K. H., Egmond, M. R., and Dijkstra, B. W. (2002) Crystal structure of the copper-containing quercetin 2,3-dioxygenase from *Aspergillus japonicus*, *Structure (London, England : 1993)* 10, 259-268.
- ⁹⁰ Gopal, B., Madan, L. L., Betz, S. F., and Kossiakoff, A. A. (2005) The crystal structure of a quercetin 2,3-dioxygenase from *Bacillus subtilis* suggests modulation of enzyme activity by a change in the metal ion at the active site(s), *Biochemistry* 44, 193-201.

-
- ⁹¹ Steiner, R. A., Kalk, K. H., and Dijkstra, B. W. (2002) Anaerobic enzyme-substrate structures provide insight into the reaction mechanism of the copper-dependent quercetin 2,3-dioxygenase, *Proceedings of the National Academy of Sciences of the United States of America* 99, 16625-16630.
- ⁹² Sara Bowen (2010) Insights into the Role of the Metal-Binding Sites of Quercetin 2,3-Dioxygenase from *Bacillus subtilis*. PhD dissertation, Arizona State University.
- ⁹³ Bugg, T. D. H., and Lin, G. (2001) Solving the riddle of the intradiol and extradiol catechol dioxygenases: how do enzymes control hydroperoxide rearrangements?, *Chemical Communications*, 941-952.
- ⁹⁴ Dai, Y., Pochapsky, T. C., and Abeles, R. H. (2001) Mechanistic studies of two dioxygenases in the methionine salvage pathway of *Klebsiella pneumoniae*, *Biochemistry* 40, 6379-6387.
- ⁹⁵ Schaab, M. R., Barney, B. M., and Francisco, W. A. (2006) Kinetic and spectroscopic studies on the quercetin 2,3-dioxygenase from *Bacillus subtilis*, *Biochemistry* 45, 1009-1016.
- ⁹⁶ Scarpellini, M., Wu, A. J., Kampf, J. W., and Pecoraro, V. L. (2005) Corroborative models of the cobalt(II) inhibited Fe/Mn superoxide dismutases, *Inorganic chemistry* 44, 5001-5010.
- ⁹⁷ Parschat, K., Overhage, J., Strittmatter, A. W., Henne, A., Gottschalk, G., and Fetzner, S. (2007) Complete nucleotide sequence of the 113-kilobase linear catabolic plasmid pAL1 of *Arthrobacter nitroguajacolicus* Ru61a and transcriptional analysis of genes involved in quinaldine degradation, *Journal of bacteriology* 189, 3855-3867.
- ⁹⁸ Niewerth, H., Schuldes, J., Parschat, K., Kiefer, P., Vorholt, J. A., Daniel, R., and Fetzner, S. (2012) Complete genome sequence and metabolic potential of the quinaldine-degrading bacterium *Arthrobacter* sp. Rue61a, *BMC genomics* 13, 534.
- ⁹⁹ Pustelny, C., Albers, A., Buldt-Karentzopoulos, K., Parschat, K., Chhabra, S. R., Camara, M., Williams, P., and Fetzner, S. (2009) Dioxygenase-mediated quenching of quinolone-dependent quorum sensing in *Pseudomonas aeruginosa*, *Chemistry & biology* 16, 1259-1267.
- ¹⁰⁰ Fischer, F., Kunne, S., and Fetzner, S. (1999) Bacterial 2,4-dioxygenases: new members of the alpha/beta hydrolase-fold superfamily of enzymes functionally related to serine hydrolases, *Journal of bacteriology* 181, 5725-5733.
- ¹⁰¹ Nardini, M., and Dijkstra, B. W. (1999) Alpha/beta hydrolase fold enzymes: the family keeps growing, *Current opinion in structural biology* 9, 732-737.

-
- ¹⁰² Bugg, T. D. (2004) Diverse catalytic activities in the alphabeta-hydrolase family of enzymes: activation of H₂O, HCN, H₂O₂, and O₂, *Bioorganic chemistry* 32, 367-375.
- ¹⁰³ Gabison, L., Chopard, C., Colloc'h, N., Peyrot, F., Castro, B., Hajji, M. E., Altarsha, M., Monard, G., Chiadmi, M., and Prangé, T. (2011) X-ray, ESR, and quantum mechanics studies unravel a spin well in the cofactor-less urate oxidase, *Proteins: Structure, Function, and Bioinformatics* 79, 1964-1976.
- ¹⁰⁴ Frerichs-Deeken, U., Ranguelova, K., Kappl, R., Huttermann, J., and Fetzner, S. (2004) Dioxygenases without requirement for cofactors and their chemical model reaction: compulsory order ternary complex mechanism of 1H-3-hydroxy-4-oxoquinoline 2,4-dioxygenase involving general base catalysis by histidine 251 and single-electron oxidation of the substrate dianion, *Biochemistry* 43, 14485-14499.
- ¹⁰⁵ Fetzner, S. (1998) Bacterial degradation of pyridine, indole, quinoline, and their derivatives under different redox conditions, *Applied microbiology and biotechnology* 49, 237-250.
- ¹⁰⁶ Ilangovan, A., Fletcher, M., Rampioni, G., Pustelny, C., Rumbaugh, K., Heeb, S., Cámara, M., Truman, A., Chhabra, S. R., Emsley, J., and Williams, P. (2013) Structural Basis for Native Agonist and Synthetic Inhibitor Recognition by the *Pseudomonas aeruginosa* Quorum Sensing Regulator PqsR (MvfR), *PLoS Pathog* 9, e1003508.
- ¹⁰⁷ Thierbach, S., Bui, N., Zapp, J., Chhabra, S. R., Kappl, R., and Fetzner, S. (2014) Substrate-assisted O₂ activation in a cofactor-independent dioxygenase, *Chemistry & biology* 21, 217-225.
- ¹⁰⁸ Philip J. Brandhuber, (2009) Methods for the detection of residual concentration of hydrogen peroxide in advanced oxidation processes, WateReuse Foundation.
- ¹⁰⁹ Samuni, A., Goldstein, S., Russo, A., Mitchell, J. B., Krishna, M. C., and Neta, P. (2002) Kinetics and mechanism of hydroxyl radical and OH-adduct radical reactions with nitroxides and with their hydroxylamines, *Journal of the American Chemical Society* 124, 8719-8724.
- ¹¹⁰ Morris, S., Sosnovsky, G., Hui, B., Huber, C. O., Rao, N. U., and Swartz, H. M. (1991) Chemical and electrochemical reduction rates of cyclic nitroxides (nitroxyls), *Journal of pharmaceutical sciences* 80, 149-152.
- ¹¹¹ Sushma Manda, Kei Ohkubo, Haruko Yakumaru, Ken-ichiro Matsumoto, Toshihiko Ozawa, Nobuo Ikota, Shunichi Fukuzumi and Kazunori Anzai. (2007) Nitroxyl radicals: electrochemical redox behaviour and structure–activity relationships, *Organic & biomolecular chemistry* 5, 3877-4024.

-
- ¹¹² Soule, B. P., Hyodo, F., Matsumoto, K., Simone, N. L., Cook, J. A., Krishna, M. C., and Mitchell, J. B. (2007) The chemistry and biology of nitroxide compounds, *Free Radical Biology and Medicine* 42, 1632-1650.
- ¹¹³ Israeli, A., Patt, M., Oron, M., Samuni, A., Kohen, R., and Goldstein, S. (2005) Kinetics and mechanism of the comproportionation reaction between oxoammonium cation and hydroxylamine derived from cyclic nitroxides, *Free Radical Biology and Medicine* 38, 317-324.
- ¹¹⁴ Baur, J. E., Wang, S., and Brandt, M. C. (1996) Fast-scan voltammetry of cyclic nitroxide free radicals, *Analytical Chemistry* 68, 3815-3821.
- ¹¹⁵ Dikalov, S. I., Vitek, M. P., Maples, K. R., and Mason, R. P. (1999) Amyloid β Peptides Do Not Form Peptide-derived Free Radicals Spontaneously, but Can Enhance Metal-catalyzed Oxidation of Hydroxylamines to Nitroxides, *Journal of Biological Chemistry* 274, 9392-9399.
- ¹¹⁶ Dikalov, S., and Fink, B. (2005) ESR techniques for the detection of nitric oxide in vivo and in tissues, *Methods in enzymology* 396, 597-610.
- ¹¹⁷ Khatri, J. J., Johnson, C., Magid, R., Lessner, S. M., Laude, K. M., Dikalov, S. I., Harrison, D. G., Sung, H. J., Rong, Y., and Galis, Z. S. (2004) Vascular oxidant stress enhances progression and angiogenesis of experimental atheroma, *Circulation* 109, 520-525.
- ¹¹⁸ Dikalov, S. I., Vitek, M. P., and Mason, R. P. (2004) Cupric-amyloid beta peptide complex stimulates oxidation of ascorbate and generation of hydroxyl radical, *Free radical biology & medicine* 36, 340-347.
- ¹¹⁹ Halliwell B., Gutteridge J.M. (1999) *Free Radicals in Biology and Medicine*. Oxford, U.K.: Oxford University Press.
- ¹²⁰ Berglund, G. I., Carlsson, G. H., Smith, A. T., Szoke, H., Henriksen, A., and Hajdu, J. (2002) The catalytic pathway of horseradish peroxidase at high resolution, *Nature* 417, 463-468.
- ¹²¹ Gorris, H. H., and Walt, D. R. (2009) Mechanistic Aspects of Horseradish Peroxidase Elucidated through Single-Molecule Studies, *Journal of the American Chemical Society* 131, 6277-6282.
- ¹²² Mohanty, J. G., Jaffe, J. S., Schulman, E. S., and Raible, D. G. (1997) A highly sensitive fluorescent micro-assay of H₂O₂ release from activated human leukocytes using a dihydroxyphenoxazine derivative, *Journal of immunological methods* 202, 133-141.

-
- ¹²³ Towne, V., Will, M., Oswald, B., and Zhao, Q. (2004) Complexities in horseradish peroxidase-catalyzed oxidation of dihydroxyphenoxazine derivatives: appropriate ranges for pH values and hydrogen peroxide concentrations in quantitative analysis, *Anal Biochem* 334, 290-296.
- ¹²⁴ Reszka, K. J., Wagner, B. A., Burns, C. P., and Britigan, B. E. (2005) Effects of peroxidase substrates on the Amplex red/peroxidase assay: antioxidant properties of anthracyclines, *Anal Biochem* 342, 327-337.
- ¹²⁵ Dikalov, S. I., Dikalova, A. E., Bikineyeva, A. T., Schmidt, H. H., Harrison, D. G., and Griendling, K. K. (2008) Distinct roles of Nox1 and Nox4 in basal and angiotensin II-stimulated superoxide and hydrogen peroxide production, *Free radical biology & medicine* 45, 1340-1351.
- ¹²⁶ Busi, E., Sinicropi, A., Terzuoli, L., Marinello, E., and Basosi, R. (2007) Identification and structural characterization of a transient radical species in the uricase reaction mechanism, *Appl. Magn. Reson.* 31, 471-482.
- ¹²⁷ Brett, A. M. O., and Ghica, M. E. (2003) Electrochemical oxidation of quercetin, *Electroanalysis* 15, 1745-1750.
- ¹²⁸ Timbola, A. K., de Souza, C. D., Giacomelli, C., and Spinelli, A. (2006) Electrochemical oxidation of quercetin in hydro-alcoholic solution, *Journal of the Brazilian Chemical Society* 17, 139-148.
- ¹²⁹ Merkens, H., Kappl, R., Jakob, R. P., Schmid, F. X., and Fetzner, S. (2008) Quercetinase QueD of *Streptomyces* sp FLA, a Monocupin Dioxygenase with a Preference for Nickel and Cobalt, *Biochemistry* 47, 12185-12196.
- ¹³⁰ Merkens, H., Sielker, S., Rose, K., and Fetzner, S. (2007) A new monocupin quercetinase of *Streptomyces* sp. FLA: identification and heterologous expression of the queD gene and activity of the recombinant enzyme towards different flavonols, *Archives of microbiology* 187, 475-487.
- ¹³¹ van Faassen, E. and Vanin, A. (eds.) (2007) Radicals for life: The various forms of nitric oxide. Elsevier, Amsterdam.
- ¹³² van Faassen, E. and Vanin, A. (2004) "Nitric Oxide", in Encyclopedia of Analytical Science, 2nd ed., Elsevier.
- ¹³³ Kuzkaya, N., Weissmann, N., Harrison, D. G., and Dikalov, S. (2003) Interactions of peroxynitrite, tetrahydrobiopterin, ascorbic acid, and thiols: implications for uncoupling endothelial nitric-oxide synthase, *The Journal of biological chemistry* 278, 22546-22554.

-
- ¹³⁴ Belousov, V. V., Fradkov, A. F., Lukyanov, K. A., Staroverov, D. B., Shakhbazov, K. S., Terskikh, A. V., and Lukyanov, S. (2006) Genetically encoded fluorescent indicator for intracellular hydrogen peroxide, *Nature methods* 3, 281-286.
- ¹³⁵ Malinouski, M., Zhou, Y., Belousov, V. V., Hatfield, D. L., and Gladyshev, V. N. (2011) Hydrogen Peroxide Probes Directed to Different Cellular Compartments, *PLoS ONE* 6, e14564.
- ¹³⁶ Averill, B. A., Moulijn, J. A., van Santen, R. A., and van Leeuwen, P. W. N. M. (1999) *Catalysis: An Integrated Approach: An Integrated Approach*, Elsevier Science.
- ¹³⁷ Muller, K. (1996) Antipsoriatic anthrones: aspects of oxygen radical formation, challenges and prospects, *General pharmacology* 27, 1325-1335.
- ¹³⁸ Balogh-Hergovich, É. and Speier, G. (2001) Kinetics and Mechanism of the Base-Catalyzed Oxygenation of Flavonol in DMSO–H₂O Solution, *The Journal of Organic Chemistry* 66, 7974-7978.

PUBLICATIONS

Sven Thierbach, **Nguyen Bui**, Josef Zapp, Siri Ram Chhabra, Reinhard Kappl, Susanne Fetzner, Substrate-assisted O₂ activation in a cofactor-independent dioxygenase, *Chemistry and Biology Journal*, **2014**, 21 217–225.

Bui N.N., Nianios D, Fetzner S, Kappl R. Oxidizing intermediates in Ni²⁺- and Co²⁺-containing quercetin 2,4-dioxygenase (manuscript in preparation).

Bui N.N., Mirceski V, Kappl R. Voltammetric and electron spin resonance studies of cyclic hydroxylamine CMH (CPH) applying for the detection of reactive oxygen species (ROS) (manuscript in preparation).

CONFERENCES

N.N. Bui, B. Pasiaka, E.J. Slowik, I. Bogeski, M. Hoth, S. Thierbach, D. Nianios, S. Fetzner, R. Kappl (2014) IX Conference of European Federation of EPR Societies, EFEPR, 7-11 September 2014, Marseille, France: Cyclic Hydroxylamines for EPR Detection of Transient Radicals and Reactive Oxygen Species (Poster).

Bastian Pasiaka, **Nguyen Bui**, David Conrad, Ivan Bogeski, Markus Hoth, Reinhard Kappl (2012) The 45th Annual International Meeting of the EPR Spectroscopy Group of the Royal Society of Chemistry, 25th – 29th March 2012, Manchester, England: A “physiological” ST/EPR study: activation and superoxide radical production of NADPH-Oxidase in human monocytes (Poster).

ACKNOWLEDGEMENTS

First and foremost, I would like to express my deep gratitude to my advisor Dr. Reinhard Kappl. This dissertation would have been impossible if there were no intellectual support and patient guidance from Dr. Kappl. During my entire PhD period, I have received not only scientific knowledge but countless support of my everyday life from him, some kind of life without any understanding of the native language: Deutsch. Besides many hours of lecturing knowledge and discussing experimental details, he even helped me out in paper and thesis writing which caused him many extra hours of work beyond his duties. I am deeply indebted and feel very proud and lucky to be a student in his group. Dr. Kappl sets a lifetime's worth of example for me to follow, as a scientist and as a person.

I would also like to acknowledge Prof. Dr. Markus Hoth for offering me an opportunity and all facilities to work as a member in his group. I also give my special thanks to Prof. Dr. Richard Zimmerman as my committee member.

I thank our collaborators, Prof. Dr. Susanne Fetzner, Dr. Dimitrios Nianios and Dr. Sven Thierbach from university of Münster for their valuable cooperation and Prof. Dr. Valentin Mirceski from Ss. Cyril and Methodius University in Macedonia for exchanging the electrochemical knowledge that helped me to improve my professional qualification.

I would also like to thank Regine Kaleja, our secretary, who helped me a lot with official paper-work and many thanks to Gerhard Bracic, Josef Marx, and Rüdiger Stumpf for their technical assistances.

I am very much grateful to Dr. Monika Bozem, who has always been a very warm person helping and encouraging me with many good advices and helpful lessons. Special thanks to my friends and colleagues in the group of Biophysics for their friendship, encouragement and discussions. I thank Chuong H Nguyen and Khon C Huynh for their long-lasting friendship that helped me to withstand and handle a lot of difficulties in a new country. I thank David Przybilla, Katerina Stankoska, Christian Holzmann and Ewa Slowik for many pleasant and helpful conversations, for their patience of listening to my endless thoughts and concerns and thank all Vietnamese friends who were in Saarbrücken for all the fun we had. As being far away from home, I was greatly fortunate to be with you all this time together.

Above all, as always, I would like to thank my family for their unlimited love and constant support. Without them, I would not have gone this far.

In the final, I would like to express my appreciation for those people who had helped and contributed to the accomplishment of the thesis but have not been mentioned above.

CURRICULUM VITAE

Full Name: NHAT NGUYEN BUI

Phone: +49(0)6841/16-16218

Nationality: Vietnamese

Mobile: +49 176 7386 6837

Sex: Female

E-mail: nguyen.bui@uks.eu

Date of birth: November 07th, 1984

RESEARCH INTEREST and EXPERIENCES

- 2011 – Present PhD fellowship, Biophysics Department, Medical Faculty, Saarland University, Saarland, Federal Republic of Germany.
- 2010 – 2011 Research assistant, Applied Physical Chemistry Laboratory, Faculty of Chemistry, University of Sciences (Vietnam National University – Ho Chi Minh City) (VNU-HCM), Vietnam.
- 2007 – 2010 Master work, Organometallic Laboratory, Division of Energy Systems Research, Ajou University, Suwon, Republic of Korea.
- 2005 – 2006 Bachelor work, Electrochemical Laboratory, Physical Chemistry Department, University of Sciences (VNU – HCM), Vietnam.
-

EDUCATION

- | | | |
|------|---|----|
| 2010 | Organometallic Laboratory, Division of Energy System Research, Ajou University, Republic of Korea. | MS |
| 2006 | Department of Physical Chemistry, Vietnam National University of Ho Chi Minh City (VNU – HCM), Vietnam. | BS |
-

PUBLICATIONS and CONFERENCES**Publications**

1. Sven Thierbach, **Nguyen Bui**, Josef Zapp, Siri Ram Chhabra, Reinhard Kappl, Susanne Fetzner, Substrate-assisted O₂ activation in a cofactor-independent dioxygenase, *Chemistry and Biology Journal*, **2014**, 21, 217–225.
2. Thoa Thi Phuong Nguyen, Bao Kim Duong Do, **Nguyen Nhat Bui**, Minh Anh Pham, Thinh Viet Nguyen, Selectiveness of copper and polypyrrole modified copper electrodes for nitrate electroreduction: a comparative study and application in ground water, *ECS Transaction*, **2013**, 53 (16) 41-52.
3. **Nhat Nguyen Bui**, Duc Viet Dinh, Viet Thinh Nguyen, Thi Phuong Thoa Nguyen, Nitrate electroreduction in aqueous solution using polypyrrole modified copper electrode *J. Chem. (Vietnam)* **2010**(4C) 283-290.
4. Thi Phuong Thoa Nguyen, Viet Thinh Nguyen, **Nhat Nguyen Bui**, Duong Kim Bao Do, Anh Minh Pham, Synthesis of nano-structured polypyrrole/ copper electrodes for nitrate and nitrite electroreduction, *Adv. Nat. Sci.: Nanosci. Nanotechnol.* **2010**, 1, 035013.
5. **Nhat-Nguyen Bui**, Xuan-Huong Ho, Sun-il Mho, and Hye-Young Jang*, Organocatalyzed α -Oxyamination of Aldehydes Using Anodic Oxidation, *Eur. J. Org. Chem.* **2009**, 31, 5309-5312.
6. **Nhat-Nguyen Bui**, Jong-Tai Hong, Xuan-Huong Ho, Sun-il Mho, and Hye-Young Jang*, Correlation of Electrochemical Characteristics and Catalytic Activity of Rh₂(OAc)₄ in the Presence of Various Phosphines, *Bull. Korean Chem. Soc.* **2008**, 29(8), 1624-1626.
7. **Nhat-Nguyen Bui**, Jong-Tai Hong, Sun-il Mho, and Hye-Young Jang* “A Ferrocene Derivative Redox Sensor for Mercuric Ion: Synthesis and Electrochemical Study”, *Bull. Korean Chem. Soc.* **2008**, 29(7) 1395-1398.

8. Viet Thinh Nguyen, Viet Hai Le, **Nhat-Nguyen Bui**, Dang Thi Kim Thoa, Nguyen-Thi Phuong Thoa, Electroreduction of nitrate ions on copper and copper modified by pyrrole electrodes, *Journal Science & Technology Development(Vietnam)* **2008**, 11(1) 68-73.
9. Nguyen Viet Thinh, Le Viet Hai, **Bui Nhat Nguyen**, Nguyen Thi Phuong Thoa, Le Viet Hung, Factors influence on nitrate- and nitrite- reduction activity of the copper electrode modified by polypyrrole, *J. of Science and Technology (Vietnam)* **2008**, 46 (4A) 85-92.
10. Jong-Tai Hong, **Nhat-Nguyen Bui**, Sun-il Mho, Won-Seob Cho, Hye-Young Jang*, Synthesis and Electrochemical Studies of a Ferrocene Derivative for the Application to Metal Ion Sensor, *Bull. Korean Chem. Soc.* **2008**, 29(11) 2097-2102.
11. Sung Jae Na, Bun Yeoul Lee, **Nhat-Nguyen Bui**, Sun-il Mho, Hye-Young Jang*, A new dirhodiumtetraacetatecarbenoid: Synthesis, crystal structure and catalytic application, *J. Organomet. Chem.* **2007**, 692,5523–5527.

Conferences

1. The IXth European Federation of Electron Paramagnetic Resonance (EF-EPR) conference, 7th – 11th September **2014**, Marseilles, France.
2. Redox Biology Symposium, 11th – 12th April **2013**, Kaiserslautern, Rhineland – Palatinate, Germany.
3. Redox Biology Symposium, 17th – 18th September **2012**, Kaiserslautern, Rhineland-Palatinate, Germany.
4. Engineering of Functional Interfaces (EnFI) Workshop, 16th – 17th July **2012**, Zweibrücken, Rhineland – Palatinate, Germany.
5. The 45th Annual International Meeting of the EPR Spectroscopy Group of the Royal Society of Chemistry, 25th – 29th March **2012**, Manchester, England
6. The 5th National Chemistry Conference, November **2010**, Hanoi, Vietnam.

7. The 5th International Workshop on Advanced Materials Science and Nanotechnology (IWAMSN2010), November **2010**, Hanoi, Vietnam.
 8. The 6th Asian Conference on Electrochemistry ACEC, **2008**, Taipei.
 9. Korean Chemical Society 102nd National Meeting, October **2008** ICC, Jeju, Korea.
 10. Korean Chemical Society 101st National Meeting, April **2008** KINTEX, Goyang-si, Korea.
 11. The First International Workshop on Nanotechnology and Application IWNA **2007**, Ho Chi Minh City, Viet Nam.
 12. Scientific conference **2006**, University of Natural Sciences, Vietnam National University of HCM city, Viet Nam.
-

HONORS and AWARDS

- | | |
|-------------|-------------------------------------|
| 2007 – 2009 | Brain Korea 21 Fellowships (BK21) |
| 2007 – 2009 | Ajou University's Honor Scholarship |

SKILLS/STRENGTHS

- ✚ Spectroscopy, chromatography, and voltammetry
 - Strong understanding of Electron Paramagnetic Resonance (EPR): detection and quantification of reactive oxygen species (ROS) including superoxide, hydrogen peroxide in chemical, biological and cellular systems.
 - Experienced on working with Nuclear Magnetic Resonance (NMR), X-ray spectroscopy, UV-Vis spectroscopy, High performance liquid chromatography (HPLC), Gas chromatography (GC) and Column chromatography: determination of molecular structure of synthetic organic compounds and characterization of nano-particles.
 - Strong understanding of Electrochemical processes, defining electron transfer mechanism and redox properties of redox active species, back-

ground knowledge of voltammetry techniques: cyclic voltammetry (CV), square-wave voltammetry (SWV), differential pulse voltammetry (DPV)...

- ✚ Well understanding about the Synthesis of Organo-metallic Compounds, good at defining Organic Reaction Mechanism.
- ✚ Protein (enzyme) reaction mechanism
- ✚ Languages: Vietnamese (Native), English (Fluent), Korean (Basic).